Thèse de Doctorat

Domaine: STIC

Spécialité: Traitement du Signal

Ecole Doctorale "Sciences et Technologies de l'Information, des Télécommunications et des Systèmes"

Présentée par:

Jonathan PISANE

Sujet:

Reconnaissance automatique de cibles par signaux de radars passifs bistatiques

Automatic target recognition using passive bistatic radar signals

Soutenue le 04 avril 2013 devant les membres du jury:

M. Sylvain Azarian	SONDRA, SUPELEC	Encadrant
M. René Garello	Telecom-Bretagne	Rapporteur
M. Hugh Griffiths	University College London	Examinateur
M. Marc Lesturgie	ONERA/SONDRA, SUPELEC	Directeur de thèse
M. Xavier Neyt	Royal Military Academy	Rapporteur
M. Jacques Verly	University of Liège	Directeur de thèse
M. Luc Vignaud	ONERA	Examinateur
M. Eric Walter	SUPELEC	Examinateur
M. Louis Wehenkel	University of Liège	Examinateur

Abstract

We present the design, development, and test of three novel, distinct automatic target recognition (ATR) systems for the recognition of airplanes and, more specifically, non-cooperative airplanes, *i.e.* airplanes that do not provide information when interrogated, in the framework of passive bistatic radar systems. Passive bistatic radar systems use one or more illuminators of opportunity (already present in the field), with frequencies up to 1 GHz for the transmitter part of the systems considered here, and one or more receivers, deployed by the persons managing the system, and not co-located with the transmitters. The sole source of information are the signal scattered on the airplane and the direct-path signal that are collected by the receiver, some basic knowledge about the transmitter, and the geometrical bistatic radar configuration.

The three distinct ATR systems that we built respectively use the radar images, the bistatic complex radar cross-section (BS-RCS), and the bistatic radar cross-section (BS-RCS) of the targets. We use data acquired either on scale models of airplanes placed in an anechoic, electromagnetic chamber or on real-size airplanes using a bistatic testbed consisting of a VOR transmitter and a software-defined radio (SDR) receiver, located near Orly airport, France.

We describe the radar phenomenology pertinent for the problem at hand, as well as the mathematical underpinnings of the derivation of the bistatic RCS values and of the construction of the radar images.

For the classification of the observed targets into pre-defined classes, we use either extremely randomized trees or subspace methods. A key feature of our approach is that we break the recognition problem into a set of sub-problems by decomposing the parameter space, which consists of the frequency, the polarization, the aspect angle, and the bistatic angle, into regions. We build one recognizer for each region.

We first validate the extra-trees method on the radar images of the MSTAR dataset, featuring ground vehicles. We then test the method on the images of the airplanes constructed from data acquired in the anechoic chamber, achieving a probability of correct recognition up to 0.99.

We test the subspace methods on the BS-CRCS and on the BS-RCS of the airplanes extracted from the data acquired in the anechoic chamber, achieving a probability of correct recognition up to 0.98, with variations according to the frequency band, the polarization, the sector of aspect angle, the sector of bistatic angle, and the number of (Tx,Rx) pairs used.

The ATR system deployed in the field gives a probability of correct recognition of 0.82, with variations according to the sector of aspect angle and the sector of bistatic angle.

Keywords: Automatic target recognition (ATR), non-cooperative target recognition (NCTR), classification, extremely randomized trees (extra-trees), subspace, passive radar, bistatic radar, radar cross-section, complex radar cross-section, illuminator of opportunity, VOR, software-defined radio (SDR), airplanes, anechoic chamber, air traffic control.

Acknowledgements

This work could not have been performed without the contributions of various persons. These persons all guided me and supported me at some time along my work.

In particular, I wish to thank my two supervisors, Marc Lesturgie, Director of the SONDRA lab of SUPELEC, and Jacques Verly, Professor in the Department of Electricity, Electronics, and Computer Science of the University of Liège, for having accepted to coach me during this thesis. Their advice throughout the entire duration of the thesis was invaluable. I really enjoyed the various discussions we have had, whether technical or not. I hope they have made me a better scientist, a better engineer, and a better person.

I also wish to express my deepest gratitude to Sylvain Azarian for his technical advice throughout the last two years of the thesis, and for his various comments that helped me make this manuscript clearer. I also thank him for his invaluable help during the experiments that could not have been performed without him. I also wish to thank Raphaël Marée for the various discussions we have had on the different classification techniques, and for his help in understanding extra-trees and the PiXiT software.

I wish to thank Professor Garello, Professor Griffiths, Professor Neyt, Doctor Vignaud, Doctor Walter, and Professor Wehenkel for having accepted to be part of my jury. I am really grateful for the interest they show for my work.

During this thesis, I have had the opportunity to work both at the SONDRA lab of SUPELEC, and among the Department of Electricity, Electronics, and Computer Science of the University of Liège. Let the people of these two entities be thanked for the nice time I have enjoyed with them. I have had a particularly great time with Frédéric Brigui, Chin Yuan Chong, Jacques El-Khoury, Jérôme Euzière, Pierre Formont, Israël Hinostroza, Mélanie Mahot, Azza Mokadem, and Danny Tan at SONDRA, and with Nicolas Crosset, Géraldine Guerri, Samuel Hiard, Nicolas Marchal, François Schnitzler, and Xavier Werner at the University of Liège. I also wish to thank all the PhD students of the "Réseau des Doctorants" of the University of Liège for the projects we did together, especially the 2009 "Rentrée des Doctorants" and the discussions we have had.

During these four years, I have had the opportunity to coach several MS theses at the University of Liège, in the context of the OUFTI-1 project. Since I believe this experience has enriched me, I would like to thank all the members of such a nice project, and the different students I tried to guide the best I could.

I also wish to thank Anne-Hélène Picot at SONDRA and Marie-Berthe Lecomte, Danielle Bonten, and Sandrine Lovinfosse at the University of Liège for having made the administrative side of my thesis easier to deal with.

Let me also thank the Belgian National Fund for Scientific Research (FRS-FNRS) for having granted me a scholarship of the Fund for Research in Industry and Agriculture (FRIA) during these fours years.

Table of Contents

x

Résumé

I Introduction

I.1 Problème à traiter

Dans cette thèse, nous étudions le problème de la reconnaissance automatique de cibles en utilisant des signaux de radars passifs bistatiques, afin de détecter des anomalies dans le trafic aérien civil. Les cibles considérées sont donc des avions.

Dans cette section, nous décrivons d'abord le fonctionnement du contrôle du trafic aérien civil, et expliquons les raisons pour lesquelles des anomalies peuvent se produire. Nous présentons ensuite la solution que l'on implémente, et en particulier, les différents concepts que sont les radars passif bistatiques et la reconnaissance automatique de cibles.

I.2 Contexte: le contrôle du trafic aérien civil

Le trafic aérien civil est contrôlé par deux types de radars: les radars primaires et les radars secondaires. Les radars primaires détectent la présence d'avions. Ils émettent un signal qui est réfléchi sur les avions. Par calcul à partir du signal réfléchi, ils détectent et localisent les avions.

Les radars secondaires servent à l'identification des avions. Les radars secondaires interrogent les transpondeurs des avions, et ceux-ci leur répondent en envoyant des informations telles que leur identification ICAO et leur position acquise par GPS.

L'identification d'avions requiert donc un radar secondaire et un transpondeur de bord. Des avions tels que les petits avions personnels n'étant pas équipés de tels transpondeurs, leur identification n'est pas garantie par des radars secondaires. Pour reconnaitre des avions, nous utilisons, dans cette thèse, des radars passifs bistatiques.

I.3 Solution au problème posé

Nous procédons à la reconnaissance des avions, appelés cibles, par l'utilisation de signaux de radars passifs bistatiques. Le schéma de la figure 1 représente une situation réaliste du problème traité. Un avion inconnu est illuminé par le signal émis par un émetteur d'opportunité. Ce signal est réfléchi par l'avion, et acquis par un récepteur. Le système de reconnaissance automatique de cibles (RAC) détermine ensuite la classe de l'avion sur base de ce signal réfléchi.

Les classes des avions à reconnaitre sont définies sur la base des caractéristiques physiques de ces avions (aspect et taille). Par exemple, deux avions de même taille se verront attribuer la même classe, même s'ils sont de marques et/ou de compagnies aériennes différentes.
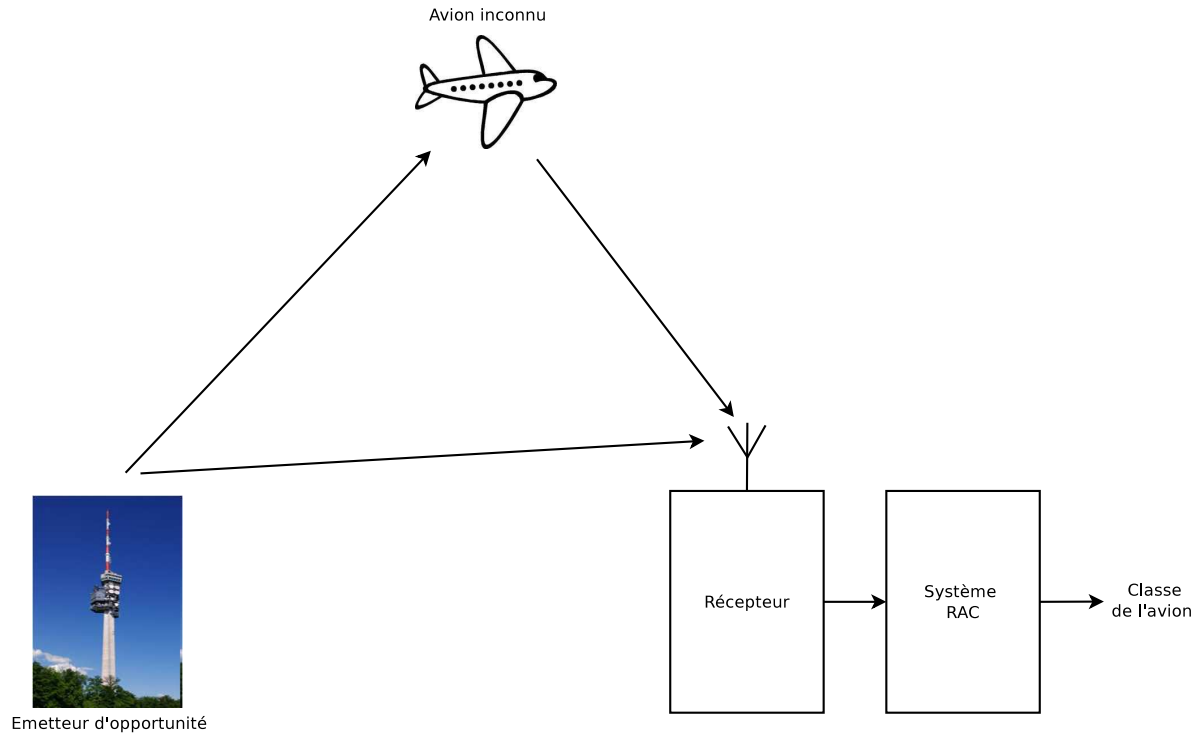
Figure 1: *Configuration du système de RAC par radar passif bistatique servant à déterminer la classe de l'avion.*

Un radar bistatique se caractérise par le fait que l'émetteur (Tx) et le récepteur (Rx) ne sont pas co-localisés, comme représenté à la figure 2. L'angle bistatique β est un paramètre-clé de la configuration bistatique. Un radar est dit passif quand l'émetteur utilisé est déjà présent dans l'environnement, et n'est pas conçu ni utilisé spécifiquement à des fins de radar. Les émetteurs de radio FM sont un exemple d'émetteur d'opportunité.

A partir du signal réfléchi par un avion et acquis par le récepteur, la surface équivalente radar, complexe (SERC) ou réelle (SER), de cet avion peut être calculée. L'image radar de cet avion peut être construite à partir de sa SERC. Chacun des trois systèmes RAC que nous discutons dans cette thèse se base sur une de ces trois quantités. La système RAC utilisant l'image radar des avions est discuté à la section III, celui utilisant la SERC ou la SER acquise à partir de mesures en chambre anéchoïque est discuté à la section IV, et celui utilisant la SER acquise à partir de mesures en extérieur est discuté à la section V.

Dans cette thèse, nous nous plaçons dans le contexte de l'apprentissage supervisé, c'est-à-dire que le nombre de classes est connu au préalable, et que des données (images, SERC ou SER) pour chacune de ces classes sont disponibles, tant au moment
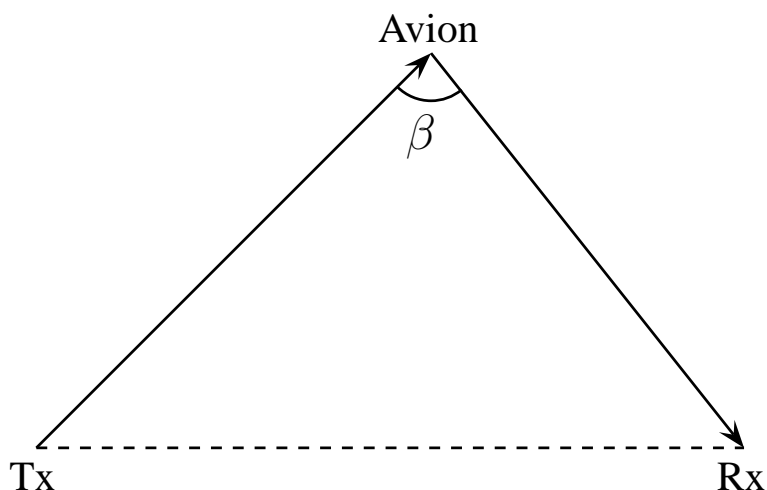
Figure 2: *Illustration de la configuration bistatique.*

de la construction du modèle de reconnaissance que du test de ce modèle. La figure 3 montre le bloc-diagramme schématique de l'étage de reconnaissance d'un système RAC. Les données sont séparées en un ensemble d'apprentissage (LS) et un ensemble de test (TS). Un certain nombre de vecteurs d'attributs sont extraits des données de chaque ensemble. Les vecteurs d'attributs du LS servent à construire un modèle de reconnaissance/classification qui est ensuite testé sur les vecteurs d'attributs du TS.
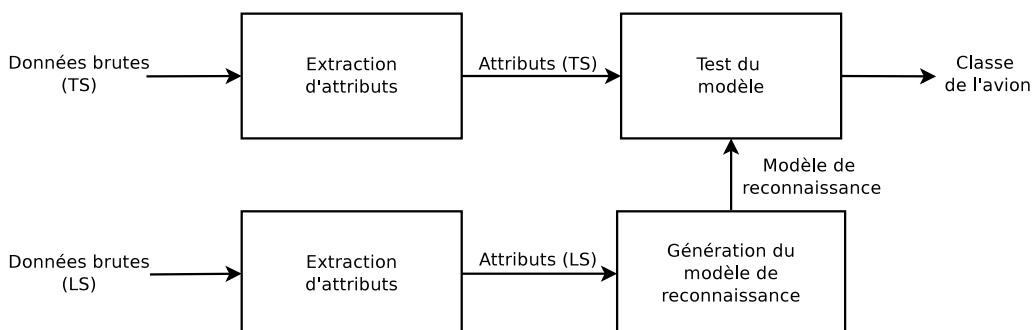
Figure 3: *Bloc-diagramme de l'étage de reconnaissance des systèmes RAC.*

Deux techniques de classification sont utilisées dans cette thèse; le modèle de reconnaissance consiste soit en un ensemble d'arbres de décision rendus extrêmement aléatoires (extra-trees), soit en un ensemble de sous-espaces vectoriels. Chacun des trois systèmes RAC utilise l'une ou l'autre de ces deux méthodes de classification.

I.4 Organisation du résumé

Le présent résumé est organisé comme suit. La section II résume les concepts de phénoménologie importants pour le problème traité, ainsi que la stratégie de reconnaissance que nous définissons à partir de la phénoménologie radar bistatique. La section III discute le système RAC basé sur les images des avions. La section IV discute le système RAC basé sur les SERC et les SER des avions acquises en chambre

anéchoïque. La section V discute le système RAC basé sur les SER d'avions acquises par un banc expérimental déployé dans le cadre de cette thèse. La section VI conclut le travail et résume les perspectives envisagées.

II Phénoménologie radar bistatique et stratégie de reconnaissance

Les trois systèmes de reconnaissance automatique de cibles (RAC) discutés dans les sections suivantes se basent sur la notion de surface équivalente radar, complexe (SERC) ou réelle (SER). Nous présentons dans cette section les éléments-clés de la phénoménologie radar bistatique qui nous permettent de définir une stratégie de reconnaissance.

II.1 Surface équivalente radar complexe et réelle

La figure 4 représente la géométrie d'une configuration bistatique. La cible illuminée est située au centre d'un repère orthonormé. L'émetteur est situé au point T et le récepteur au point R, à des distances respectives r_T et r_R de la cible. Les polarisations de l'émetteur et du récepteur sont respectivement notées par $\hat{\underline{\theta}}_T$ et $\hat{\underline{\phi}}_T$, et par $\hat{\underline{\theta}}_R$, $\hat{\underline{\phi}}_R$.
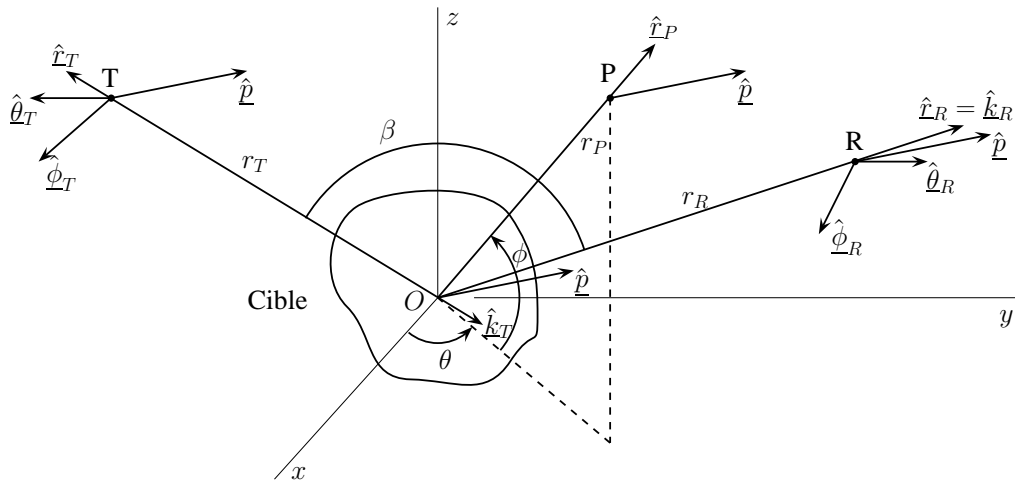
Figure 4: *Géométrie de la configuration bistatique considérée.*

La surface équivalente radar réelle (SER) d'un objet, ici la cible, dénotée par σ, est définie dans la littérature comme étant la mesure de l'énergie d'un signal qui est réfléchie par cet objet dans la direction du récepteur. On l'exprime comme

$$\sigma = \lim_{r_R \to \infty} 4\pi r_R^2 \frac{|\bar{\underline{E}}^r(\underline{r}_R)|^2}{|\bar{\underline{E}}^t(\underline{0})|^2}, \tag{1}$$

où r_R est la distance entre l'objet et le récepteur, $\bar{\underline{E}}^r(\underline{r}_R)$ le champ électrique au récepteur, et $\bar{\underline{E}}^t(\underline{0})$ le champ électrique transmis à la cible.

La surface équivalente radar complexe (SERC) d'un objet, dénotée par $\sqrt{\sigma}$, est définie dans la littérature par

$$\sqrt{\sigma} = \lim_{r_R \to \infty} 2\sqrt{\pi} r_R \frac{\underline{\bar{E}}^r(\underline{r}_R)}{\underline{\bar{E}}^t(\underline{0})} e^{jkr_R}, \tag{2}$$

avec les mêmes notations que pour la définition de la SER σ.

La littérature montre que, pour une configuration bistatique, la SERC et la SER d'un objet dépendent de quatre facteurs: la fréquence f du signal illuminant l'objet, le couple *Pol* de polarisations de l'émetteur et du récepteur, l'angle d'aspect α, et l'angle bistatique β. La figure 5 illustre la définition des angles α et β. L'angle α est défini comme l'angle entre la bissectrice $\underline{\hat{b}}$ de l'angle bistatique et la direction de vue de l'objet $\underline{\hat{s}}$.
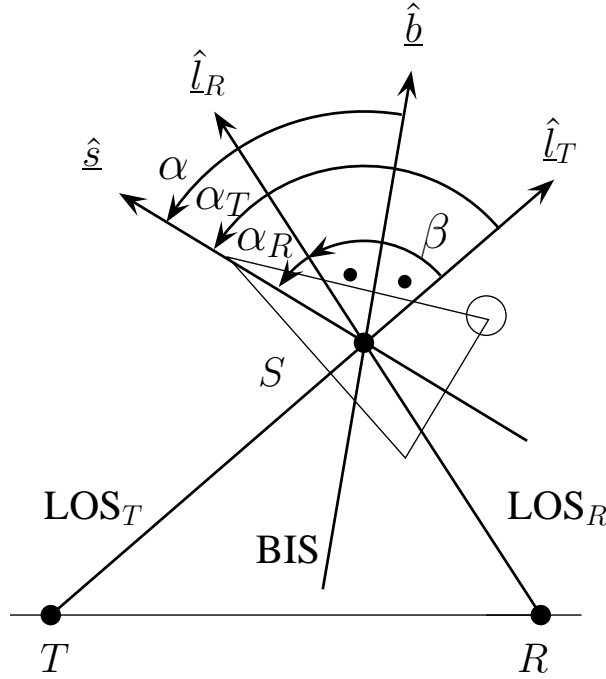
Figure 5: *Illustration des angles d'aspect α et bistatique β.*

L'angle bistatique β est défini comme l'angle entre les lignes de vue de l'émetteur et du récepteur, dénotées respectivement par $\underline{\hat{l}}_T$ et $\underline{\hat{l}}_R$. On distingue trois régions de bistatisme: la région pseudo-monostatique pour laquelle $\beta \leq 5°$, la région purement bistatique pour laquelle $5° \leq \beta \leq 180°$, et la région de diffusion vers l'avant pour laquelle $\beta \to 180°$. Dans cette thèse, nous nous plaçons dans la région purement bistatique.

Les quatre paramètres f, *Pol*, α et β définissent ainsi l'espace des paramètres de la SER, complexe ou réelle, d'un objet.

II.2 Régions de diffusion et définition des classes d'avions

Parmi les quatre paramètres dont dépendent la SER et la SERC, nous étudions brièvement, dans cette section, l'influence de la fréquence sur la SER et la SERC. En effet, la littérature montre que, selon la zone de diffusion dans laquelle se produisent les mécanismes de diffusion contribuant à la SER, soit la taille soit la forme de l'objet prédomine. La zone de diffusion est déterminée suivant le rapport λ/D, où λ correspond à la longueur d'onde du signal transmis, et D à la dimension caractéristique de l'objet. Ceci peut être résumé comme suit:

$$\begin{cases} \dfrac{\lambda}{D} \gg 1 \Rightarrow \text{Région de Rayleigh} \Rightarrow \text{Le volume est important pour la SER} \\[2mm] \dfrac{\lambda}{D} \approx 1 \Rightarrow \text{Région de résonance} \Rightarrow \text{Le volume et la taille sont importants pour la SER} \\[2mm] \dfrac{\lambda}{D} \ll 1 \Rightarrow \text{Région optique} \Rightarrow \text{La taille est importante pour la SER} \end{cases}$$

$$(3)$$

Cette notion de région de diffusion est utilisée dans la suite pour définir les classes des avions à reconnaitre. En effet, deux avions de même taille dont les mécanismes de diffusion sont en région de Rayleigh pourront difficilement être discriminés, et seront donc considérés comme appartenant à la même classe.

II.3 Stratégie de reconnaissance

La SER, complexe ou réelle, dépend des quatre paramètres que sont la fréquence f du signal émis, le couple de polarisations Pol de l'émetteur et du récepteur, l'angle d'aspect α et l'angle bistatique β.

Afin de définir la stratégie de reconnaissance, considérons une trajectoire d'un avion telle que celle représentée en deux dimensions à la figure 6. On considère que plusieurs émetteurs (Tx) et plusieurs récepteurs (Rx) sont présents dans le voisinage de l'avion, définissant ainsi un certain nombre de paires Tx-Rx. A chaque échantillon de la trajectoire de l'avion, nous pouvons y associer une valeur de SER (ou SERC) qui est fonction de la localisation (x,y) de l'avion, de la fréquence f_i et du couple de polarisation Pol_i de la $i^{\text{ème}}$ paire Tx-Rx.

Afin de relier l'espace physique à l'espace des paramètres, nous utilisons la figure 5 pour passer des coordonnées en (x,y) aux angles (α,β). La trajectoire d'un avion dans l'espace physique peut être alors représentée par plusieurs trajectoires dans l'espace des paramètres, comme illustré à la figure 7 pour deux paires Tx-Rx dans le voisinage de l'avion, les deux paires opérant à la même fréquence et la même polarisation.

Il est réaliste de supposer qu'un avion n'est observé que sur une partie de sa trajectoire. De plus, les couloirs aériens sont déterministes. Il est donc logique de penser qu'un avion ne sera observé que sur une partie du plan (α,β). Il est donc légitime de partitionner le plan (α,β) en régions, comme illustré à la figure 8, et de construire un classificateur par région. On procèdera alors à une expérience de classification par région.

L'espace des paramètres est également partitionné suivant la bande de fréquences, étant donné que les mécanismes de diffusion ne contribuent pas de la même manière
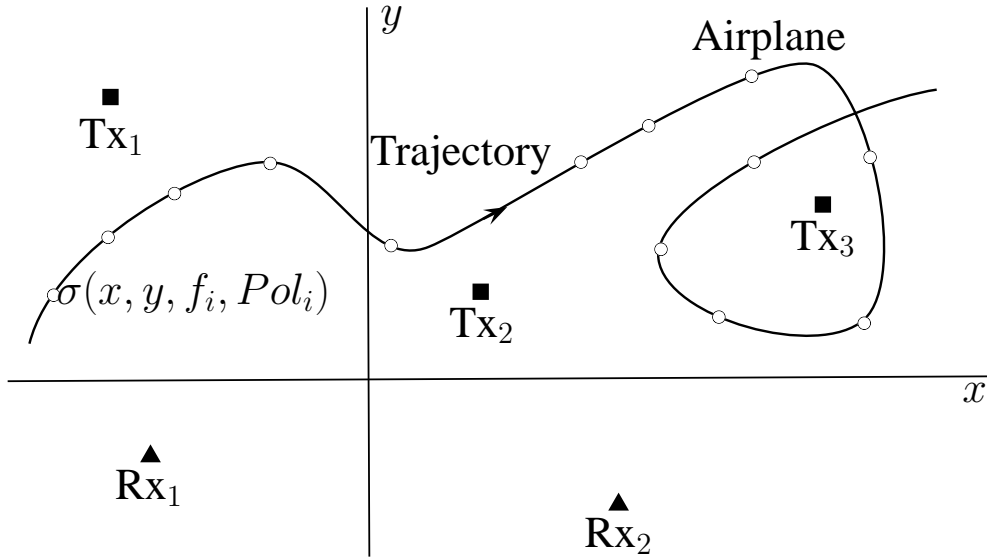
Figure 6: *Représentation de l'espace physique des paramètres.*
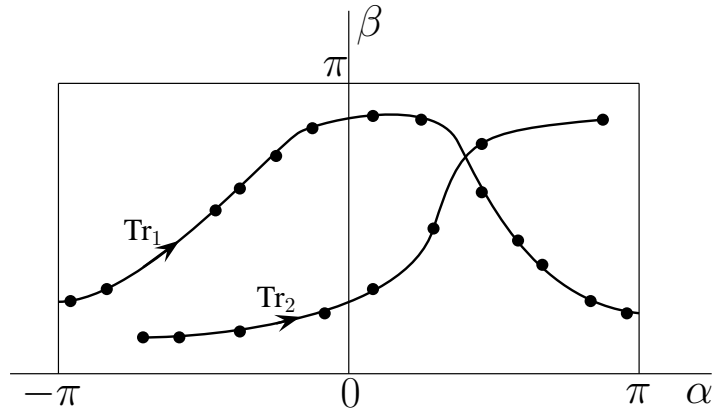
Figure 7: *Représentation de la trajectoire d'un avion dans le plan (α, β) de l'espace des paramètres.*

suivant la fréquence utilisée. De même, l'espace des paramètres est partitionné suivant la polarisation. En résumé, on a donc un espace de paramètres à quatre dimensions, f, *Pol*, α, β, que l'on partitionne en régions suivant chacune des quatre dimensions. Un classificateur sera construit pour chaque région et une expérience de reconnaissance sera conduite pour chaque région. Les développements des sections suivantes concernent systématiquement une seule région.

II.4 Conclusion

Dans cette section, les notions de SER, complexe et réelle, ont été définies, ainsi que les quatre paramètres dont elles dépendent, étant donné que les systèmes de reconnaissance automatique de cibles discutés dans les sections suivantes sont tous basés sur la notion de SER, complexe ou réelle.

Nous avons montré comment exprimer un échantillon de la trajectoire d'un avion
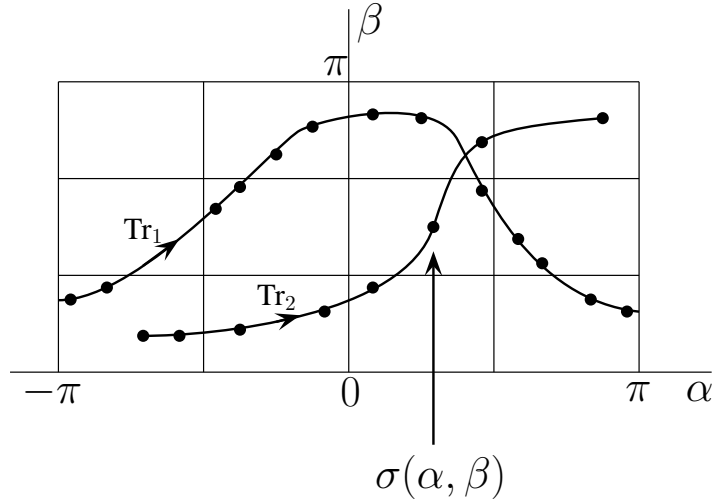
Figure 8: *Illustration du partitionnement en régions du plan (α, β) de l'espace des paramètres.*

en fonction de ces paramètres. Cette expression a permis de définir une stratégie de reconnaissance, consistant en le partitionnement de l'espace de ces paramètres en régions, avec la construction d'un classificateur par région.

III   Reconnaissance de cibles via leurs images radars

III.1   Introduction

Un grand nombre d'algorithmes de reconnaissance automatique de cibles (RAC) utilisent les images radars de ces cibles pour les reconnaitre. Il apparait donc logique de reconnaitre des avions sur base de leurs images radars, à partir de données acquises en mode bistatique. A cette fin, nous utilisons la surface équivalente radar complexe (SERC) d'avions, extraite à partir de données acquises en chambre anéchoïque de l'ONERA. Comme le montre le bloc-diagramme de la figure 9, les images radars sont construites à partir de ces SERC. Les cibles sont ensuite reconnues à partir de leurs images radars à l'aide d'arbres de décision construits de manière aléatoire (par opposition aux arbres de décision classiques, construits de manière déterministe).

III.2   Construction d'images radars

La construction d'images à partir de la SERC est basée sur les principes de la tomographie. Nous illustrons le principe de la construction d'images dans le cas monostatique, c'est-à-dire quand l'émetteur et le récepteur sont co-localisés, et simplement appelés le radar.

Comme indiqué à la figure 10, le radar illumine l'objet, en l'occurrence un avion, et reçoit le signal réfléchi. Le signal est transmis à une certaine fréquence f, pour un certain angle de vue α. La transformée de Fourier à deux dimensions appliquée sur ce signal réfléchi donne un point dans l'espace de Fourier, dont la valeur est la SERC.
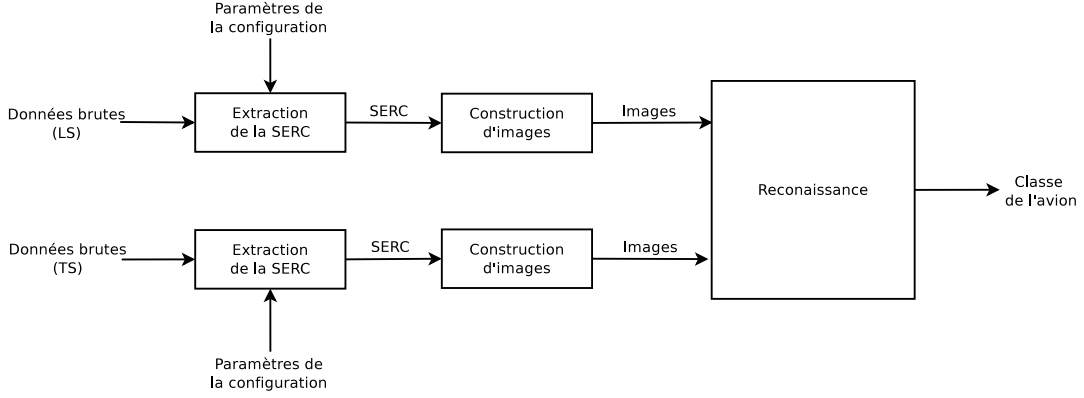
Figure 9: *Bloc-diagramme du système de reconnaissance automatique de cibles basé sur les images radars des avions.*

En illuminant l'objet sur une certaine bande de fréquences et à différents angles α, on remplit l'espace de Fourier. Bien entendu, étant donné que l'on est limité à une certaine bande de fréquences et un certain espace angulaire, les valeurs de SERC ne sont disponibles que pour une certaine portion de l'espace de Fourier, comme indiqué à la figure 11. L'image radar de l'objet illuminé est construite par application de la transformée de Fourier à deux dimensions aux valeurs de SERC.
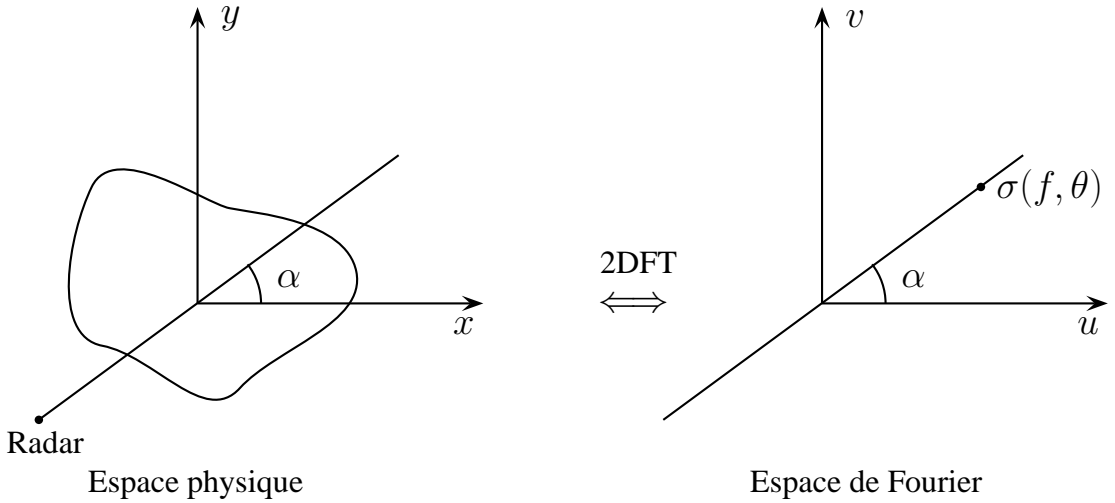
Figure 10: *Illustration de mesures de SERC en mode monostatique.*

On généralise au cas bistatique en ajoutant à l'angle d'aspect le demi-angle bistatique. L'image radar bistatique $I(x, y)$ est alors obtenue à partir de la SERC $\sqrt{\sigma}(f, \alpha)$ par l'équation suivante:

$$I(x,y) = \int_0^{+\infty} \int_0^{2\pi} \sqrt{\sigma}(f,\phi)e^{4\pi j\frac{f}{c}\cos(\beta/2)(x\cos(\alpha+\beta/2)+y\sin(\alpha+\beta/2)}|\frac{4f\cos^2(\beta/2)}{c^2}|d\beta df, \quad (4)$$

où l'intégration est faite sur l'angle bistatique (et non pas sur l'angle d'aspect) car, dans la chambre anéchoïque, l'émetteur et l'objet sont fixes, tandis que le récepteur
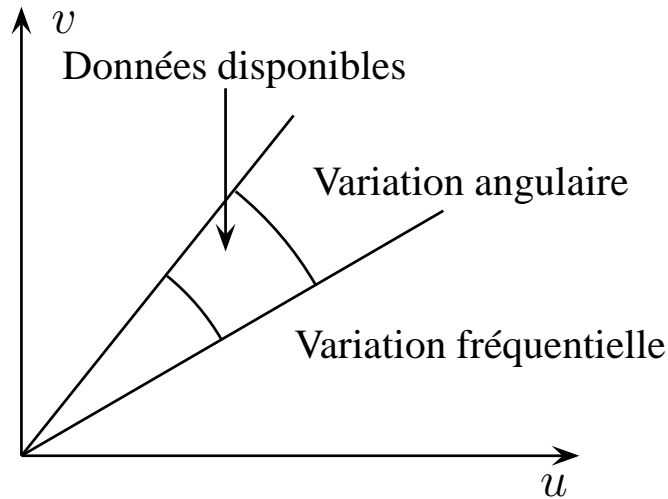
Figure 11: *Illustration du remplissage de l'espace de Fourier disponible dans les données.*

varie, et fait donc varier l'angle bistatique.

En pratique, étant donné que le but est la classification des images radars, il est primordial de construite un nombre important d'images. A partir des données de SERC disponibles, des sous-tableaux de SERC sont sélectionnés. Une image radar est construite pour chaque sous-tableau. La figure 12 montre des exemples d'images radars de Beechcraft construites pour chacune des quatre bandes de fréquences utilisées dans la chambre anéchoïque.

Pour la plus basse bande de fréquences, l'image consiste en un seul point brillant. C'est dû au fait que pour cette bande de fréquences, la résolution de l'image est à peu près égale à la taille de l'avion. Plus on croît en fréquence, meilleure est la résolution, et donc plus de points brillants apparaissent sur les images.

III.3   Reconnaissance par arbres extrêmement aléatoires

L'algorithme de reconnaissance est basé sur l'utilisation conjointe de la technique d'extraction de fenêtres et d'arbres rendus extrêmement aléatoires. Comme indiqué à la figure 13, les données, qui sont ici les images radars, sont séparées en un ensemble d'apprentissage (LS) et un ensemble de test (TS).

Pour chaque image du LS, un certain nombre N_{LS} de fenêtres sont extraites par la technique d'extraction de fenêtres, illustrée à la figure 14. Chaque fenêtre est choisie aléatoirement, et est d'une taille aléatoire. Une fenêtre est caractérisée par les valeurs des pixels à l'intérieur de cette fenêtre. Les fenêtres sont ensuite re-dimensionnées, de telle manière à ce qu'elles contiennent toutes le même nombre de pixels, car ce sont les pixels qui sont utilisés comme attributs. Chaque fenêtre est labellisée par la classe de son image d'origine.

Les fenêtres extraites sont utilisées pour construire un ensemble de T arbres
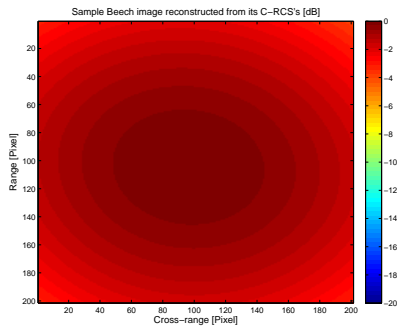
(a) *Première bande de fréquences:* $[20; 80]$
MHz
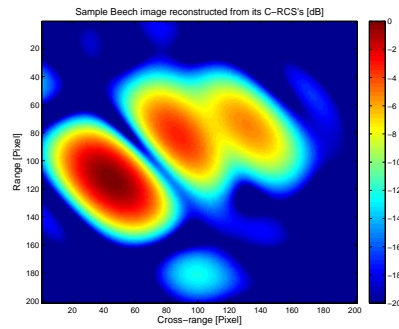
(b) *Seconde bande de fréquences:*
$[190; 250]$ *MHz*
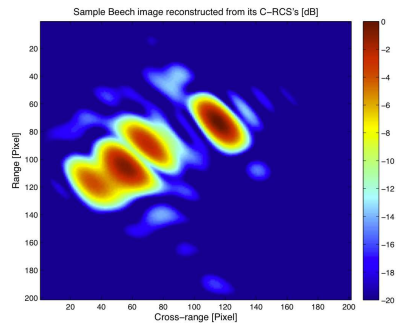
(c) *Troisième bande de fréquences:*
$[450; 550]$ *MHz*
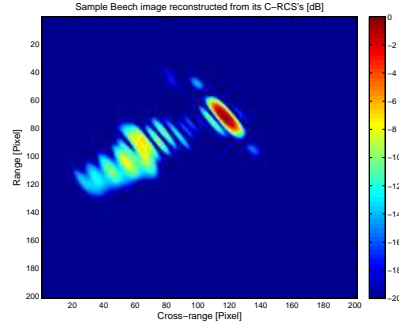
(d) *Quatrième bande de fréquences:*
$[1.2; 1.3]$ *GHz*

Figure 12: *Exemple d'images radars de Beechcraft construites à partir de SERC, pour chacune des quatre bandes de fréquences utilisées.*
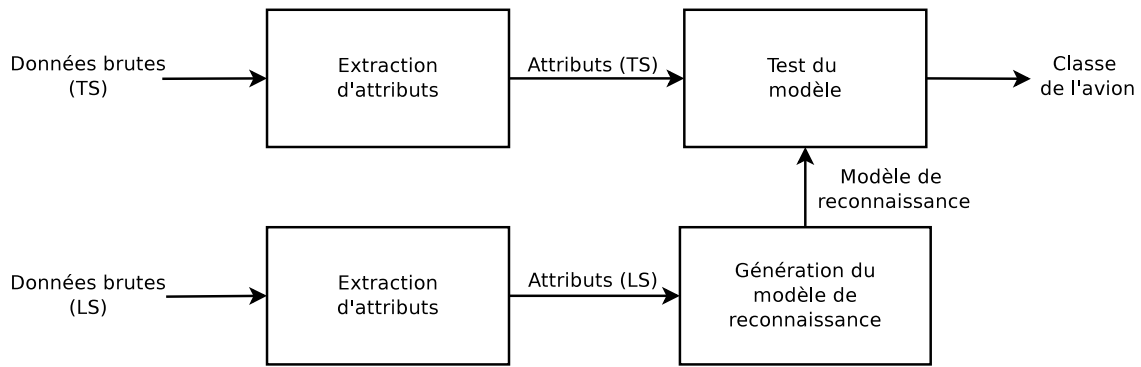
Figure 13: *Bloc-diagramme du classificateur.*
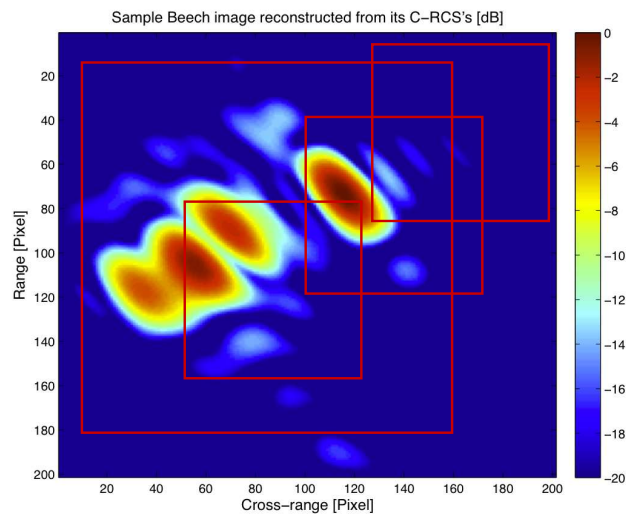
Figure 14: *Illustration de l'extraction de fenêtres sur une image. Les attributs sont les pixels de ces fenêtres préalablement mises à la même échelle, de sorte que chaque fenêtre contient le même nombre de pixels.*

extrêmement aléatoires (extra-trees). La figure 15 illustre un arbre de décision. Un arbre de décision est un ensemble hiérarchique de nœuds reliés entre eux par des branches. A chaque nœud, on teste un des attributs des fenêtres, l'un des pixels des fenêtres en l'occurrence. On sépare ensuite l'ensemble des fenêtres en deux sous-ensembles, suivant le résultat du test. On continue à développer l'arbre jusqu'à ce qu'un nœud ne contienne que des fenêtres appartenant toutes à la même classe.

La différence entre un arbre de décision classique et un extra-tree réside dans le choix du couple attribut-valeur seuil (a_i, v_i) pour chaque nœud. Dans un arbre de décision classique, le meilleur couple est choisi à chaque nœud. Pour un arbre aléatoire, le meilleur couple est choisi parmi un ensemble restreint de couples choisis aléatoirement.

La classe d'une image du TS est déterminée de la manière suivante: un nombre N_{TS} de fenêtres sont extraites de l'image et ensuite re-dimensionnées. Chacune de ces fenêtres est propagée dans chacun des T extra-trees du modèle de reconnaissance.
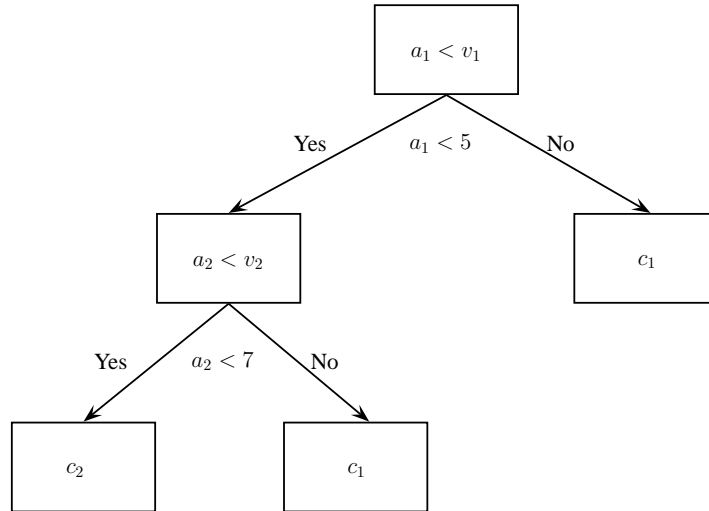
Figure 15: *Illustration d'un arbre de décision.*

La classe de l'image est déterminée par un vote de majorité sur les $N_{TS} \times T$ classes obtenues par la propagation de chaque fenêtre dans chaque arbre.

III.4 Expériences de reconnaissance

L'algorithme de reconnaissance a été conçu pour être utilisé principalement sur des images optiques. Il importe donc d'abord de le valider sur des images radars. Pour ce faire, nous le testons sur les images de la base de données MSTAR afin de comparer les résultats obtenus avec ceux obtenus par d'autres méthodes et publiés dans la litérature. Ensuite, l'algorithme est testé sur les images construites à partir des données de la chambre anéchoïque de l'ONERA.

III.4.1 Reconnaissance sur les images MSTAR

La version de la base de données MSTAR utilisée se compose d'images de 5 objets; les chars BMP-2 et BTR-70, le tank T-72, des fausses cibles, et d'images d'environnement, telles qu'illustrées à la figure 16. Chaque type d'objets est considéré comme une seule classe. Il y a donc cinq classes d'objets.

En appliquant l'algorithme de reconnaissance à la base de données MSTAR, on obtient des résultats de classification correcte de l'ordre de 98%, à condition de réduire le speckle présent dans les images autour des objets en eux-mêmes. Ce taux de reconnaissance est parmi les meilleurs résultats publiés dans la litérature. L'application de l'algorithme de reconnaissance basé sur les extra-trees à des images radars est donc expérimentalement validé.

III.4.2 Reconnaissance sur les images ONERA

Les données sont acquises en chambre anéchoïque pour 4 types d'avions (figure 17) sur 4 bandes de fréquences (FB1 = $[20; 80]$ MHz, FB2 = $[190; 250]$ MHz, FB3 = $[450; 550]$ MHz et FB4 = $[1.2; 1.3]$ GHz), sur 4 couples de polarisation émetteur-récepteur (HH, HV, VH et VV), pour 3 angles d'aspect ($\alpha \in \{0°, 45°, 90°\}$), et pour

(a) *Char BMP-2.*   **(b)** *Char BTR-70.*   **(c)** *Tank T-72.*

(d) *Exemple d'image de* **(e)** *Exemple d'image* **(f)** *Exemple d'image fausse cible.* *d'environnement.* *d'environnement.*
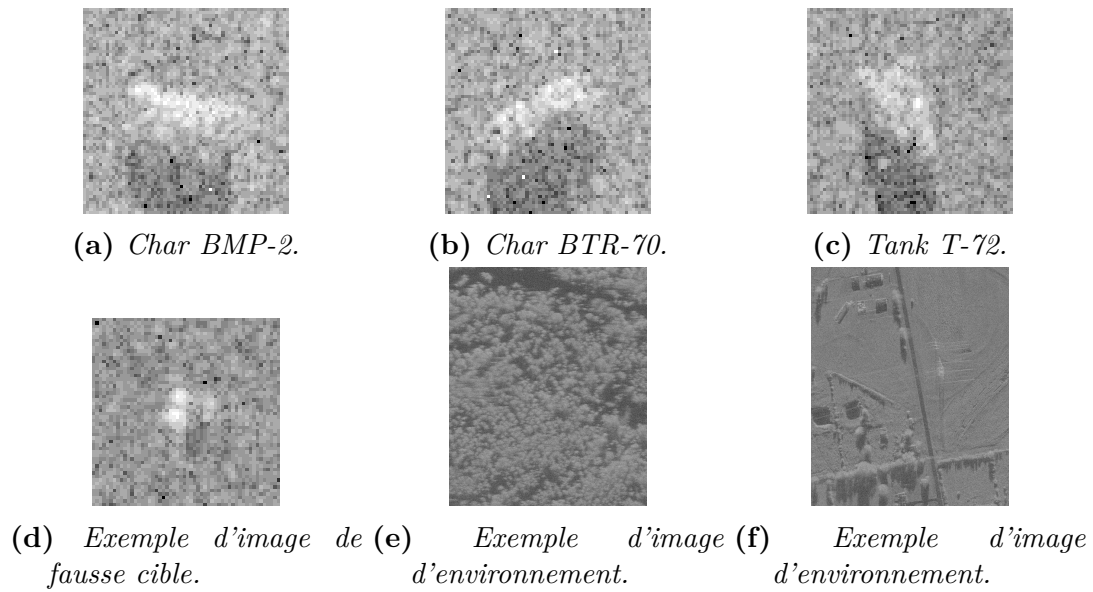
Figure 16: *Illustration des cinq classes des données MSTAR.*

des angles bistatiques allant de 6° à 160°. Les images sont construites en utilisant les données acquises pour la polarisation HH.

(a) *Beechcraft.*   **(b)** *F117.*

(c) *F16.*   **(d)** *Learjet.*
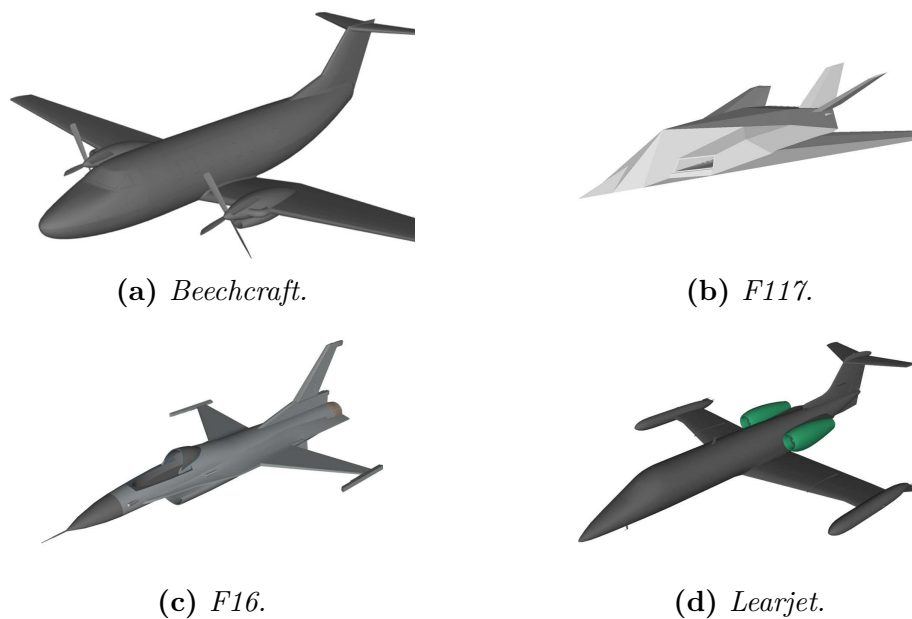
Figure 17: *Modèle CAD de chacun des avions utilisés.*

Les résultats obtenus donnent un taux de reconnaissance d'à peu près 30% pour les images de la FB1. Ce faible taux de reconnaissance s'explique par (1) la faible résolution des images qui est comparable à la taille des avions, et (2) par le fait que pour la FB1, la taille des avions influence plus la SERC que leur forme et que tous les avions sont de même taille. A l'inverse, les taux de reconnaissance sont proches de

100% pour les trois hautes bandes de fréquences car la résolution dès images est plus élevée et que la forme des avions influence plus la SERC que leur taille.

III.5 Conclusion

Dans cette section, nous avons procédé à la reconnaissance des avions en utilisant leurs images radars et un algorithme de reconnaissance basé sur l'utilisation d'arbres rendus extrêmement aléatoires. L'algorithme de reconnaissance a d'abord été testé sur des images radars de la base de données MSTAR, et ensuite sur les images radars construites à partir des SERC d'avions fournies par des mesures en chambre anéchoïque. Les taux de reconnaissance avoisinent les 100%, à l'exception de la bande de fréquences disponible la plus basse, étant donné que tous les avions sont de même taille et, à cette fréquence, n'apparaissent chacun que comme un seul point brillant.

IV Reconnaissance de cibles via leurs SER complexes et réelles

IV.1 Introduction

La reconnaissance par imagerie, bien que très performante, nécessite la construction d'images radars des cibles. Pour construire une image radar d'une cible, un utilisateur doit disposer de valeurs de SERC sur une certaine partie de l'espace de Fourier. Il faut donc pouvoir disposer de paires émetteurs-récepteurs opérant sur des fréquences adjacentes et dont les angles bistatiques soient également adjacents. En pratique, à cause des principes d'allocation des fréquences, il est invraisemblable de pouvoir disposer d'émetteurs opérant sur des fréquences adjacentes et étant adjacents.

On cherche donc à reconnaitre les avions en utilisant directement leur SER, réelle ou complexe, acquise à partir d'un nombre limité de paires émetteur-récepteur, comme indiqué à la figure 18. Par rapport au bloc-diagramme de la figure 9, l'étape de construction d'images radars a été supprimée.

IV.2 Reconnaissance par méthodes de sous-espaces

La figure 19 montre le bloc-diagramme de l'étage de reconnaissance de la figure 18. L'algorithme de reconnaissance est basé sur les méthodes de sous-espaces.

Les données, soit de SER, soit de SERC, sont séparées en un ensemble d'apprentissage (LS) et un ensemble de test (TS). Des vecteurs d'attributs sont formés pour chaque classe représentée dans le LS. Chaque vecteur d'attributs consiste en une séquence de valeurs de SER ou de SERC acquises à des angles bistatiques consécutifs. Chaque vecteur d'attributs peut donc être vu comme la réalisation d'une variable aléatoire représentant la SER ou la SERC pour ces angles bistatiques. Pour chaque classe, l'ensemble des vecteurs d'attributs est concaténé dans une matrice, notée X.

Chaque classe est caractérisée par un sous-espace construit par décomposition en valeurs singulières de la matrice X. On a donc $X : U\Sigma V^H$, où U est la matrice
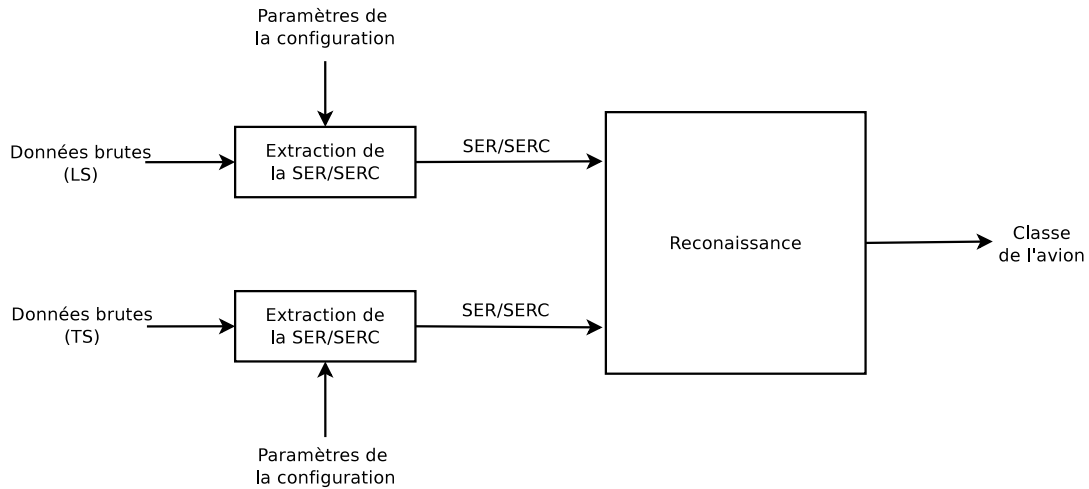
Figure 18: *Bloc-diagramme du système de reconnaissance automatique de cibles basé sur les SER complexes (SERC) ou réelles (SER) des avions.*

des vecteurs singuliers, et Σ la matrice diagonale des valeurs singulières. Le meilleur sous-espace est constitué en gardant les vecteurs singuliers de U correspondant aux valeurs singulières de Σ les plus grandes. Le modèle de reconnaissance consiste donc en un ensemble de sous-espaces, chaque sous-espace représentant une classe.

La classe d'un vecteur d'attributs du TS est déterminée de la manière suivante. Le vecteur est projeté dans chacun des sous-espaces du modèle de reconnaissance. Ensuite, une mesure de chaque projection, équivalente à l'énergie de la projection du vecteur dans chacun des sous-espaces, est calculée. La classe attribuée à ce vecteur est celle correspondant au sous-espace dont l'énergie de la projection est la plus grande.

IV.3 Expériences de reconnaissance sur les données ONERA

Le modèle de reconnaissance automatique de cibles décrit plus haut est testé successivement sur les SER puis sur les SERC des quatre avions présentés précédemment. Rappelons que les valeurs de SER et de SERC sont acquises en chambre anéchoïque. Le cas d'une seule paire émetteur-récepteur est d'abord testé. Les taux de reconnaissance sont indiqués à la figure 20 par bande de fréquences, pour la polarisation HH.

Pour la bande de fréquences la plus faible, les taux de reconnaissance sont très faibles, alors qu'ils augmentent aux fréquences plus élevées, et ce pour les mêmes raisons que dans le cas des images radars. Pour chaque bande de fréquences, le taux de reconnaissance varie suivant la région de l'espace (α, β) dans laquelle l'objet est illuminé.

On voit aussi clairement qu'il est plus intéressant de travailler avec la SER complexe (donc la phase) que réelle. C'est probablement dû à la différence dans les formes des avions utilisés.

Le cas de trois paires émetteur-récepteur est ensuite considéré. La classe d'un avion est déterminée par vote de majorité sur les résultats de classification de chaque
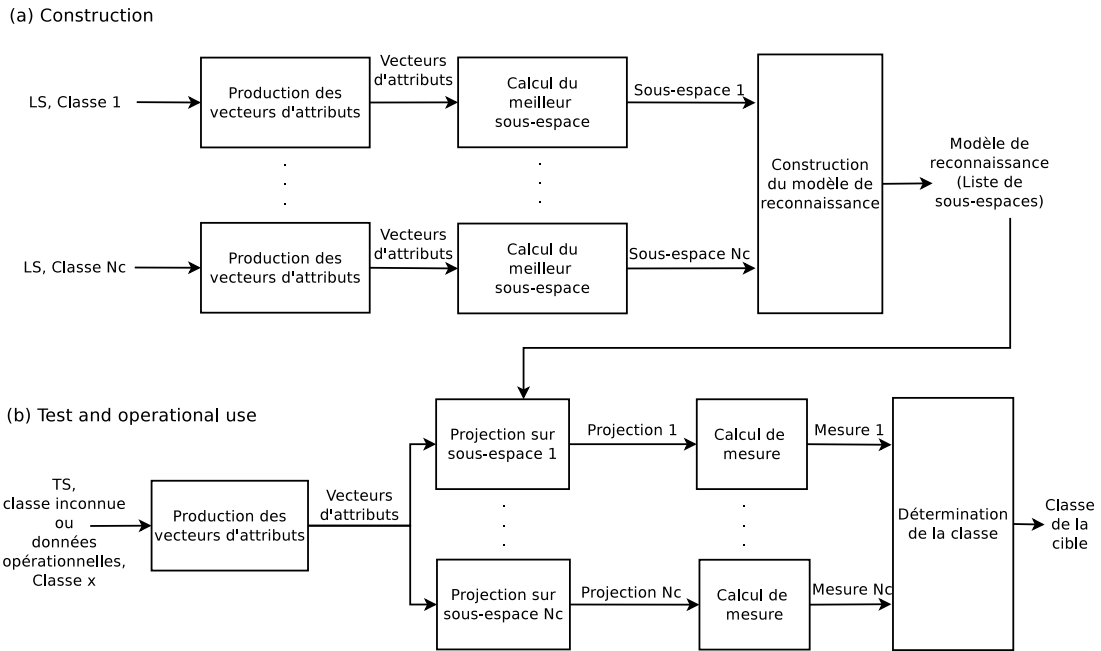
Figure 19: *Bloc-diagramme du classificateur basé sur les sous-espaces.*

paire émetteur-récepteur. On considère un seul émetteur et trois récepteurs dont les angles bistatiques sont différents les uns des autres. La figure 21 montre les taux de reconnaissance par bande de fréquences, pour la polarisation HH.

On voit clairement que la combinaison de plusieurs récepteurs augmente le taux de reconnaissance aux fréquences plus élevées. Ceci est à mettre en parallèle avec les résultats obtenus sur les images radars, pour lesquels un nombre plus important de paires émetteur-récepteur ont été nécessaires.

IV.4   Conclusion

Dans cette section, nous avons montré que l'on pouvait reconnaitre des avions sur base de leur SER, complexe ou réelle, acquise en chambre anéchoïque par un nombre limité de paires émetteur-récepteur. L'algorithme de classification repose sur des méthodes de sous-espaces, chaque classe d'avions étant représentée par un sous-espace.
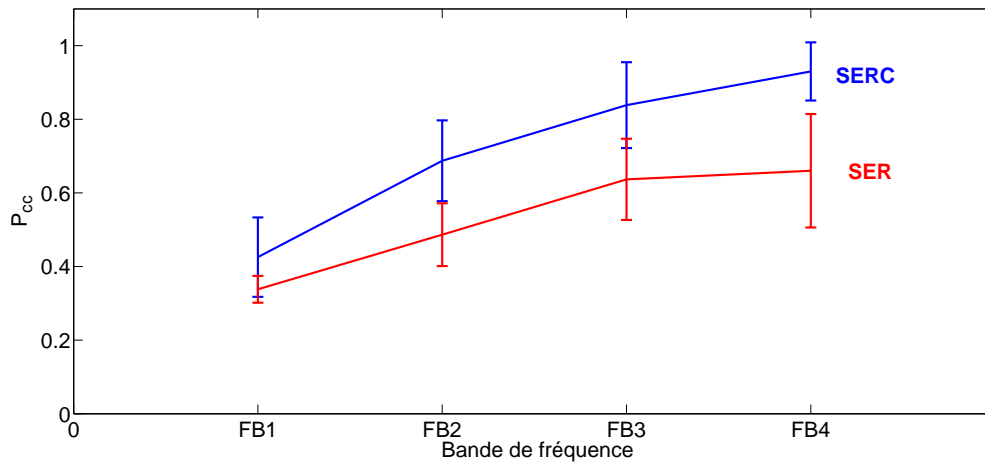
Figure 20: *Taux de reconnaissance moyen par bande de fréquences, pour une seule paire Tx-Rx. La variation au sein d'une même bande dépend de la région du plan (α, β) dans laquelle l'objet est illuminé.*
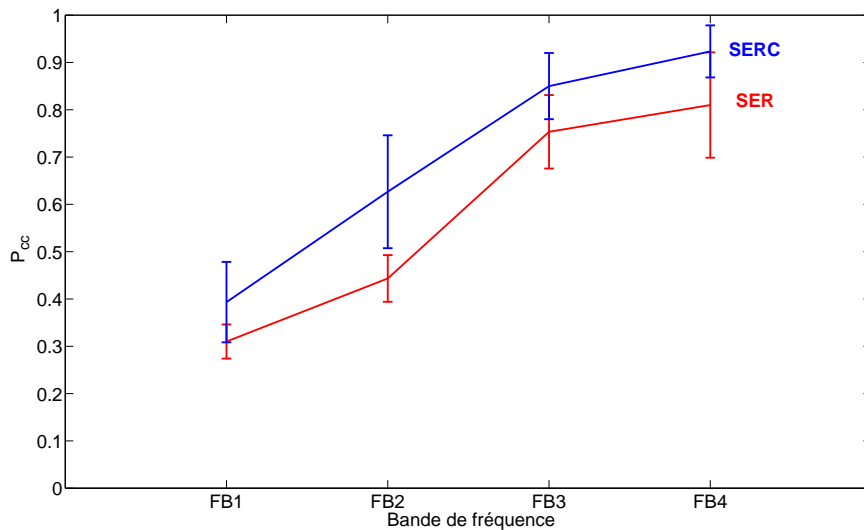
Figure 21: *Taux de reconnaissance moyen par bande de fréquences, pour trois paires Tx-Rx. La variation au sein d'une même bande dépend de la région du plan (α, β) dans laquelle l'objet est illuminé.*

V Reconnaissance de cibles via leurs SER réelles, acquises expérimentalement

V.1 Introduction

Dans la section précédente, on a montré que l'on pouvait reconnaitre de manière performante des avions en utilisant leur SER, complexe ou réelle, acquise en chambre anéchoïque. On teste maintenant la reconnaissance d'avion en utilisant leur SER réelle acquise à partir d'un banc de test basé sur un radar passif bistatique, déployé en extérieur.

Les opérations à mener ont été décrites à la figure 1. Les avions doivent d'abord être détectés et localisés. Un émetteur d'opportunité est sélectionné afin d'acquérir son signal qui est réfléchi par les avions détectés. La SER des avions est extraite de ce signal acquis, et sert ensuite à leur reconnaissance. La figure 22 représente le bloc-diagramme de ce système de reconnaissance.
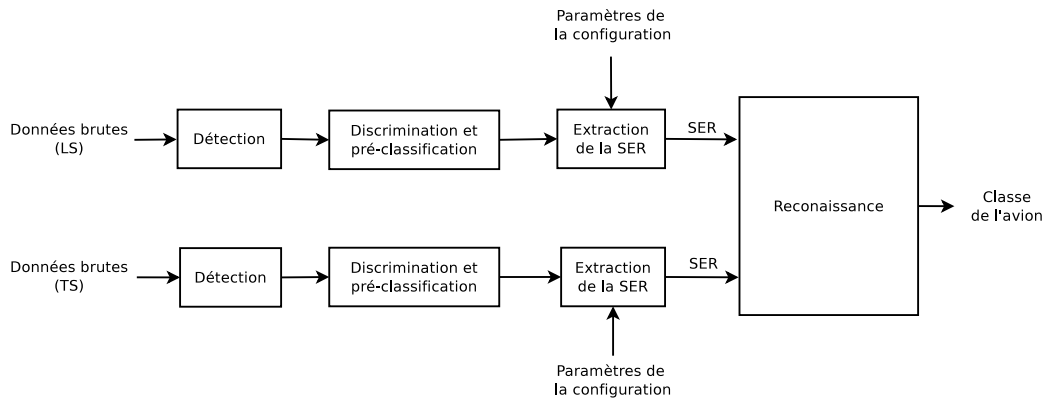
Figure 22: *Bloc-diagramme du système de reconnaissance automatique de cibles basé sur les SER des avions acquises par banc de test expérimental.*

V.2 Banc de test de radar passif bistatique

Le banc de test déployé aux alentours de l'aéroport d'Orly (figure 23) consiste en un récepteur ADS-B et un récepteur SDR basé sur la radio-logicielle. Les signaux ADS-B servent à la détection et à la localisation des avions, étant donné que les signaux ADS-B émis par les avions commerciaux contiennent leurs informations de localisation.

Le récepteur ADS-B a permis de détecter 1329 avions pendant une campagne ayant duré une dizaine de jours. Parmi ces avions, les 47 Airbus de la famille des A340 (65 mètres de long, 4 moteurs) sont utilisés comme classe de grands avions, et les 549 Airbus de la famille des A320 (35 mètres de long, 2 moteurs) comme classe d'avions de taille moyenne.

L'émetteur d'opportunité sélectionné est un VOR (celui de Rambouillet) servant à la navigation aérienne. Plus précisément, une sous-porteuse de son signal est utilisée comme signal d'opportunité. Le récepteur SDR permet d'acquérir à

Figure 23: *Configuration du banc de test déployé. L'émetteur sélectionné est le VOR de Rambouillet. Les récepteurs sont localisés au point marqué "HOUSE". Le cercle indique la région dans laquelle les avions sont détectés, de par le rapport signal-sur-bruit suffisamment élevé des signaux réfléchis par les avions.*

la fois le signal émis par le VOR qui est reçu directement, et le signal réfléchi par un avion, comme le montre l'exemple de spectrogramme des signaux reçus à la figure 24. Ces deux signaux sont utilisés pour le calcul de la SER des avions détectés.

La SER des avions est calculée de la manière suivante. La puissance du signal direct, notée P_{RD}, et la puissance du signal réfléchi, notée P_{RS}, correspondent, à chaque instant t, aux pics du signal direct et du signal réfléchi sur le spectrogramme de la figure 24. En combinant l'équation radar bistatique et l'équation de bilan de liaison, la SER peut s'exprimer comme

$$\sigma = \frac{P_{RS}}{P_{RD}}\frac{G_{RT}}{G_{RS}}G\frac{(4\pi)^3 R_{TS}^2 R_{RS}^2}{\lambda^2 L}, \tag{5}$$

où les différentes grandeurs sont indiquées sur la figure 25. La figure 26 montre les valeurs de SER des avions de taille moyenne en fonction des angles d'aspect α et bistatique β. Il est clair que les valeurs sont cohérentes d'un avion à l'autre, et qu'elles peuvent donc être utilisées pour reconnaitre les avions.

Afin d'ajouter une classe d'avions, la SER d'avions de petite taille (4 mètres de long) est simulée de manière numérique en utilisant les trajectoires des avions de taille moyenne. Ce type d'avions n'étant pas équipé d'émetteur ADS-B, le banc de test ne permet pas de les détecter, d'où le recours à la simulation.

La base de données consiste donc en des valeurs de SER de trois classes d'avions. Pour chaque classe d'avions, un tiers des avions détectés forme l'ensemble d'apprentissage, et les deux autres tiers forment l'ensemble de test.

V.3   Reconnaissance par méthodes de sous-espaces

Le même algorithme de classification basé sur les méthodes de sous-espaces et décrit précédemment est utilisé pour procéder à la reconnaissance des avions. La figure 27 montre le taux de reconnaissance obtenu par région de l'espace (α, β). Les régions en bleu correspondent à des zones pour lesquelles aucune donnée n'a pu être récoltée. Le taux de reconnaissance obtenus pour les autres régions varie de 40% à 99%. Le taux
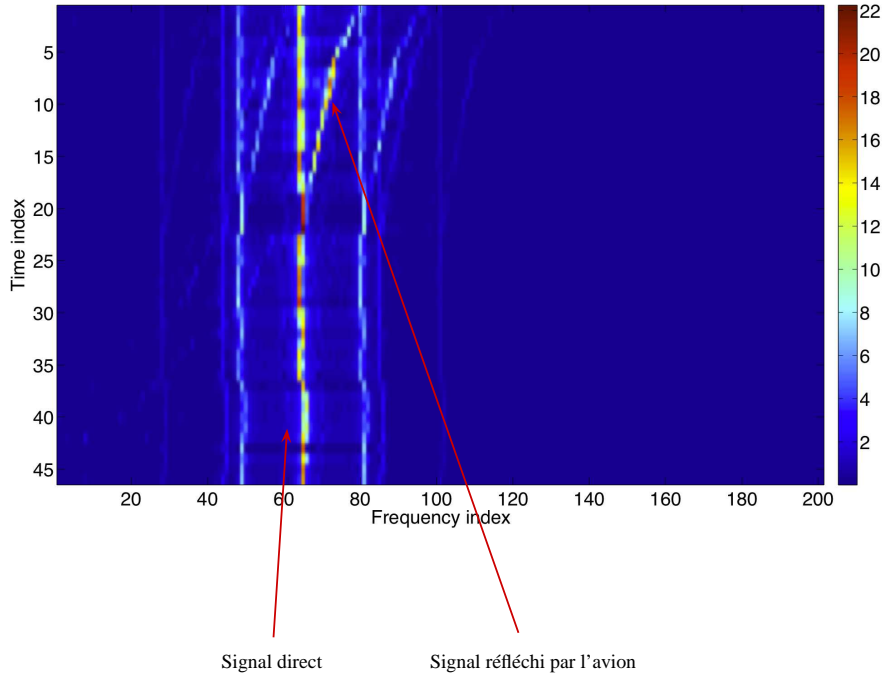
Figure 24: *Exemple de spectrogramme d'un signal reçu. On distingue le signal direct par sa fréquence fixe, et le signal réfléchi par un avion présentant un shift Doppler.*

global de reconnaissance obtenu est de 83%.

Certaines régions apparaissent donc plus intéressantes que d'autres pour la reconnaissance des classes d'avions décrites ci-dessus. Étant donné que les couloirs aériens sont déterministes, il convient alors de bien choisir l'emplacement du récepteur pour obtenir un taux de reconnaissance élevé.

V.4   Conclusion

Dans cette section, on a montré que des avions commerciaux peuvent être reconnus de manière performante sur base de leur SER réelle acquise à partir d'un banc de test déployé aux alentours de l'aéroport d'Orly et basé sur un radar passif bistatique utilisant un VOR comme émetteur d'opportunité et un récepteur de radio-logicielle.
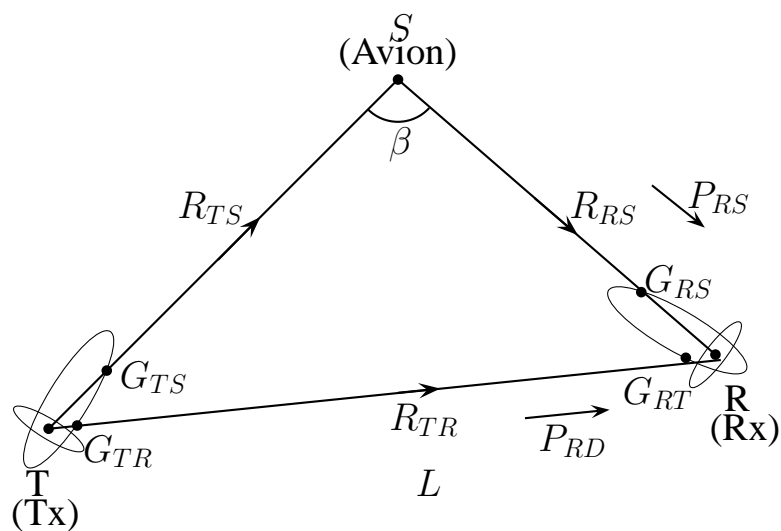
Figure 25: *Configuration radar bistatique correspondant à une paire Tx-Rx et un avion. T, R, and S indiquent les positions du Tx, du Rx, et de l'avion, respectivement. Le graphe montre les diagrammes de rayonnement des antennes d'émission et de réception. Les différents paramĕtres de l'équation (5) y sont indiqués.*
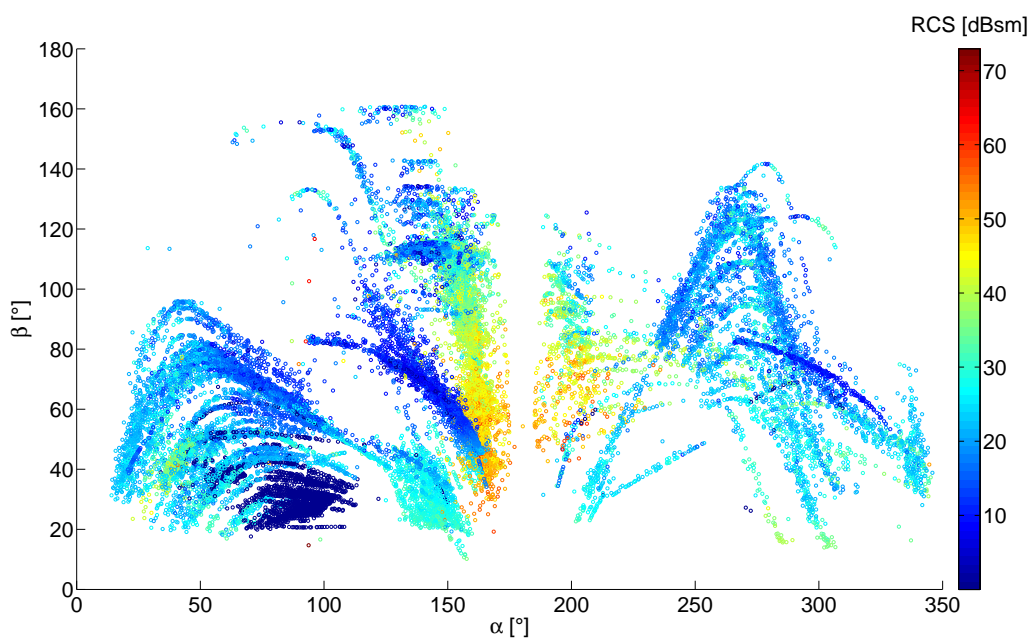
Figure 26: *Valeurs de SER pour les avions de taille moyennes, dans le plan (α, β).*
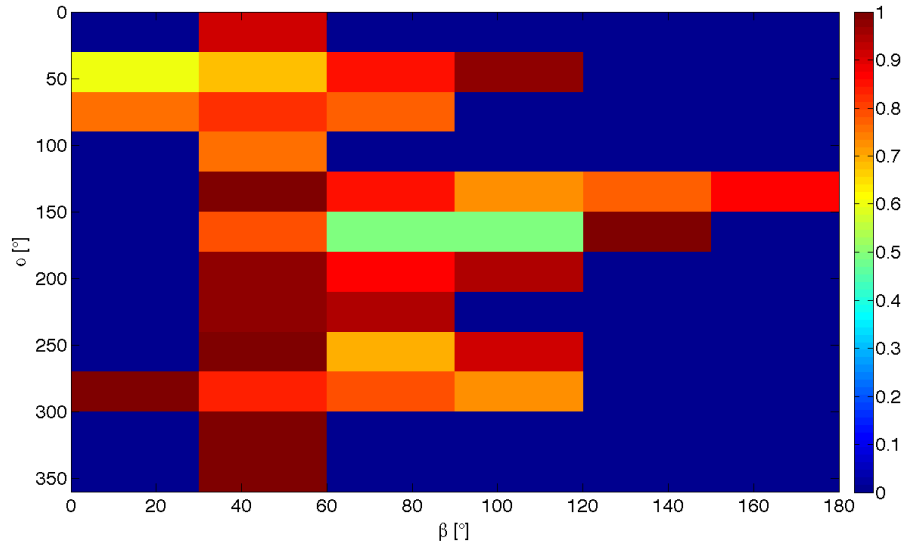
Figure 27: *Taux de reconnaissance des avion par région de l'espace (α, β).*

VI   Conclusions et perspectives

Dans cette thèse, nous avons étudié la problématique de la reconnaissance d'avions (aussi appelés cibles) en utilisant des signaux de radars passifs bistatiques, en vue de la détection d'anomalies dans le trafic aérien civil. Une anomalie peut en effet survenir quand un avion n'est pas équipé pour répondre aux interrogations de radars secondaires.

Une stratégie de reconnaissance a d'abord été définie, basée sur la phénoménologie radar. En effet, la SER, complexe ou réelle, d'un objet dépend de quatre facteurs que sont la fréquence du signal transmis, le couple de polarisation de l'émetteur et du récepteur, l'angle d'aspect et l'angle bistatique. Etant donné que les mécanismes de diffusion contribuant à la SER dépendent de ces quatre paramètres et qu'il est par ailleurs invraisemblable d'observer un avion sur l'entièreté de sa trajectoire, la stratégie de reconnaissance consiste en la séparation de cet espace de paramètres en régions, et en la construction d'un classificateur par région.

Les premières expériences de reconnaissance ont été menées sur des données acquises en chambre anéchoïque. Les avions ont d'abord été reconnus en utilisant leurs images radars construites à partir des SER complexes, et en appliquant l'algorithme des arbres rendus extrêmement aléatoires sur ces images radars. Bien qu'ayant obtenus des taux de reconnaissance excellents, la construction d'images demande l'utilisation d'un certain nombre de paires émetteur-récepteur. Les avions ont donc été reconnus en utilisant directement leur SER, réelle ou complexe, et en utilisant un classificateur basé sur les méthodes de sous-espaces. Les taux de reconnaissance obtenus varient suivant la région de l'espace des paramètres dans laquelle est illuminé l'avion, et peuvent atteindre 98%.

Afin de tester l'algorithme de reconnaissance sur des données de SER réelles, un

banc de test basé sur un radar passif bistatique a été dŕployé aux alentours de l'aéroport d'Orly. Le banc de test détecte et localise les avions en utilisant leurs signaux ADS-B. Le signal d'opportunité choisi est la sous-porteuse du signal émis par un VOR. La SER des avions est calculée sur base du ratio entre la puissance du signal réfléchi sur les avions et la puissance du signal direct, ces signaux étant collectés par un récepteur de radio-logicielle. L'algorithme de reconnaissance est basé sur les méthodes de sous-espaces. Le taux de reconnaissance obtenu est de 83% et varie suivant les régions de l'espace des paramètres, démontrant ainsi expérimentalement la faisabilité de la reconnaissance de cibles par utilisation de signaux de radars passifs bistatiques.

Différentes perspectives sont envisagées afin de rendre le système le plus opérationnel possible. Tout d'abord, il convient de pouvoir détecter et localiser les cibles d'une autre manière qu'en utilisant les signaux ADS-B, par définition des anomalies dans le trafic aérien. Ensuite, différents émetteurs d'opportunité peuvent être utilisés et combinés, la bonne localisation des récepteurs et des émetteurs pouvant permettre d'augmenter significativement le taux de reconnaissance. L'utilisation de la phase de la SER peut aussi contribuer à améliorer les résultats de reconnaissance. Étant donné que les taux de reconnaissance varient suivant la polarisation, l'angle d'aspect et l'angle bistatique, il conviendrait d'étudier théoriquement l'influence de ces paramètres. Enfin, nous donnons quelques pistes concernant la reconnaissance elle-même, telles que l'utilisation d'autres techniques de classification, ou la définition des classes de cibles suivant des méthodes d'apprentissage non-supervisé comme le clustering.

Chapter 1

Introduction

Contents

1.1 Motivation for the thesis

The motivation for this thesis is the automatic recognition of targets using passive bistatic radar signals. The objective of the thesis is to design, implement, and test a system able to recognize, at low cost, targets. We call this system an automatic target recognition (ATR) system. In this section, we define the types of targets that are considered, and the notions of ATR, target class, bistatic radar, and passive radar.

1.1.1   Targets considered

In this work, we consider non-cooperative targets. Non-cooperative targets are targets that do not provide information about their identity or location when asked to do so, by contrast with cooperative targets that provide this information. Examples of non-cooperative targets are personal cars. In general, we often refer to targets as objects.

Without loss of generality, we consider non-cooperative air targets. Non-cooperative air targets are not able to reply to requests from air traffic control (ATC) radars, either because of the absence of a transponder on-board, because of a failure of such a transponder, or because the transponder is off (willingly or not). ATC is described in Section 1.3. We discuss the application of the proposed ATR systems, described in Section 1.2, to other types of targets in Chapter 9.

1.1.2   Automatic target recognition (ATR)

Automatic target recognition (ATR) is defined as the process of recognizing targets without human involvement [17, 95, 173]. ATR is called non-cooperative target recognition (NCTR) in case of non-cooperative targets, as in this thesis, and identification friend-or-foe (IFF) in case of cooperative targets [187]. NCTR aims at recognizing a target from the radar echo signals received from the target to be recognized. IFF systems rely on the interrogation of the transponder on-board the target that sends its identification back to the interrogator.

The word "recognition" in ATR implies classification. We equivalently use both terms in this thesis. Classification is defined as the act of assigning to input data one class among a set of pre-defined classes [54, 134]. The task of the classifier is to assign a class to an unknown object described by features, called attributes. To do so, the classifier derives rules from objects described by attributes and for which their respective class is known. Usually, a classification model describing these rules is derived using a subset of the available data called the learning set (LS). The classification model is tested on another subset of the data called the test set (TS). Other ways of partitioning the data, such as cross-validation, can be used [134]. Cross-validation is used when the amount of data is insufficient to create an LS and a TS that are independent, and that each contains a sufficient amount of objects. We do not consider cross-validation in this thesis since a particular effort is made to obtain a dataset as complete as possible. The fact that we learn and train the ATR systems, described in Section 1.2, on real data, making up complete datasets, is another key feature of this thesis. Indeed, as will be explained in Chapter 2, many ATR systems for passive radar rely on simulated data.

Classification is a part of supervised learning [54, 134]. In supervised learning problems, objects belong to different categories, called classes. Supervised learning aims at deriving relationships between the attributes of objects. These relationships are used to predict the true class of an object. Supervised learning problems are either regression problems or classification problems. In regression problems, the prediction is a (continuous) numerical value, whereas in classification problems the predicted output is a discrete class.

Supervised learning is a part of machine learning. Machine learning is a subfield of automatic learning that aims at designing rules that are similar to those that human experts derive [221]. In machine learning problems, each object is characterized by a set of features called attributes. Machine learning is divided into supervised learning and unsupervised learning. Unsupervised learning, also called clustering, aims at deriving probabilistic or causal relationships between objects. For example, clustering methods try to form groups of objects based on the features of the objects. The use of unsupervised learning in our ATR problem is part of our future work, and is discussed in Chapter 9.

In short, the problem addressed in this thesis is an ATR problem, and more specifically, an NCTR problem. We aim at classifying/recognizing non-cooperative air targets. Air targets are characterized by some number of attributes.

1.1.3 Class of a target

In this work, the proposed ATR systems label each unknown target of interest with a particular target class. The notion of target class is not uniquely defined in the radar ATR literature. The nature of the prediction of a classifier thus varies from one ATR system to the other. For example, a target is defined in [187] first according to its general nature, which can be defined as aircraft, ship, or bird. Each type of general nature of target is then divided into different target types. Example target types for airplanes are fighter planes and helicopters. Each target type can be further separated into different target classes that can be F16, F22, and B2. The callsign of a target, such as AF123, can eventually be determined. This latter operation is referred to as identification, and not as classification/recognition. Identification is usually implemented in a cooperative target recognition system (IFF), since it requires the target to send its identification number or identification code.

In this thesis, we use a single target class for all airplanes sharing the same physical properties. Looking ahead to Chapter 8, large-size airplanes and mid-size airplanes shall be labelled two different classes, while an A318 airplane and an A319 airplane shall be labelled the same class, since they are both mid-size airplanes.

1.1.4 Bistatic radar

A radar system is called bistatic (BS) when the transmitter and the receiver are not co-located, as shown in Fig. 1.1, by contrast with the monostatic (MS) radar for which the transmitter and the receiver are co-located [89]. By comparison with MS configurations, a BS configuration is characterized by an additional parameter, which is the bistatic angle, β. The bistatic angle β is defined as the angle (defined to be positive and less than 180°) between the transmitter and the receiver, with its vertex at the target [224].

1.1.5 Passive radar

Passive radars are radars that use illuminators of opportunity as transmitters. Illuminators of opportunity are transmitters that are already present in the environment,
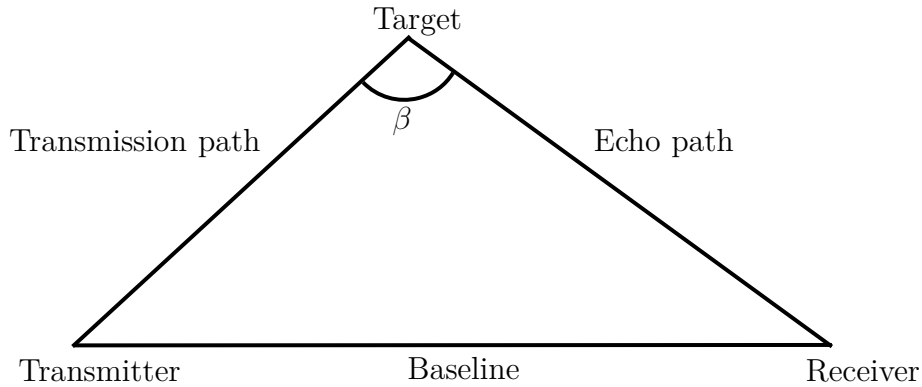
Figure 1.1: *Bistatic geometry for one pair of transmitter and receiver.*

such as analog TV transmitters, digital video broadcast - terrestrial (DVB-T) TV transmitters, or mobile phone base transceiver stations (BTSs). We propose to use one or multiple illuminators of opportunity as source of radar illumination, as in [225]. It is assumed that the different characteristics of the signals transmitted illuminators of opportunity, such as their location, frequency, modulation, and polarization are known but are not controlled.

The qualifier "passive" means that the transmitter is not aware of being used as a radar transmitter, although it must evidently be active. The transmitter is thus called non-cooperative. The different illuminators of opportunity that are used in actual passive radar systems are presented in Chapter 2.

Since the transmitter used is already present, the implementation of a passive radar requires few technical investments, especially since fast digital signal processors that make the acquisition and the processing of the scattered signals easy are available. Using illuminators of opportunity thus contributes to the low-cost aspect of the solution. Another advantage of a passive radar is that, since the transmitter is already operational, it allows for an immediate access to the frequency spectrum. The main disadvantage is that the characteristics of the signal transmitted are not controlled, since such a transmitter is usually not designed specifically for radar purposes.

Illuminators of opportunity considered in this work operate on the "low" frequency bands, defined here as frequencies lower than 1 GHz. The use of low frequencies for classification/recognition purposes is justified by the following reasons. First, since the wavelength is of the order of several meters, and since the length of the targets are of the order of tens of meters, the radar signature and its variations are essentially dependent on the larger parts of a target, and less sensitive to its smaller parts. The signature is thus robust and reproducible from one aircraft to the other at low frequencies. Second, transmitters operating at low frequencies are present everywhere in the environment: radio transmitters, TV transmitters, mobile phone BTSs. Therefore, the use of signals transmitted at these corresponding frequencies is straightforward. Third, low frequencies are suitable to defeat the possible stealthiness of air targets. Indeed, at low frequencies, no material can efficiently absorb the energy of the incident wave and be used in operation. Absorbing energy at these low

frequencies would require that the size of the stealth layer be very large, of the order of the wavelength, *i.e.* of about 3 m for a signal transmitted at a frequency of 100 MHz.

Passive radars are inherently bistatic. Such radars are called passive bistatic radars (PBRs). As explained in Chapter 2, PBRs are mainly used today for detection and location purposes. The use of PBRs for the recognition of air targets is a key feature of this thesis.

1.2 Developed techniques

We use radar signals transmitted by one or multiple transmitters (Tx's) of opportunity, scattered by a target, and collected by one or multiple receivers (Rx's). The configuration of the radar system is shown in Fig. 1.2 for a single (Tx,Rx) pair. The three ATR systems implemented in this thesis assign a class to the unknown, detected air target from the signal scattered by this air target and from the direct signal. The performances of the three proposed ATR systems will be compared in Chapter 9, in terms of (1) their probabilities of correct recognition, defined as the ratio of the number of objects correctly recognized to the total number of objects, and (2) the number of (Tx,Rx) pairs needed.
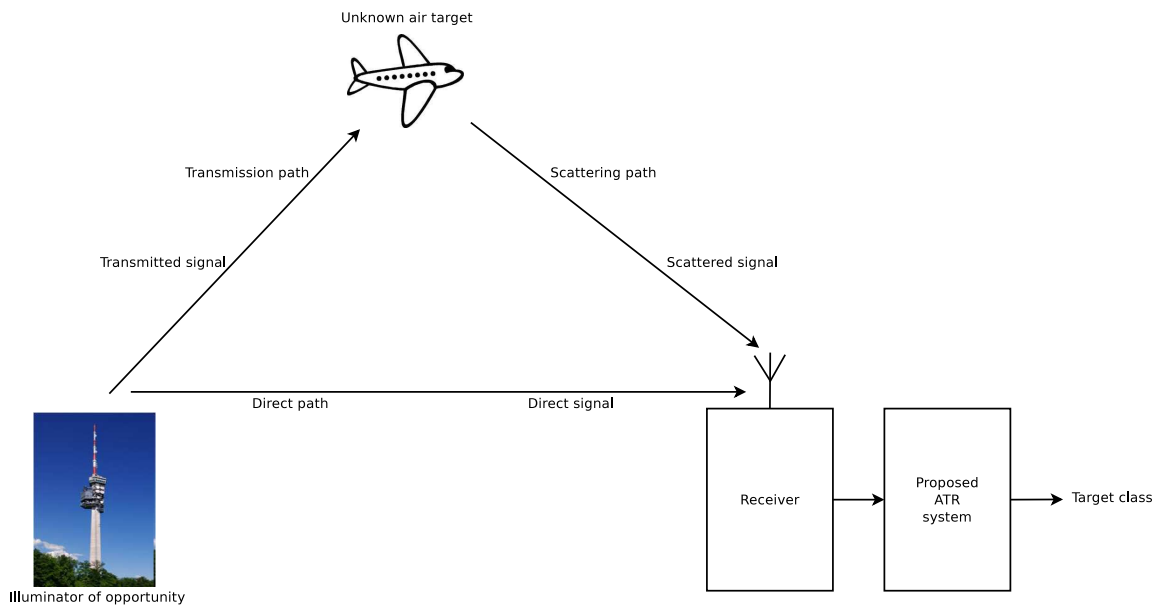
Figure 1.2: *Configuration of the radar system for a single (Tx,Rx) pair. An ATR system assigns a class to the unknown, detected air target based on the received scattered signal.*

1.2.1 Scene parameters

We assume that an unknown airplane to recognize has already been detected and tracked: we know its position and line-of-sight, *i.e.* its direction. However, we do not know its exact orientation, *i.e.* its yaw, pitch, and roll angles. These assumptions are realistic since the detection and tracking of an airplane is performed by a primary

surveillance radar (PSR) when the airplane is taking-off or landing, as described in Section 1.3. When the airplane is en-route, passive bistatic radars (PBRs) can detect and track airplanes, as explained in Chapter 2.

We assume that we know the location, polarization, and frequency of the Tx(s) of opportunity used, but we do not control them. We also assume that we know the location and polarization of the Rx(s), since the Rx(s) are under our full control. We call these parameters the scene parameters.

1.2.2   Quantities used for the recognition of targets

Consider the case of a PBR consisting of a single Tx of opportunity and a single Rx. One can extract, from the signal transmitted by the Tx, scattered by the unknown, detected air target, and collected by the Rx, the bistatic complex radar cross-section (BS-CRCS) and the bistatic radar cross-section (BS-RCS), which both characterize the target. We present the notions of BS-CRCS and BS-RCS in Chapter 3. The extraction of both the BS-CRCS and the BS-RCS from the signal scattered by an (air) target is explained in Chapter 4.

As described in Chapter 2, images of targets are often used in ATR. The radar image of a target is defined as a two-dimensional (2D) BS-CRCS density. We thus first perform the recognition of targets by using their radar images constructed from their BS-CRCS.

However, constructing radar images of air targets based on signals transmitted by illuminators of opportunity is difficult, as the required space and frequency diversity constraints (described in Chapter 5) would be difficult to meet in an operational system. Therefore, in a second step, we suggest to recognize targets by using either their BS-CRCS or their BS-RCS.

We test the first two ATR systems on data acquired in an anechoic chamber. For the third ATR system, we recognize targets by using their real-life BS-RCS, since, as shown in Chapter 8, the phase of the BS-CRCS is difficult to acquire in an operational, outdoor ATR system.

1.2.3   Proposed automatic target recognition (ATR) systems

We present three ATR systems. The three systems share the following characteristics:

- The raw input data of each ATR system consists of the signals transmitted by an illuminator of opportunity, scattered by a detected air target, and collected by a receiver. The input data is separated into a learning set (LS), and a test set (TS).

- The scene parameters are known, and are an input of each of the three ATR systems.

- The recognition, that we also call the classification, consists in a learning step and a test step. The learning step consists in the construction of the target class

model based on data in the LS. The test step consists in the determination of the target class of data in the TS, thus attributing a class to each data instance of the TS.

- The output of each of the three ATR systems is the class of the unknown, detected air target. We quantify the performance of each of the three ATR systems by computing the probability of correct recognition for each.

The three following subsections give a block diagram of each of our three ATR systems, as well as the characteristics of each of them.

ATR system using radar images

Our first ATR system recognizes targets by using their radar images. We will use this system as a reference to evaluate our two other ATR systems, which recognize targets by using either their BS-CRCS or their BS-RCS.

Figure 1.3 shows the block diagram of this first ATR system. The BS-CRCS of the targets are extracted from the raw input data, for both the LS and the TS (Chapter 4). The images of targets are then constructed from these BS-CRCS (Chapter 5). The images in the LS are used to generate the target class model. The target class of each image of the TS is determined by passing each image in the TS through the target class model (Chapter 6).
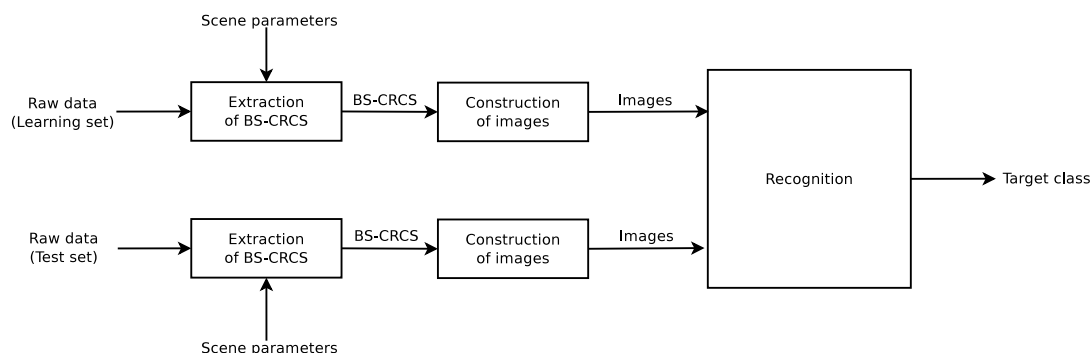
Figure 1.3: *Block diagram of our ATR system using radar images of targets.*

ATR system using either bistatic complex RCS (BS-CRCS) or bistatic RCS (BS-RCS)

Since the construction of images of targets is not feasible in an operational low-frequency passive bistatic radar system, as will be described in Chapter 5, we recognize targets by directly using either their BS-CRCS or their BS-RCS. Figure 1.4 shows the block diagram of our second ATR system. The BS-CRCS or the BS-RCS of the targets are extracted from the raw input data, for both the LS and the TS (Chapter 4). The class of unknown targets is determined by passing either their BS-CRCS or their BS-RCS through the target class model (Chapter 7).
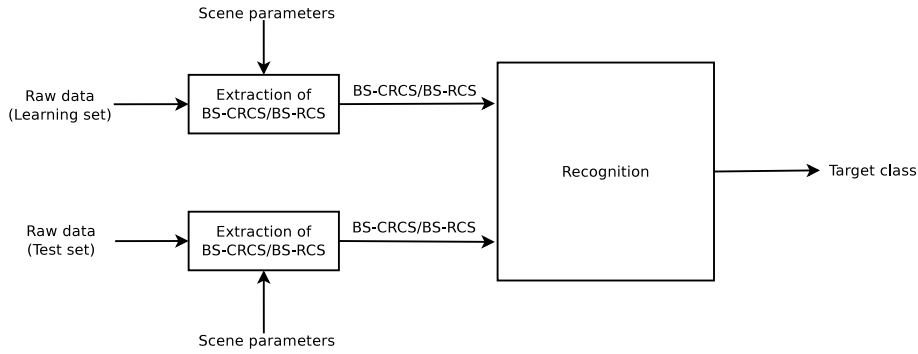
Figure 1.4: *Block diagram of our ATR system using the bistatic complex radar cross-sections or the bistatic radar cross-sections of targets.*

ATR system using real-life bistatic radar cross-sections (BS-RCSs)

In order to design an operational ATR system, we add a detection stage and a discrimination and pre-classification stage to the second ATR system, as shown in Fig. 1.5. This ATR system, that we discuss in Chapter 8, will be tested in an operational mode. For reasons to be explained in Chapter 8, we use the BS-RCS and not the BS-CRCS of air targets.
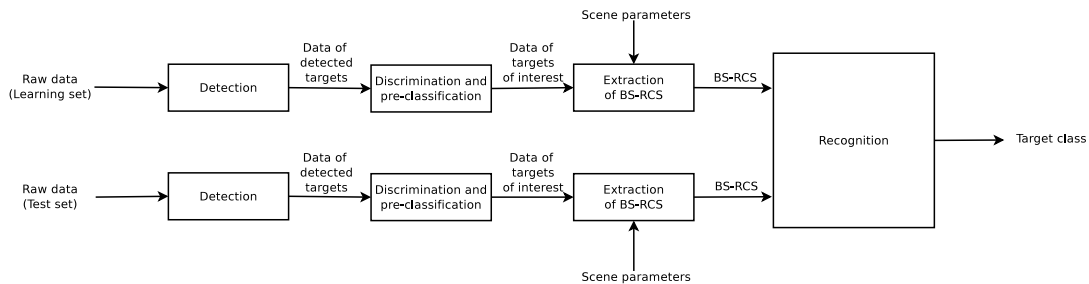
Figure 1.5: *Block diagram of our ATR system using real-life bistatic radar cross-sections of targets.*

We perform the discrimination between detected targets of interest and other detected man-made targets in the discrimination and pre-recognition stage. The BS-RCS of the targets of interest are extracted in the extraction of BS-RCS stage, and are the input of the recognition stage. The class of targets of interest is determined by passing their BS-RCS through the target class model.

1.3   Background: conventional air traffic control (ATC)

In this thesis, we address the problem of the recognition of non-cooperative targets, called non-cooperative target recognition (NCTR). Since the targets considered in this work are air targets, we describe the principles of air traffic control (ATC).

In Europe, ATC is performed by secondary surveillance radars (SSRs) when airplanes are en-route. Around airports, *i.e.* for take-off and landing operations, ATC is performed by airport surveillance radars (ASRs), consisting in the joint use of primary surveillance radars (PSRs) and SSRs. In the United States, ASRs are used both en-route and near airports [204]. We now briefly describe PSRs and SSRs, in order to point out their limitations for ATC for the recognition of non-cooperative airplanes.

1.3.1 Primary surveillance radar

A primary surveillance radar (PSR), also called moving target detector (MTD), is a particular type of moving target indicator (MTI) radar [187, 204]. As for any radar, it sends out electromagnetic pulses. If an (air) target is present, the surface of this target will reflect the incident pulse back to the radar. The time taken by the pulse to reach the target and return to the PSR gives the distance from the radar antenna to the target according to

$$D = \frac{c\tau}{2}, \tag{1.1}$$

where D is the distance from the antenna to the target, c the speed of light, and τ the round-trip delay.

The bearing of the target is given by the azimuth orientation of the PSR antenna. The elevation angle of the target is not measured. The PSR radar scans the entire horizon at some scan rate, which means that a particular portion of the sky is not continuously monitored, therefore limiting the dwell time.

Figure 1.6 shows the key stages of a PSR radar [137]. First, the signal scattered on the target is digitized by an analog-to-digital converter (ADC). Second, the signal scattered on the target is separated from clutter by using clutter cancellation filters, such as digital Doppler filters. Then, the signal scattered on the target is separated from thermal noise using a constant false alarm rate (CFAR) thresholding algorithm. A scan-to-scan correlation-and-tracking algorithm generates a single report per target, from a cluster of range-azimuth-Doppler target reports, so that a target is represented by a single dot on the plan-position indicator (PPI).
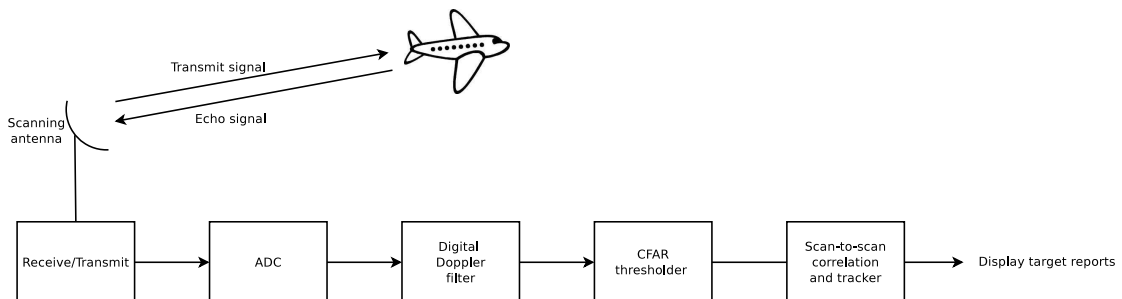
Figure 1.6: *Simplified block diagram of a primary surveillance radar.*

The main advantage of the PSR is that it does not require the cooperation of the target itself. It is also capable of detecting small energy responses, making it available to monitor weather. The main disadvantage of the PSR is its inability to discriminate

between targets presenting the same level of return energy. Another disadvantage of the PSR is the large amount of transmitting power required so that the echo signal has a power high enough to be measurable. This limits its range. Moreover, echo signals are subject to external factors such as changes of target attitude, resulting in fading of these echo signals.

1.3.2   Secondary surveillance radar

A secondary surveillance radar (SSR) is used to identify an air target, whether it has been detected by a PSR radar [192] if the air target is near airports, or not if it is en-route. SSRs can be seen as the civilian adaptation of the military identification friend-or-foe (IFF) radar systems that were initially developed during World War II [68]. During this war, air targets equipped with IFF systems had to respond with a specific signal to signals transmitted by ground-based transmitters. A correct response made the aircraft be identified as friend, while an incorrect response made the aircraft be identified as foe.

Figure 1.7 shows the principle of an SSR. The SSR transmitter sends out an interrogation signal to the transponder (transmitter/receiver working on radar frequencies) carried aboard the cooperative target. The on-board transponder responds to the SSR interrogation by sending a signal containing information such as the target identity (squawk code) and position. Upon reception, the response signal is processed by the receiver in order to identify the target on the operator plan-position indicator (PPI). If the target transponder does not respond, it is considered as a non-cooperative target in civilian aviation, and as an enemy in military aviation.
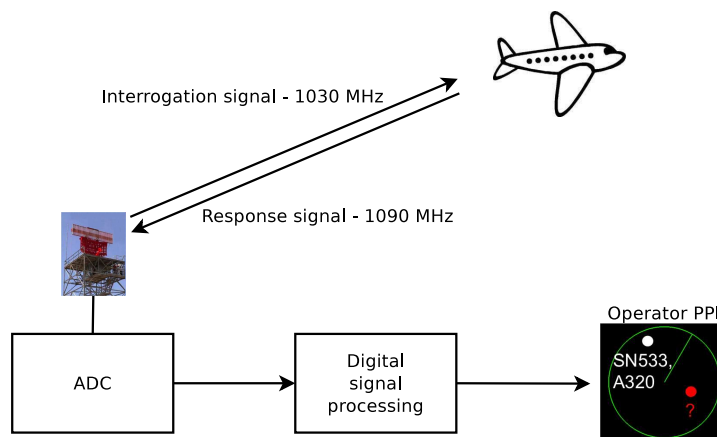
Figure 1.7: *Simplified block diagram of the receiving stage of a secondary surveillance radar.*

The main advantage of the SSR is that the transmitting power from the SSR transmitter can be reduced. Indeed the power of the received signal decreases by a factor of D^2 instead of D^4 in the PSR case, since both the radar and the target transmit in the SSR case. Another advantage is the complete identification and location of the air target through the information sent from the target.

The automatic dependent surveillance (ADS) system is the SSR used today. An ADS system relies on a transponder aboard an air target that transmits data, such as its position, altitude, and speed, to the ground station. Today, the automatic dependent surveillance- broadcast (ADS-B) mode [22, 209], which is part of the new Traffic Alert and Collision Avoidance System (TCAS), is used [9].

1.3.3 Non-cooperative target recognition (NCTR) within air traffic control (ATC)

As described above, the identification process is based on the presence of a transponder aboard the air target, and on the confidence in the response from such transponder. In case there is no transponder aboard the target, or its transponder is not working properly, or it is turned off, the target cannot be identified.

Near airports, one could think of analyzing the signals transmitted by the PSR and scattered by the air target back to the PSR to characterize the target. However, for conventional and existing PSRs, as the scan rate is high, the dwell time is limited, of the order of a few milliseconds. Moreover, as the range is important, the distance resolution is also low. It is therefore difficult to analyze the target using a PSR, and even more difficult to create an image or a high-resolution range profile of the target to recognize it. Furthermore, because of the limited "time-on-target", PSRs will not be used as transmitters of opportunity.

However, studies aiming at designing new PSRs that would be able to combine both tracking and identification modes within the same scan are currently on-going. These new PSRs are not considered here, as they are not operational yet.

In conclusion, the use of conventional PSRs and SSRs does not allow one to identify non-cooperative targets. Moreover, even though SSRs are able to identify cooperative targets, SSRs do not provide any verification mean, since SSRs trust the information received from the target transponder.

1.4 Contributions of the thesis

We list here the main contributions of the thesis. First, we use low-frequency passive bistatic radar signals for the classification/recognition of air targets. Indeed, many passive bistatic radar signals are used for the detection and location of targets, but not for their recognition. The use of illuminators of opportunity contributes to the low-cost aspect of the proposed solution. The use of low-frequency radar signals for the recognition of targets is not common, since many automatic target recognition (ATR) systems operate at higher frequencies.

Our first ATR system recognize targets by using their radar images. Although the expression for the construction of the radar image of a target from its bistatic complex radar cross-section (BS-CRCS) is known, we provide its derivation from the principles of tomographic imaging, as second contribution. The reason is that we could not find this derivation in the literature.

Third, we recognize non-cooperative air targets, based on either their BS-CRCS or their bistatic radar cross-section (BS-RCS). This is a major difference with many ATR systems that mainly use either high-resolution range profiles or radar images of targets.

Fourth, we developed three ATR systems that use two recognition techniques, which are the extremely randomized trees and the subspace methods. To the best of our knowledge, the use of tree-based classification methods in the radar ATR domain is novel. To the best of our knowledge, vector subspaces are mainly used in the radar domain for detection, and not for classification/recognition.

Fifth, we learn and train the recognition stage of each of our three ATR systems on real data.

Sixth, we deploy a passive bistatic radar that we use for the acquisition of real-life passive bistatic radar signals. We extract the real-life BS-RCS of commercial airplanes from these signals.

1.5 Organization of the manuscript

Chapter 2 presents a literature review of passive bistatic radars, illuminators of opportunity, and automatic target recognition (ATR).

Chapter 3 presents the notions of bistatic complex radar cross-section (BS-CRCS) and bistatic radar cross-section (BS-RCS), and their variations according to different physical parameters. The reason is that our three ATR systems rely on either the BS-CRCS or the BS-RCS of targets.

Chapter 4 presents the extraction of both the BS-CRCS and the BS-RCS of targets, and illustrates experimentally the variations of both the BS-CRCS and the BS-RCS of air targets as a function of different physical parameters.

Chapter 5 presents the theoretical and practical computation of the radar images of targets from their BS-CRCS, for both a monostatic configuration and a bistatic configuration.

Chapter 6 presents the design, implementation, and test of the recognition stage of the ATR system recognizing targets by using their radar images.

Chapter 7 presents the design, implementation, and test of the recognition stage of the ATR system recognizing targets by using either their BS-CRCS or their BS-RCS.

Chapter 8 presents the design, implementation, and test of the ATR system recognizing targets by using their real-life BS-RCS. This chapter also presents the experimental testbed we implemented to acquire real-life, outdoor passive bistatic radar signals from which we extract the BS-RCS of the air targets of interest.

Chapter 9 summarizes the work performed in this thesis. It also compares the

performances of our three ATR systems, and discusses future developments to be performed to validate an operational ATR system based on passive bistatic radar signals.

1.6 Conclusion

In this chapter, we presented the motivation for this thesis, which consists in the low-cost classification/recognition of non-cooperative air targets. We recognize such air targets by the use of signals transmitted by low-frequency illuminators of opportunity, and scattered by these air targets. The automatic target recognition (ATR) systems proposed here thus use passive bistatic radar. The notions of ATR, target class, passive radar, and bistatic radar were defined.

We presented three different ATR systems. The input of each ATR system consists in the known parameters of the scene, and in the signals scattered by an air target. The output of each ATR system consists in the class of this unknown air target. The three ATR systems recognize targets by respectively using their radar images, their bistatic complex radar cross-section (BS-CRCS), and their bistatic radar cross-section (BS-RCS).

Since we consider non-cooperative air targets, we briefly described some key principles of air traffic control (ATC), which is based on primary surveillance radars (PSRs) and secondary surveillance radars (SSRs). We discussed the reasons why current PSRs and SSRs cannot be used for the recognition of non-cooperative air targets.

We listed the contributions of this thesis, and we presented the organization of this manuscript.

Chapter 2

Passive bistatic radar, illuminators of opportunity, and automatic target recognition: state-of-art

Contents

In this chapter, we review the literature about passive bistatic radars and automatic target recognition. Section 2.1 describes the state-of-art of passive bistatic radars. Section 2.2 lists the different illuminators of opportunity used in actual passive bistatic radar systems. Section 2.3 describes the state-of-art of automatic target recognition. Section 2.4 concludes.

2.1   Passive bistatic radar

The word "RADAR" is an acronym meaning "RAdio Dection And Ranging" [187]. The first radar experiments were conducted by Christian Hulsmeyer, in 1904 [84]. He publicly demonstrated the capability of detecting a ship from the Hohenzoellern Bridge over the Rhine River in Cologne, Germany. However, since the demonstration failed to capture the attention of the military authorities, the invention was forgotten. The theories of bistatic radar [186] and bistatic radar cross-section [48, 49, 98] were developed in the 1950s. A complete history of radar and, more specifically, of bistatic radar can be found in [187, 224, 225].

A bistatic radar is a particular type of radar for which the transmitter and the receiver are not co-located, by constrast with a monostatic radar for which the transmitter and the receiver are necessarily co-located. The first radar systems were

essentially bistatic, mainly for technical reasons. Indeed, the duplexer, that enables one to use a common transmit and receive antenna, was invented only in 1936. Thus, the transmit and receive antennas had to be isolated from each other. In practice, the transmitter and the receiver were separated by a distance equal to the distance between the transmitter and the target [224].

Although many bistatic radar experiments were conducted in the 1920s and 1930s, bistatic radar was heavily developed during World War II. For example, during this war, the German receiver, called the "Klein Heidelberg", detected the presence of Allied airplanes by receiving the signals transmitted by the British "Chain Home", which is a series of transmitters, and scattered by the Allied airplanes crossing the English Channel. This made the receiving system undetectable. The Klein Heidelberg appears to be the first use of non-cooperative transmitters [78, 187]. This type of transmitter is referred to as a "transmitter of opportunity" or as an "illuminator of opportunity" [75]. This type of radar is called a passive bistatic radar (PBR). The term "passive" refers to the fact that the transmitter used is not specifically dedicated to this particular radar application.

The geometry of (passive) bistatic radar systems is thoroughly described in [91, 224]. The principles, advantages, and disadvantages of PBRs are extensively described in [224], and summarized in [73–75]. Some key points are:

- The bistatic radar receiver is potentially simple, and thus cheap.

- The bistatic radar receiver is passive, and thus covert.

- The modulation of the transmitted signals of opportunity is not chosen for radar purposes.

- The use of low frequencies enables to counter stealth (as explained in Chapter 1).

- The cancellation of the direct-path signal, of multipath signals, and of interference signals requires one to use sophisticated signal processing at the receiver.

- The bistatic radar cross-section of a given target is generally different from its monostatic radar cross-section (as discussed in Chapter 3).

Today, PBRs are mainly used for detection and location purposes. PBRs are thus often called passive coherent location (PCL) radar [75]. Different passive bistatic radar systems are presented, and their performance discussed, in [6, 7, 18, 47, 76, 112, 115, 121, 172, 200, 207]. The different illuminators of opportunity used are now briefly described.

2.2   Illuminators of opportunity

Passive bistatic radars are called passive since they use the signal broadcast by a transmitter designed for other purposes, such as FM radio, DAB (Digital Audio Broadcast) radio, analog TV, digital TV, or mobile phones communications. A comprehensive list of illuminators of opportunity used today in passive bistatic radar systems is given in [73]. The most commonly used illuminators of opportunity in passive bistatic radar (PBR) systems are AM radio transmitters [172], FM radio

transmitters [86, 116, 172], DAB transmitters [45, 71, 159, 172, 206], analog TV transmitters [77, 85, 172], digital video broadcast (DVB) transmitters [71, 159], and mobile phone base stations [120, 197, 198, 201–203]. All these transmitters operate on low frequency bands, *i.e.* at frequencies lower than 1 GHz. Their signals are narrowband, except for DVB signals.

Among the other illuminators of opportunity used, wireless networks, such as in [80, 81], are used for limited-range applications, due to the low power of the transmitters. Satellite-based transmitters are also used, as in [42]. Since satellites carrying these transmitters are not geostationary, these transmitters do not illuminate the same geographic region permanently, in contrast to fixed ground-based transmitters of opportunity, such as FM radio stations. Satellite-based transmitters and wireless networks are thus not considered in this thesis.

2.3 Automatic target recognition (ATR)

In this section, we first describe the canonical block diagram of usual ATR systems, as presented in the literature. We then present the adaptation of this canonical block diagram to our problem. The block diagrams of the three ATR systems (Chapter 1) are designed according to this adapted block diagram.

We then present the input data and the classification techniques of the main ATR systems reported in the literature.

2.3.1 Canonical block diagram of a conventional automatic target recognition (ATR) system

Figure 2.1 presents the canonical block diagram of a conventional ATR system, as presented in [17, 44]. The block diagrams of other recognition systems published in the literature [106, 214, 215, 229] are designed according to this canonical block diagram. Starting with raw data, the first stage consists in the detection of a potential target in the midst of thermal noise. The second stage, called discrimination, consists in differentiating between a potential target and surrounding clutter. The pre-classification stage distinguishes between targets of interest and targets that are not of interest. The fourth stage consists in the classification of the targets of interest. It assigns a class to every object to be classified. The last stage is the identification stage. It can be seen as a refining classification stage, as each object is being assigned a sub-class. It should be noted that the representation of Fig. 2.1 is not the only one possible, but it has the advantage of comprising the key stages of most ATR systems.

Raw data → Detection → Discrimination → Pre-classification → Classification → Identification → Class & sub-class
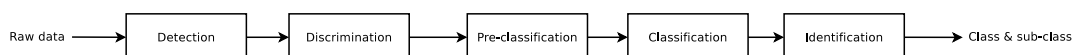
Figure 2.1: *Block diagram of a canonical ATR system [44].*

2.3.2 Adaptation of the canonical ATR block diagram to our problem

In this section, we discuss the adaptation of the canonical block diagram of an ATR system to our problem. Here, the raw data consist of any signal collected by the receiver of the passive bistatic radar system. The detection stage consists in detecting an air target. The discrimination stage and the pre-classification stages are performed together. Indeed, since the signal echoed by an air target has a Doppler shift due to the motion of the air target, and since this Doppler shift is higher than the Doppler shift induced by ground-moving vehicles, an air target is separated from clutter and from ground-moving targets by a Doppler processing stage, as will be seen in Chapter 8.

We add a signal processing stage to compute either the bistatic complex radar cross-section, the bistatic radar cross-section, or images of the targets from the signal transmitted by an illuminator of opportunity, scattered by a detected target, and collected by the receiver.

The classification stage, which we also call the recognition stage, computes the target class model, and assigns a target class to the unknown targets.

There is no identification step in our ATR systems, as this requires the target to be cooperative. Indeed, the callsign of an air target is known only if sent by the air target, since it does not rely on any physical parameter of the air target.

Figure 2.2 presents the adapted block diagram of the ATR system. We design each of the three proposed ATR systems described in Section 1.2.3 according to this adapted block diagram.
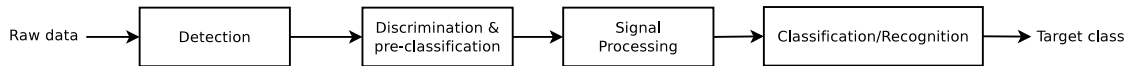
Figure 2.2: *Block diagram of the implemented automatic target recognition system.*

2.3.3 Input data and classification techniques of usual automatic target recognition (ATR) systems

This section describes the input data of the recognition stage (Fig.2.2) and the most popular classification techniques used in ATR systems. We present the ATR systems according to the type of input data. Today, most ATR systems use two different input data; indeed, classifiers recognize targets using either their high range resolution (HRR) profiles or their radar images [4,17,44,55,148]. ATR systems are also beginning to use radar cross-sections (RCSs) of targets as input data.

First technique: ATR using high-resolution range profiles of targets

Since many ATR systems use HRR profiles, we describe such systems briefly. Some reasons for not using such HRR range profiles are also explained in the present work.

In HRR radar, a transmitter transmits a wideband signal (*e.g.* a chirp signal). A wideband signal is defined as a signal whose bandwidth is of the same order as its central frequency. The radar receiver receives the scattered pulses over a period of time. HRR range profiles are defined as the one-dimensional (1D) measurement of the target radar reflectivity along the radar to target line of sight (LOS) [133, 227]. It is known that the resolution of the range profile is inversely proportional to the bandwidth of the transmitted signal [222].

The interest of using HRR profiles for classification is discussed in [93, 133, 136]. Examples of ATR systems using HRR data are [37, 52, 66, 88, 92, 93, 101, 111, 143, 190, 218, 223, 234]. In [37, 52, 66, 88, 92, 93, 111, 223, 234], targets are classified directly based on their HRR profiles. In [101, 143, 190], explicit features such as the target length, its center of mass, or its number of scatterers are extracted using diverse signal processing methods such as MUSIC [101]. The classification techniques used are mainly the Bayes classifier [101, 234], the k-nearest neighbor algorithm (kNN) [37], the linear discriminant analysis (LDA) [190], the multiple discriminant analysis (MDA) [190], likelihood functions [92, 93], and the maximum a posteriori (MAP) criterion [88]. Many of these ATR systems reported in the literature use simulated HRR profiles of targets. For example, a method for constructing a database of HRR profiles is described in [143].

Using HRR profiles for the problem addressed in this thesis is not feasible. Indeed, as described in Section 2.2, most illuminators of opportunity work at frequencies lower than 1 GHz. Moreover, their signals are narrowband. Therefore, obtaining the signal scattered by a target over a wide frequency band would require to use a large number of illuminators of opportunity operating on adjacent frequency bands. A large number of receivers would also be needed in order to consider the same bistatic angle for each (Tx,Rx) pair, since the transmitters would not be located at the same point. It thus seems unrealistic to obtain HRR profiles by using illuminators of opportunity as transmitters of a passive bistatic radar system.

Second technique: ATR using radar images of targets

Many ATR systems recognize targets by using radar images of these targets. A two-dimensional (2D) radar image of a target is defined as the 2D complex radar cross-section density of this target. We derive the expression of the radar image of targets in Chapter 5. In practice, a 2D radar image of a target is obtained by applying a 2D inverse Fourier Transform to a 2D array of complex radar cross-sections of targets. Elements of the 2D array vary according to two different parameters that can be frequency, aspect angle, or bistatic angle [24, 138, 167, 189]. Usually, targets are acquired at different frequencies (over a limited frequency band) and at different angular values [102, 158, 196]. Therefore, diversity in both frequency and angle is needed in order to fill the Fourier space, so that images of targets can be constructed. Usually, images are constructed at a high resolution, and thus, at frequencies higher than the ones used by illuminators of opportunity [131, 165].

Today, many image-based ATR systems reported in the literature use Synthetic Aperture Radar (SAR) images. The formation of SAR images is discussed in [32, 51, 114, 191], and will not be treated here, as it is beyond the scope of this work. A thorough literature review of SAR ATR can be found in [140]. Among the different

approaches, let us mention [166], which extracts scattering centers and contours from each image, and then classifies targets using a nearest neighbor algorithm. In [38] and [217], features are extracted out of images of targets by using time-frequency techniques such as those based on wavelets. A bistatic SAR ATR system is described in [132].

Many image-based ATR algorithms use the standard MSTAR data [174], where MSTAR stands for "Moving Stationary Target Acquisition and Recognition". The MSTAR data consists of SAR images of targets collected and distributed under the DARPA MSTAR program. The MSTAR data allows researchers to test and compare their ATR algorithms. Various reports and articles in the literature present different classification methods, such as support vector machines (SVMs) [83, 228, 231], adaptive boosting [199], neural networks [144], template-matching [31], likelihood test [31], and MINACE filters [145]. In [144], tree-structured directional filter banks (DFB) extract features from SAR images, and high-order neural networks (HONN) classify targets. In [231], SVMs are a fairly good classifier, but a pose estimator as in [232] is needed to estimate the poses of the targets. Other classification techniques tested, such as k-nearest neighbor (kNN) [228] and SVM [83, 228], all rely on feature extraction techniques, such as principal component analysis (PCA). In [199], the use of adaptive boosting also needs pose estimation and feature extraction. Template-matching [31] is also an efficient classification technique. However, it requires to determine a matching score function such as the mean-squared error (MSE) between the test image and the template. In [145], the MINACE filter requires to tune the filter parameters, and to compute the inverse of the images' spectral envelope matrix, which is computationally demanding.

ATR systems in other domains, such as Laser Detection and Ranging (LADAR), also rely on the use of images of targets as in [213, 215, 216].

There are several limitations to the implementation of an image-based passive radar ATR system. Even though the need for angular diversity could be satisfied by using a sufficient number of transmitters and receivers, and by locating the receivers appropriately, the need for frequency diversity appears to be difficult to meet. Indeed, it is very unlikely that a sufficient number of transmitters of opportunity, operating on adjacent frequencies and in a common geographical region, are available. However, since image-based ATR systems are very popular, our first ATR system recognizes targets by using their radar images. This system will be used as a basis of comparison for our two other ATR systems.

Third technique: ATR using RCS of targets

In [13], Bares investigated the recognition of air targets based on their low-frequency RCSs. The classification methods use either kNNs or NNs. The RCSs of air targets were both simulated using the Numerical Electromagnetic Code (NEC2) software and obtained from experimental data. As described in [13, 30], the radar used, called MOSAR-4F, operates on the high frequency (HF) and very high frequency (VHF) bands, in a monostatic configuration. The monostatic configuration, and thus, the use of an active radar is a major difference with the problem addressed in this thesis, since we recognize targets based on signals transmitted by illuminators of opportunity

("passive" transmitters), and collected by a receiver, with the transmitters and the receiver being in a bistatic configuration.

In [82], Herman reported a new ATR system based on passive radar. This system also bypasses the construction of images of targets by using directly their RCS. The RCS of targets are numerically computed using the method of moments implemented in the FISC (Fast Illinois Solver Code) software. However, the computational costs of the implemented particle filter used for tracking and classification are prohibitive, as stated in [82].

In [59–64, 168], Ehrman *et al.* developed a less computationally-intensive ATR system that is based on passive radar and that classifies targets directly from their RCS. The RCS of different airplanes along simulated trajectories are computed by jointly using the FISC software, a coordinated flight model, the NEC2 software, and the Advanced Refractive Effects Prediction System (AREPS). The power of the signal scattered by an airplane and collected by the receiver antenna is generated by the joint use of FISC and a coordinated flight model. The flight model is used to estimate the yaw, roll, and pitch angles of the airplane, in order to compute the RCS of this airplane as accurately as possible. AREPS takes into account the propagation losses, and NEC2 models the gain of the receiver antenna [61].

The target class model consists of a library of such pre-computed RCSs. The RCS of an unknown, detected airplane to be classified is computed by using the signal scattered on the airplane, and the flight model. A class is assigned to an unknown airplane by comparing its RCS to the precomputed RCSs of known airplanes using a Rician likelihood model.

The key feature of the ATR system proposed by Ehrman *et al.* is to model as accurately as possible the RCS of an airplane along its trajectory. Different airplane trajectories were simulated in [59, 61, 63, 64].

To the best of our knowledge, the ATR system implemented by Ehrman *et al.* is the only ATR system that recognizes targets by directly using their RCS, and that is based on a passive (bistatic) radar. The fact that this ATR system is based on simulation is a major difference with the ATR systems implemented in this thesis, which all rely on data acquired either in an anechoic chamber (Chapter 4) or operationally (Chapter 8).

2.4 Conclusion

This chapter presented the state-of-art of passive (bistatic) radar (PBR). We showed that PBRs are so far mainly used for detection and location purposes. We enumerated the different illuminators of opportunity that are used in today's passive bistatic radar systems.

We presented the canonical block diagram of a usual automatic target recognition (ATR) system, and described its successive stages, *i.e.* the detection of a target, the discrimination between a target and surrounding clutter, the pre-classification of this target as being of interest or not, the classification of this target, and its identification.

We also presented the adaptation of this canonical representation to our problem, resulting in the grouping of the discrimination and pre-classification stages, and in the discarding of the identification stage.

We showed that current radar ATR systems classify targets mainly by using either the high range resolution (HRR) profiles or the radar images of these targets. We also listed the main classification techniques that have been used in ATR systems to date, such as support vector machines (SVM), neural networks (NN), and template-matching. We stated the reasons for using neither HRR profiles nor radar images of targets in an operational ATR system for a PBR. We described the few existing passive bistatic radar ATR systems that classify targets based on their RCSs, and we stated their limitations.

Chapter 3

Bistatic radar phenomenology

Contents

Section 3.1 presents the motivation for the presentation of bistatic radar phenomenology. Section 3.2 presents the notations used in this chapter. Section 3.3 defines the geometry of the bistatic configuration considered. Section 3.4 defines the notions of bistatic complex radar cross-section (BS-CRCS) and of bistatic radar cross-section (BS-RCS). Section 3.5 presents the scattering mechanisms responsible for the radar cross-section (RCS) of a target, whether real or complex, and whether monostatic or bistatic. Section 3.6 presents the different scattering regions. Section 3.7 presents the theoretical computation of the BS-RCS of a simple generic object, a perfectly conducting sphere, thus highlighting the parameters that the BS-RCS is a function of. Section 3.8 discusses the application of the monostatic-to-bistatic equivalence theorems for the computation of the BS-RCS of an object. Section 3.9 concludes.

3.1 Motivation for the presentation of bistatic radar phenomenology

In the radar domain, targets, also referred to as objects, are characterized either by their complex radar cross-section (CRCS), traditionally denoted by the monolithic symbol $\sqrt{\sigma}$, or by their radar cross-section (RCS), traditionally denoted by σ [103,188]. We emphasize that $\sqrt{\sigma}$ is complex-valued, whereas σ is real-valued. We also emphasize that $\sqrt{\sigma}$ is a symbol, *i.e.* $\sqrt{\sigma}$ must not be interpreted as the mathematical square root of σ.

Our three automatic target recognition (ATR) systems presented in Chapter 1 and discussed in Chapters 6, 7, and 8, respectively, rely on either the bistatic CRCS (BS-CRCS) or the bistatic RCS (BS-RCS). Our first ATR system recognizes targets by using their radar images that are constructed from their BS-CRCS (Chapter 5). Our second ATR system recognizes targets by using either their BS-CRCS or their BS-RCS, without computing their radar images. Our third ATR system detects targets, and then recognizes them by using their BS-RCS.

The design of each of our three ATR systems thus relies heavily on the notions of BS-CRCS and BS-RCS, and more specifically on the physical parameters upon which they depend. Indeed, as will be discussed later, targets can be accurately recognized, *i.e.* discriminated from one another, only if their respective BS-RCS, whether complex or real, differ. It is thus of primary importance to have a complete understanding of the notions of BS-CRCS and BS-RCS, and of the parameters that they are function of.

3.2 Notations

In this chapter, unless otherwise specified, we use the following notations for a quantity "x":

- a real number in $\mathbb{R}$ is denoted by x,

- a complex number in $\mathbb{C}$, is denoted with an overbar, such as $\bar{x}$,

- a (real) geometrical vector in the (x, y, z) axes, *i.e.* in $\mathbb{R}^3$, is denoted by an underline, such as $\underline{x}$,

- a geometrical unit vector in the (x, y, z) axes, *i.e.* in $\mathbb{R}^3$, is denoted with both an underline and a hat, such as $\underline{\hat{x}}$,

- a complex vector (in the complex plane $\mathbb{C}$) is denoted by $\underline{\bar{x}}$,

- a matrix of complex vectors is denoted by $\bar{\underline{\bar{x}}}$.

3.3 Bistatic scattering geometry

Figure 3.1 shows the geometry of the bistatic (BS) configuration considered in this chapter. A generic target for which the expressions of both its bistatic complex radar

cross-section (BS-CRCS) and its bistatic radar cross-section (BS-RCS) are derived is placed at the origin of the coordinate system. Even though we can envision the use of multiple transmitters and receivers, we consider here the case of a single transmitter (Tx) and a single receiver (Rx), thus forming a single (Tx,Rx) pair. The Tx is located at point (x_T, y_T, z_T), *i.e.* at a distance r_T from the target and, more precisely, from the center of the coordinate system located somewhere on, or near, the object. The Rx is located at point (x_R, y_R, z_R), *i.e.* at a distance r_R from the target. We consider both distances to be equal, and thus $|\underline{r}_T| = |\underline{r}_R| = r$. In summary, we have

$$|r_T| = |r_R| = r$$
$$|\hat{\underline{r}}_T| = |\hat{\underline{r}}_R| = 1$$
$$\underline{r}_T = r\hat{\underline{r}}_T$$
$$\underline{r}_R = r\hat{\underline{r}}_R.$$

The wave transmitted by the Tx travels from T to O in the direction of $-\underline{r}_T$, and is characterized by its wave vector $\underline{k}_T$, with orientation $-\underline{r}_T$. The wave travelling from O to R in the direction $\underline{r}_R$ is characterized by its wave vector $\underline{k}_R$. Both wave vectors have same magnitude $k = 2\pi/\lambda = 2\pi f/c$, where λ is the wavelength, and c is the speed of light. We thus have

$$\underline{k}_T = k\hat{\underline{k}}_T,$$
$$\underline{k}_R = k\hat{\underline{k}}_R$$
$$|k_T| = |k_R| = k$$
$$|\hat{\underline{k}}_T| = |\hat{\underline{k}}_R| = 1.$$

The pairs of unit vectors $\hat{\underline{\phi}}_t$ and $\hat{\underline{\theta}}_t$, and $\hat{\underline{\phi}}_r$ and $\hat{\underline{\theta}}_r$, will be introduced in Section 4.2 to denote the polarization basis of the transmitter and the receiver, respectively.
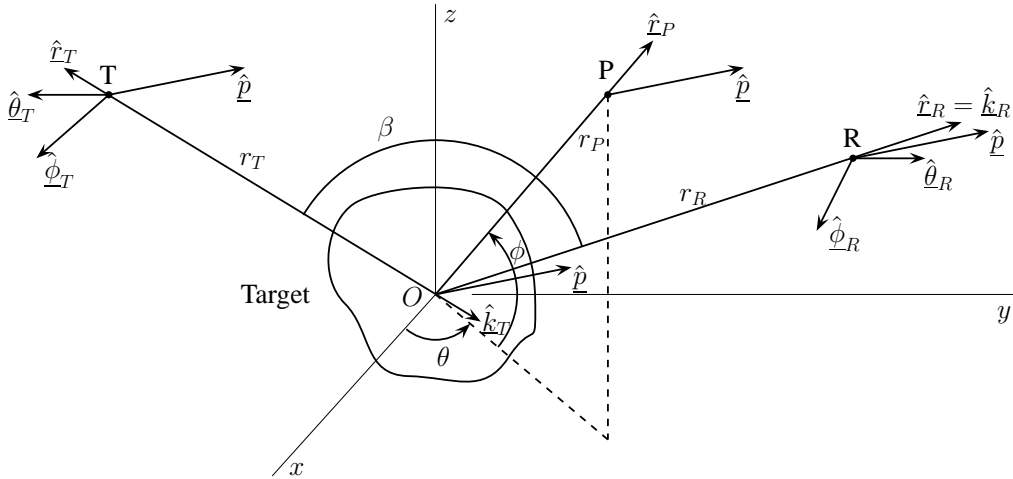
Figure 3.1: *Geometry of the bistatic configuration considered.*

A major characteristic of BS configurations is that the Tx and the Rx are not necessarily co-located. Therefore, at least $x_T \neq x_R$, $y_T \neq y_R$, or $z_T \neq z_R$. Since the Tx and the Rx are not co-located, a major characteristic of BS configurations is the

bistatic angle β, defined as the angle between the Tx and the Rx with vertex at the target, *i.e.* at the origin O of the coordinate system (Fig. 3.1). One can intuitively understand that the bistatic angle β will influence the bistatic radar cross-section of an object, whether complex or not, as is discussed below.

The monostatic (MS) configuration (Fig. 3.2), *i.e.* a configuration for which the Tx and the Rx are co-located, is a particular case of the BS configuration. In an MS configuration, $x_T = x_R$, $y_T = y_R$, and $z_T = z_R$. In Fig. 3.2, we also show the representation of the location of a generic point P in the spherical coordinates (r, θ, ϕ).
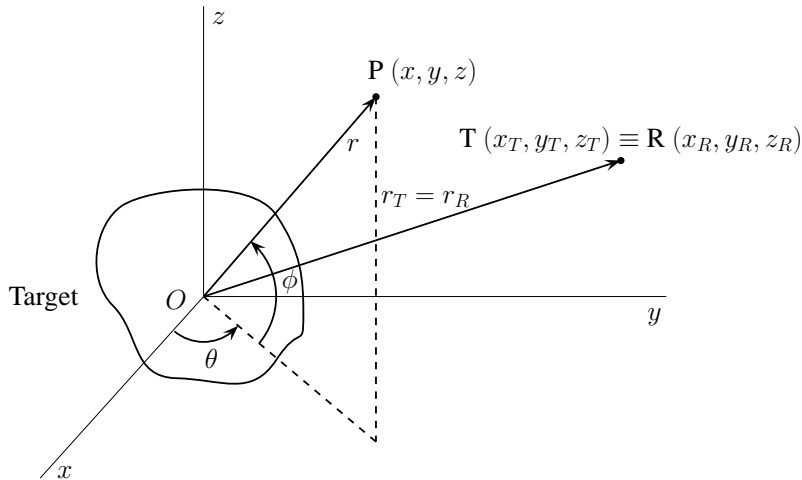
Figure 3.2: *Geometry of a monostatic configuration.*

3.4   Definitions of the bistatic complex RCS and the bistatic RCS

We define the notions of complex and real RCS. Since we deal with bistatic configurations, we introduce the bistatic complex radar cross-section (BS-CRCS), denoted by $\sqrt{\sigma}^{BS}$, and the bistatic radar cross-section (BS-RCS) denoted by σ^{BS}. The superscript "BS" is used in order to avoid confusion with the monostatic MS-CRCS $\sqrt{\sigma}$ and the monostatic MS-RCS σ. The superscript "BS" will be dropped when the context is clear enough.

The agreed definition of the BS-CRCS $\sqrt{\sigma}^{BS}$ is [46, 170, 205, 212]

$$\sqrt{\sigma}^{BS} = \lim_{r_R \to \infty} 2\sqrt{\pi} r_R \frac{\bar{E}^r(\underline{r}_R)}{\bar{E}^t(\underline{0})} e^{jkr_R}, \tag{3.1}$$

where r_R is the range from the target to the receiver, $\bar{E}^r(\underline{r}_R)$ is the electric field (E-field) at the Rx, and $\bar{E}^t(\underline{0})$ is the Tx E-field at the target.

The BS-RCS σ^{BS} is defined in [8, 188] as a "measure of energy scattered from the

target in the direction of the receiver". It is expressed as

$$
\begin{aligned}
\sigma^{BS} &= \lim_{r_R \to \infty} 4\pi r_R^2 \frac{|\bar{E}^r(\underline{r_R})|^2}{|\bar{E}^t(\underline{0})|^2} \\
&= \lim_{r_R \to \infty} 4\pi r_R^2 \frac{|\bar{H}^r(\underline{r_R})|^2}{|\bar{H}^t(\underline{0})|^2},
\end{aligned}
\tag{3.2}
$$

where r_R is the range from the target to the Rx, $|\bar{E}^r(\underline{r_R})|$ the magnitude of the scattered E-field at the Rx, and $|\bar{E}^t(\underline{0})|$ the magnitude of the incident E-field at the target. Similarly, $|\bar{H}^r(\underline{r_R})|$ is the magnitude of the scattered magnetic field $\bar{H}^r(\underline{r_R})$ at the Rx, and $|\bar{H}^t(\underline{0})|$ the magnitude of the incident magnetic field $\bar{H}^t(\underline{0})$ at the target. The expression (3.2) for the BS-RCS will be used in Chapter 4 for its practical computation.

The coherency of the notation $\sqrt{\sigma}^{BS}$ for the BS-CRCS and the notation σ^{BS} for the BS-RCS is verified by replacing Eq. (3.1) into Eq. (3.2), which gives

$$
\begin{aligned}
\sigma^{BS} &= \lim_{r_R \to \infty} 4\pi r_R^2 \frac{\left| \frac{e^{-jk_R r_R}}{2\sqrt{\pi} r_R} \sqrt{\sigma}^{BS} \underline{\bar{E}}^t(\underline{0}) \right|^2}{\left| \bar{E}^t(\underline{0}) \right|^2} \\
&= \lim_{r_R \to \infty} 4\pi r_R^2 \frac{\left| \sqrt{\sigma}^{BS} \right|^2}{4\pi r_R^2} \\
&= \sigma^{BS}.
\end{aligned}
\tag{3.3}
$$

It must be emphasized that Eqs. (3.1) and (3.2) are valid only when the receiver and the transmitter are "in-view" of each other. In the case of forwardscattering (Section 3.7.4), *i.e.* when $\beta = 180°$, these formulas are not valid. Instead, Cherniakov proposed another definition in [41]. Since we do not deal with forwardscattering, we do not further examine this here.

3.5 Scattering mechanisms

When illuminated by an incident wave, a conducting object scatters an echo signal. This echo signal is collected by the receiver. In order to be able to recognize targets, the characteristics of the echo signal must be understood in terms of the basic echo sources, called scattering mechanisms. In [104], Knott lists seven basic scattering mechanisms that contribute to the echo signal, and thus, to the radar cross-section, whether complex or real, of a typical airborne target (Fig. 3.3). Unlike canonical objects such as spheres or dihedrals, airplanes are complex targets, *i.e.* their total echo signal is the result of the combined action of different elementary scattering mechanisms.

According to Knott [104], for a monostatic configuration, the following mechanisms contribute to the total echo signal: (1) re-entrant structures such as exhausts ducts or jet intake ducts, (2) specular scatterers that are surfaces oriented perpendicular to the line-of-sight to the radar, (3) travelling-wave echoes, (4) diffraction at tips, edges, and corners, that increases with the square of the wavelength, (5) surface discontinuities, (6) creeping waves that occur for smooth surfaces such as spheres, and (7) interactions
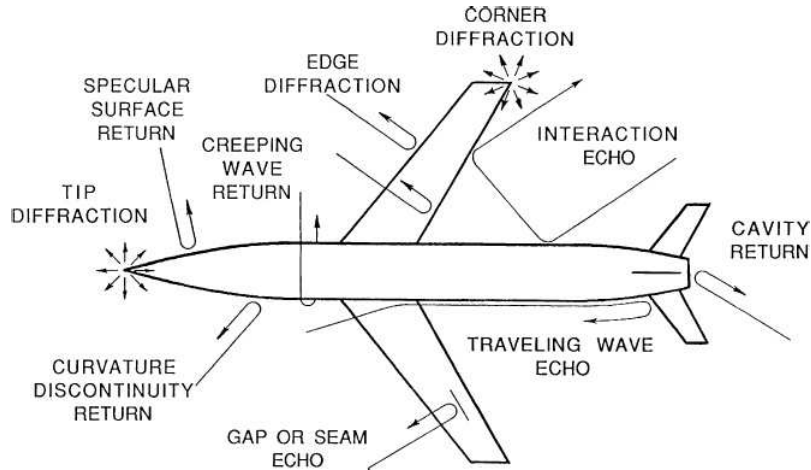
Figure 3.3: *Scattering mechanisms that occur for a synthetic airplane [104].*

between different surfaces occurring at particularly favorable aspect angles. In [104], the importance of each echo source is discussed for a monostatic (MS) configuration.

As stated in [104], the importance of each scattering mechanism in the total echo signal depends on the aspect angle in a very significant way. As shown in Fig. 3.4(a) for an MS configuration, the aspect angle is defined as the angle between the line-of-sight $\underline{\hat{s}}$ of the target and the line-of-sight $\underline{\hat{l}}$ of the radar, with vertex at the reference point on the target. We denote the aspect angle by θ, for a two-dimensional configurations.

For a bistatic (BS) configuration, as illustrated in Fig. 3.4(b), there are two aspect angles to be taken into consideration, which are the aspect angle of the target relative to the transmitter, denoted by α_T, and the aspect angle relative to the receiver, denoted by α_R. In this work, we choose to use the aspect angle α and the bistatic angle β instead of the aspect angles α_T and α_R. As illustrated in Fig. 3.4(b), α is defined as the angle between the line-of-sight $\underline{\hat{s}}$ of the target and the bisector $\underline{\hat{b}}$ of the bistatic angle, with vertex at the reference point on the target. While, in an MS configuration, the notion of line-of-sight between the radar and the target is quite obvious, this is not the case for a BS configuration. In the BS case, we find it useful to define this line-of-sight $\underline{\hat{b}}$ of the bisector of the bistatic angle as the line-of-sight for a single (Tx,Rx) pair.

In [65], five of the above mechanisms are recognized as important for BS configurations; they are (1) end region (reentrant structures), (2) creeping wave, (3) diffraction at tips, edges, and corners, (4) multibounce from interactions, and (5) specular reflections. However, the importance of each scattering mechanism on the total echo signal as a function of the aspect angle α and the bistatic angle β is not discussed in [65]. Since the focus is put in this work on measured data, we leave the theoretical study of the importance of the elementary mechanisms on the total echo signal as part of future work (Chapter 9). However, one can intuitively understand that the echo signal, and thus the BS-CRCS and the BS-RCS of a target, depend on the aspect angle of the target, and on the bistatic angle between the transmitter and the receiver.
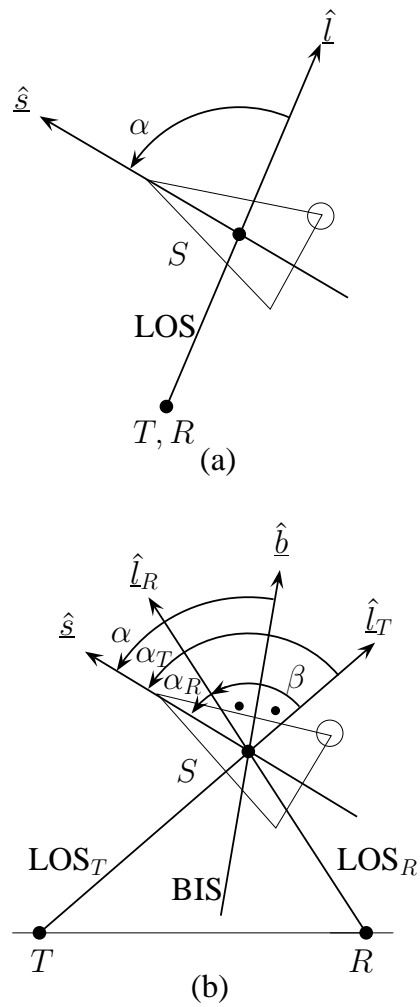
Figure 3.4: *Illustration of the aspect and bistatic angles for (a) a monostatic configuration, and (b) a bistatic configuration.*

3.6   Scattering regions

As explained in [65, 104, 187], the scattering mechanisms, and thus the complex and the real RCS, depend on the ratio of the characteristic dimension of an object, denoted by D, to the wavelength of the transmitted signal, denoted by λ, this for either a monostatic or a bistatic configuration.

In [65, 104, 187], three different regions are defined: the Rayleigh region, the resonance region (also called the Mie region), and the optical region. When the ratio λ/D is much larger than unity, the scattering mechanisms occur in the Rayleigh region. In the Rayleigh region, the phase distribution of the scatterers of an object varies little, and the echo signal of this object is determined mainly by its volume, rather than by its shape. When the ratio λ/D is close to unity, the scattering mechanisms are said to occur in the resonance region. In the resonance region, both the volume and the shape of the target strongly influence its (C)RCS, since the phase distribution starts to vary over the surface. When the ratio λ/D is much smaller than unity, the scattering mechanisms occur in the optical region. In the optical region, the (C)RCS of the target is determined by a distribution of discrete scatterers determined by the shape of the object (or its components), rather than by its volume. In the optical region, changes of aspect angle (and of bistatic angle in the bistatic case) have a strong impact on the (C)RCS level and its fluctuations. In summary, we can write

$$\begin{cases} \dfrac{\lambda}{D} \gg 1 \Rightarrow \text{Rayleigh region} \Rightarrow \text{Volume is significant for RCS} \\[2mm] \dfrac{\lambda}{D} \approx 1 \Rightarrow \text{resonance region} \Rightarrow \text{Volume and shape are significant for RCS} \\[2mm] \dfrac{\lambda}{D} \ll 1 \Rightarrow \text{optical region} \Rightarrow \text{Shape is significant for RCS} \end{cases} \quad (3.4)$$

In [41] and [188], the variation of the RCS of a perfectly conducting sphere as a function of frequency, and the corresponding scattering region, for an MS configuration is shown (Fig. 3.5).

We will use this notion of scattering region to determine the separation of the different types of airplanes into classes (Chapters 4 and 8). For example, it will a priori be difficult to discriminate between two airplanes having the same volume and illuminated by electric fields at frequencies such that the scattering mechanisms occur in the Rayleigh region.
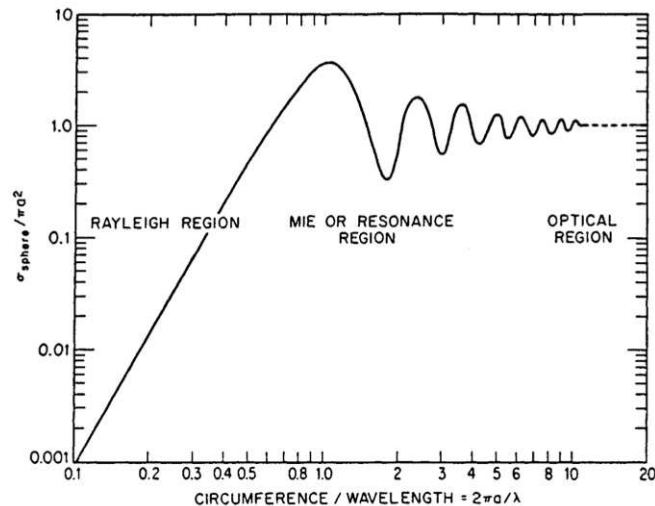
Figure 3.5: *RCS of a perfectly conducting sphere as a function of the ratio of its circumference to the wavelength. The three scattering regions are also shown [188].*

3.7 Computation of the bistatic RCS of a simple object, the perfectly conducting sphere

In the previous sections, we investigated the mechanisms responsible for the echo signal, and thus the bistatic radar cross-section (BS-RCS) and the bistatic complex radar cross-section (BS-CRCS) of a target. It was intuitively shown that the nature of the target, the aspect angle at which it is viewed, the frequency of the incident wave, and the bistatic angle between the transmitter (Tx) and the receiver (Rx) are parameters that influence the value of both the BS-RCS and the BS-CRCS.

In order to completely define the parameters that the BS-CRCS and the BS-RCS depend on, and to provide physical insight into the nature of the BS-RCS, we derive, in this section, the exact expression for the BS-RCS of the perfectly conducting sphere. Given the complexity of the derivation for an object as simple as a sphere, it is easy to understand that it is difficult to derive the exact expression for the BS-RCS of a complex object in an analytical way. This derivation will show that the theoretical formulation of the BS-RCS of a complex target is difficult to obtain. The derivation is similar for the BS-CRCS.

The derivation of exact and approximated expressions for the BS-RCS of objects is performed in [49, 180, 182, 194, 195]. We give here the main steps for the derivation of the exact expression for the BS-RCS of a generic object, so that this expression can be discussed in terms of its parameters, exactly as in [50, 65, 98, 181, 188].

The geometry considered is the one described in Section 3.3. An electromagnetic field is transmitted by a Tx, considered to be a point source. The electromagnetic field is scattered by the target, and then collected by an Rx. According to Eqs. (3.1) and (3.2), in order to compute either the BS-CRCS or the BS-RCS of the object, we have to compute either the ratio of the received electric field (E-field) to the

transmitted E-field, or the ratio of the received magnetic field (H-field) to the transmitted H-field. Even though we can use either the H-field or the E-field, we adopt the common convention of using the H-field in the computations below [49, 180, 182]. Therefore, the computations below aim at expressing the received H-field in terms of the transmitted H-field.

In Section 3.6, we showed that both the BS-CRCS and the BS-RCS depend on the scattering region (Rayleigh, resonance, or optical). As will be seen in Chapters 4 and 8, the scattering mechanisms of the air targets that we classify occur mainly in the optical region, *i.e.* when the characteristic dimension D of a target is much greater than the wavelength λ of the transmitted and scattered signals. Therefore, we will use the physical optics approximation when possible, exactly as in [180, 182]. The use of the physical optics approximation is justified in [182]. The computation of the RCS of generic targets in the Rayleigh and resonance scattering regions can be found in [50, 180]. Other RCS prediction techniques, such as numerical methods, can be found in [188].

3.7.1 Hypotheses

We perform the derivation of the expression for the BS-RCS under four common assumptions [49, 182, 194, 195]. First, we assume the far-field conditions are met. Second, we assume that the waves transmitted by any transmission source are plane in the far-field [212]. Third, we assume that the generic object for which the BS-RCS is derived is perfectly conducting. Fourth, we assume that the scattering surface dimensions are large compared to the wavelength of the incident wave. Below, we explain the first two assumptions.

Far-field condition

Three spatial regions around a transmitter are defined: the reactive near-field region, the near-field region, also called the Fresnel region, and the far-field region, also called the Fraunhofer region [8, 23, 109]. We consider the far-field region for the derivation of the expression of the BS-RCS. In [8, 23, 109], the far-field region is defined as the region of space where the angular field distribution is, for all practical purposes, independent of the distance from the antenna. The far-field region is reached when the following three conditions are all met:

$$\begin{cases} r_T > \frac{2D^2}{\lambda} \\ r_R > \frac{2D^2}{\lambda} \\ D \geq \lambda, \end{cases} \tag{3.5}$$

where D is the characteristic dimension of the target, λ is the wavelength of the transmitted signal, and r_T and r_R the distances from the target to the Tx and the Rx, respectively.

We consider the far-field region, since it will be the case of the subsequent configurations considered. For example, in Chapter 8, the characteristic dimension of the large-size airplanes for which the BS-RCS is computed is 65 m at most, and the wavelength of the transmitted signal is $3 \times 10^8/(114.7 \times 10^6) = 2.616$ m. Therefore, in order to satisfy the far-field condition, r_T and r_R must be at least 3.23 km, which is the case

for the configuration used, as described in Chapter 8. Of course, the characteristic dimension $D = 65$ m is greater than the wavelength $\lambda = 2.616$ m. The far-field condition is thus satisfied.

Plane waves

Being in the far-field region allows one to use the hypothesis of plane waves. The plane wave assumption is explained as follows. We assume that the signal emitted by a point source, denoted here by Tx, is monochromatic, and isotropic (Fig. 3.6). We also assume that the transmitted signal has a constant amplitude. We can thus express the transmitted signal $s^t(t)$, with superscript t standing for "transmit", via a periodic complex exponential

$$s^t(t) = Ae^{j\omega t},\tag{3.6}$$

where A represents the constant amplitude of the signal, and ω the (constant) pulsation of the signal, related to its frequency via $\omega = 2\pi f$. Note that we will often abusively refer to ω as the frequency of the signal. Also note that ω, and thus f, are signed quantities.

For simplicity, we perform the development below in a two-dimensional (2D) plane. One can easily extend it to a three-dimensional space. Around the point source, we assume that the front wave is circular, since the point source is assumed to be isotropic. The plane wave condition means that, at a distance large enough from the point source, both the amplitude and the the phase of the signal are the same for all points on any line segment perpendicular to the direction of propagation of the signal, *i.e.* the wavefront. For example, as shown in Fig. 3.6, both the amplitude and the phase of the signal $s^t(t)$ at points P_1 and P_2 are the same, under the plane wave condition.
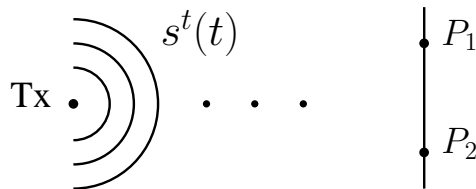
Figure 3.6: *Illustration of the plane wave condition.*

3.7.2 Transmitted electric and magnetic fields

The electric field (E-field) transmitted by a monochromatic point source Tx can be expressed as [108]

$$\underline{\bar{E}}^t(\underline{r}, t) = \underline{\bar{E}}_0(\underline{r})e^{j(\omega t - \underline{k} \cdot \underline{r})},\tag{3.7}$$

where E_0 is the amplitude of the field, ω the pulsation, $\underline{k}$ the wave vector, and $\underline{r}$ a position vector in $\mathbb{R}^3$.

At any point P, the E-field can be expressed as [108]

$$\bar{E}(\underline{r}_P, t) = \bar{E}_0(\underline{r}_P)e^{-j\underline{k} \cdot \underline{r}_P}e^{j\omega t} = \bar{E}(\underline{r}_P)e^{j\omega t}.\tag{3.8}$$

In Eq. (3.8), $\bar{E}(\underline{r}_P, t)$, $\bar{\underline{E}}(\underline{r}_P)$, and $e^{j\omega t}$ are complex-valued. $\bar{\underline{E}}(\underline{r}_P)$ is a complex number that is specific to point P. It is multiplied by the complex exponential $e^{j\omega t}$ to produce the time-varying complex-valued representation of the E-field at P, $i.e.$ $\bar{E}(\underline{r}_P, t)$. $\bar{E}(\underline{r}_P, t)$ is a complex value that varies with time (for a given location) and with location (for a given time).

From a signal processing point of view, the multiplication of $\bar{E}(\underline{r}_P)$ by $e^{j\omega t}$ can usefully be interpreted as the rotation of the fixed complex number $\bar{E}(\underline{r}_P)$ by an angle ωt in the complex plane, as illustrated in Fig 3.7. Therefore, the E-field representation, which is defined in Eq. (3.8) as being the product of $\bar{E}(\underline{r}_P)$ by $e^{j\omega t}$, can be viewed as a vector of length $|\bar{E}(\underline{r}_P)|$ rotating at angular speed ω in the complex plane, starting at angle $\angle \bar{E}(\underline{r}_P)$ (the phase of $\bar{E}(\underline{r}_P)$) at $t = 0$. $\bar{E}(\underline{r}_P)$ and $\bar{E}(\underline{r}_P, t)$ are both called phasors. We will refer to $\bar{E}(\underline{r}_P)$ as a fixed phasor, and to $\bar{E}(\underline{r}_P, t)$ as a time-varying phasor or, more specifically, as a rotating phasor.
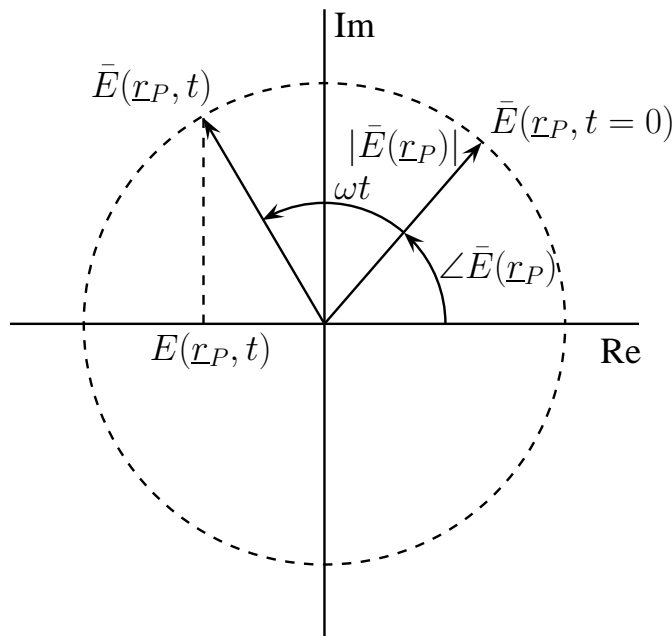
Figure 3.7: *Representation of $\bar{E}(\underline{r}_P, t)$ in the complex plane.*

Carefully note that, to determine the complex value of $\bar{E}(\underline{r}_P, t)$ at a given point P, and for all t's, we only need to know the fixed phasor $\bar{E}(\underline{r}_P)$ specific to point P (and of course, ω). Note that $\bar{E}(\underline{r}_P)$ is not completely arbitrary. If the direction of propagation $\hat{\underline{k}}$ of the plane wave and the value of $\bar{E}(\underline{r}_P)$ at some point such as the origin O are known, the value of $\bar{E}(\underline{r}_P)$ can be automatically determined for all points P in the (x, y, z) axes.

Of course, in real life, all physical electric fields are real-valued. But the actual value of the physical E-field can be obtained by projecting, at any time t, the complex-valued rotating phasor $\bar{E}(\underline{r}_P, t)$ on the real axis of the complex plane. This means that the real-valued physical E-field, which is denoted by $E(\underline{r}_P, t)$, is also simply the real part

of the rotating phasor $\bar{E}(\underline{r}_P, t)$,

$$E(\underline{r}_P, t) = \Re\{\bar{E}(\underline{r}_P, t)\} = \Re\{\bar{E}(\underline{r}_P)e^{j\omega t}\}, \tag{3.9}$$

as illustrated in Fig. 3.7. Observe that we use $\bar{E}$ for the complex-valued E-field and E for the corresponding physical real-valued E-field. Below, we deal with both the electric field and the magnetic field. We can similarly express the H-field transmitted by a point source as

$$\underline{\bar{H}}^t(\underline{r}, t) = \underline{\bar{H}}_0(\underline{r})e^{j(\omega t - \underline{k} \cdot \underline{r})}, \tag{3.10}$$

and one can make the same reasoning as for the E-field.

3.7.3 Scattered electric field

We derive the expression for the scattered electric field (E-field) according to [49, 182, 194, 195]. The derivation starts from the Maxwell equations [23, 109, 194]

$$\nabla \times \underline{\bar{E}} = -\frac{\partial \bar{B}}{\partial t}, \tag{3.11}$$

$$\nabla \times \bar{H} = \frac{\partial \underline{\bar{D}}}{\partial t} + \underline{\bar{J}}, \tag{3.12}$$

$$\nabla \cdot \underline{\bar{D}} = \rho, \tag{3.13}$$

$$\nabla \cdot \underline{\bar{B}} = 0, \tag{3.14}$$

where $\underline{\bar{E}}$ represents the electric field, $\underline{\bar{B}}$ the magnetic induction, $\underline{\bar{H}}$ the magnetic field, $\underline{\bar{D}}$ the electric displacement, $\underline{\bar{J}}$ the current density, and ρ the charge density. By assuming an harmonic time dependence of $\underline{\bar{E}}$ and $\underline{\bar{H}}$ of the form of $e^{j\omega t}$, and by assuming an homogeneous, isotropic, and source-free region, $\underline{\bar{E}}$ and $\underline{\bar{H}}$ both satisfy the wave equation [23, 49, 109, 182, 194, 195]

$$\left(\nabla^2 + k^2\right)\underline{\bar{\psi}} = 0, \tag{3.15}$$

where $\underline{\bar{\psi}}$ can represent either $\underline{\bar{E}}$ or $\underline{\bar{H}}$.

At the interface of two perfect dielectrics, the boundary conditions of continuity can be expressed as

$$\hat{\underline{n}} \times (\underline{\bar{E}}^1 - \underline{\bar{E}}^2) = 0 \tag{3.16}$$

$$\hat{\underline{n}} \times (\underline{\bar{H}}^1 - \underline{\bar{H}}^2) = 0 \tag{3.17}$$

$$\hat{\underline{n}} \cdot (\underline{\bar{D}}^1 - \underline{\bar{D}}^2) = 0 \tag{3.18}$$

$$\hat{\underline{n}} \cdot (\underline{\bar{B}}^1 - \underline{\bar{B}}^2) = 0, \tag{3.19}$$

where $\hat{\underline{n}}$ stands for the normal unit vector, and the superscripts 1 and 2 stand for each side of the interface, as shown in Fig. 3.8.

Since we assume that the object is perfectly conducting, we have

$$\hat{\underline{n}} \times \bar{E} = 0 \tag{3.20}$$

$$\hat{\underline{n}} \cdot \underline{\bar{B}} = 0. \tag{3.21}$$
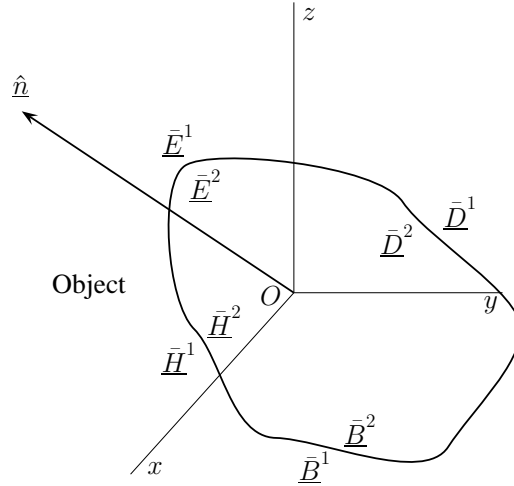
Figure 3.8: *Simplified illustration of the different electric and magnetic fields at the interface between two perfect dielectrics.*

Since we assume an incident plane wave, both $\underline{\bar{E}}$ and $\underline{\bar{H}}$ are of the form

$$\underline{\bar{\psi}} = \underline{\bar{\psi}}^I + \underline{\bar{\psi}}^S, \tag{3.22}$$

where the superscripts I and S stand for the incident and scattered fields, respectively. The general solution of Eq. (3.15), expressed in its scalar form, is [49]

$$\psi(\bar{r}) = \psi^I(\bar{r}) + \int_S \left(f\frac{\partial G}{\partial n} - gG \right) dS, \tag{3.23}$$

where $f = \psi$ and $g = \partial\psi/\partial n$. In the case of $\bar{E}$ and $\bar{H}$, and by using the boundary conditions of Eq. (3.19), one can get [49]

$$\underline{\bar{E}} = \underline{\bar{E}}^I + \frac{1}{ik}\nabla \times \int_S \nabla\underline{G} \times \left(\hat{n} \times \underline{\bar{H}} \right) dS, \tag{3.24}$$

$$\underline{\bar{H}} = \underline{\bar{H}}^I - \int_S \nabla\underline{G} \times \left(\hat{n} \times \underline{\bar{H}} \right) dS, \tag{3.25}$$

where $\underline{G}$ is the Green function defined by

$$\underline{G}(\underline{r}, \underline{r}') = \frac{1}{4\pi}\frac{e^{-jk|\underline{r}-\underline{r}'|}}{|\underline{r} - \underline{r}'|}, \tag{3.26}$$

where $\underline{r}$ is the distance vector from the center of the coordinate system to the observation point, *i.e.* the receiver, and $\underline{r}'$ the distance vector from the center of the coordinate system to the integration point on the surface S of the object. We can rewrite this last expression as

$$\underline{G}(\underline{R}) = \frac{1}{4\pi}\frac{e^{-jk|\underline{R}|}}{|\underline{R}|}, \tag{3.27}$$

where $\underline{R} = \underline{r} - \underline{r}'$. The gradient of the Green function is written as

$$\nabla\underline{G} = \frac{1}{4\pi}\left(-jk\frac{e^{-jkR}}{R} - \frac{e^{-jkR}}{R^2} \right)\hat{R} \tag{3.28}$$

$$= \frac{1}{4\pi}\left(-jk\frac{e^{-jk(r-r')}}{r-r'} - \frac{e^{-jk(r-r')}}{(r-r')^2} \right)\hat{\underline{r}}. \tag{3.29}$$

Since the distance r is very large, one can approximate the gradient of the Green function as

$$\nabla \underline{G} \approx -\frac{e^{jkr}}{4\pi r} jk\hat{\underline{r}} e^{-jk\hat{\underline{r}} \cdot \underline{r}'} \tag{3.30}$$

We can thus express the scattered electric and magnetic fields as [49]

$$\underline{\bar{E}}^S = -\frac{e^{jkr}}{4\pi r}\hat{r}\nabla \times \int_S e^{-jk\hat{\underline{r}} \cdot \underline{r}'} \times \left(\hat{\underline{n}} \times \underline{\bar{H}}\right) dS \tag{3.31}$$

$$\underline{\bar{H}}^S = \frac{e^{jkr}}{4\pi r}jk\hat{\underline{r}} \times \int_S e^{-jk\hat{\underline{r}} \cdot \underline{r}'} \left(\hat{\underline{n}} \times \underline{\bar{H}}\right) dS. \tag{3.32}$$

In [182], the scattered magnetic field $\underline{\bar{H}}^S$ is equivalently expressed as

$$\underline{\bar{H}}^S = \frac{1}{4\pi} \int_S \left(\hat{\underline{n}} \times \underline{\bar{H}}\right) \times \nabla \left(\frac{e^{-jkR}}{R}\right) dS, \tag{3.33}$$

where $\hat{\underline{n}}$ still denotes the unit vector normal to the surface S, k is still the wave number, and S is the integration region, which is the outer surface of the object. R is now the distance from the observation point, *i.e.* the receiver, to the integration point on S. $\underline{\bar{H}}$ denotes the tangential component of the magnetic field on the surface of the object.

Since we assume that the dimensions of the surface of the object are large compared to the wavelength, we can use the physical optics approximation as in [182] to express the magnetic field $\underline{\bar{H}}$ as

$$\underline{\bar{H}} = \begin{cases} 2\underline{i}_T H_0 e^{-j\underline{k} \cdot \underline{r}}, & \text{on the illuminated side of the object} \\ 0, & \text{otherwise}, \end{cases} \tag{3.34}$$

where $\underline{i}_T = \hat{\underline{a}} - (\hat{\underline{a}} \cdot \hat{\underline{n}})\hat{\underline{n}}$, where $\hat{\underline{a}}$ represents the direction of propagation of the incident magnetic field, H_0 stands for the magnitude of the incident magnetic field, $\underline{k}$ the wave number vector, and $\underline{r}$ the distance vector from the origin of the coordinate system to any point on the surface of the object.

By using Eq. (3.30), and assuming $H_0 = 1$, we get [182]

$$\underline{\bar{H}}^S = \frac{e^{-jkR'}}{R'} \underline{\bar{F}}(\beta), \tag{3.35}$$

where R' is the distance from the center of the coordinate system to the receiver, and where $\underline{\bar{F}}(\beta)$ is expressed as

$$\underline{\bar{F}}(\beta) = \frac{jk}{2\pi} \left[(\hat{\underline{n}}_0 \cdot \hat{\underline{a}}) \underline{\bar{f}} - \left(\hat{\underline{n}}_0 \cdot \underline{\bar{f}}\right) \hat{\underline{a}}\right], \tag{3.36}$$

where $\hat{\underline{n}}_0$ is the unit vector from the receiver to the origin, and $\underline{\bar{f}}$ is defined as

$$\underline{\bar{f}} = \int_{S'} \hat{\underline{n}} e^{-jk\underline{r} \cdot (\hat{\underline{n}}_0 + \hat{\underline{k}})} dS, \tag{3.37}$$

where S' stands for the illuminated side of the object.

By using Eq. (3.2), we can thus express the BS-RCS of the object as

$$\sigma(\beta) = 4\pi|\bar{\underline{F}}(\beta)|^2. \tag{3.38}$$

The dependence of the BS-RCS on the aspect angle, the bistatic angle, and the frequency appears through the definition of $\bar{\underline{f}}$ (Eq. (3.37)). More precisely, the dependence of the BS-RCS on the aspect angle appears through the vector $\underline{r}$. The dependence of the BS-RCS on the bistatic angle is expressed through the addition of the vectors $\hat{\underline{n}}_0$ and $\hat{\underline{k}}$. This dependence is discussed in Section 3.7.4. The dependence of the BS-RCS on the frequency f comes through the wave number $k = 2\pi/\lambda = 2\pi f/c$.

Up to now, we have not introduced the polarization of the incident and scattered electromagnetic fields. In [182], the polarization of the receiver is introduced through unit vector $\hat{\underline{d}}$. We thus express the BS-RCS as

$$
\begin{aligned}
\sigma(\beta) &= 4\pi|\bar{\underline{F}} \cdot \hat{\underline{d}}|^2 \\
&= \frac{4\pi}{\lambda^2} \left| (\hat{\underline{n}}_0 \cdot \hat{\underline{a}}) \left(\bar{\underline{f}} \cdot \hat{\underline{d}}\right) - \left(\hat{\underline{n}}_0 \cdot \bar{\underline{f}}\right) \left(\hat{\underline{a}} \cdot \hat{\underline{d}}\right) \right|^2.
\end{aligned}
\tag{3.39}
$$

In order to analytically determine the BS-RCS of any object, Eq. (3.37) requires that one be able to give an analytical expression for the outer surface of the object. While it is possible to give an analytical expression for the scattering surface of simple objects such as spheres, spheroids, or cones, it is, however, extremely difficult, if not impossible, to give such expression for complex objects, such as airplanes. For illustration purposes, we present the simple example of a sphere in Section 3.7.5.

3.7.4 Bistatic complex RCS and bistatic RCS as a function of the bistatic angle

The bistatic geometry is characterized by the bistatic angle β [91]. We showed in Section 3.7.3 that the BS-CRCS and the BS-RCS depend on the value of the bistatic angle β, among other parameters.

In [188], three different regions of bistatic RCS are defined, according to the value of the bistatic angle: the pseudo-monostatic RCS region, the bistatic RCS region, and the forwardscatter RCS region. The pseudo-monostatic RCS region corresponds to $\beta \leq 5°$. In this region, one can compute the BS-RCS by using the monostatic-bistatic equivalence theorem (MBET), as shown in Section 3.8. The MBET states that the BS-RCS of an object is equal to its monostatic RCS measured at an aspect angle equal to $\beta/2$, and at a frequency equal to $f \csc(\beta/2)$.

The bistatic RCS region corresponds to $5° \leq \beta \leq 180°$. When the bistatic angle is higher than $5°$, the monostatic-bistatic equivalence theorem can no longer be applied. The reasons, explained in [98, 188], are that the relative phases between the different (discrete) scatterers constituting the object change, and that the amplitude and phase of the different scatterers vary according to the bistatic angle. To our knowledge, no theoretical model for the computation of the BS-RCS of a complex object exists for the bistatic RCS region.

The forwardscatter RCS region corresponds to $\beta \to 180°$. Around this value of the bistatic angle, it is shown in [181] that the BS-RCS of an object is equal to $4\pi A^2/\lambda^2$, where A is the effective area of the object. Methods for predicting the forwardscatter RCS of different targets are discussed in [43, 184, 185]. The recognition of objects based on their forwardscatter RCS is discussed in [39, 40].

For illustration purposes, and in preparation for Chapter 8, we compute the BS-RCS of a sample airplane as a function of the azimuth aspect angles with respect to the transmitter and the receiver, denoted by θ_{Tx} and θ_{Rx}, respectively. The model of the airplane consists of a fuselage of size 5.42m × 1m, and two wings of size 2.58m × 1m. A stationary current runs through the fuselage and the wings. Figure 3.9 shows the BS-RCS of this airplane at a frequency of 115 MHz. As explained above, when $\theta_{Tx} + \theta_{Rx} \approx 180°$, *i.e.* in forwardscattering, the BS-RCS of the airplane is maximum, constant, and equal to $10\log(4\pi A^2/\lambda^2) \approx 20$ dB.

One can also see in Fig. 3.9 that, for the pseudo-monostatic region, when the bistatic angle β is small, *i.e.* when $\theta_{Tx} \approx \theta_{Rx}$ (on the anti-diagonal of the graph), the value of the $\csc(\beta/2)$ is small, and therefore the amplitude of the BS-RCS does not vary much. The variations are much noticeable for large bistatic angles, but smaller than 180°.
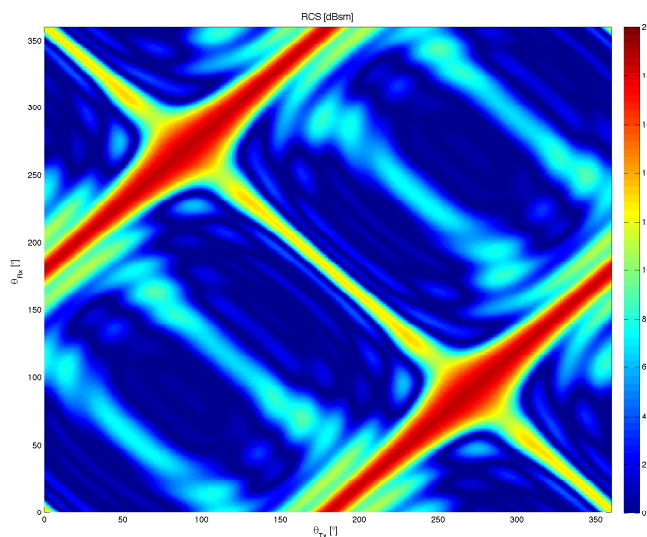
Figure 3.9: *RCS of a sample airplane as a function of its aspect angles with respect to the transmitter and the receiver, denoted by θ_{Tx} and θ_{Rx}, respectively.*

In this work, we focus on the bistatic RCS region. Since the BS-RCS of complex objects cannot be easily predicted by any theoretical model, there is a crucial need for experimental data. Moreover, since we focus on the recognition of such complex objects, the amount of data must be sufficient, in order to perform meaningful classification experiments.

3.7.5   Application to the case of the perfectly conducting sphere

In this section, we compute the BS-RCS of a sphere of radius R_0, from the equations derived in Section 3.7.3. Since the sphere is a symmetric object in all directions, one can intuitively understand that its BS-RCS does not depend on the aspect angle.

As in [49, 182], and as shown in Fig. 3.10, we assume that the transmitter is located at T, on the positive side of the z-axis, thus resulting $\hat{\underline{k}} = -\hat{\underline{i}}_z$. We also assume that the direction of propagation $\hat{\underline{a}}$ of the incident magnetic field is directed along the y-axis. We assume that the receiver is located at R, in the yz-plane, and that its polarization is directed along the y-axis, $\hat{\underline{i}}_y$. The sphere is located at O.
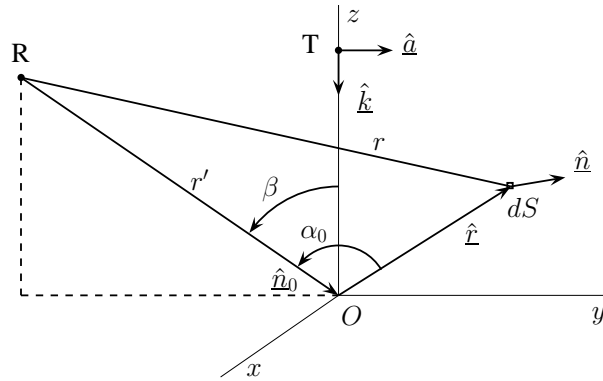
Figure 3.10: *Configuration used for the theoretical computation of the BS-RCS of a sphere, as in [49, 182].*

Under these assumptions (and those used from Section 3.7.1 to Section 3.7.3), it is shown in [181, 182] that, for a prolate spheroid with major axis a and minor axis b, the inner part of Eq. (3.39) is equal to

$$2\pi b^2 \int_0^1 \int_0^{2\pi} \eta e^{-j\left(kb\sin\beta\sqrt{1-\eta^2}\sin\phi - ka(1+\cos\beta) - ka(1+\cos\beta)\eta\right)} d\phi d\eta, \qquad (3.40)$$

where η and ϕ are the (angular) spherical coordinates of a generic point on the prolate spheroid. By using the fact that [1]

$$\int_0^{2\pi} e^{-jk\psi\sin\phi} d\phi = 2\pi J_0(k\psi), \qquad (3.41)$$

where J_0 is the zero-order Bessel function, and by performing the change of variables $\eta = \sin\theta$, Eq. (3.40) becomes

$$2\pi b^2 \int_0^{\pi/2} \sin\theta \cos\theta J_0(kb\sin\beta\sin\theta) e^{jka(1+\cos\beta)\cos\theta} d\theta. \qquad (3.42)$$

In the case of a sphere, $a = b = R_0$, and the expression reduces to

$$2\pi R_0^2 \int_0^{\pi/2} \sin\theta \cos\theta J_0(kR_0\sin\beta\sin\theta) e^{jkR_0(1+\cos\beta)\cos\theta} d\theta. \qquad (3.43)$$

The BS-RCS of the sphere is thus equal to

$$\sigma(\beta) = \frac{4\pi}{\lambda^2} 4\pi^2 R_0^2 \left| \int_0^{\pi/2} \sin\theta \cos\theta J_0(kR_0 \sin\beta \sin\theta) e^{jkR_0(1+\cos\beta)\cos\theta} d\theta \right|. \qquad (3.44)$$

As explained in [181, 182], this integral is evaluated by the double stationary phase theorem, which is applicable when the characteristic dimension D of the object is much larger than the wavelength of the incident field (physical optics approximation). The results achieved is exactly the same as the result achieved by geometrical optics. In the case of the prolate spheroid, we get

$$\sigma(\beta) \approx \frac{4\pi b^4}{a^2} \left((1 + \cos\beta + \frac{b^2}{a^2}(1 - \cos\beta) \right)^{-2}. \qquad (3.45)$$

In the case of the sphere, $a = b = R_0$, and we thus get

$$\sigma(\beta) \approx \pi R_0^2. \qquad (3.46)$$

One must notice that the bistatic angle β does not appear on the right-hand side of this equation. In [182], a comparison with measured BS-RCSs of a sphere shows that the result of Eq. (3.46) is valid for bistatic angle smaller than 120°.

3.7.6 Bistatic RCS of canonical objects

In Section 3.7.5, we presented the theoretical computation of the sphere, which is a particular canonical object. In this section, we list the BS-RCS values for other canonical objects, computed under the same assumptions as those used for the sphere.

The BS-RCS of the finite cone of length r_0 and half cone angle γ is expressed in [181, 182] as

$$\begin{aligned}
\sigma(\beta) \approx &\frac{4\pi r_0^2 \sin(4\gamma)}{(\sin^2\beta \sin^2\gamma - \cos^2\gamma(1+\cos\beta)^2)^2} \\
&\left[\cos\gamma(1+\cos\beta) J_0^2(kr_0 \sin\beta \sin\gamma) + \right. \\
&\left. \sin^2\beta \sin^2\gamma J_1^2(kr_0 \sin\beta \sin\gamma) \right].
\end{aligned} \qquad (3.47)$$

Similarly, the BS-RCS of the paraboloid defined by

$$x^2 + y^2 = -4Pz \qquad (3.48)$$

is expressed as [181, 182]

$$\sigma(\beta) = 4\pi P^2 \sec^4(\beta/2). \qquad (3.49)$$

The BS-RCS of the ellipsoid defined by

$$\frac{x^2}{A^2} + \frac{y^2}{B^2} + \frac{z^2}{C^2} = 1 \qquad (3.50)$$

is expressed as [181, 182]

$$\sigma(\beta) = \frac{4\pi A^2 B^2}{C^2} \left[(1 + \cos\beta) + \frac{B^2}{C^2}(1 - \cos\beta) \right]^{-2}. \qquad (3.51)$$

One can find expressions for the BS-RCS of other canonical objects in [181, 182]. Comparisons with measurements of BS-RCS of objects are available in [41, 49, 224, 225]. In all cases considered in this section, the BS-RCS σ depends explicitly on the bistatic angle β.

3.8   Monostatic-to-bistatic equivalence theorems

In Section 3.7, we presented the theoretical computation of the bistatic radar cross-section (BS-RCS) of a perfectly conducting sphere. The main difficulty lied in the analytical formulation of the shape of the object. Another way of getting the BS-RCS of an object is to obtain its value from its monostatic radar cross-section (MS-RCS), which is the purpose of the monostatic-to-bistatic equivalence theorem (MBET).

In [98], Kell proposed the following MBET for relatively smooth objects

$$\sigma^{BS}(\theta = \beta, f) = \sigma^{MS}\left(\theta = \frac{\beta}{2}, f \csc\left(\frac{\beta}{2}\right)\right), \tag{3.52}$$

where σ^{BS} represents the BS-RCS, σ^{MS} the MS-RCS, θ the azimuth angle of the object, β the bistatic angle, and f the frequency.

In [48], Crispin and Siegel proposed another MBET, extended for complex objects,

$$\sigma^{BS}(\theta = \beta, f) = \sigma^{MS}\left(\theta = \frac{\beta}{2}, f\right), \tag{3.53}$$

which is identical to Eq. (3.52) for $\beta = 0$.

Eigel performed the analysis of both MBET's on three simple objects: a plate and two cylinders mounted on a base [65]. Eigel showed that both MBET's start to fail at bistatic angles larger than 20°, mainly due to the change of scattering centers growing with increasing bistatic angle. One can find a more thorough analysis of MBET's in [41]. Because of this limitation, we will not use MBET's to obtain the BS-RCSs of complex objects such as airplanes.

3.9   Conclusion

Our three automatic target recognition (ATR) systems, that we further discuss in Chapters 6, 7, and 8, all use either the bistatic complex radar cross-section (BS-CRCS) or the bistatic radar cross-section (BS-RCS). In this chapter, we defined these two quantities, and we identified the parameters they depend on.

In particular, we defined the BS-CRCS and of BS-RCS in terms of the transmitted and scattered electromagnetic fields. We presented the different scattering mechanisms that are responsible for both the BS-CRCS and the BS-RCS. We also defined the three scattering regions: the Rayleigh region, the resonance region, and the optical region. The dominant scattering mechanisms that contribute to both the BS-CRCS and the BS-RCS of an object differ according to the ratio of the characteristic dimension of the object to the wavelength of the transmitted electromagnetic field. In particular, the separation of targets into different classes in our three ATR systems relies on the determination of the scattering region in which the scattering mechanisms occur.

We also defined the different bistatic RCS regions, according to the value of the bistatic angle β: the pseudo-monostatic region, the bistatic region, and the forwardscatter region. We illustrated the variations of the BS-RCS as a function of the bistatic angle on a simple model of a small airplane.

The BS-RCS depends on the following parameters: the nature of the object, the aspect angle of this object with respect to either the transmitter or the receiver, the bistatic angle between the transmitter and the receiver, the polarizations of the transmitter and the receiver, and the frequency of the illuminating wave. Our three ATR systems all take advantage of the analysis of the variation of either the BS-CRCS or the BS-RCS in terms of these parameters. In order to illustrate the influence of these parameters on the BS-RCS, we presented the theoretical computation of the BS-RCS of the simple perfectly conducting sphere, under the physical optics approximation. We showed that the theoretical computation of the BS-RCS of a generic target requires the analytical expression of its shape. Since this analytical expression is not available for complex objects, the geometry of complex objects is often discretized by an ensemble of canonical shapes, such as spheres or dihedrals. It follows that the BS-CRCS and BS-RCS of such targets cannot be computed exactly, and that their computation requires either a large amount of time or a large amount of computational resources.

We also expressed the limitations of the monostatic-to-bistatic equivalence theorems that aim at computing the BS-RCS of an object from the values of the monostatic RCS of this object. These theorems will thus not be used for the computation of the BS-RCSs of complex objects such as airplanes. Therefore, since a large amount of data is needed to perform meaningful classification experiments, we will put a particular effort, in Chapters 4 and 8, into the collection of a sufficient amount of data.

Chapter 4

Extraction and illustrations of the bistatic complex and real RCS of targets

Contents

In this chapter, we extract both the bistatic complex radar cross-section (BS-CRCS) and the bistatic radar cross-section (BS-RCS) of targets from the transmitted and received electric fields. We also describe the experimental setup used to collect the received electric fields. We then illustrate the variations of both the BS-CRCS and the BS-RCS as a function of the parameters investigated in Chapter 3.

Section 4.1 states the motivation for the extraction of both the BS-CRCS and the BS-RCS. Section 4.2 presents the computation of both the BS-CRCS and the BS-RCS of a generic target from the transmitted and received electric fields. Section 4.3 presents the experimental setup we used for the extraction of both the BS-CRCS and the BS-RCS of targets. Section 4.4 defines the scattering regions in the frequency bands of interest. Section 4.5 defines the classes of targets to classify. Section 4.6 illustrates the variations of both the BS-CRCS and the BS-RCS as a function of the different parameters that we described in Chapter 3. Section 4.7 concludes.

4.1   Motivation for the extraction of the bistatic complex and real RCS of targets

Our first automatic target recognition system (ATR), whose block diagram is shown in Fig. 4.1, recognizes targets by using their radar image. We compute the radar images of targets from the bistatic complex radar cross-section (BS-CRCS) of these targets (Chapter 5). Our second ATR system, whose block diagram is represented in Fig. 4.2, recognizes targets by using either their BS-CRCS or their bistatic radar cross-section (BS-RCS).
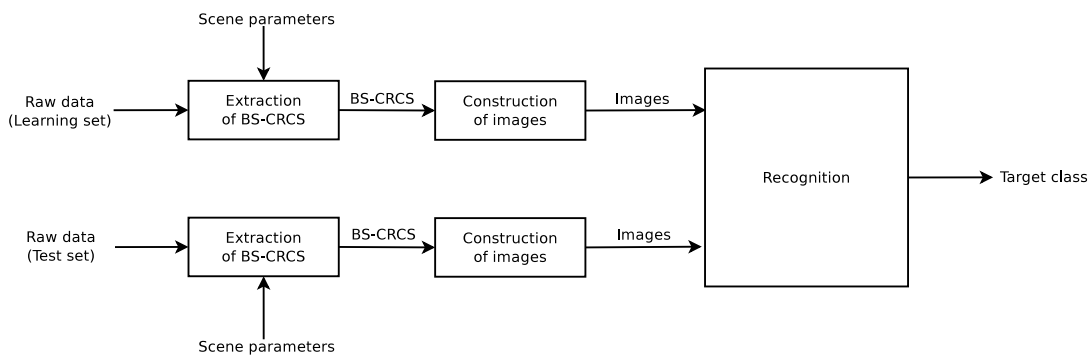
Figure 4.1: *Block diagram of our ATR system using radar images of targets.*

We consider, in this chapter, the first stage of these two ATR systems, which is the extraction of either the BS-CRCS or the BS-RCS of targets, for both the learning set (LS) and the test set (TS).
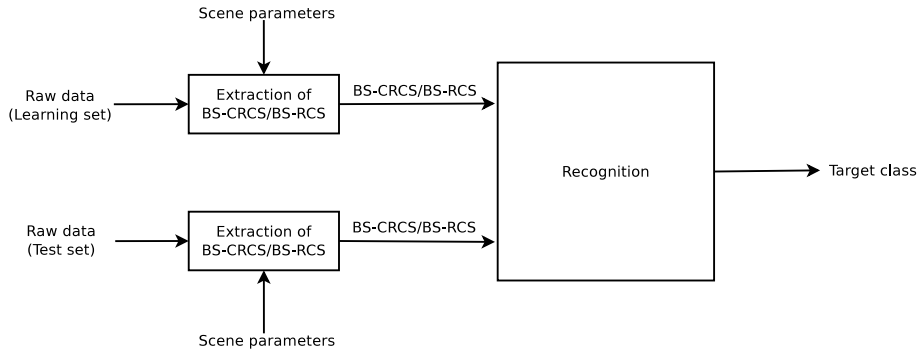
Figure 4.2: *Block diagram of our ATR system using the bistatic complex radar cross-sections or the bistatic radar cross-sections of targets.*

4.2 Extraction of the bistatic complex and real RCS of an object from the Tx and Rx electromagnetic fields

We showed in Chapter 3 that the theoretical computation of both the bistatic complex radar cross-section (BS-CRCS) and the bistatic radar cross-section (BS-RCS) of a generic object requires the analytical expression of the shape of such object. Since analytical expressions for the scattering surface of complex objects such as an airplane are not available, we have to compute both the BS-CRCS and the BS-RCS of complex objects from the incident and scattered electric (or magnetic) fields, according to the definitions of both the BS-CRCS and the BS-RCS (Eqs. (3.1) and (3.2), respectively). This computation is the object of the present section.

We consider the same bistatic (BS) configuration as that of Chapter 3, that we reproduce here in Fig. 4.3 for convenience. The object is located at the center of the coordinate system, and illuminated by a single transmitter (Tx). A single receiver (Rx) collects the signal scattered by the object.

The discussion that follows is strongly inspired by [212]. We made slight adaptations to the notations in [212], in order to consider the bistatic configuration.

4.2.1 Transmitted electric field

As in Section 3.7.2, we can express the transmitted electric field (E-field) at any point P as

$$\bar{E}(\underline{r}_P, t) = \bar{E}_0(\underline{r}_P)e^{-j\underline{k} \cdot \underline{r}_P}e^{j\omega t} = \bar{E}(\underline{r}_P)e^{j\omega t}, \qquad (4.1)$$

where $\bar{E}$ denotes the complex value of the E-field at point P, $\bar{E}_0$ its amplitude at point P, k the wave number, $\underline{r}_P$ the distance vector of point P, and ω the angular frequency of the wave. The interpretation is exactly the same as in Section 3.7.2, in particular the interpretation of the E-field as a phasor.
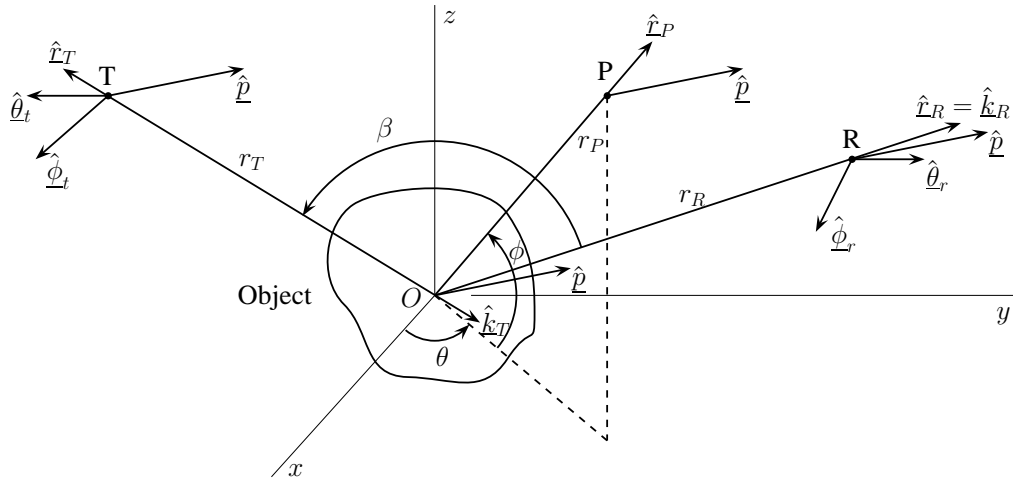
Figure 4.3: *Geometry of the bistatic configuration considered.*

4.2.2 Polarization

In contrast to the theoretical computation of the BS-RCS, we introduce the polarization of the incident and scattered electric fields from the start. For simplicity, we start with linear polarization. If an electromagnetic field (EM-field), or wave, is linearly polarized, the polarization is necessarily characterized by an orientation in space, *i.e.* in the (x, y, z) axes of Fig. 4.3. As is customary, we choose the orientation of the electric field $\underline{E}$ to characterize the orientation of the polarization [108]. Alternatively, one could choose the orientation of the magnetic field $\underline{H}$.

In the case of a propagating plane wave characterized by its wave vector $\underline{k}$, and thus travelling in the direction of $\underline{k}$ (and $\hat{k}$), we know that the electric field $\underline{E}$ (E-field) and the magnetic field (H-field) are perpendicular to $\underline{k}$. The unit vector $\hat{p}$ characterizing the orientation of the linearly polarized E-field $\underline{E}$ is shown in Fig. 4.3. We show $\hat{p}$ "attached" not only to O but also to Tx, to Rx, and to some arbitrary point P. In any case, $\hat{p}$ can be thought of as being located in the plane perpendicular to the direction of propagation $\hat{k}$.

A linearly-polarized E-field is characterized by the direction $\hat{p}$ of its polarization, and by its real-valued amplitude $E(\underline{r}_P, t)$. The corresponding E-field vector in the (x, y, z) axes is denoted by $\underline{E}(\underline{r}_P, t)$ and given, by inspection and construction, by

$$\underline{E}(\underline{r}_P, t) = E(\underline{r}_P, t)\hat{p}. \tag{4.2}$$

Keep in mind that $\underline{E}$ and $\hat{p}$ are three-element vectors in the (x, y, z) axes.

Before moving on, it is critical to have a crystal-clear view of the notations used so far, and of the quantities they represent.

- $\hat{p}$ represents the direction of polarization, which is assumed linear. It is a unit vector in the (x, y, z) axes, *i.e.* in $\mathbb{R}^3$. As all vectors of $\mathbb{R}^3$, it has three elements and these are real-valued.

- $\underline{r}_P$ is the position vector of some point P. It is a vector in the (x, y, z) axes, *i.e.* in $\mathbb{R}^3$.

- $E(\underline{r}_P, t)$ is the real value (*i.e.* the time-varying amplitude) of the linearly polarized E-field vector at location $\underline{r}_P$, *i.e.* at P, and at time t.

- $\underline{E}(\underline{r}_P, t)$ is the real value of the physical E-field vector at $\underline{r}_P$ and t, characterized by the orientation $\hat{\underline{p}}$ and the physical (real-valued, scalar) time-varying amplitude $E(\underline{r}_P, t)$. It is a vector in the (x, y, z) axes, *i.e.* in $\mathbb{R}^3$.

- $\bar{E}(\underline{r}_P, t)$ is the complex time-varying rotating phasor representation of the value of the time-varying amplitude $E(\underline{r}_P, t)$. It rotates counterclockwise at angular speed ω. It is a complex number in the complex plane $\mathbb{C}$. As any complex number, it can also be viewed as a two-element vector with real-valued components (its real and imaginary parts), and thus as a vector in $\mathbb{R}^2$.

- $\bar{E}(\underline{r}_P)$ is a fixed phasor corresponding to $\bar{E}(\underline{r}_P, t)$. It is a fixed complex number. It can also be viewed as a two-element vector with real-valued components, and thus as a vector in $\mathbb{R}^2$.

Horizontal and vertical linear polarizations

The horizontal polarization (often denoted by H) and the vertical polarization (often denoted by V) are perhaps the most fundamental and the most common types of linear polarization. (Please do not mix up the symbol H used for both the magnetic field and the horizontal polarization.) Furthermore, other types of polarization, such as circular polarization, are naturally described as the proper combinations of some H and V polarizations [108].

To define the linear H polarization and the linear V polarization, we simply need to indicate what the corresponding vectors $\hat{\underline{p}}$ in the (x, y, z) axes are. With reference to Fig. 4.3, we have

$$\hat{\underline{p}} = \hat{\underline{\phi}} \text{ for } H \text{ polarization}$$
$$\hat{\underline{p}} = \hat{\underline{\theta}} \text{ for } V \text{ polarization,}$$

where the unit vectors $\hat{\underline{\phi}}$ and $\hat{\underline{\theta}}$ are defined as follows. $\hat{\underline{\theta}}$ is the unit vector "located" in the plane defined by the z-axis and the direction of propagation $\hat{\underline{k}}$, perpendicular to $\hat{\underline{k}}$, and oriented in the positive sense of the (polar) angle θ. $\hat{\underline{\phi}}$ is the unit vector "located" in the horizontal plane, perpendicular to $\hat{\underline{k}}$, and oriented in the positive sense of the (azimuth) angle ϕ.

Carefully note that the direction $\hat{\underline{\phi}}$ of horizontal (H) polarization and the direction $\hat{\underline{\theta}}$ of vertical (V) polarization form a right-handed system of axes with $\hat{\underline{k}} = -\hat{\underline{r}}$, but not with $\hat{\underline{r}}$. This is perfect since what really matters from an electromagnetic standpoint is the direction of propagation (*i.e.* $\hat{\underline{k}}$) and the directions of the H and V polarizations.

It should be noted that, while $\hat{\underline{\phi}}$ is oriented parallel to the horizontal plane, and is thus horizontal, $\hat{\underline{\theta}}$ is not oriented vertically. However, $\hat{\underline{\theta}}$ is in a vertical plane. One should thus be careful concerning the meaning of the qualifiers "horizontal" and "vertical" when talking about polarization. The V polarization is generally not vertical, and it could be horizontal if $\hat{\underline{k}}$ is aligned with the z-axis. A particular case is when $\hat{\underline{\phi}}$ is in

the horizontal plane, and when the receiver is at a long distance from the target. In this case, $\hat{\underline{\theta}}$ is vertical.

Arbitrary linear polarizations

We have indicated that the orientation vector $\hat{p}$ of a given linear polarization is necessarily perpendicular to the direction of propagation $\hat{\underline{k}}$. This means that this vector $\hat{p}$ is in the plane defined by $\hat{\underline{\phi}}$ (H polarization) and $\hat{\underline{\theta}}$ (V polarization). Therefore, the real-valued E-field vector corresponding to an arbitrary linear polarization can be expressed in terms of its real-valued components along the $\hat{\underline{\phi}}$ and $\hat{\underline{\theta}}$ vectors (or axes).

More generally, we can define an arbitrary polarization by defining the (time-varying) real-valued amplitudes associated with the (physical) directions $\hat{\underline{\phi}}$ and $\hat{\underline{\theta}}$. In other words, we express the E-field vector $\underline{E}(\underline{r}_P, t)$ corresponding to this arbitrary polarization in terms of its components along the $\hat{\underline{\phi}}$ and $\hat{\underline{\theta}}$ axes,

$$\underline{E}(\underline{r}_P, t) = \underline{E}_{\hat{\underline{\phi}}}(\underline{r}_P, t) + \underline{E}_{\hat{\underline{\theta}}}(\underline{r}_P, t), \tag{4.3}$$

where the terms on the right-hand side are defined by a simple adaptation of Eq. (4.2)

$$\underline{E}_{\hat{\underline{\phi}}}(\underline{r}_P, t) = E_{\hat{\underline{\phi}}}(\underline{r}_P, t)\hat{\underline{\phi}} \tag{4.4}$$

$$\underline{E}_{\hat{\underline{\theta}}}(\underline{r}_P, t) = E_{\hat{\underline{\theta}}}(\underline{r}_P, t)\hat{\underline{\theta}}, \tag{4.5}$$

which gives

$$\underline{E}(\underline{r}_P, t) = E_{\hat{\underline{\phi}}}(\underline{r}_P, t)\hat{\underline{\phi}} + E_{\hat{\underline{\theta}}}(\underline{r}_P, t)\hat{\underline{\theta}}. \tag{4.6}$$

Once again, in Eq. (4.6), $E_{\hat{\underline{\phi}}}(\underline{r}_P, t)$ and $E_{\hat{\underline{\theta}}}(\underline{r}_P, t)$ are the components of the E-field vector $\underline{E}(\underline{r}_P, t)$ along the $\hat{\underline{\phi}}$ and $\hat{\underline{\theta}}$ axes, respectively.

By dropping the time component, *i.e.* the term $e^{j\omega t}$, we can write

$$\underline{E}(\underline{r}_P) = \bar{E}_{\hat{\underline{\phi}}}(\underline{r}_P)\hat{\underline{\phi}} + \bar{E}_{\hat{\underline{\theta}}}(\underline{r}_P)\hat{\underline{\theta}}. \tag{4.7}$$

Equation (4.7) is very important for subsequent developments. One of its advantages is that time t does not appear in it. Specifically, $e^{j\omega t}$ does not appear. All the information is contained in the phasors $\bar{E}_{\hat{\underline{\phi}}}(\underline{r}_p)$ and $\bar{E}_{\hat{\underline{\theta}}}(\underline{r}_p)$, which are fixed phasors for each given point P.

Although we have focused on linear polarizations, it is important to understand that the above discussion and formulas can be extended to arbitrary polarizations by proper choices of $\bar{E}_{\hat{\underline{\phi}}}(\underline{r}_P)$ and $\bar{E}_{\hat{\underline{\theta}}}(\underline{r}_P)$. Changes of polarization bases come in handy for this [20, 21, 212].

4.2.3   Expressions for the transmitted and received electromagnetic fields

Equation (4.7) expresses the three-element complex vector representing a polarized plane wave, whether it is linearly polarized or not, travelling in the direction of $\hat{\underline{k}}$.

We assume, for both the wave arriving on the scatterer at O and the wave scattered towards the receiver at Rx, the hypothesis of a plane wave (defined in Section 3.7.1) as long as the target is in the far-field of both the Tx and the Rx. This means that we can use Eq. (4.7) to express both the transmitted (Tx) E-field and the received (Rx) E-field. We use the superscripts t and r to distinguish the Tx quantities and the Rx quantities, respectively.

We can express both the transmitted (Tx) electric field (E-field) and the received (Rx) E-field in terms of their polarization basis. The polarization bases for the Tx and the Rx are denoted by $\hat{\underline{\phi}}_t$ and $\hat{\underline{\theta}}_t$, and $\hat{\underline{\phi}}_r$ and $\hat{\underline{\theta}}_r$, respectively.

We thus adapt Eq. (4.7) to the bistatic configuration, which gives, for the Tx E-field at $\underline{r}_T$ and for the Rx E-field at $\underline{r}_R$,

$$\bar{\underline{E}}^t(\underline{r}_T) = \bar{E}^t_{\hat{\underline{\phi}}_t}(\underline{r}_T)\hat{\underline{\phi}}_t + \bar{E}^t_{\hat{\underline{\theta}}_t}(\underline{r}_T)\hat{\underline{\theta}}_t \tag{4.8}$$

$$\bar{\underline{E}}^r(\underline{r}_R) = \bar{E}^r_{\hat{\underline{\phi}}_t}(\underline{r}_R)\hat{\underline{\phi}}_r + \bar{E}^r_{\hat{\underline{\theta}}_r}(\underline{r}_R)\hat{\underline{\theta}}_r. \tag{4.9}$$

Similarly, we write the relations between the Rx phasors at $\underline{r}_R$, $\bar{E}^r_{\hat{\underline{\phi}}_r}(\underline{r}_R)$ and $\bar{E}^r_{\hat{\underline{\theta}}_r}(\underline{r}_R)$, and the Tx phasors at $\underline{r}_P = \underline{0}$, $\bar{E}^t_{\hat{\underline{\phi}}_t}(\underline{0})$ and $\bar{E}^t_{\hat{\underline{\theta}}_t}(\underline{0})$, as

$$\bar{\underline{E}}^t(\underline{0}) = \bar{E}^t_{\hat{\underline{\phi}}_t}(\underline{0})\hat{\underline{\phi}}_t + \bar{E}^t_{\hat{\underline{\theta}}_t}(\underline{0})\hat{\underline{\theta}}_t, \tag{4.10}$$

$$\bar{\underline{E}}^r(\underline{r}_R) = \bar{E}^r_{\hat{\underline{\phi}}_r}(\underline{r}_R)\hat{\underline{\phi}} + \bar{E}^r_{\hat{\underline{\theta}}_r}(\underline{r}_R)\hat{\underline{\theta}}. \tag{4.11}$$

In the present case, the ultimate goal is to relate the Rx phasors $\bar{E}^r_{\hat{\underline{\phi}}_r}(\underline{r}_R)$ and $\bar{E}^r_{\hat{\underline{\theta}}_r}(\underline{r}_R)$ to the Tx phasors $\bar{E}^t_{\hat{\underline{\phi}}_t}(\underline{0})$ and $\bar{E}^t_{\hat{\underline{\theta}}_t}(\underline{0})$. The Tx phasors at $\underline{0}$, $\bar{E}^t_{\hat{\underline{\phi}}_t}(\underline{0})$ and $\bar{E}^t_{\hat{\underline{\theta}}_t}(\underline{0})$, and the Tx phasors at $\underline{r}_T$, $\bar{E}^t_{\hat{\underline{\phi}}_t}(\underline{r}_T)$ and $\bar{E}^t_{\hat{\underline{\theta}}_t}(\underline{r}_T)$, are related by

$$\bar{E}^t_{\hat{\underline{p}}}(\underline{r}_T) = \bar{E}^t_{\hat{\underline{p}}}(\underline{0})e^{-j\underline{k}_T \cdot \underline{r}_T}, \tag{4.12}$$

with $\hat{\underline{p}}$ being either $\hat{\underline{\phi}}_t$ or $\hat{\underline{\theta}}_t$. This can also be expressed as

$$\begin{aligned}
\bar{\underline{E}}^t(\underline{r}_T) &= \bar{E}^t_{\hat{\underline{\phi}}_t}(\underline{0})e^{-j\underline{k}_T \cdot \underline{r}_T}\hat{\underline{\phi}}_t + \bar{E}^t_{\hat{\underline{\theta}}_t}(\underline{0})e^{-j\underline{k}_T \cdot \underline{r}_T}\hat{\underline{\theta}}_t \\
&= \left[\bar{E}^t_{\hat{\underline{\phi}}_t}(\underline{0})\hat{\underline{\phi}}_t + \bar{E}^t_{\hat{\underline{\theta}}_t}(\underline{0})\hat{\underline{\theta}}_t\right]e^{-j\underline{k}_T \cdot \underline{r}_T} \\
&= \bar{\underline{E}}^t(\underline{0})e^{-j\underline{k}_T \cdot \underline{r}_T}. \tag{4.13}
\end{aligned}$$

Note that we have

$$\underline{k}_T \cdot \underline{r}_T = kr\hat{\underline{k}}_T \cdot \hat{\underline{r}}_T. \tag{4.14}$$

In the present context, we denote the scalar product of two vectors $\underline{a}$ and $\underline{b}$ by $\underline{a} \cdot \underline{b}$. Although the alternate notation $\underline{a}^T\underline{b}$ with $()^T$ denoting "transpose" is preferred, we do not use it here because the transpose sign would make some equations cumbersome, such as in Eq. (4.13). Note that if $\underline{a}$ is complex-valued, we should use $\underline{a}^\dagger\underline{b}$, where $()^\dagger$ denotes "complex conjugate".

Since the unit vectors $\underline{\hat{k}}_T$ and $\underline{\hat{r}}_T$ point in opposite directions, we have $\underline{\hat{k}}_T \cdot \underline{\hat{r}}_T = -1$, and thus

$$\underline{k}_T \cdot \underline{r}_T = -kr. \tag{4.15}$$

Equation (4.12) thus becomes

$$\bar{E}^t_{\underline{\hat{p}}}(\underline{r}_T) = \bar{E}^t_{\underline{\hat{p}}}(\underline{0})e^{-j\underline{k}_T \cdot \underline{r}_T}. \tag{4.16}$$

Using Eq. (4.15), we get

$$\bar{E}^t_{\underline{\hat{p}}}(\underline{r}_T) = \bar{E}^t_{\underline{\hat{p}}}(\underline{0})e^{jkr}, \tag{4.17}$$

as well as the inverse relation

$$\bar{E}^t_{\underline{\hat{p}}}(\underline{0}) = \bar{E}^t_{\underline{\hat{p}}}(\underline{r}_T)e^{-jkr}. \tag{4.18}$$

4.2.4   Bistatic polarization scattering matrix

As indicated in [87, 100, 183, 211, 212], it is well-known that $\bar{E}^r_{\underline{\hat{\phi}}_r}(\underline{r}_R)$ and $\bar{E}^r_{\underline{\hat{\theta}}_r}(\underline{r}_R)$ are each linearly related to both $\bar{E}^t_{\underline{\hat{\phi}}_t}(\underline{0})$ and $\bar{E}^t_{\underline{\hat{\theta}}_t}(\underline{0})$. This linear relation is expressed in matrix form as

$$\begin{pmatrix} \bar{E}^r_{\underline{\hat{\phi}}_r}(\underline{r}_R) \\ \bar{E}^r_{\underline{\hat{\theta}}_r}(\underline{r}_R) \end{pmatrix} = \alpha(k_R, r_R) \begin{pmatrix} S^{BS}_{\underline{\hat{\phi}}_t\underline{\hat{\phi}}_r} & S^{BS}_{\underline{\hat{\theta}}_t\underline{\hat{\phi}}_r} \\ S^{BS}_{\underline{\hat{\phi}}_t\underline{\hat{\theta}}_r} & S^{BS}_{\underline{\hat{\theta}}_t\underline{\hat{\theta}}_r} \end{pmatrix} \begin{pmatrix} \bar{E}^t_{\underline{\hat{\phi}}_t}(\underline{0}) \\ \bar{E}^t_{\underline{\hat{\theta}}_t}(\underline{0}) \end{pmatrix}, \tag{4.19}$$

or as

$$\bar{\underline{E}}^r(\underline{r}_R) = \alpha(k_R, r_R)S^{BS}\bar{\underline{E}}^t(\underline{0}), \tag{4.20}$$

where $\bar{\underline{E}}^r(\underline{r}_R)$ and $\bar{\underline{E}}^t(\underline{0})$ are special cases of two-element complex vectors,

$$\bar{\underline{E}}^r(\underline{r}_P) = \begin{pmatrix} \bar{E}^r_{\underline{\hat{\phi}}_r}(\underline{r}_P) \\ \bar{E}^r_{\underline{\hat{\theta}}_r}(\underline{r}_P) \end{pmatrix} \tag{4.21}$$

$$\bar{\underline{E}}^t(\underline{r}_P) = \begin{pmatrix} \bar{E}^t_{\underline{\hat{\phi}}_t}(\underline{r}_P) \\ \bar{E}^t_{\underline{\hat{\theta}}_t}(\underline{r}_P) \end{pmatrix}, \tag{4.22}$$

and where $\alpha(k_R, r_R)$ is a factor further discussed below, and

$$S^{BS} = \begin{pmatrix} S^{BS}_{\underline{\hat{\phi}}_t\underline{\hat{\phi}}_r} & S^{BS}_{\underline{\hat{\theta}}_t\underline{\hat{\phi}}_r} \\ S^{BS}_{\underline{\hat{\phi}}_t\underline{\hat{\theta}}_r} & S^{BS}_{\underline{\hat{\theta}}_t\underline{\hat{\theta}}_r} \end{pmatrix}. \tag{4.23}$$

The elements of the scattering matrix S^{BS} are complex-valued. The superscript BS denotes the fact that the scattering matrix corresponds to a bistatic configuration. Since S^{BS} depends on the frequency of the illuminating wave, on the aspect angle θ at which the object is illuminated, and on the bistatic angle β, S^{BS} should, strictly speaking, be noted as $S^{BS}(f, \theta, \beta)$. This notation will not be used, in order to simplify the equations.

For completeness, let us rewrite the matrix relation (4.19) in terms of the two scalar equations, as

$$\bar{E}^r_{\underline{\hat{\phi}}_r}(\underline{r}_R) = \alpha(k_R, r_R)S^{BS}_{\underline{\hat{\phi}}_t\underline{\hat{\phi}}_r}\bar{E}^t_{\underline{\hat{\phi}}_t}(\underline{0}) + \alpha(k_R, r_R)S^{BS}_{\underline{\hat{\theta}}_t\underline{\hat{\phi}}_r}\bar{E}^t_{\underline{\hat{\theta}}_t}(\underline{0}) \tag{4.24}$$

$$\bar{E}^r_{\underline{\hat{\theta}}_r}(\underline{r}_R) = \alpha(k_R, r_R)S^{BS}_{\underline{\hat{\phi}}_t\underline{\hat{\theta}}_r}\bar{E}^t_{\underline{\hat{\phi}}_t}(\underline{0}) + \alpha(k_R, r_R)S^{BS}_{\underline{\hat{\theta}}_t\underline{\hat{\theta}}_r}\bar{E}^t_{\underline{\hat{\theta}}_t}(\underline{0}). \tag{4.25}$$

The reason for the factor $\alpha(k_T, r_R)$ in Eqs. (4.19) and (4.20) is that there is no universal agreement in the literature concerning the definitions of the elements of S^{BS}, and thus of S^{BS} itself [212]. Typical values found in the literature for $\alpha(k_T, r_R)$ are 1, $\frac{e^{-jk_T r_R}}{r_R}$, and $\frac{e^{-jk_T r_R}}{k_T r_R}$, where r_R is the range from the object to the receiver. $\alpha(k_T, r_R)$ is thus denoted as $\alpha(k, r)$, since $|k_T| = k$, and since $|r_R| = r$. The rationale for the possible factors 1 and e^{-ikr} is likely related to the choice of using the value at the origin or at the radar for the Tx E-field [212].

In any case, the matrix S^{BS} is called the bistatic polarization scattering matrix (BS-PSM), or simply the bistatic scattering matrix (BS-SM). We will call its elements the bistatic polarization scattering coefficients (BS-PSC), or simply the bistatic scattering coefficients (BS-SCs). It is clear that the BS-SCs depend on the frequency f of the Tx E-field, on the polarization *Pol* of both the Tx and Rx E-fields, on the pair (θ, ϕ) of aspect angles (where θ is the aspect angle in the horizontal plane, and ϕ the aspect angle in the vertical plane), and on the bistatic angle β. The main difference with the monostatic scattering coefficients described in [87, 100, 183, 211, 212] is that the BS-SCs also depend on the bistatic angle.

4.2.5 Components of the bistatic polarization scattering matrix

This section describes the way the coefficients $S_{\hat{\underline{p}}_t \hat{\underline{p}}_r}$ of the bistatic polarization scattering matrix (BS-PSM) S can be experimentally measured. Once again, the presentation that follows closely follows that of [212].

Let us consider a Tx E-field that is linearly polarized, either along $\hat{\underline{\phi}}_t$ or along $\hat{\underline{\theta}}_t$. To be specific, let us consider the case where the linear polarization is along $\hat{\underline{\phi}}_t$. Let us denote the corresponding $\bar{E}^t_{\hat{\underline{\phi}}_t}(\underline{0})$ by E_0,

$$\bar{E}^t_{\hat{\underline{\phi}}_t}(\underline{0}) = E_0. \tag{4.26}$$

Of course, E_0 is a fixed phasor, *i.e.* a fixed complex number. Since the linear polarization is along $\hat{\underline{\phi}}_t$, we have

$$\bar{E}^t_{\hat{\underline{\theta}}_t}(\underline{0}) = 0. \tag{4.27}$$

The matrix expression (4.19) thus becomes

$$\begin{pmatrix} \bar{E}^r_{\hat{\underline{\phi}}_r}(\underline{r}) \\ \bar{E}^r_{\hat{\underline{\theta}}_r}(\underline{r}) \end{pmatrix} = \alpha(k_R, r_R) \begin{pmatrix} S^{BS}_{\hat{\underline{\phi}}_t \hat{\underline{\phi}}_r} & S^{BS}_{\hat{\underline{\theta}}_t \hat{\underline{\phi}}_r} \\ S^{BS}_{\hat{\underline{\phi}}_t \hat{\underline{\theta}}_r} & S^{BS}_{\hat{\underline{\theta}}_t \hat{\underline{\theta}}_r} \end{pmatrix} \begin{pmatrix} \bar{E}_0 \\ 0 \end{pmatrix}, \tag{4.28}$$

which gives

$$\bar{E}^r_{\hat{\underline{\phi}}_r}(\underline{r}) = \alpha(k_R, r_R) S^{BS}_{\hat{\underline{\phi}}_t \hat{\underline{\phi}}_r} \bar{E}_0 \tag{4.29}$$

$$\bar{E}^r_{\hat{\underline{\theta}}_r}(\underline{r}) = \alpha(k_R, r_R) S^{BS}_{\hat{\underline{\phi}}_t \hat{\underline{\theta}}_r} \bar{E}_0. \tag{4.30}$$

It follows that

$$S^{BS}_{\hat{\underline{\phi}}_t\hat{\underline{\phi}}_r} = \frac{1}{\alpha(k_R, r_R)}\frac{\bar{E}^r_{\hat{\underline{\phi}}_r}(\underline{r})}{\bar{E}_0} \tag{4.31}$$

$$S^{BS}_{\hat{\underline{\phi}}_t\hat{\underline{\theta}}_r} = \frac{1}{\alpha(k_R, r_R)}\frac{\bar{E}^r_{\hat{\underline{\theta}}_r}(\underline{r})}{\bar{E}_0}. \tag{4.32}$$

Therefore, by measuring $\bar{E}^r_{\hat{\underline{\phi}}_r}(\underline{r})$ and $\bar{E}^r_{\hat{\underline{\theta}}_r}(\underline{r})$, one can easily obtain the values for $S^{BS}_{\hat{\underline{\phi}}_t\hat{\underline{\phi}}_r}$ and $S^{BS}_{\hat{\underline{\phi}}_t\hat{\underline{\theta}}_r}$.

We now further examine the expression (4.31) for $S_{\hat{\underline{\phi}}_t\hat{\underline{\phi}}_r}$. (We consider later the three other elements of the BS-PSM.) The factor $\bar{E}^r_{\hat{\underline{\phi}}_r}(\underline{r})$ appearing in it can be expressed in a different form. Indeed, let us consider Eq. (4.11). By taking the scalar product of each side with $\hat{\underline{\phi}}_r$, we have

$$\begin{aligned}
\bar{\underline{E}}^r(\underline{r}) \cdot \hat{\underline{\phi}}_r &= \bar{E}^r_{\hat{\underline{\phi}}_r}(\underline{r})\hat{\underline{\phi}}_r \cdot \hat{\underline{\phi}}_r + \bar{E}^r_{\hat{\underline{\theta}}_r}(\underline{r})\hat{\underline{\theta}}_r \cdot \hat{\underline{\phi}}_r \\
&= \bar{E}^r_{\hat{\underline{\phi}}_r}(\underline{r}),
\end{aligned} \tag{4.33}$$

where we have used the fact that $\hat{\underline{\phi}}_r$ and $\hat{\underline{\theta}}_r$ are of unit length and perpendicular to each other. This gives an alternate expression for $\bar{E}^r_{\hat{\underline{\phi}}_r}(\underline{r})$

$$\bar{E}^r_{\hat{\underline{\phi}}_r}(\underline{r}) = \bar{\underline{E}}^r(\underline{r}) \cdot \hat{\underline{\phi}}_r. \tag{4.34}$$

By substituting into Eq. (4.31), we get

$$S^{BS}_{\hat{\underline{\phi}}_t\hat{\underline{\phi}}_r} = \frac{1}{\alpha(k_R, r_R)}\frac{\bar{\underline{E}}^r(\underline{r}) \cdot \hat{\underline{\phi}}_r}{\bar{E}_0}. \tag{4.35}$$

By starting from Eq. 4.31, one can easily find the corresponding result for $S^{BS}_{\hat{\underline{\phi}}_t\hat{\underline{\theta}}_r}$,

$$S_{\hat{\underline{\phi}}_t\hat{\underline{\theta}}_r} = \frac{1}{\alpha(k_R, r_R)}\frac{\bar{\underline{E}}^r(\underline{r}) \cdot \hat{\underline{\theta}}_r}{\bar{E}_0}. \tag{4.36}$$

In Eqs. (4.35) and (4.36), the quantity $\bar{\underline{E}}^r(\underline{r})$ is the complex vector representing the E-field received at R as a results of transmitting an E-field that is linearly polarized along $\hat{\underline{\phi}}_t$, *i.e.*

$$\begin{pmatrix} \bar{E}^t_{\hat{\underline{\phi}}_t}(\underline{0}) \\ \bar{E}^t_{\hat{\underline{\theta}}_t}(\underline{0}) \end{pmatrix} = \begin{pmatrix} \bar{E}_0 \\ 0 \end{pmatrix}. \tag{4.37}$$

To remember that the transmitted polarization is along $\hat{\underline{\phi}}_t$ (in this case), we rewrite $\bar{\underline{E}}^r(\underline{r})$ as $\bar{\underline{E}}^r_{\hat{\underline{\phi}}_t}(\underline{r})$. As a result, Eqs. (4.35) and (4.36) are rewritten as

$$S^{BS}_{\hat{\underline{\phi}}_t\hat{\underline{\phi}}_r} = \frac{1}{\alpha(k_R, r_R)}\frac{\bar{\underline{E}}^r_{\hat{\underline{\phi}}_t}(\underline{r}) \cdot \hat{\underline{\phi}}_r}{\bar{E}_0} \tag{4.38}$$

$$S^{BS}_{\hat{\underline{\phi}}_t\hat{\underline{\theta}}_r} = \frac{1}{\alpha(k_R, r_R)}\frac{\bar{\underline{E}}^r_{\hat{\underline{\phi}}_t}(\underline{r}) \cdot \hat{\underline{\theta}}_r}{\bar{E}_0}. \tag{4.39}$$

By transmitting an E-field linearly polarized along $\hat{\underline{\theta}}_t$, one can obtain the corresponding expressions for $S^{BS}_{\hat{\underline{\theta}}_t\hat{\underline{\phi}}_r}$ and $S^{BS}_{\hat{\underline{\theta}}_t\hat{\underline{\theta}}_r}$,

$$S^{BS}_{\hat{\underline{\theta}}_t\hat{\underline{\phi}}_r} = \frac{1}{\alpha(k_R, r_R)}\frac{\bar{\underline{E}}^r_{\hat{\underline{\theta}}_t}(\underline{r}) \cdot \hat{\underline{\phi}}_r}{\bar{E}_0} \tag{4.40}$$

$$S^{BS}_{\hat{\underline{\theta}}_t\hat{\underline{\theta}}_r} = \frac{1}{\alpha(k_R, r_R)}\frac{\bar{\underline{E}}^r_{\hat{\underline{\theta}}_t}(\underline{r}) \cdot \hat{\underline{\theta}}_r}{\bar{E}_0}. \tag{4.41}$$

The four Eqs. (4.38), (4.39), (4.40), and (4.41) can be generically written as

$$S^{BS}_{\hat{\underline{p}}_t\hat{\underline{p}}_r} = \frac{1}{\alpha(k_R, r_R)}\frac{\bar{\underline{E}}^r_{\hat{\underline{p}}_t}(\underline{r}) \cdot \hat{\underline{p}}_r}{\bar{E}_0}. \tag{4.42}$$

This generic expression will prove useful later. It is important to keep in mind the meaning of all quantities appearing in this expression, in particular the meaning of $\bar{\underline{E}}^r_{\hat{\underline{p}}_t}(\underline{r})$. For memory, it is a complex vector. Indeed, keep in mind that $\bar{\underline{E}}^r_{\hat{\underline{p}}_t}(\underline{r})$ is the complex vector $\bar{\underline{E}}^r(\underline{r})$ that was introduced initially, and that is specialized to the case of the E-field received at the radar receiver at $\underline{r}$, and for the case where the transmitted E-field is linearly polarized along $\hat{\underline{p}}_t$.

4.2.6 Bistatic complex RCS

Contrary to the definition of the elements of the bistatic polarization scattering matrix (BS-PSM), *i.e.* the bistatic polarization scattering coefficients (BS-PSCs), there appears to be a general agreement on the definition of the complex bistatic radar cross-section (BS-CRCS), which is denoted in this work by $\sqrt{\sigma_{\hat{\underline{p}}_t\hat{\underline{p}}_r}}^{BS}$, where $\hat{\underline{p}}_t$ and $\hat{\underline{p}}_r$ are the polarization of the Tx E-field and the polarization of the Rx E-field, respectively [212]. As for the definition of the BS-CRCS introduced in Section 3.4, note that the full, monolithic "$\sqrt{\sigma_{\hat{\underline{p}}_t\hat{\underline{p}}_r}}^{BS}$" symbol constitutes the notation for the BS-CRCS. This means that $\sqrt{\sigma_{\hat{\underline{p}}_t\hat{\underline{p}}_r}}^{BS}$ should not be interpreted as the square root operation. It is an integral part of the symbol for the BS-CRCS.

Using the notations introduced above, the agreed definition for the BS-CRCS $\sqrt{\sigma_{\hat{\underline{p}}_t\hat{\underline{p}}_r}}^{BS}$ is [46, 170]

$$\sqrt{\sigma_{\hat{\underline{p}}_t\hat{\underline{p}}_r}}^{BS} = \lim_{r_R\to\infty} 2\sqrt{\pi}r_R\frac{\bar{\underline{E}}^r_{\hat{\underline{p}}_t}(\underline{r}_R) \cdot \hat{\underline{p}}_r}{\bar{E}_0}e^{jkr_R}. \tag{4.43}$$

Compared to the definitions introduced in Section 3.4, we simply added the polarization basis. Assuming that r_R is large enough (since we use a far-field approximation), we ignore the taking of the limit, and we write

$$\sqrt{\sigma_{\hat{\underline{p}}_t\hat{\underline{p}}_r}}^{BS} = 2\sqrt{\pi}r_R\frac{\bar{\underline{E}}^r_{\hat{\underline{p}}_t}(\underline{r}_R) \cdot \hat{\underline{p}}_r}{\underline{E}_0}e^{jkr_R}. \tag{4.44}$$

By combining Eqs. (4.44) and (4.42), we get

$$\sqrt{\sigma_{\hat{\underline{p}}_t\hat{\underline{p}}_r}}^{BS} = 2\sqrt{\pi}r\alpha(k_R, r_R)S^{BS}_{\hat{\underline{p}}_t\hat{\underline{p}}_r}e^{jkr_R}, \tag{4.45}$$

i.e.

$$S_{\underline{\hat{p}}_t \underline{\hat{p}}_r}^{BS} = \beta(k_R, r_R)\sqrt{\sigma_{\underline{\hat{p}}_t \underline{\hat{p}}_r}}^{BS},$$

(4.46)

where

$$\beta(k_R, r_R) = \frac{e^{-jkr_R}}{\sqrt{\pi}r_R \alpha(k_R, r_R)}.$$

(4.47)

The three possible values for $\beta(k_R, r_R)$ result directly from the three possible values for $\alpha(k_R, r_R)$.

Expression (4.46) relates the BS-PSC $S_{\underline{\hat{p}}_t \underline{\hat{p}}_r}^{BS}$ and the BS-CRCS $\sqrt{\sigma_{\underline{\hat{p}}_t \underline{\hat{p}}_r}}^{BS}$. We emphasize that there is universal agreement on the definition of the BS-CRCS $\sqrt{\sigma_{\underline{\hat{p}}_t \underline{\hat{p}}_r}}^{BS}$, but not on the bistatic polarization scattering coefficient $S_{\underline{\hat{p}}_t \underline{\hat{p}}_r}^{BS}$.

We emphasize that the Eq. (4.42), used to relate $\sqrt{\sigma_{\underline{\hat{p}}_t \underline{\hat{p}}_r}}^{BS}$ and $S_{\underline{\hat{p}}_t \underline{\hat{p}}_r}^{BS}$, was initially introduced for providing a means of measuring the BS-PSCs.

4.2.7   Bistatic polarization complex radar cross-section matrix (BS-PCRCSM)

In this section, we introduce the matrix that is the counterpart of matrix S^{BS} for the $\sqrt{\sigma_{\underline{\hat{p}}_t \underline{\hat{p}}_r}}^{BS}$'s. We continue to closely follow the developments in [212]. We call this matrix the "bistatic polarization CRCS matrix" (BS-PCRCSM), and we denote it by the symbol $\sqrt{\sigma}^{BS}$. The BS-PCRCSM is thus defined as

$$\sqrt{\sigma}^{BS} = \begin{pmatrix} \sqrt{\sigma_{\hat{\phi}_t \hat{\phi}_r}}^{BS} & \sqrt{\sigma_{\hat{\phi}_t \underline{\hat{\theta}}_r}}^{BS} \\ \sqrt{\sigma_{\underline{\hat{\theta}}_t \hat{\phi}_r}}^{BS} & \sqrt{\sigma_{\underline{\hat{\theta}}_t \hat{\theta}_r}}^{BS} \end{pmatrix}.$$

(4.48)

This is the counterpart of Eq. 4.23. Matrices S^{BS} and $\sqrt{\sigma}^{BS}$ are related by

$$S^{BS} = \beta(k_R, r_R)\sqrt{\sigma}^{BS}.$$

(4.49)

The key equation in which S^{BS} appears is Eq. (4.20). By using Eqs. (4.49) and (4.47), Eq. (4.20) can be expressed as

$$\begin{aligned} \bar{\underline{E}}^r(\underline{r}_R) &= \alpha(k_R, r_R)\beta(k_R, r_R)\sqrt{\sigma}^{BS}\bar{\underline{E}}^t(\underline{0}) \\ &= \frac{e^{-jk_R r_R}}{2\sqrt{\pi}r_R}\sqrt{\sigma}^{BS}\bar{\underline{E}}^t(\underline{0}), \end{aligned}$$

(4.50)

where $\bar{\underline{E}}^r(\underline{r}_R)$ and $\bar{\underline{E}}^t(\underline{0})$ are special cases of two-element complex vectors, as in Eq. (4.20). Observe that the quantity $\alpha(k_R, r_R)$ has disappeared from this equation, which is excellent since there is no general agreement on the nature of the expression for $\alpha(k_R, r_R)$.

For conciseness, Eq. (4.50) is rewritten as

$$\bar{\underline{E}}^r(\underline{r}_R) = \gamma(k_R, r_R)\sqrt{\sigma}^{BS}\bar{\underline{E}}^t(\underline{0}),$$

(4.51)

where we introduced $\gamma(k_R, r_R)$ defined by

$$\gamma(k_R, r_R) = \frac{e^{-jkr_R}}{2\sqrt{\pi}r_R}. \tag{4.52}$$

The major advantage of Eq. (4.51) over Eq. (4.20) is that there is a unique expression for $\gamma(k_R, r_R)$, this by contrast with $\alpha(k_R, r_R)$ for which there are at least three candidate expressions.

Equation (4.51) can be expressed as

$$\begin{pmatrix} \bar{E}^r_{\hat{\underline{\phi}}_r}(\underline{r}_R) \\ \bar{E}^r_{\hat{\underline{\theta}}_r}(\underline{r}_R) \end{pmatrix} = \gamma(k_R, r_R) \begin{pmatrix} \sqrt{\sigma_{\hat{\underline{\phi}}_t\hat{\underline{\phi}}_r}}^{BS} & \sqrt{\sigma_{\hat{\underline{\phi}}_t\hat{\underline{\theta}}_r}}^{BS} \\ \sqrt{\sigma_{\hat{\underline{\theta}}_t\hat{\underline{\phi}}_r}}^{BS} & \sqrt{\sigma_{\hat{\underline{\theta}}_t\hat{\underline{\theta}}_r}}^{BS} \end{pmatrix} \begin{pmatrix} \bar{E}^t_{\hat{\underline{\phi}}_t}(\underline{0}) \\ \bar{E}^t_{\hat{\underline{\theta}}_t}(\underline{0}) \end{pmatrix}, \tag{4.53}$$

which is the counterpart of Eq. (4.19). Once again, the quantities $\sqrt{\sigma_{\hat{\underline{p}}_t\hat{\underline{p}}_r}}^{BS}$ are "monolithic" symbols.

In case there is any doubt, the $\sqrt{\sigma_{\hat{\underline{p}}_t\hat{\underline{p}}_r}}^{BS}$'s are complex numbers. We could make this appear more explicitly by adding an overbar, but this would not be the conventional notation. The BS-CRCS depends on the frequency f of the Tx E-field, on the polarization *Pol* of both the Tx and Rx E-fields, on the pair (θ, ϕ) of aspect angles, and on the bistatic angle β. The BS-CRCS depends on the same parameters as the BS-SCs.

4.2.8 Position of the transmitter as reference for the transmitted electric field

The value of the Tx E-field at the transmitter is often used, rather than at the origin. The expression relating the value of the Tx E-field at $\underline{0}$ and at $\underline{r}_P$ is given by Eq. (4.12). Using Eq. (4.15), we get

$$\bar{E}^t_{\hat{\underline{p}}}(\underline{r}_T) = \bar{E}^t_{\hat{\underline{p}}}(\underline{0})e^{jkr_T}, \tag{4.54}$$

Using this last relation in Eq. (4.20) gives

$$\bar{\underline{E}}^r(\underline{r}_R) = \alpha(k_R, r_R)e^{-jkr_T}S^{BS}\bar{\underline{E}}^t(\underline{r}_T). \tag{4.55}$$

We can proceed in exactly the same fashion with the other fundamental relation, *i.e.* Eq. (4.51), linking $\bar{\underline{E}}^r(\underline{r}_R)$ and $\bar{\underline{E}}^t(\underline{0})$. Indeed, by using Eqs. (4.52) and (4.54), we get

$$\bar{\underline{E}}^r(\underline{r}_R) = \frac{e^{-jk(r_T+r_R)}}{2\sqrt{\pi}r_R}\sqrt{\sigma}^{BS}\bar{\underline{E}}^t(\underline{r}_T). \tag{4.56}$$

The roundtrip distance $r_T + r_R$ appears in the first factor of the right-hand side of Eq. (4.56). In the case of forwardscattering, *i.e.* when the bistatic angle is equal to 180°, $\hat{\underline{r}}_T = -\hat{\underline{r}}_R$, and the exponential term of Eq. (4.56) is equal to 1.

We can use Eqs. (4.55) and (4.56) to compute both the BS-CRCS and the BS-RCS from the Tx E-field at $\hat{\underline{r}}_T$ and the Rx E-field located at $\hat{\underline{r}}_R$.

4.2.9   Case of a single linear polarization

Let us consider the case of a single linear polarization, meaning that the Tx E-field is polarized along some (physical) direction $\hat{\underline{p}}$, and that we sense only the component of the Rx E-field along the same direction $\hat{\underline{p}}$. For simplicity, we consider here only the cases of horizontal polarization ($\hat{\underline{p}} = \hat{\underline{\phi}}$) and of vertical polarization ($\hat{\underline{p}} = \hat{\underline{\theta}}$).

If we transmit along $\hat{\underline{\phi}}$ and we receive along $\hat{\underline{\phi}}$, it should be clear that the only part of interest that remains from Eq. (4.56) is

$$\bar{E}^r_{\hat{\underline{\phi}}}(\underline{r}_R) = \frac{e^{-jk(r_T+r_R)}}{2\sqrt{\pi}r_R}\sqrt{\sigma}_{\hat{\phi}\hat{\phi}}\bar{E}^t_{\hat{\underline{\phi}}}(\underline{r}_T). \tag{4.57}$$

If we transmit along $\hat{\underline{\theta}}$ and we receive along $\hat{\underline{\theta}}$, the corresponding relation is

$$\bar{E}^r_{\hat{\underline{\theta}}}(\underline{r}_R) = \frac{e^{-jk(r_T+r_R)}}{2\sqrt{\pi}r_R}\sqrt{\sigma}_{\hat{\theta}\hat{\theta}}\bar{E}^t_{\hat{\underline{\theta}}}(\underline{r}_T). \tag{4.58}$$

If the polarization is not considered, all the subscripts can be dropped, which results in

$$\bar{E}^r(\underline{r}_R) = \alpha'(k, r_T, r_R)\sqrt{\sigma}\bar{E}^t(\underline{r}_T), \tag{4.59}$$

where

$$\alpha'(k, r_T, r_R) = \frac{e^{-jk(r_T+r_R)}}{2\sqrt{\pi}r_R}. \tag{4.60}$$

Equation (4.59) will be used in Chapter 5 for the construction of images of targets from their BS-CRCS.

From Eq. (4.59), we can express the BS-CRCS $\sqrt{\sigma}$ as

$$\sqrt{\sigma} = \frac{1}{\alpha'(k, r_T, r_R)}\frac{\bar{E}^r(\underline{r}_R)}{\bar{E}^t(\underline{r}_T)} \tag{4.61}$$

$$= 2\sqrt{\pi}r_R e^{jk(r_T+r_R)}\frac{\bar{E}^r(\underline{r}_R)}{\bar{E}^t(\underline{r}_T)}, \tag{4.62}$$

which is exactly the definition of the BS-CRCS given by Eq. (3.1).

Similarly, we can express the BS-RCS σ as

$$\sigma = 4\pi r_R^2\frac{|\bar{E}^r(\underline{r}_R)|^2}{|\bar{E}^t(\underline{r}_T)|^2}, \tag{4.63}$$

which is, not surprisingly, exactly the definition of the BS-RCS expressed in Eq. (3.2). We can thus express both the BS-CRCS and the BS-RCS of a target in function of the transmitted and received electric fields, provided that we know the distances r_T and r_R.

4.2.10 Practical measurement of the bistatic RCS of targets

In [119, 122], it is indicated how the BS-RCS of targets can be measured in practice. A calibration is needed for both outdoor measurements (in the field) and indoor measurements (in the anechoic chamber).

The calibration phase consists in the successive measurement of the scattering coefficients, *i.e.* of the elements of the bistatic polarization scattering matrix (BS-PSM), of (1) the target of interest in background clutter, (2) background clutter, and (3) an object of reference, called a calibration object in background clutter. Indoor, the practical BS-RCS σ^{BS} of a target at some frequency f_i and some aspect angle θ_i is then computed as

$$\sigma^{BS} = \left| \frac{\left(S_1^{BS} - S_2^{BS} \right) (f_i, \theta_i)}{\left(S_3^{BS} - S_2^{BS} \right) (f_i, \theta_0)} S_0^{BS}(f_i, \theta_0) \right|^2, \tag{4.64}$$

where S_0^{BS} is the theoretical bistatic scattering coefficient due to the calibration object with aspect angle θ_0, usually a sphere, S_1^{BS} the measured bistatic scattering coefficient due to the target in background clutter, S_2^{BS} the measured bistatic scattering coefficient due to background clutter, and S_3^{BS} the measured bistatic scattering coefficient due to the calibration object in background clutter.

4.3 Acquisition of raw data: experimental setup

This section describes the experimental setup used for the acquisition of raw data. Raw data consist in signals sent out by a transmitter (Tx), scattered by a target of interest (here an airplane), and collected by a receiver (Rx). The acquisition of raw data was conducted using scaled models of airplanes in an anechoic chamber at ONERA, Palaiseau, France. We thus call this data the ONERA data. We extract the bistatic complex radar cross-section (BS-CRCS) and the bistatic radar cross-section (BS-RCS) from the raw data acquired, as described in Section 4.2.

We successively describe the reason for using scaled models of targets, the experimental setup used for the acquisition of raw data, and the acquisition of raw data.

4.3.1 Motivation for using scaled models in an anechoic chamber

The far-field conditions described in Section 3.7 imply (1) that the distances r_T (from the transmitter to the target) and r_R (from the target to the receiver) must both be larger than the ratio of twice the square of the characteristic dimension D of the target to the wavelength λ of the transmitted signal, and (2) that D is much larger than λ,

$$\begin{cases} r_T, r_R \gg \frac{2D^2}{\lambda} \\ D \gg \lambda. \end{cases} \tag{4.65}$$

The frequencies f at which the scattered signals must be measured are comprised between 20 MHz and 1 GHz. The maximum wavelength corresponds to the lowest

frequency (since $\lambda = c/f$). More specifically, for the minimum frequency of 20 MHz, the corresponding wavelength is 15 m. This is the maximum wavelength we must handle. We will see in Section 4.3.4 that the characteristic dimension D of the targets of interest is 15 m. Therefore, according to the far-field conditions in Eq. (4.65), r_T and r_R must be both larger than 30 m. Since the anechoic chamber at ONERA cannot handle such ranges, one must resort to using scale models of the targets of interest.

Since we use scale models, we measure the BS-CRCS $\sqrt{\sigma}$ of targets at a frequency f' different from the desired frequency f. The frequency f' is equal to the product of the desired frequency f and the scale factor s, $f' = f \times s$. A scale factor s of 10 means that the scale model of an object is 10 times smaller than the real-size object. This ensures that the contribution of the scale model illuminated at frequency f' to the echo-path signal is the same as would be the contribution of the real-size target illuminated at frequency f. This homothety is applicable since scale models are made of perfectly conducting materials.

To obtain the full-scale BS-CRCS at frequency f, one can show that one must simply multiply by the scale factor the BS-CRCS obtained from the BS-CRCS measured on the scale model [104]:

$$\sqrt{\sigma}(\text{full scale}, f) = \sqrt{\sigma}(\text{scale } s, f') \times s. \tag{4.66}$$

As a consequence of the definitions of the BS-CRCS and the BS-RCS, we have [104]

$$\sigma(\text{full scale}, f) = \sigma(\text{scale } s, f') \times s^2. \tag{4.67}$$

4.3.2 Configuration geometry

Figure 4.4 shows the configuration geometry. The origin of the coordinate system is located at the turntable, in the center of the anechoic chamber. The target of interest S, also called the object, is fixed and placed on the turntable, and thus at the origin O of the coordinate system. The transmitter (Tx) is fixed, and located on the x-axis, at a distance r_T from the origin O. The receiver (Rx) can move along one-half of the circumference of a circle, in the xy-plane, in order to make the bistatic angle β vary. The distance r_T from the transmitter to the object is kept constant and equal to the distance r_R from the object to the receiver. Thus, $r_T = r_R = r$.

We define the orientation of the object as the angle between the line-of-sight of this object and the x-axis. The orientation of the object is defined in terms of both its azimuth angle θ and its elevation angle ϕ (Fig. 4.4). The azimuth angle θ is the angle measured positively from the x-axis to the projection of the longitudinal axis of the airplane in the (x, y) plane. The elevation angle ϕ is the angle measured positively from the x-axis to the projection of the longitudinal axis of the airplane in the (y, z) plane.

In the configuration described above, the airplane and the Tx are fixed. The Rx moves, thus making the bistatic angle β vary. The rotation of the receiver around the fixed airplane is equivalent to the rotation, in the opposite direction, of the airplane with a fixed receiver. Experiments are thus conducted as if airplanes were rotating.
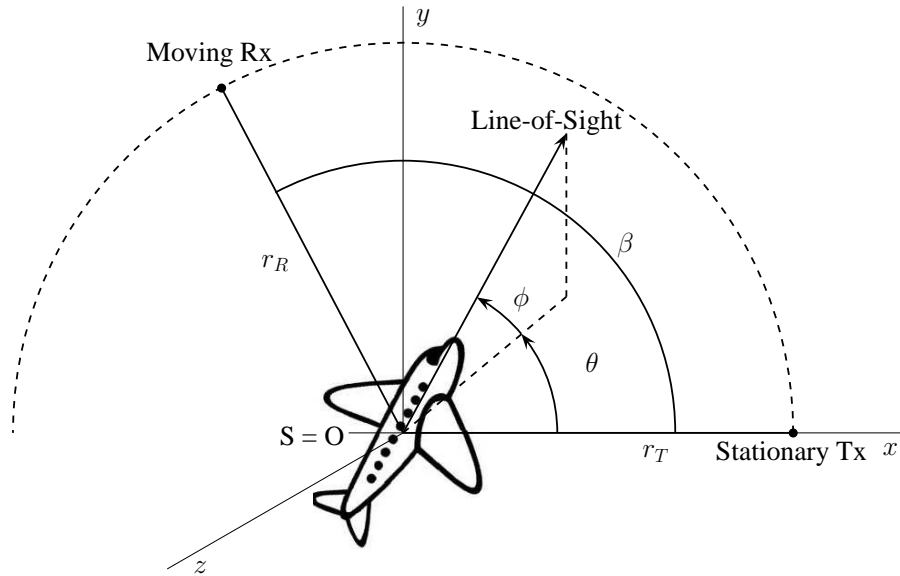
Figure 4.4: *Experimental setup used to collect raw data in an anechoic chamber.*

In real-life situations, although airplanes can fly arbitrary trajectories, they generally fly according to a linear trajectory, at least locally. In a linear trajectory, for a fixed transmitter and a fixed receiver, the bistatic angle β varies with the translation of the airplane, as shown in Fig. 4.5. Figure 4.6 illustrates the variation of the bistatic angle β along a real-life airplane trajectory, as will be seen in Chapter 8. Therefore, the rotation of the receiver in the anechoic chamber corresponds to the translation of an airplane along its trajectory.
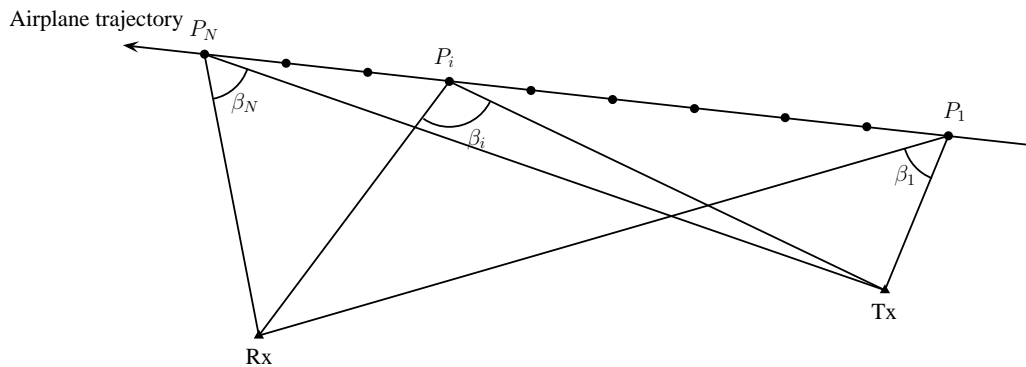
Figure 4.5: *Illustration of the variation of the bistatic angle β for an airplane flying a linear trajectory.*

4.3.3 Acquisition of raw data

In the anechoic chamber, at a particular time instant, the Tx sends out a signal at a particular carrier frequency f and at a particular polarization Pol_t, where t stands for "transmitter". The signal is scattered by a target with a fixed orientation, *i.e.* with fixed angles θ and ϕ. The Rx is at a fixed location. The bistatic angle β is thus fixed. The Rx collects the scattered signal at a particular polarization Pol_r, where
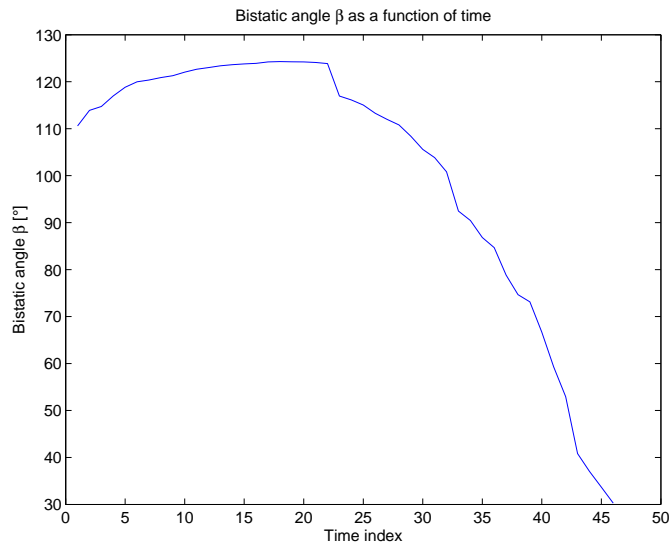
Figure 4.6: *Example evolution of the bistatic angle β through time, for an A319 airplane flying a real trajectory, probably close to linear.*

the subscript r stands for "receiver". The values used for the azimuth angle θ and the elevation angle ϕ of the target, for the bistatic angle β, for the polarizations Pol_t and Pol_r, and for the frequency f are listed below. As explained in Chapter 3, these parameters all influence the value of both the BS-CRCS and the BS-RCS.

Orientation of the target

The orientation of the target is determined by both its azimuth angle θ and its elevation angle ϕ. Data was recorded for the following values of θ and ϕ: $\theta \in \{0°, 45°, 90°\}$ and $\phi \in \{-10°, 0°, 5°\}$.

Frequencies

Our goal is to use frequencies from 20 MHz to 1.3 GHz. Note that these are the real-life frequencies of interest, and that these must be scaled for use with the scale models. The above frequency range is covered with the four following frequency bands: FB1 ([20; 80] MHz), FB2 ([190; 250] MHz), FB3 ([450; 550] MHz), and FB4 ([1.2; 1.3] GHz). These are the four frequency bands for which raw data was acquired. We use several frequencies within each band, spaced by 0.1 MHz for FB1, and by 1 MHz for the three others.

Bistatic angles

Since we only consider the bistatic RCS region (Section 3.7.4), we kept the bistatic angle β in the range from 5° to 180°. More specifically, we kept the bistatic angle between 6° and 160°, so that $\beta \in [0°; 180°]$. The increment in β was varied according to the frequency band used: $\Delta\beta = 2°$ for FB1, $\Delta\beta = 1°$ for FB2, $\Delta\beta = 0.5°$ for FB3, and $\Delta\beta = 0.25°$ for FB4.

Polarizations

The polarizations of the Tx and the Rx are generally denoted by the pair $Pol_t\,Pol_r$. For linear polarizations, *i.e.* horizontal (H) and vertical (V) polarizations, the possible polarization pairs are HH, HV, VH, VV. For circular polarizations, *i.e.* left (L) and right (R) polarizations, the possible polarization pairs are LL, LR, RL, RR. In our experiments, we used the linear polarizations only.

4.3.4 Airplanes of interest

The four airplanes considered for the experiments in the anechoic chamber are a Super King Air 200 (Beechcraft), an F117 stealth fighter (F-117), an F16 fighter, and a Learjet. These airplanes are illustrated in Figs. 4.7, 4.8, 4.9, and 4.10, respectively. The illustrating views were generated from Computer-Aided Design (CAD) models.

In order to constitute the different classes of targets, it is useful to examine the differences in shape and sizes among these four airplanes. They all have a length of 15 meters, and wingspans of about 10 meters. They thus do not differ in size. However, they present major differences in shape. The Beechcraft is made of a rounded fuselage and has two propeller engines located on the wings. It also has a horizontal stabilizer at its rear. The F117 is made of numerous planar facets in order to defeat radar. The F16 is made of a rounded fuselage, two triangular wings, a rudder, and a sharp nose. It also has two missiles at the wingtips. The Learjet is similar to the Beechcraft, but with jet engines located directly on the fuselage, and above the wings. It also has one fuel tank at each wingtip.

Figure 4.7: *Perspective view of a Beechcraft produced from a three-dimensional CAD model [210].*
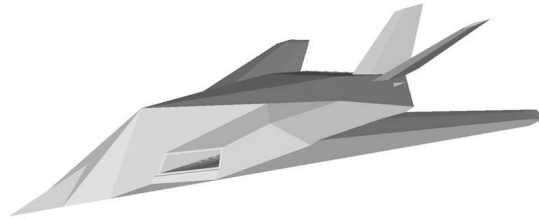
Figure 4.8: *Perspective view of an F117 produced from a three-dimensional CAD model [210].*

Figure 4.9: *Perspective view of an F16 produced from a three-dimensional CAD model [210].*
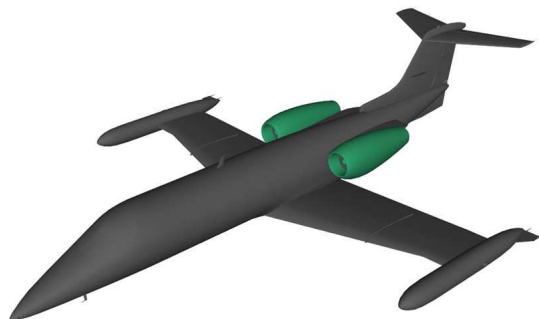
Figure 4.10: *Perspective view of a Learjet produced from a three-dimensional CAD model [210].*

4.4 Scattering regions for the frequency bands of interest

We saw in Section 3.6 that the scattering mechanisms, and thus the scattering regions, are functions of the ratio λ/D, where $\lambda = c/f$ is the illuminating wavelength, and D the characteristic dimension of the airplane. Table 4.1 gives, for each frequency band of interest, the ratio λ/D for the two frequencies at the edges of the band for $D = 15$ m, which is the characteristic dimension of all airplanes of interest. This allows one to determine the scattering region for each of the bands. These are shown at the bottom of the columns. Note that the scattering region for FB2 is mostly optical.

Freq. band	FB1		FB2		FB3		FB4	
Freq. limits	$F1_{Min}$ 20MHz	$F1_{Max}$ 80MHz	$F2_{Min}$ 190MHz	$F2_{Max}$ 250MHz	$F3_{Min}$ 450MHz	$F3_{Max}$ 550MHz	$F4_{Min}$ 1.2GHz	$F4_{Max}$ 1.3GHz
λ (m)	15	3.75	1.5	1.2	0.66	0.55	0.25 m	0.2
λ/D	1	0.25	0.1	0.08	0.044	0.0367	0.0167	0.0133
Scatt. region	Resonance		Resonance/optical		Optical		Optical	

Table 4.1: *Determination of the scattering region for each frequency band, according to the ratio λ/D, with $D = 15$ m.*

We saw in Section 3.6 that the geometric parameter that most affects the scattering in each of the three scattering regions are the following:

- Rayleigh region: volume,

- Resonance region: volume and shape,

- Optical region: shape.

Since the scattering mechanisms at work for FB1 are those of the resonance region, we conclude that the measured values of both the BS-CRCS and the BS-RCS for this band will be more a function of the volume than of the shape. Since the volumes of the four airplanes are similar, one cannot expect high classification rates for the first frequency band. Since the scattering mechanisms at work for FB2, FB3, and FB4 are those of the optical region, we conclude that the measured values of both the BS-CRCS and the BS-RCS will be more a function of the shape than of the volume for these three bands.

4.5 Classes of airplanes

The conclusion just reached above indicates that it makes a lot of sense to define as many classes of airplanes as there are significantly different shapes of airplanes of interest. As a result, the four airplanes of interest, here Beechcraft, F117, F16, and Learjet, certainly deserve their own individual class.

4.6   Illustration of the bistatic complex and real RCS of targets

We now show examples of the squared magnitude and phase of the bistatic complex radar cross-section (BS-CRCS) $\sqrt{\sigma}$ for the different targets of interest. The squared magnitude of the BS-CRCS is equal to the bistatic radar cross-section (BS-RCS), as discussed in Chapter 3. We illustrate the variation of both the squared magnitude and the phase of the BS-CRCS as a function of the different parameters that have an influence on the BS-CRCS, *i.e.* the bistatic angle, the frequency, the polarizations of both the transmitter and the receiver, and the orientation (in both azimuth and elevation) of the target. We also show how the squared magnitude and phase of the BS-CRCS vary according to the type of target. We will see that the four airplanes of interest exhibit differences.

As indicated in Section 4.3, we acquired the BS-CRCS $\sqrt{\sigma}$ for four airplanes, over four different frequency bands, four polarization pairs, and for bistatic angles varying from 6° to 160°, all this for three different azimuth angles θ and three different elevation angles ϕ. For confidentiality reasons, the maximum value of the squared magnitude of the BS-CRCS is not reported, but the graphs are normalized according to a common reference for all airplanes, so that it is possible to compare the squared magnitudes and the phase of the BS-CRCS of different airplanes. The squared magnitudes are displayed on a logarithmic scale, and the phase is always reduced to the interval $[0, 2\pi[$.

For conciseness, we do not show the total amount of data acquired. We simply show the variations of both the squared magnitude and the phase of the BS-RCS for one parameter at a time. Figure 4.11 is used as the reference for the comparison of the variation of the BS-CRCS as a function of the different parameters. The figure shows the squared magnitude and the phase of the BS-CRCS of a Beechcraft at an azimuth angle $\theta = 0°$ and an elevation angle $\phi = -10°$. We show the values of the BS-CRCS for FB2, *i.e.* for frequencies ranging from 190 MHz to 250 MHz, for the HH polarization pair, and for bistatic angles ranging from 6° to 160°.

4.6.1   Variation of the bistatic complex RCS as a function of the bistatic angle

Figure. 4.12 shows the variation of both the squared magnitude (in dBs) and the phase of the BS-CRCS as a function of the bistatic angle β for each of the four airplanes of interest at the center frequency of FB1, *i.e.* 50 MHz. Figures 4.13, 4.14, and 4.15 show the corresponding graphs for the three other frequency bands, *i.e.* FB2 to FB4.

For a particular frequency, the variations of both the squared magnitude and the phase of the BS-CRCS as a function of β do not seem to be particular. Therefore, we do not *a priori* favor any bistatic angle for the recognition of the four airplanes of interest.
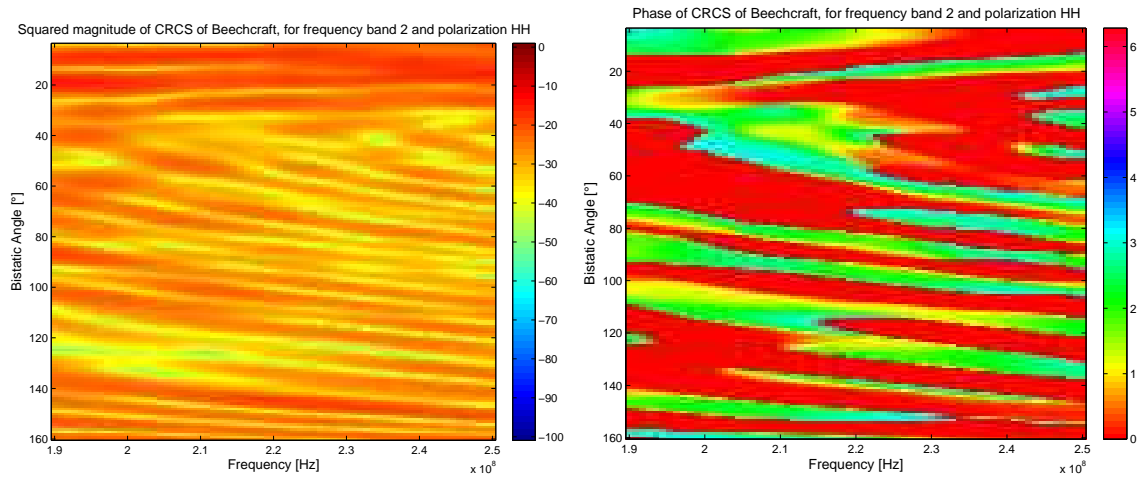
Figure 4.11: *Squared magnitude (left) and phase (right) of the BS-CRCSs of a Beechcraft as a function of the frequency f and bistatic angle β, for FB2 ($f \in [190; 250]$ MHz), and for the following fixed parameters: $Pol = HH$, $\theta = 0°$, and $\phi = -10°$.*
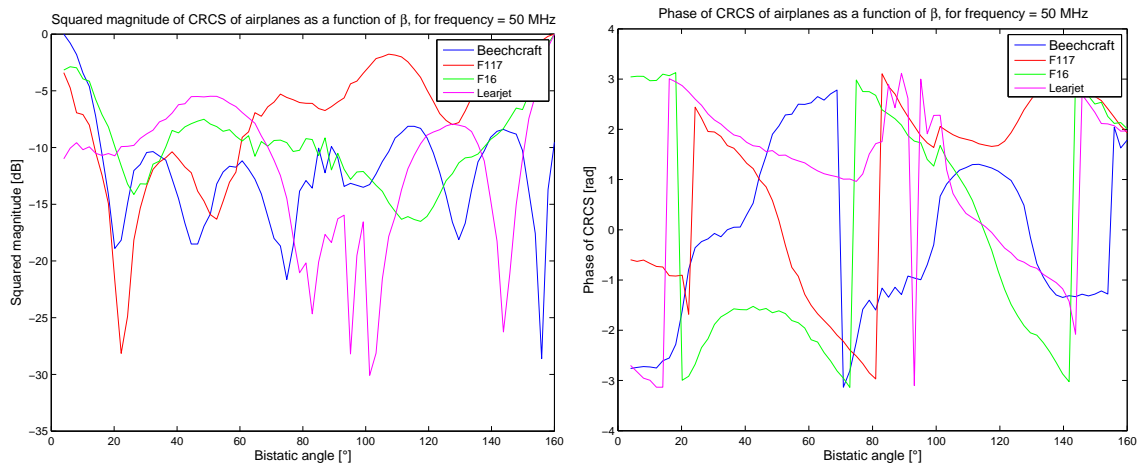
Figure 4.12: *Squared magnitude (left) and phase (right) of the BS-CRCSs as a function of β for each of the four airplanes of interest, for the following fixed parameters: $f = 50$ MHz (in FB1), $Pol = HH$, $\theta = 0°$, and $\phi = -10°$.*
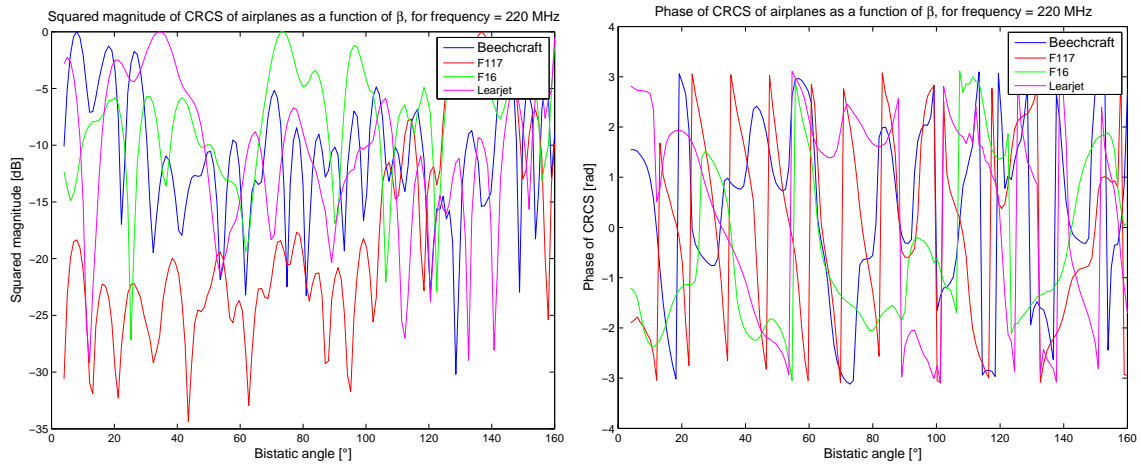
Figure 4.13: *Squared magnitude (left) and phase (right) of the BS-CRCSs as a function of β for each of the four airplanes of interest, for the following fixed parameters: $f = 220$ MHz (in FB2), $Pol = HH$, $\theta = 0°$, and $\phi = -10°$.*
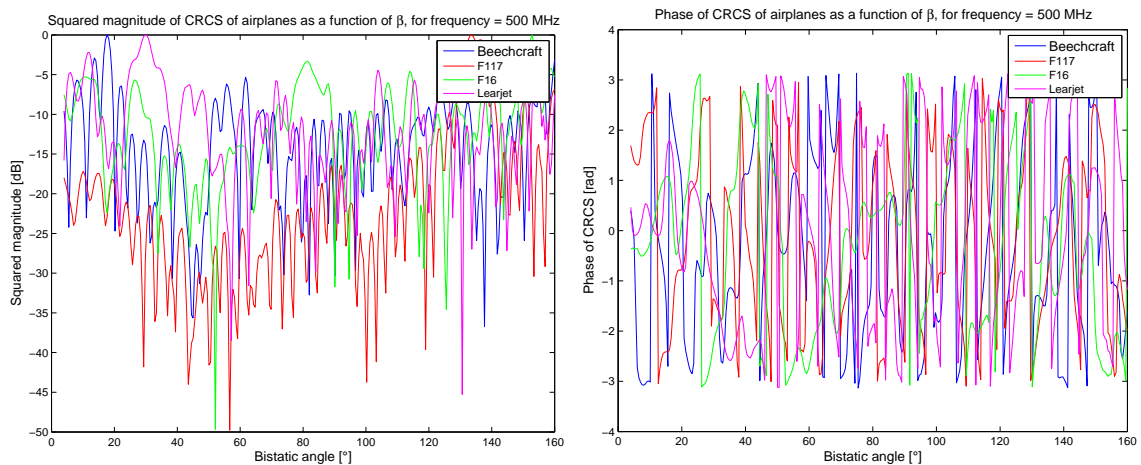
Figure 4.14: *Squared magnitude (left) and phase (right) of the BS-CRCSs as a function of β for each of the four airplanes of interest, for the following fixed parameters: $f = 500$ MHz (in FB3), $Pol = HH$, $\theta = 0°$, and $\phi = -10°$.*
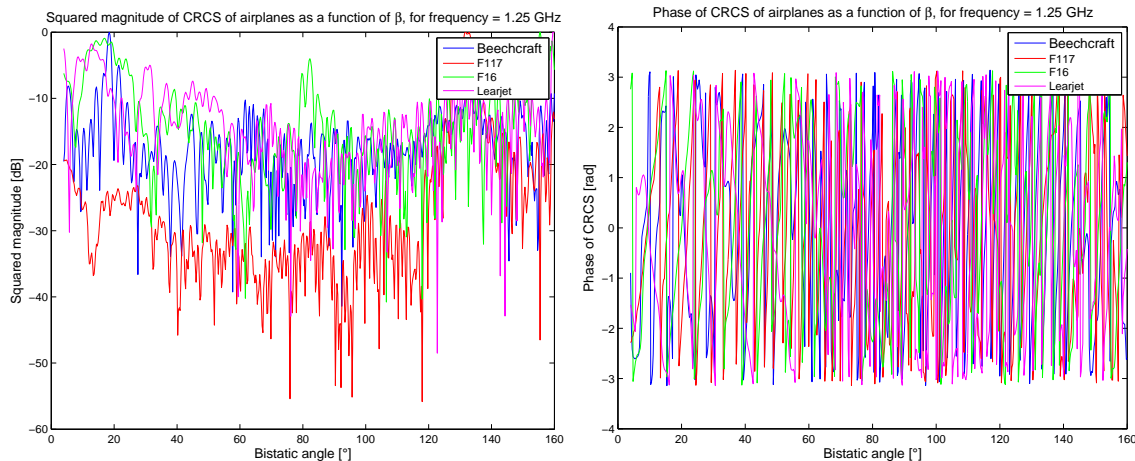
Figure 4.15: *Squared magnitude (left) and phase (right) of the BS-CRCSs as a function of β for each of the four airplanes of interest, for the following fixed parameters: $f = 1.25$ GHz (in FB4), $Pol = HH$, $\theta = 0°$, and $\phi = -10°$.*

4.6.2   Variation of the bistatic complex RCS as a function of the frequency

We illustrate here the variations of the squared magnitude and the phase of the BS-CRCS as a function of the frequency, for the four airplanes of interest. Figure 4.11 already illustrated the variations of both the squared magnitude and the phase of the BS-CRCS of the Beechcraft as a function of frequency, for FB2. Figures 4.16, 4.17, and 4.18 illustrate the variations of both the squared magnitude and the phase of the BS-CRCS of the same Beechcraft for the three other frequency bands. Although we do not show the variations of both the squared magnitude and the phase of the BS-CRCS for the three other airplanes (F16, F117, and Learjet), their variations are similar, and the conclusions drawn for the Beechcraft apply to the three other airplanes.

More specifically, it can be seen in Figs. 4.11, 4.16, 4.17, and 4.18 that the number of oscillations of the phase of the BS-CRCS as a function of the bistatic angle (over the range $\beta = [6°; 160°]$), at a particular frequency, is approximately equal to the ratio of the characteristic dimension $D = 15$ m of the target to the wavelength λ. For example, at a frequency of 220 MHz, $\lambda \approx 1.36$ m, and thus $D/\lambda = 11$, which is approximately the number of oscillations of the phase of the BS-CRCS for each of the four types of targets, as can be seen in Fig. 4.11. Similar observations can be made for the other frequency bands, *i.e.* at 50 MHz in Fig. 4.16, at 500 MHz in Fig. 4.17, and at 1.25 GHz in Fig. 4.18.

We illustrate in Figs. 4.19, 4.20, 4.21, and 4.22 the squared magnitude and the phase of the BS-CRCS of the four targets as a function of frequency, for a bistatic angle $\beta = 20°$, for each of the four frequency bands. The number of oscillations of the squared magnitude of the BS-CRCS of the four airplanes increases as the frequency increases. This is explained by the fact that the scattering mechanisms move from the resonance region for the first frequency band, to the optical region for the fourth frequency band. Similar variations of the squared magnitude of the
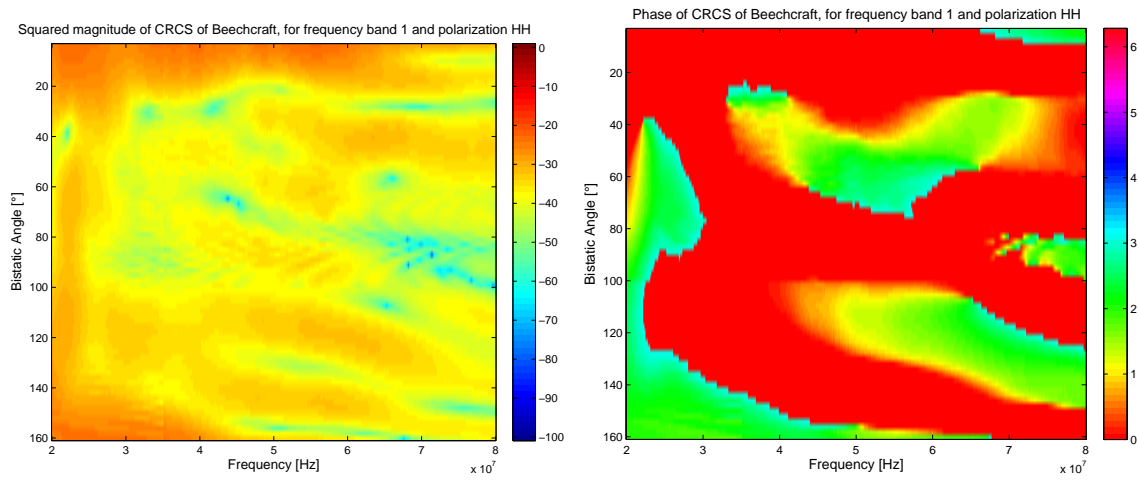
Figure 4.16: *Squared magnitude (left) and phase (right) of the BS-CRCSs of a Beechcraft as a function of frequency f and bistatic angle β, for FB1 ($f \in [20; 80]$ MHz), and for the following fixed parameters: $Pol = HH$, $\theta = 0°$, and $\phi = -10°$.*
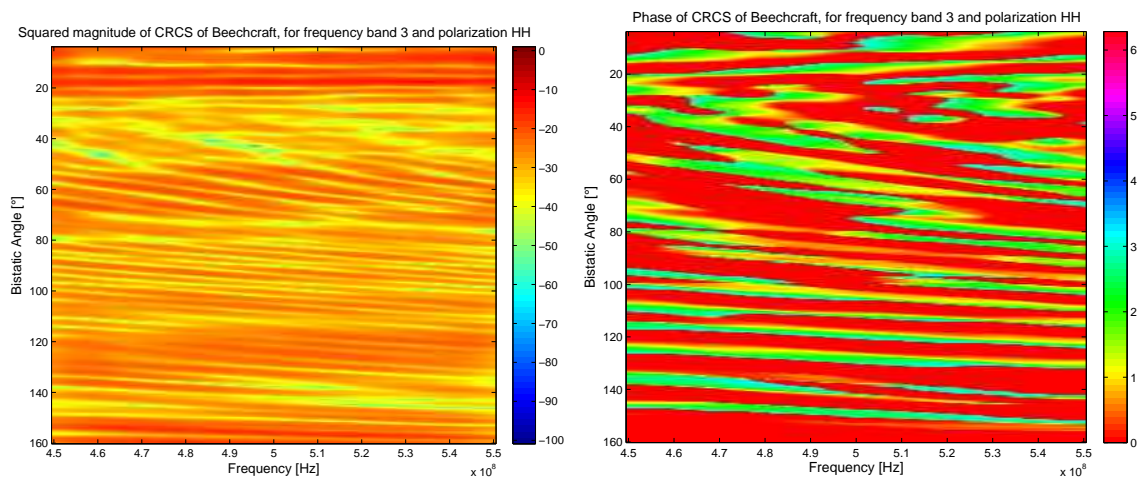
Figure 4.17: *Squared magnitude (left) and phase (right) of the BS-CRCSs of a Beechcraft as a function of frequency f and bistatic angle β, for FB3 ($f \in [450; 550]$ MHz), and for the following fixed parameters: $Pol = HH$, $\theta = 0°$, and $\phi = -10°$.*
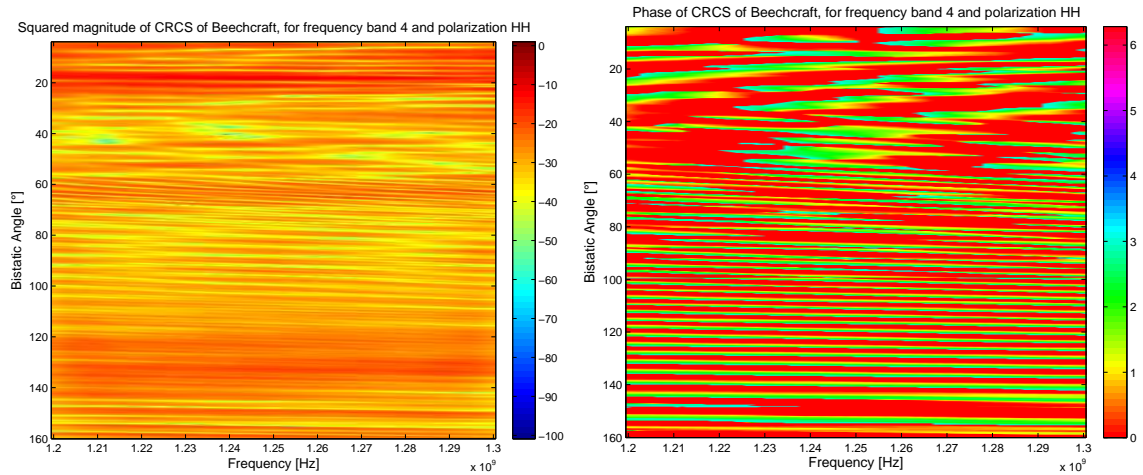
Figure 4.18: *Squared magnitude (left) and phase (right) of the BS-CRCSs of a Beechcraft as a function of frequency f and bistatic angle β, for FB4 ($f \in [1.2; 1.30]$ GHz), and for the following fixed parameters: $Pol = HH$, $\theta = 0°$, and $\phi = -10°$.*

BS-CRCS occur at the other available bistatic angles, but we do not discuss them here.
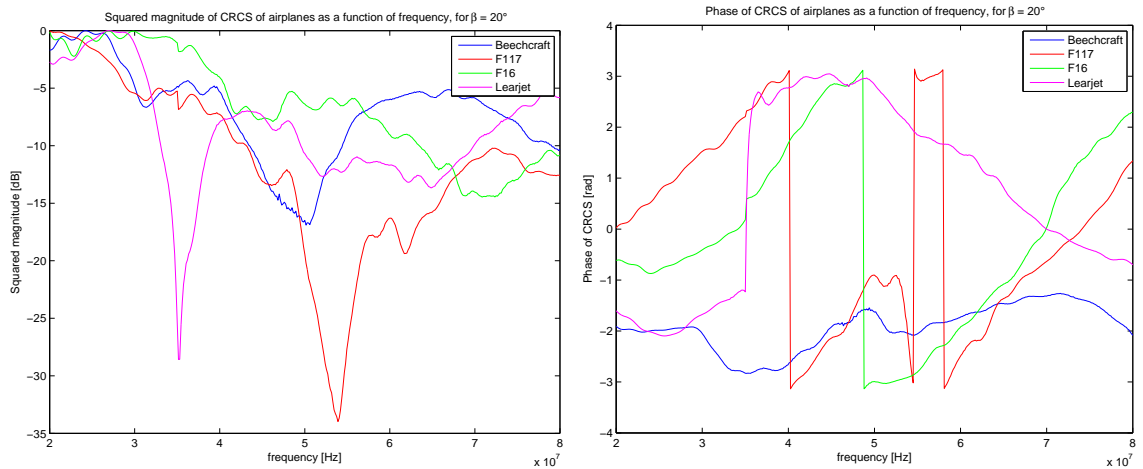
Figure 4.19: *Squared magnitude (left) and phase (right) of the BS-CRCSs as a function of the frequency f for each of the four airplanes of interest, for FB1 ($f \in [20; 80]$ MHz), and for the following fixed parameters: $\beta = 20°$, $Pol = HH$, $\theta = 0°$, and $\phi = -10°$.*

For a particular bistatic angle, the variations of both the squared magnitude and the phase of the BS-CRCS as a function of the frequency f do not seem to be particular. Therefore, we do not *a priori* favor any frequency for the recognition of the four airplanes of interest.
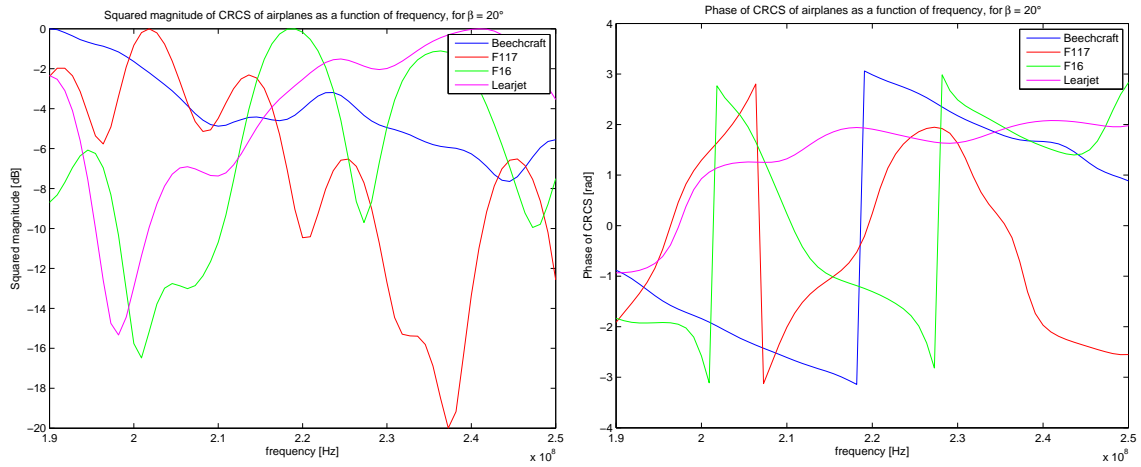
Figure 4.20: *Squared magnitude (left) and phase (right) of the BS-CRCSs as a function of the frequency f for each of the four airplanes of interest, for FB2 (f ∈ [190; 250] MHz), and for the following fixed parameters: $\beta = 20°$, $Pol = HH$, $\theta = 0°$, and $\phi = -10°$.*
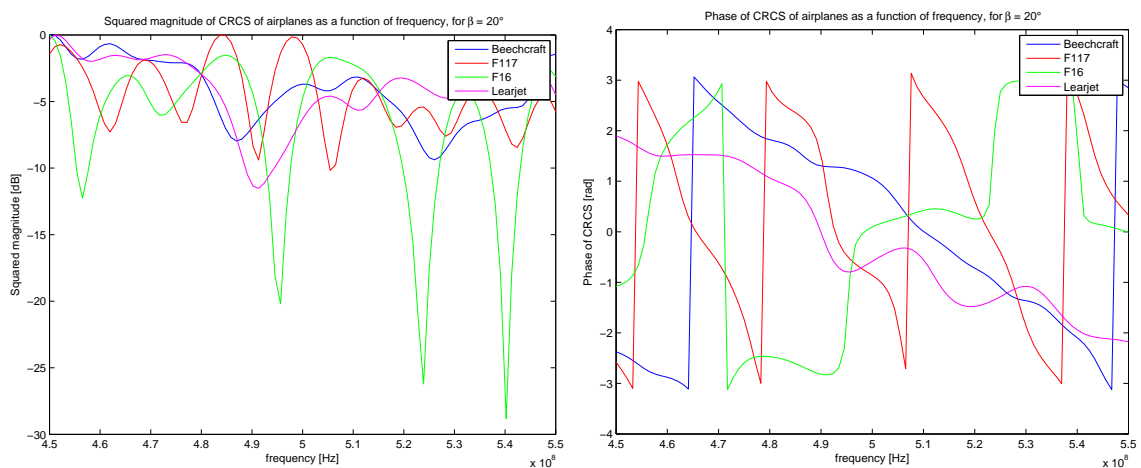
Figure 4.21: *Squared magnitude (left) and phase (right) of the BS-CRCSs as a function of the frequency f for each of the four airplanes of interest, for FB3 (f ∈ [450; 550] MHz), and for the following fixed parameters: $\beta = 20°$, $Pol = HH$, $\theta = 0°$, and $\phi = -10°$.*
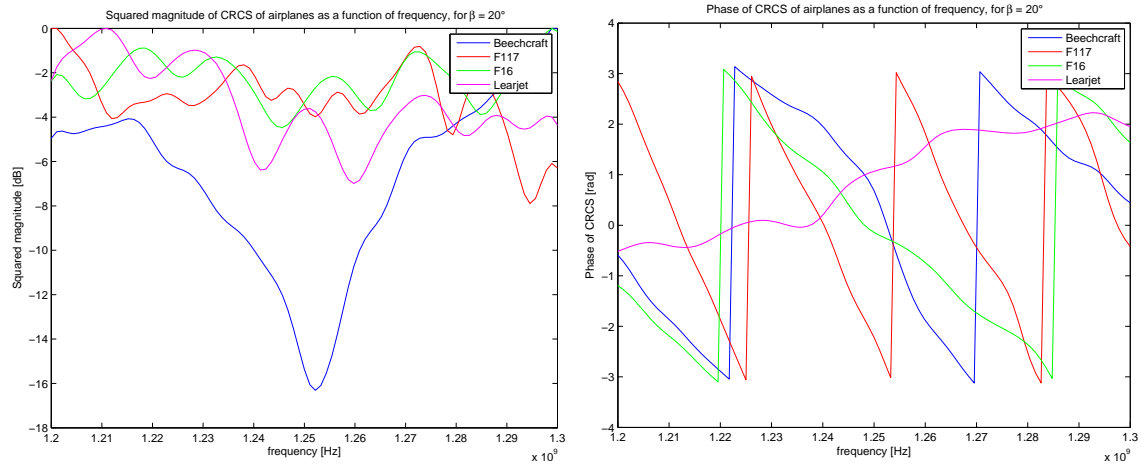
Figure 4.22: *Squared magnitude (left) and phase (right) of the BS-CRCSs as a function of the frequency f for each of the four airplanes of interest, for FB4 (f ∈ [1.2; 1.3] GHz), and for the following fixed parameters: β = 20°, Pol = HH, θ = 0°, and φ = −10°.*

4.6.3 Variation of the bistatic complex RCS as a function of the polarization

We illustrate here the variations of both the squared magnitude and the phase of the BS-CRCS as a function of the polarization, for the Beechcraft, for each polarization pair, *i.e.* HH, HV, VH, and VV, in Figs. 4.11, 4.23, 4.24, and 4.25, respectively. One must notice, as expected, that both the squared magnitude and the phase of the BS-CRCS obtained for the cross-polarizations VH and HV are not equal, since we are in a bistatic configuration, while they would be equal in a monostatic configuration.

Although we do not show the variations of both the squared magnitude and the phase of the BS-CRCS for the three other airplanes (F16, F117, and Learjet), their variations are similar, and the conclusions drawn for the Beechcraft apply to the three other airplanes.

Since the variations of the squared magnitude and the phase of the BS-CRCS are similar from one polarization to the other, we do not *a priori* favor any particular polarization for the recognition of the four airplanes of interest.

4.6.4 Variation of the bistatic complex RCS as a function of the orientation

We illustrate here the variations of both the squared magnitude and the phase of the BS-CRCS as a function of the orientation of the airplane, for the Beechcraft. We consider different orientation pairs $(θ, φ)$: $(0°, −10°), (45°, −10°), (90°, −10°), (0°, −5°)$, and $(0°, 0°)$ in Figs. 4.11, 4.26, 4.27, 4.28, and 4.29, respectively.

Since the variations of the squared magnitude and the phase of the BS-CRCS are similar from one orientation pair to the other, we do not *a priori* favor any particular
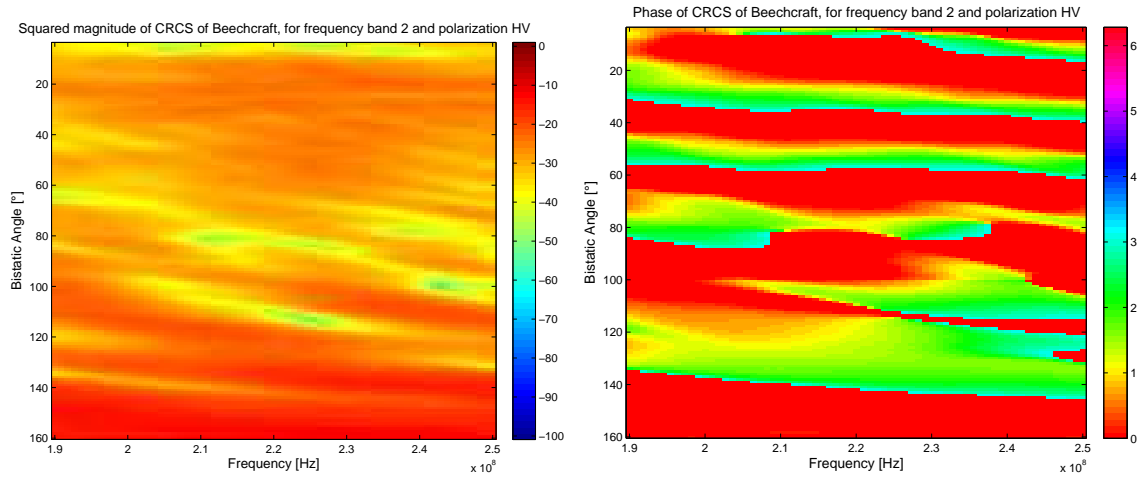
Figure 4.23: *Squared magnitude (left) and phase (right) of the BS-CRCSs of a Beechcraft as a function of the frequency f and bistatic angle β, for HV polarization, and for the following fixed parameters: f ∈ [190; 250] MHz, θ = 0°, and φ = −10°.*

Figure 4.24: *Squared magnitude (left) and phase (right) of the BS-CRCSs of a Beechcraft as a function of the frequency f and bistatic angle β, for VH polarization, and for the following fixed parameters: f ∈ [190; 250] MHz, θ = 0°, and φ = −10°.*

Figure 4.25: *Squared magnitude (left) and phase (right) of the BS-CRCSs of a Beechcraft as a function of the frequency f and bistatic angle β, for VV polarization, and for the following fixed parameters: $f \in [190; 250]$ MHz, $\theta = 0°$, and $\phi = -10°$.*

orientation for the recognition of the four airplanes of interest.
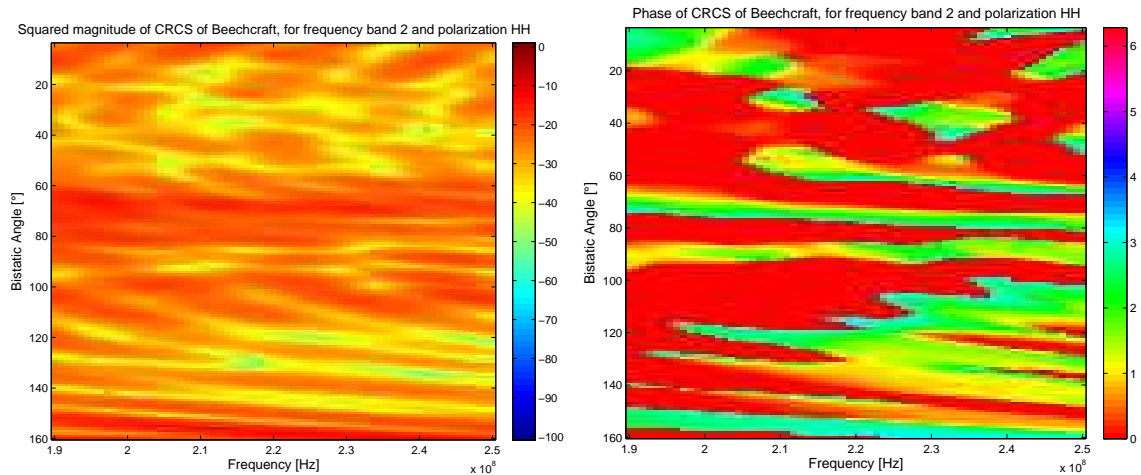
Figure 4.26: *Squared magnitude (left) and phase (right) of the BS-CRCSs of a Beechcraft as a function of the frequency f and bistatic angle β, for $\theta = 45°$ and $\phi = -10°$, and for the following fixed parameters: $f \in [190; 250]$ MHz, and $Pol = HH$.*

4.6.5 Conclusions about the variations of the bistatic complex RCS as a function of the bistatic angle, frequency, polarizations, and orientation

The above sections confirmed, based on real data, that both the squared magnitude and the phase of the BS-CRCS vary with the bistatic angle, the frequency, the polarizations of the Tx and the Rx, the azimuth angle, and the elevation angle. In
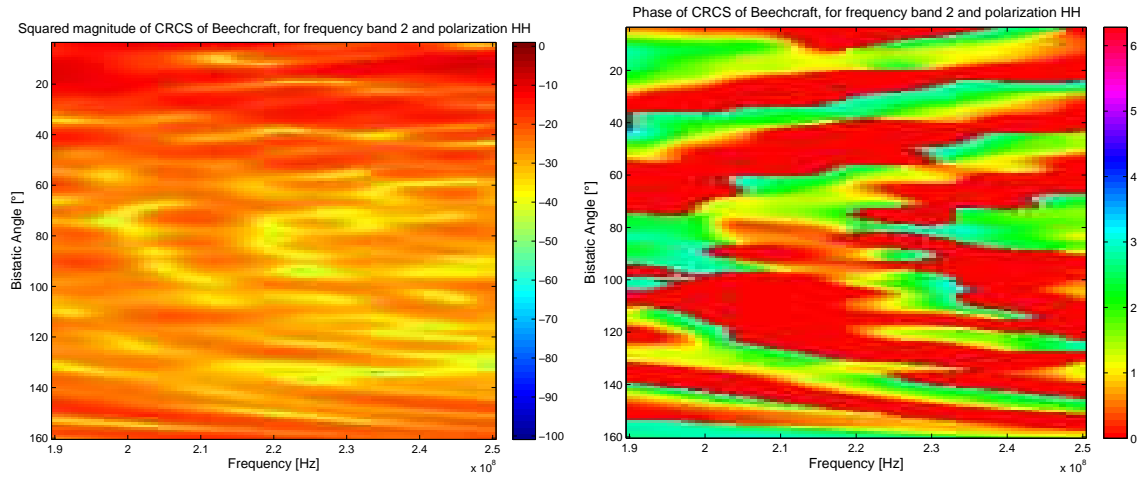
Figure 4.27: *Squared magnitude (left) and phase (right) of the BS-CRCSs of a Beechcraft as a function of the frequency f and bistatic angle β, for $\theta = 90°$ and $\phi = -10°$, and for the following fixed parameters: $f \in [190; 250]$ MHz, and $Pol = HH$.*
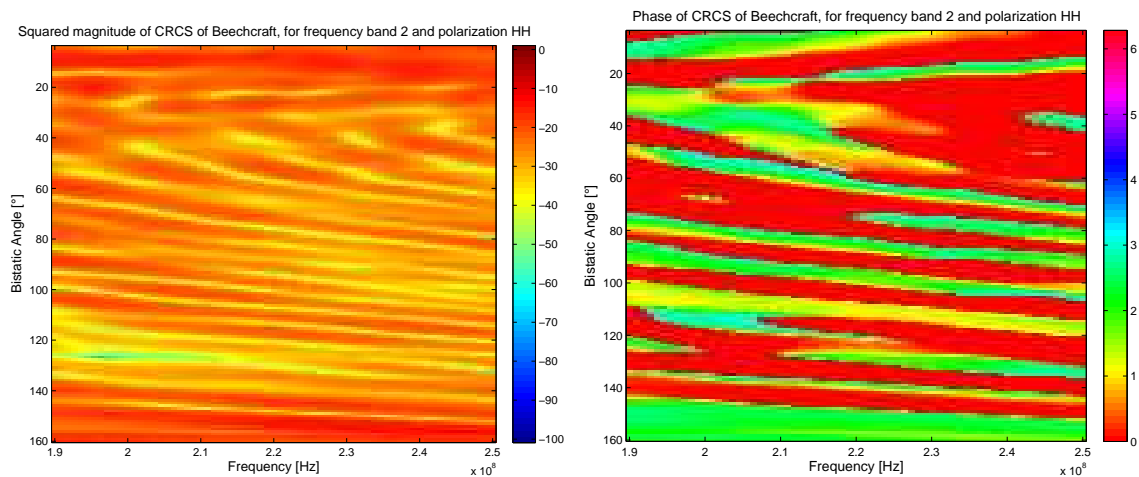
Figure 4.28: *Squared magnitude (left) and phase (right) of the BS-CRCSs of a Beechcraft as a function of the frequency f and bistatic angle β, for $\theta = 0°$ and $\phi = -5°$, and for the following fixed parameters: $f \in [190; 250]$ MHz, and $Pol = HH$.*
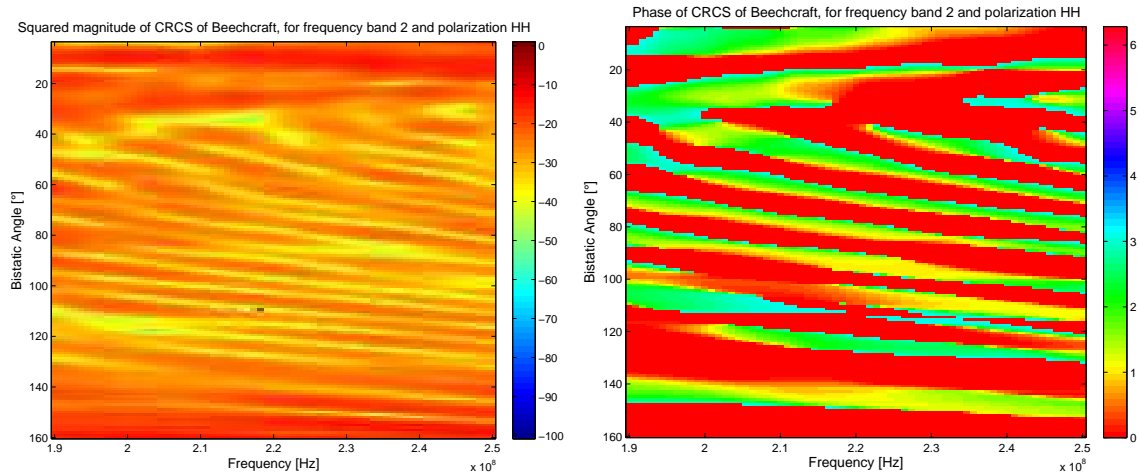
Figure 4.29: *Squared magnitude (left) and phase (right) of the BS-CRCSs of a Beechcraft as a function of the frequency f and bistatic angle β, for θ = 0° and φ = 0°, and for the following fixed parameters: f ∈ [190; 250] MHz, and Pol = HH.*

particular, we illustrated the fact that the scattering mechanisms occur in different scattering regions according to the frequency band. We also illustrated the fact that the oscillation rate of both the squared magnitude and the phase of the BS-CRCS vary according to the ratio D/λ. This will influence the classification rate. Indeed, if both the squared magnitude and the phase of the BS-CRCS are similar for each of the four airplanes of interest (Beechcraft, F117, F16, and Learjet), the recognition rate is expected to be smaller than if they vary significantly.

According to the examples shown, we cannot *a priori* consider that a particular bistatic angle, a particular frequency band, a particular polarization, or a particular orientation would be preferable for the recognition of the four airplanes of interest. This observation will be confirmed by the achieved classification rates (Chapter 6).

4.7 Conclusion

The first step of each of the first two automatic target recognition (ATR) systems is the extraction of either the bistatic complex radar cross-section (BS-CRCS) or the bistatic radar cross-section (BS-RCS) of targets. In this chapter, we presented the computation of both the BS-CRCS and the BS-RCS of a generic object from the transmitted electric field and the received electric field, the latter being the raw data used at input of each of the first two ATR systems.

We presented the experimental setup used to acquire the raw data in an anechoic chamber. In particular, we explained the reasons for using scale models of the airplanes of interest. We also presented the geometry of the setup, and the parameters used for the acquisition of raw data, which are four frequency bands ranging from 20 MHz to 1.3 GHz, the four polarization pairs HH, HV, VH, and VV, the bistatic angles of interest, *i.e.* from 6° to 160°, the azimuth angle that is equal to either 0°, 45°, or 90°, and the elevation angle that is equal to either 0°, 5°, or −10°. We also described the

four airplanes of interest, *i.e.* a Beechcraft, an F117 stealth fighter, an F16 fighter, and a Learjet.

We determined the scattering region which the scattering mechanisms occur in, for each frequency band. We also determined that the scattering is more influenced by the shapes of the airplanes than by their volumes, except for the first frequency band. This made us consider each type of airplane as one class.

We illustrated the variations of both the squared magnitude and the phase of the BS-CRCS of the four airplanes of interest as a function of the bistatic angle, the frequency, the polarization, the azimuth angle, and the elevation angle. According to the examples shown, it seems that no particular bistatic angle, no particular frequency, no particular polarization, no particular azimuth angle, and no particular elevation angle seem to be *a priori* preferable for the recognition of the four airplanes of interest.

Chapter 5

Construction of radar images

Contents

Section 5.1 states the motivation for the construction of radar images of the airplanes of interest. Section 5.2 reviews some fundamental principles used in tomographic imaging. Sections 5.3 and 5.4 describe the principles of radar imaging for a monostatic configuration and a bistatic configuration, respectively. Section 5.5 presents the practical construction of radar images of objects from the bistatic complex radar cross-sections (BS-CRCSs) of these objects. Section 5.6 shows examples of constructed radar images of the airplanes of interest. Section 5.7 concludes.

5.1 Motivation for the construction of radar images of targets

Our first automatic target recognition system (ATR), the block diagram of which is shown in Fig. 5.1, recognizes targets by using their radar images. We discuss, in this

chapter, the second stage of this ATR system, *i.e.* the construction of the radar images of targets from the bistatic complex radar cross-section (BS-CRCS) of these targets.
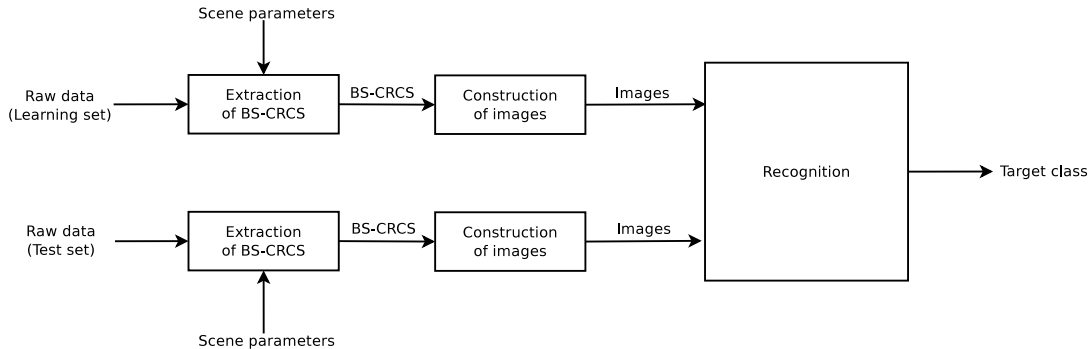
Figure 5.1: *Block diagram of our ATR system using radar images of targets.*

5.2   Review of tomographic imaging

We derive the expression for the radar image of an object in terms of the complex radar cross-sections of this object by following the principles of tomographic imaging. In this section, we review three fundamental principles that are used in tomographic imaging, which are the Radon Transform (RT), the Fourier Transform (FT), and the projection-slice theorem (PST). We also review the rotation property of the FT.

5.2.1   The Radon Transform

Figure 5.2 illustrates the Radon Transform (RT) [24,97,138,139,167]. Let us consider an object characterized by its two-dimensional (2D) density distribution $f(x,y)$. We denote the projection of $f(x,y)$ on a line x' at orientation ϕ by $p_\phi(x')$. We have

$$p_\phi(x') = \int_{l(x')} f(x,y)\, dy', \tag{5.1}$$

where $l(x')$ is any line orthogonal to line x'. $p_\phi(x')$ is also called a line integral [97].

The RT of $f(x,y)$, denoted by $\mathcal{R}f(x',\phi)$, is defined as the projection of $f(x,y)$ for any orientation ϕ. We define it mathematically as [24,97,138,139,167]

$$\mathcal{R}f(x',\phi) = \int_{-\infty}^{+\infty} \int_{-\infty}^{+\infty} f(x,y)\delta(x\cos\phi + y\sin\phi - x')\, dxdy, \tag{5.2}$$

where δ is the Dirac delta function, and the coordinates x, y, x', and ϕ are defined in Fig. 5.2.

5.2.2   The two-dimensional Fourier Transform and its rotation property

We define the one-dimensional (1D) FT $F(\omega)$ of a function $f(x)$ as [24,142]

$$F(\omega) = \hat{f}(\omega) = \int_{-\infty}^{+\infty} f(x)e^{-j\omega x}\, dx, \tag{5.3}$$
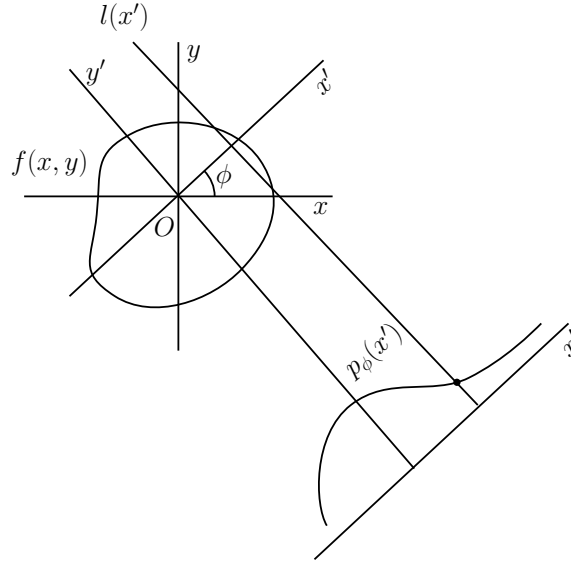
Figure 5.2: *Illustration of the Radon Transform. The projection of $f(x,y)$ on a line x' at orientation ϕ is denoted by $p_\phi(x')$.*

where ω is the pulsation. We define the inverse FT as

$$f(x) = \frac{1}{2\pi} \int_{-\infty}^{+\infty} F(\omega) e^{j\omega x} \, d\omega. \tag{5.4}$$

We similarly define the 2D FT $F(\omega_x, \omega_y)$ of a function $f(x,y)$ as [24, 142]

$$F(\omega_x, \omega_y) = \hat{f}(\omega_x, \omega_y) = \int_{-\infty}^{+\infty} \int_{-\infty}^{+\infty} f(x,y) e^{-j\pi(\omega_x x + \omega_y y)} \, dxdy. \tag{5.5}$$

The 2D inverse FT is defined as

$$f(x,y) = \frac{1}{(2\pi)^2} \int_{-\infty}^{+\infty} \int_{-\infty}^{+\infty} F(\omega_x, \omega_y) e^{-j\pi(\omega_x x + \omega_y y)} \, d\omega_x d\omega_y. \tag{5.6}$$

In polar coordinates, the function $f(x,y)$ is expressed as $f_p(r, \theta)$, where the subscript p stands for "polar", and r and θ are the polar coordinates, with $x = r\cos\theta$ and $y = r\sin\theta$, as shown in Fig. 5.3. The 2D FT $F_p(\rho, \phi)$ of a function $f_p(r, \theta)$ is defined as

$$F_p(\rho, \phi) = \int_0^{+\infty} \int_0^{2\pi} f_p(r, \theta) e^{-j2\pi\rho r \cos(\phi - \theta)} r \, d\theta dr, \tag{5.7}$$

where $\omega_x = \rho\cos\phi$, and $\omega_y = \rho\sin\phi$.

Observe that we use two possible notations for the FT of a function f, *i.e.* either F or $\hat{f}$ (Fig. 5.3). Our preferred notation is F, but it is sometimes easier to use $\hat{f}$.

The rotation theorem of the 2D FT, defined in [24], states that if a function $f_p(r, \theta)$ undergoes a rotation of angle α, so does its 2D FT, as illustrated in Fig. 5.4. Mathematically, we express it as

$$f_p(r, \theta - \alpha) \overset{2DFT}{\Longleftrightarrow} F_p(\rho, \phi - \alpha). \tag{5.8}$$
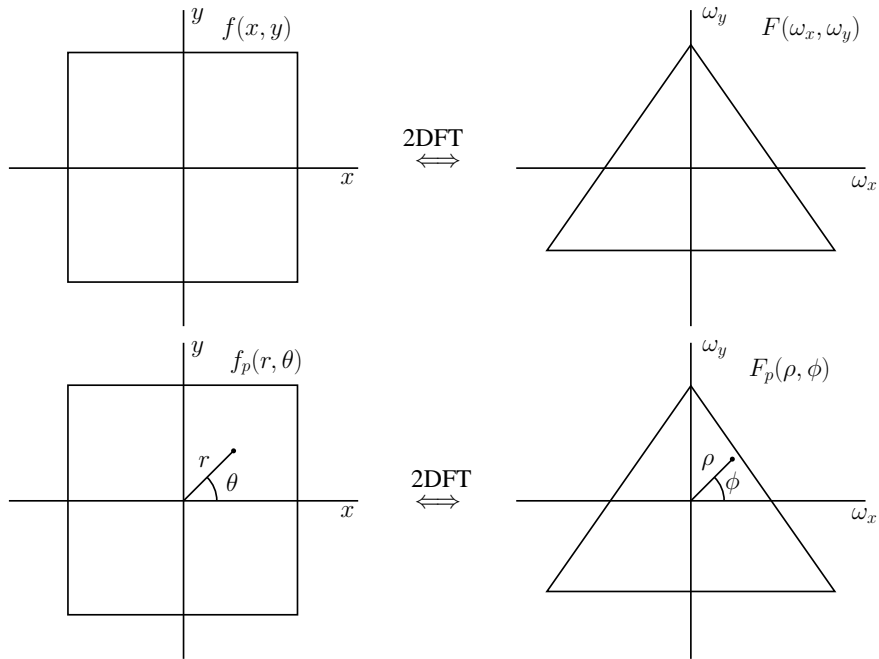
Figure 5.3: *Illustration of the correspondence between the functions $f(x,y)$ and its polar form $f_p(r,\theta)$, and their respective Fourier Transforms $F(\omega_x,\omega_y)$ and $F_p(\rho,\phi)$.*

In Cartesian coordinates, this gives

$$f(x\cos\alpha - y\sin\alpha, x\sin\alpha + y\cos\alpha) \overset{2DFT}{\Longleftrightarrow} F(\omega_x\cos\alpha - \omega_y\sin\alpha, \omega_x\sin\alpha + \omega_y\cos\alpha). \quad (5.9)$$

The rotation property is used in [24] to derive the projection-slice theorem.

5.2.3 The projection-slice theorem

Figure 5.5 illustrates the projection-slice theorem (PST). According to the PST, the 1D FT of the projection of $f(x,y)$ along lines $l(x')$ orthogonal to some line x' at orientation ϕ is equal to the slice through the 2D FT $F(\omega_x,\omega_y)$ in the same direction ϕ [24].

Mathematically, the projection of the function $f(x,y)$ in the direction ϕ is usually denoted by $p_\phi(x')$. The 1D FT of $p_\phi(x')$ is denoted by $P_\phi(\omega')$. According to the PST, $P_\phi(\omega')$ is equal to the slice through the 2D FT of $f(x,y)$ in the direction ϕ, where $F(\omega',\phi)$ is the slice of $F(\omega_x,\omega_y)$ at angle ϕ as a function of ω' (Fig. 5.5), *i.e.* $F_p(\omega',\phi)$.
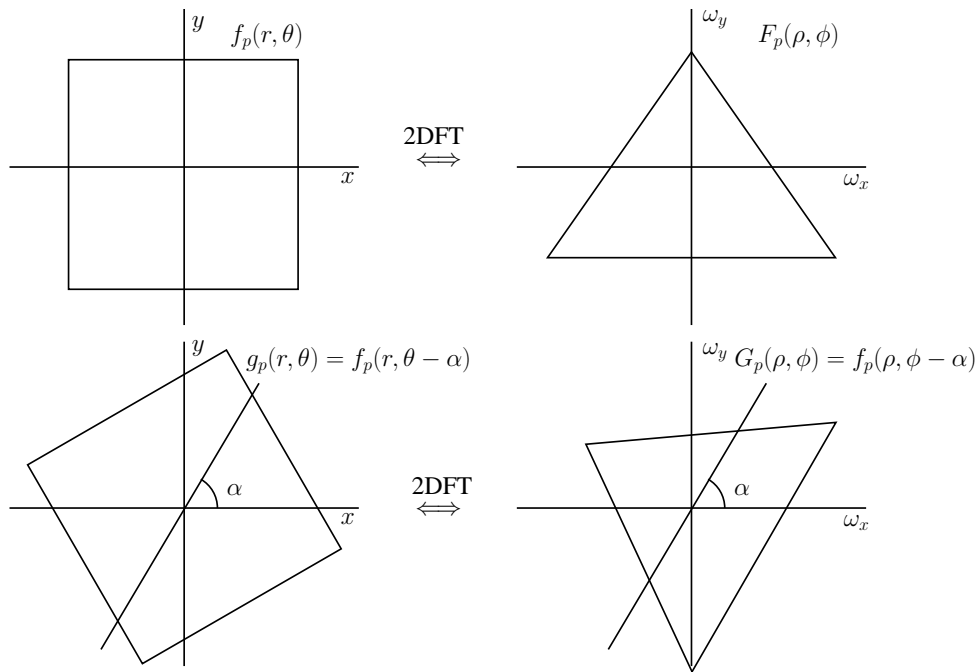
Figure 5.4: *Illustration of the rotation theorem of the 2D Fourier Transform. If a function $f_p(r, \theta)$ is rotated by an angle α, then being denoted by $g_p(r, \theta)$, so does its Fourier Transform $F_p(\rho, \phi)$, then being denoted by $G_p(\rho, \phi)$.*
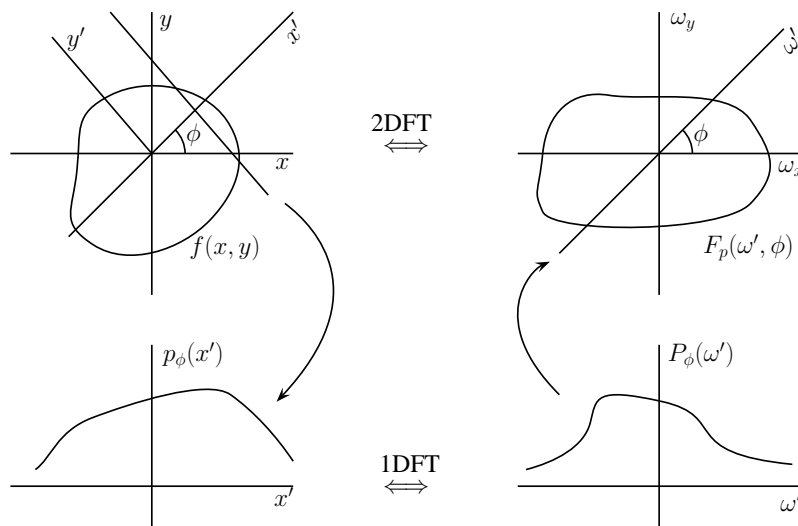
Figure 5.5: *Illustration of the projection-slice theorem. The 1D FT of the projection $p_\phi(x')$ of $f(x, y)$ is equal to the slice of the 2D FT $F_p(\omega', \phi)$ of $f(x, y)$ at orientation ϕ.*

5.3   Principles of monostatic radar imaging

In this section, we present the principles of radar imaging for a monostatic (MS) configuration. We first describe the MS configuration. We then derive the expression of the complex radar cross-section (CRCS) density of an object, *i.e.* the radar image of an object, as a two-dimensional (2D) inverse Fourier Transform (FT) of the monostatic complex radar cross-section (MS-CRCS) of this object.

5.3.1   Monostatic (MS) configuration

Figure 5.6 shows the MS configuration that we consider. Let us consider a generic object that is illuminated by a transmitter. Since we are in an MS configuration, the transmitter and the receiver are co-located, and simply called the radar.

We choose a reference point O located on or near the object. The line-of-sight of the radar, *i.e.* the line between the radar and the reference point O is the x-axis. The angle ϕ is defined as the angle between the line-of-sight of the radar and the x-axis. Here, $\phi = 0°$. The perpendicular to the x-axis at O is the y-axis.

We assume that the object is characterized by its 2D isotropic complex radar cross-section (CRCS) density, denoted by $\sqrt{\sigma}_0(x, y)$ [24]. We express the location of any point P of the object in terms of its Cartesian coordinates (x, y). We also assume that the reference point O is located at a distance r_0 from the radar, in the far-field of the radar.
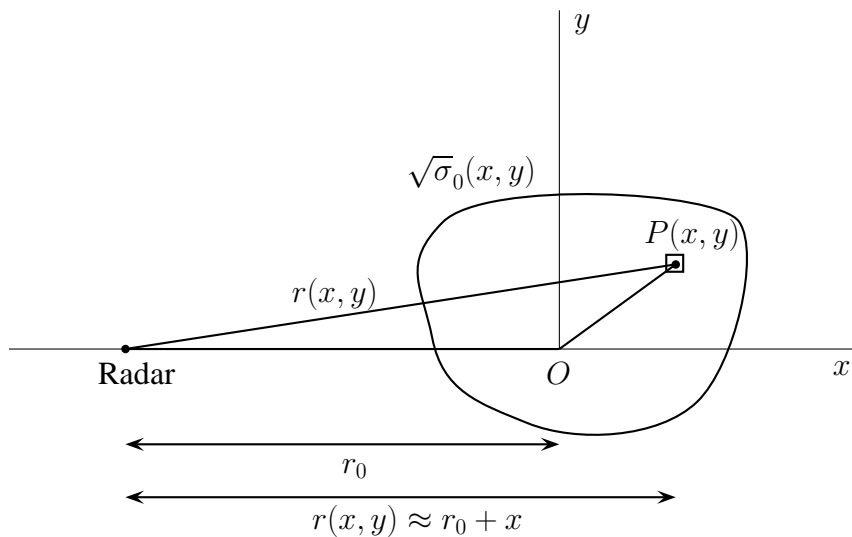
Figure 5.6: *Two-dimensional monostatic radar configuration. The object is represented by its 2D CRCS density $\sqrt{\sigma}_0(x, y)$, located at the center of the coordinate system, at a distance r_0 from the radar.*

5.3.2   Monostatic (MS) radar imaging

We start with Eq. (4.59) into which $\underline{r}_T = \underline{r}_R = \underline{r}$ since the transmitter and the receiver are co-located. The received electric field (E-field) for a point object charac-

terized by $\sqrt{\sigma}$ is thus expressed as

$$\bar{E}^r(\underline{r}) = \alpha'(k, r)\sqrt{\sigma}\bar{E}^t(\underline{r}), \tag{5.10}$$

where

$$\alpha'(k, r) = \frac{e^{-2jkr}}{2\sqrt{\pi}r}, \tag{5.11}$$

and $\bar{E}^r(\underline{r})$ is the received electric field (E-field), $\bar{E}^t(\underline{r})$ the transmitted E-field, and k the wavenumber.

For N point objects, each object being characterized by $\sqrt{\sigma}_i$, the received E-field is given by

$$\bar{E}^r(\underline{r}) = \sum_{i=1}^{N} \alpha'(k, r_i)\sqrt{\sigma}_i \bar{E}^t(\underline{r}_i), \tag{5.12}$$

For a patch $dxdy$, located at $P(x, y)$, of an object described by its CRCS density $\sqrt{\sigma}_0(x, y)$ (Fig. 5.6), the differential phasor received is, according to Eq. (5.10),

$$d\bar{E}^r(\underline{r}) = \alpha'(k, r(x, y))\sqrt{\sigma}_0(x, y)\bar{E}^t(\underline{r})dxdy. \tag{5.13}$$

For a distributed object, the full Rx E-field is obtained by "summing" the differential phasors $d\bar{E}^r(\underline{r})$ over all patches,

$$
\begin{aligned}
\bar{E}^r(\underline{r}) &= \int_{-\infty}^{+\infty}\int_{-\infty}^{+\infty} \alpha'(k, r(x, y))\sqrt{\sigma}_0(x, y)\bar{E}^t(\underline{r})dxdy \\
&= \left(\int_{-\infty}^{+\infty}\int_{-\infty}^{+\infty} \alpha'(k, r(x, y))\sqrt{\sigma}_0(x, y)dxdy\right)\bar{E}^t(\underline{r}).
\end{aligned} \tag{5.14}
$$

We express the distance $r(x, y)$ in α' in terms of the distance r_0 and the coordinates (x, y) of the patch $dxdy$. The following small-angle approximation is made, for the quantity $r(x, y)$ (Fig. 5.6),

$$
\begin{aligned}
r(x, y) &= \sqrt{(r_0 + x)^2 + y^2} \\
&= (r_0 + x)\sqrt{1 + \left(\frac{y}{r_0 + x}\right)^2} \\
&\approx r_0 + x,
\end{aligned} \tag{5.15}
$$

which is intuitively true by simple inspection of Fig. 5.6. This allows us to rewrite Eq. (5.11) as

$$
\begin{aligned}
\alpha'(k, r(x, y)) &= \frac{e^{-2jkr(x,y)}}{2\sqrt{\pi}r(x, y)} \\
&\approx \frac{e^{-2jk(r_0+x)}}{2\sqrt{\pi}(r_0 + x)}.
\end{aligned} \tag{5.16}
$$

Since we assume a far-field condition, we have $x \ll r_0$. We can thus write

$$\alpha'(k, r(x, y)) \approx \frac{e^{-2jk(r_0+x)}}{2\sqrt{\pi}r_0}. \tag{5.17}$$

By substituting Eq. (5.17) into Eq. (5.14), we have

$$
\begin{aligned}
\bar{E}^r(\underline{r}) &= \left(\frac{e^{-2jkr_0}}{2\sqrt{\pi}r_0} \int_{-\infty}^{+\infty} \int_{-\infty}^{+\infty} e^{-2jkx} \sqrt{\sigma}_0(x,y)dxdy \right) \bar{E}^t(\underline{r}) \\
&= \left(\frac{e^{-2jkr_0}}{2\sqrt{\pi}r_0} \int_{-\infty}^{+\infty} \left(\int_{-\infty}^{+\infty} \sqrt{\sigma}_0(x,y)dy \right) e^{-2jkx}dx \right) \bar{E}^t(\underline{r}).
\end{aligned}
\tag{5.18}
$$

The inner integral $\int_{-\infty}^{+\infty} \sqrt{\sigma}_0(x,y)dy$ is the projection of $\sqrt{\sigma}_0$ along the y-axis. According to the definition of the Radon Transform (RT) introduced in Section 5.2.1, the inner integral is the RT for an angle $\phi = 0°$. We thus denote the above integral by $\mathcal{R}\sqrt{\sigma}_0(x',\phi)$. Since $\phi = 0°$, $x' = x$, and we can write

$$
\mathcal{R}\sqrt{\sigma}_0(x,0) = \int_{-\infty}^{+\infty} \sqrt{\sigma}_0(x,y)dy.
\tag{5.19}
$$

Equation (5.18) thus becomes

$$
\bar{E}^r(\underline{r}) = \frac{e^{-2jkr_0}}{2\sqrt{\pi}r_0} \left(\int_{-\infty}^{+\infty} \mathcal{R}\sqrt{\sigma}_0(x,0)e^{-2jkx}dx \right) \bar{E}^t(\underline{r}).
\tag{5.20}
$$

The remaining integral has the form of a 1D FT, defined by Eq (5.3). We can thus write

$$
\int_{-\infty}^{+\infty} \mathcal{R}\sqrt{\sigma}_0(x,0)e^{-2jkx}dx = \widehat{\mathcal{R}\sqrt{\sigma}_0}(2k,0).
\tag{5.21}
$$

We can then rewrite Eq. (5.20) as

$$
\bar{E}^r(\underline{r}) = \frac{e^{-2jkr_0}}{2\sqrt{\pi}r_0} \widehat{\mathcal{R}\sqrt{\sigma}_0}(2k,0) \bar{E}^t(\underline{r}).
\tag{5.22}
$$

We usefully interpret Eq. (5.22) as follows. First, $\bar{E}^r(\underline{r})$ is the fixed phasor of the total E-field received at the radar when the object is illuminated with $\bar{E}^t(\underline{r})$. Second, Eq. (5.22) is exactly of the same form as the fundamental Eq. (5.10). By comparing these two equations, one can see that $\widehat{\mathcal{R}\sqrt{\sigma}_0}(2k,0)$ can be interpreted as the monostatic complex radar cross-section (MS-CRCS) corresponding to the entire object, *i.e.* to the entire distribution $\sqrt{\sigma}_0(x,y)$. Since the object is illuminated at an angle ϕ of zero, we denote this MS-CRCS by $\sqrt{\sigma}(k,0)$. We can thus write

$$
\sqrt{\sigma}(k,0) = \widehat{\mathcal{R}\sqrt{\sigma}_0}(2k,0),
\tag{5.23}
$$

which is a remarkable result since it links the CRCS density $\sqrt{\sigma}_0(x,y)$ of the object to the overall MS-CRCS $\sqrt{\sigma}$ of this object.

By expanding the right-hand side of Eq. (5.23), the explicit relation between the MS-CRCS and the 2D CRCS density $\sqrt{\sigma}_0(x,y)$ in the (x,y) coordinates is

$$
\sqrt{\sigma}(k,0) = \int_{-\infty}^{+\infty} \left(\int_{-\infty}^{+\infty} \sqrt{\sigma}_0(x,y)dy \right) e^{-2jkx}dx.
\tag{5.24}
$$

We use the projection slice-theorem (PST) introduced in Section 5.2.3 to generalize Eq. (5.24) for any orientation ϕ. We thus have

$$
\sqrt{\sigma}(k,\phi) = \int_{-\infty}^{+\infty} \int_{-\infty}^{+\infty} \sqrt{\sigma}_0(x,y)e^{-2jk(x\cos\phi+y\sin\phi)}dxdy.
\tag{5.25}
$$

Equation (5.25) expresses the MS-CRCS $\sqrt{\sigma}(k, \phi)$ of an object as a function of the 2D density of the MS-CRCS in the spatial domain $\sqrt{\sigma}_0(x, y)$.

By using the following change of variables

$$\omega_x = 2k \cos \phi$$
$$\omega_y = 2k \sin \phi,$$

Eq. (5.25) takes the form of a 2D FT, as defined by Eq. (5.5). By inverting the 2D FT, and performing the inverse change of variables, we get

$$\sqrt{\sigma}_0(x, y) = \frac{1}{(2\pi)^2} \int_0^{+\infty} \int_0^{2\pi} \sqrt{\sigma}(k, \phi) e^{2jk(x \cos \phi + y \sin \phi)} |4k| d\phi dk. \qquad (5.26)$$

Since it is usual to use the frequency f instead of the wavenumber k, with $k = 2\pi/\lambda = 2\pi f/c$., we can write

$$\sqrt{\sigma}_0(x, y) = \int_0^{+\infty} \int_0^{2\pi} \sqrt{\sigma}'(f, \phi) e^{4\pi j \frac{f}{c}(x \cos \phi + y \sin \phi)} |\frac{4f}{c^2}| d\phi df, \qquad (5.27)$$

where $\sqrt{\sigma}'(f, \phi)$ is the MS-CRCS expressed in terms of the frequency f and the angle ϕ. Equation (5.27) links the 2D CRCS density of an object to the MS-CRCS of this object computed at a frequency f, for an orientation ϕ of the radar.

5.4 Principles of bistatic radar imaging

In this section, we extend the principles of radar imaging to a bistatic (BS) configuration. We first describe the BS configuration. We then derive the expression of the radar image, *i.e.* the 2D CRCS density, of an object as an inverse two-dimensional (2D) Fourier Transform (FT) of the bistatic complex radar cross-section (BS-CRCS) of this object.

5.4.1 Bistatic (BS) configuration

Figure 5.7 shows the BS configuration that we consider. Let us consider a generic object that is illuminated by a transmitter. Since we are in an BS configuration, the transmitter Tx and the receiver Rx are not co-located.

We choose a reference point O located on or near the object. We denote by $\hat{l}_T$ the line-of-sight of the Tx, and by $\hat{l}_R$ the line-of-sight of the Rx. The bistatic angle β is the angle between the Tx and the Rx with vertex at the center of the object. The line between the bisector Bis of the bistatic angle and the reference point O is the x-axis. The angle ϕ is defined as the angle between the bisector Bis and the x-axis. Here, $\phi = 0°$. The perpendicular to the x-axis at O is the y-axis.

We assume that the object is characterized by its 2D isotropic complex radar cross-section (CRCS) density, denoted by $\sqrt{\sigma}_0(x, y)$ [24]. We express the location of any point P of the object in terms of either its Cartesian coordinates (x, y) or its polar coordinates (r, θ). We denote by r_T and r_R the distances from the transmitter Tx and the receiver Rx to the point P, respectively. We also assume that the reference point O is located at a distance r_0 from both the Tx and the Rx, in the far-field of both the Tx and the Rx.
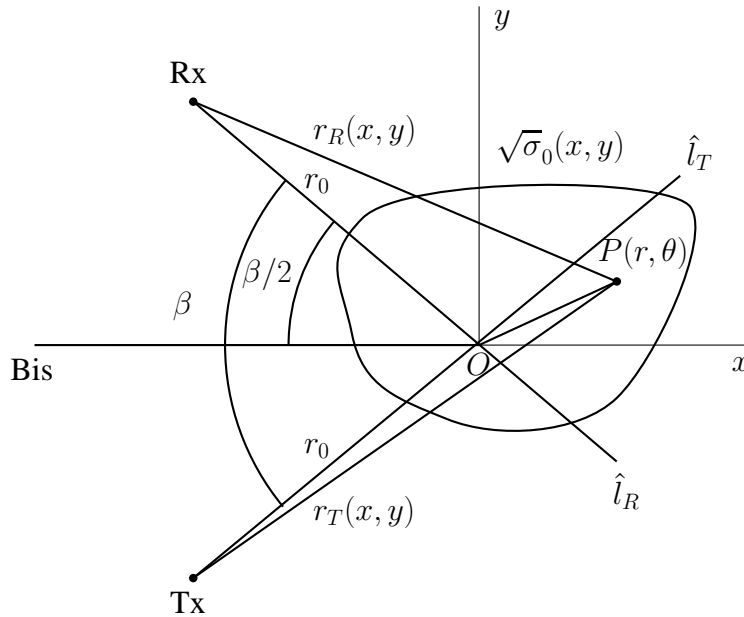
Figure 5.7: *Two-dimensional bistatic radar configuration. The object is represented by its 2D complex radar cross-section density $\sqrt{\sigma}_0(x,y)$, located at the center of the coordinate system, at a distance r_0 from the Tx and the Rx.*

5.4.2   Bistatic (BS) imaging

In the monostatic (MS) configuration, we consider the projection of $\sqrt{\sigma}_0(x,y)$ in the direction of ϕ, which is the direction of the radar. The line integrals are perpendicular to the line-of-sight of the radar.

In the bistatic (BS) configuration, we define the bistatic distance as the sum of the distance from the reference point O on the object to the Tx and the distance from the reference point O on the object to the Rx. The bistatic distance remains equal when the object moves along an ellipse whose foci are the Tx and the Rx [224]. The reflexivity property of ellipses tells us that, at any point on the ellipse, the tangent of the ellipse, and thus the line integrals, are perpendicular to the bisector of the bistatic angle [224], as shown in Fig. 5.8. Therefore, we can consider a BS configuration as an MS configuration, with the radar being located on the bisector of the bistatic angle, at a distance that is half of the sum of the distances from the Tx and the Rx to the reference point O.

If we can express the bistatic distance $r_T + r_R$ in terms of $2r_0 + X$, we can consider Eq. (5.24), into which we replace the MS roundtrip distance $2x$ by X. We thus need to compute the distances r_T and r_R.

Without loss of generality, we assume the distances from the Tx and the Rx to the center of coordinates to be equal to r_0. By inspection of Fig. 5.7, we express the
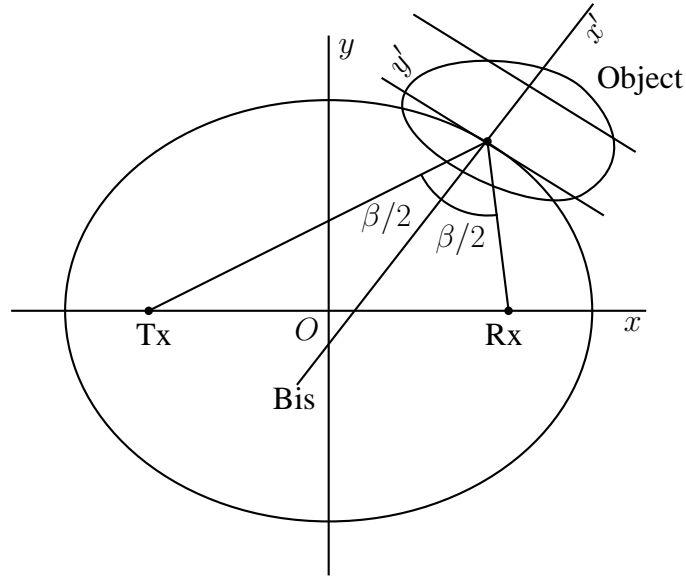
Figure 5.8: *Illustration of the reflexivity property of the ellipse with the Tx and the Rx located at its foci. The line integral are perpendicular to the bisector Bis of the bistatic angle.*

distance r_T as

$$
\begin{aligned}
r_T &= \sqrt{(r_0 + r\cos(\beta/2 - \theta))^2 + (r\sin(\beta/2 - \theta))^2} \\
&= \sqrt{r_0^2 + 2rr_0\cos(\beta/2 - \theta) + r^2} \\
&= r_0\sqrt{1 + 2\frac{r}{r_0}\cos(\beta/2 - \theta) + \frac{r^2}{r_0^2}} \\
&\approx r_0\sqrt{1 + 2\frac{r}{r_0}\cos(\beta/2 - \theta)} \\
&\approx r_0 + r\cos(\beta/2 - \theta),
\end{aligned}
\tag{5.28}
$$

where the second to last line is obtained by considering the far-field approximation ($r \ll r_0$), and the last line by performing a first-order Taylor development on the square root.

In a similar way, we obtain the distance r_R,

$$
r_R = r_0 + r\cos(\beta/2 + \theta).
\tag{5.29}
$$

We thus express the bistatic distance as

$$
\begin{aligned}
r_T + r_R &= 2r_0 + r\left(\cos(\beta/2 - \theta) + \cos(\beta/2 + \theta)\right) \\
&= 2r_0 + 2r\cos\beta/2\cos\theta \\
&= 2r_0 + 2x\cos(\beta/2)
\end{aligned}
\tag{5.30}
$$

We can thus substitute $2x$ by $2x\cos(\beta/2)$ into Eq. (5.24) to get

$$
\sqrt{\sigma}^{BS}(k, 0) = \int_{-\infty}^{+\infty} \left(\int_{-\infty}^{+\infty} \sqrt{\sigma}_0(x, y)dy\right) e^{-2jkx\cos(\beta/2)}dx.
\tag{5.31}
$$

where the superscript "BS" stands for the bistatic configuration.

We use the PST introduced in Section 5.2.3 to generalize Eq. (5.31) for any orientation ϕ of the bisector as

$$\sqrt{\sigma}^{BS}(k,\phi) = \int_{-\infty}^{+\infty} \int_{-\infty}^{+\infty} \sqrt{\sigma}_0(x,y)e^{-2jk\cos(\beta/2)(x\cos\phi+y\sin\phi)}dxdy. \tag{5.32}$$

Equation (5.32) expresses the BS-CRCS $\sqrt{\sigma}^{BS}(k,\phi)$ of an object as a function of the 2D CRCS density $\sqrt{\sigma}_0(x,y)$.

By using the following change of variables

$$\omega_x = 2k\cos(\beta/2)\cos\phi$$
$$\omega_y = 2k\cos(\beta/2)\sin\phi,$$

Eq (5.32) takes the form of a 2D FT, as defined by Eq. (5.5). By inverting the FT, and performing the inverse change of variables, we thus get

$$\sqrt{\sigma}_0(x,y) = \frac{1}{(2\pi)^2} \int_0^{+\infty} \int_0^{2\pi} \sqrt{\sigma}^{BS}(k,\phi)e^{2jk\cos(\beta/2)(x\cos\phi+y\sin\phi)}|4k\cos^2(\beta/2)|d\phi dk. \tag{5.33}$$

Since it is usual to use the frequency f instead of the wavenumber k, with $k = 2\pi/\lambda = 2\pi f/c$, we can write

$$\sqrt{\sigma}_0(x,y) = \int_0^{+\infty} \int_0^{2\pi} \sqrt{\sigma}'^{BS}(f,\phi)e^{4\pi j\frac{f}{c}\cos(\beta/2)(x\cos\phi+y\sin\phi)}|\frac{4f\cos^2(\beta/2)}{c^2}|d\phi df, \tag{5.34}$$

where $\sqrt{\sigma}'^{BS}(f,\phi)$ is the BS-CRCS expressed in terms of the frequency f. Equation (5.34) links the 2D CRCS density of an object to the BS-CRCS of this object computed at a frequency f, for an orientation ϕ of the bisector of the bistatic angle.

In the anechoic chamber that we used to extract the BS-CRCS of the airplanes of interest (Chapter 4), the Tx is fixed, and located on the x-axis. This corresponds to a rotation of $\beta/2$ of the configuration depicted in Fig 5.7. Moreover, the object is fixed, and the Rx moves around the object. We thus integrate over the bistatic angle β rather than on the aspect angle ϕ. We thus get

$$\sqrt{\sigma}_0(x,y) = \int_0^{+\infty} \int_0^{2\pi} \sqrt{\sigma}'^{BS}(f,\phi)e^{4\pi j\frac{f}{c}\cos(\beta/2)(x\cos(\phi+\beta/2)+y\sin(\phi+\beta/2))}|\frac{4f\cos^2(\beta/2)}{c^2}|d\beta df. \tag{5.35}$$

5.5   Practical construction of bistatic radar images

As shown in Fig. 5.1, we compute the radar images of the targets of interest, *i.e.* the 2D CRCS density $\sqrt{\sigma}_0(x,y)$ of these targets, from the complex radar cross-sections (CRCSs) of these targets, for a bistatic configuration. In this section, we detail the practical construction of these radar images.

Recall from Chapter 4 that the available bistatic complex radar cross-section (BS-CRCS) is computed over four different frequency bands, four different polarizations, and several bistatic angles, at three azimuth angles and three elevation angles, for the four airplanes of interest. For computational reasons, we decide to use the values of the BS-CRCS that are extracted for the HH polarization only. For a particular azimuth angle, a particular elevation angle, a particular polarization, and a particular frequency band, the BS-CRCS of a particular target is extracted over some frequency range and some range of bistatic angles. We can thus usefully represent the BS-CRCS as a two-dimensional array of values of BS-CRCS, the dimensions of the array being the frequency f and the bistatic angle β, as shown in Fig. 5.9.

For recognition purposes (Chapter 6), we split the values of the BS-CRCS into a learning set (LS), and a test set (TS). For a particular frequency band, the LS contains the values of BS-CRCS that are available over the lower half of this frequency band, and the TS contains the values of BS-CRCS that are available over the upper half of this frequency band. Images of targets are constructed using values of BS-CRCS that belong to either the LS or the TS. The constructed images thus belong to either the LS of images or the TS of images, in order to guarantee the independence of the LS and the TS in our recognition experiments [221].
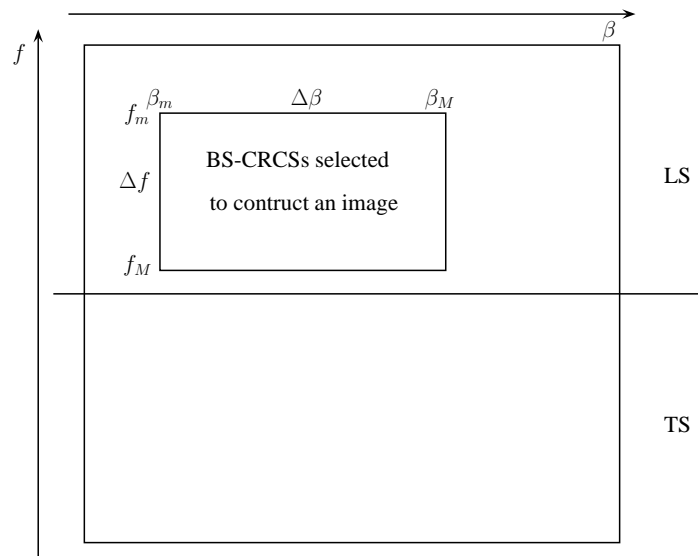
Figure 5.9: *Illustration of the practical reconstruction of an image of a target from the BS-CRCSs of this target.*

In Section 5.4, we expressed the radar images of targets as an inverse 2D Fourier Transform of the bistatic complex radar cross-section (BS-CRCS) of these targets. In particular, Eq. (5.35) states that the value of each pixel (x, y) of an image of a target is obtained by "summing" the BS-CRCS of the target over an infinite range of frequencies, and a particular range of bistatic angles. As shown in Fig. 5.9, the values of BS-CRCS that are used to construct an image of a target can thus be viewed as belonging to a sub-array of the available values of BS-CRCS. The dimensions of this sub-array are $[\beta_m; \beta_M] \times [f_m; f_M]$, where the subscripts "$m$" and "$M$" stand for the minimum and maximum values of each of the dimensions of the array, respectively.

We arbitrarily decide to fix the range of the bistatic angle as being comprised between 20° and 25°. We thus have $\Delta\beta = \beta_M - \beta_m \in [20°; 25°]$.

In order to fix the frequency range, we use the definitions of the range resolution r_x^{BS} and of the cross-range resolution r_y^{BS}, where the superscript "BS" indicates, as above, that we are in a bistatic configuration. For a monostatic (MS) configuration, the range resolution r_x^{MS} and the cross-range resolution r_y^{MS} are given by [165]

$$r_x^{MS} = \frac{c}{2\Delta f} \tag{5.36}$$

and

$$r_y^{MS} = \frac{c}{2f_c\Delta\theta}, \tag{5.37}$$

where c is the speed of light, $\Delta\theta$ is the aspect angular range (in radians), and Δf and f_c are the frequency range and the central frequency of the data selected to reconstruct an image, respectively.

For a bistatic (BS) configuration, the range resolution r_x^{BS} and the cross-range resolution r_y^{BS} are given by [41]

$$r_x^{BS} = \frac{c}{2\Delta f \cos\beta/2} \tag{5.38}$$

and

$$r_y^{BS} = \frac{c}{f_c\Delta\beta}, \tag{5.39}$$

where c is the speed of light, and β and $\Delta\beta$ are the bistatic angle and the bistatic angular range of the data selected to reconstruct an image, respectively.

Since we use the constructed images for classification, we want all the images to have similar range resolutions and similar cross-range resolutions. In order to do so, we arbitrarily decide that we want the ratio of the range resolution and the cross-range resolution of an image to be almost equal to unity. We also want to construct a number of images large enough to perform meaningful classification. We can thus express these two conditions as

$$\frac{1}{\alpha} \leq \frac{r_x^{BS}}{r_y^{BS}} \leq \alpha, \tag{5.40}$$

where α is experimentally chosen to comply with the two conditions stated above. Table 5.1 lists the chosen values of α, for each frequency band.

In short, for a given range of bistatic angle, and for a given frequency range, we compute r_x^{BS} and r_y^{BS}. If Eq. (5.40) is satisfied, we construct the radar image based on Eq. (5.35). Otherwise, we do not construct any image for the selected sub-array of values of BS-CRCS. The construction process is repeated for all possible sub-arrays.

Table 5.2 shows, for each frequency band, the mean and standard deviation of the range resolution r_x^{BS} and of the cross-range resolution r_y^{BS}, for the constructed images of the Beechcraft from the BS-CRCSs of the LS. Similarly, Table 5.3 shows, for each

Frequency band	α	$\Delta\beta$
FB1: $20 - 80$ MHz	1.001	$[20; 25]°$
FB2: $190 - 250$ MHz	1.02	$[20; 25]°$
FB3: $450 - 550$ MHz	1.2	$[20; 25]°$
FB4: $1.2 - 1.3$ GHz	2.9	$[20; 25]°$

Table 5.1: *Experimentally chosen values of α for each frequency band.*

frequency band, the mean and standard deviation of the range resolution r_x^{BS} and of the cross-range resolution r_y^{BS}, for the constructed images of the Beechcraft from the BS-CRCS of the TS.

	r_x [m]		r_y [m]	
Frequency band	Mean	Std. dev.	Mean	Std. dev.
FB1: $20 - 80$ MHz	21.07	2.30	21.06	2.31
FB2: $190 - 250$ MHz	3.12	0.11	3.12	0.10
FB3: $450 - 550$ MHz	1.61	0.03	1.38	0.04
FB4: $1.2 - 1.3$ GHz	1.58	0.02	0.55	10^{-4}

Table 5.2: *Mean and standard deviation of the range resolution r_x^{BS} and of the cross-range resolution r_y^{BS} of the reconstructed images of the Beechcraft belonging to the LS.*

	r_x [m]		r_y [m]	
Frequency band	Mean	Std. dev.	Mean	Std. dev.
FB1: $20 - 80$ MHz	11.35	1.19	11.35	1.20
FB2: $190 - 250$ MHz	3.11	0.10	3.12	0.09
FB3: $450 - 550$ MHz	1.62	0.02	1.38	0.0024
FB4: $1.2 - 1.3$ GHz	1.59	10^{-13}	0.55	10^{-14}

Table 5.3: *Mean and standard deviation of the range resolution r_x^{BS} and of the cross-range resolution r_y^{BS} of the reconstructed images of the Beechcraft belonging to the TS.*

From Tables 5.2, and 5.3, we make the following observations for the Beechcraft:

- For each frequency band, and for both the LS and the TS, the means (and standard deviation) of r_x^{BS} and r_y^{BS} are very similar. This makes sense since both r_x^{BS} and r_y^{BS} are computed from Eq. (5.40).

- For each frequency band, the mean value of r_x^{BS} is greater for the LS than for the TS, and the same is true for r_y^{BS}. This makes sense since the images of the LS and the TS are constructed from the lower part and the upper part of the frequency band, respectively.

The same observations apply to the three other airplanes of interest, since their BS-CRCSs are computed for the same parameters (frequency, polarization, bistatic angle, azimuth angle, and elevation angle).

Table 5.4 shows the number of constructed images of each type of airplane for both the LS and the TS, for each frequency band. These images are used in Chapter 6 for the recognition of the four airplanes of interest.

Frequency band	Number of images	
	LS	TS
FB1: $[20; 80]$ MHz	6,480	11,520
FB2: $[190; 250]$ MHz	12,600	11,340
FB3: $[450; 550]$ MHz	14,580	7,290
FB4: $[1.2; 1.3]$ GHz	14,040	4,680

Table 5.4: *Number of constructed images of each type of airplanes for the LS and the TS, per frequency band.*

5.6   Examples of constructed radar images

In this section, we show examples of constructed images of the four airplanes of interest. For conciseness, we choose to show images that are constructed from their BS-CRCS computed only for bistatic angles ranging from 6° to 43.5°, for an orientation angle θ of 0° and for an elevation angle ϕ of 0°. The values of the frequency and bistatic angles are chosen such that they satisfy Eq. (5.40).

Figure 5.10 shows one radar image (shown in pseudocolor for ease of visualization) for each of the four airplanes of interest. These images are constructed for the data acquired in the first frequency band, FB1. Figures 5.11, 5.12, and 5.13 give the corresponding images for the three other frequency bands, FB2, FB3, and FB4, respectively. The values in each image are normalized to a maximum value of 1 (0 dB).

Tables 5.2 and 5.3 show that the means of r_x^{BS} and of r_y^{BS} are about 21 m, which is slightly larger than the characteristic dimension of the airplanes, *i.e.* 15 m. As a result, each target appears essentially as a single bright point (Fig. 5.10). Since r_x^{BS} and r_y^{BS} decrease when the frequency increases, targets are characterized by an increasing number of smaller bright points when the frequency increases.

(a) *Beechcraft* **(b)** *F117*

(c) *F16* **(d)** *Learjet*
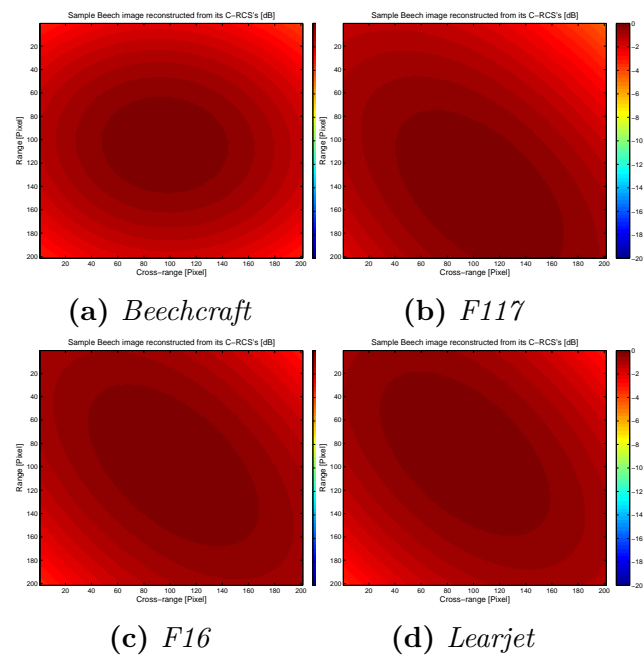
Figure 5.10: *Example radar images computed from BS-CRCSs collected over the first frequency band FB1 ([20; 80] MHz). The images are shown using a pseudocolor scale.*

(a) *Beechcraft* **(b)** *F117*

(c) *F16* **(d)** *Learjet*
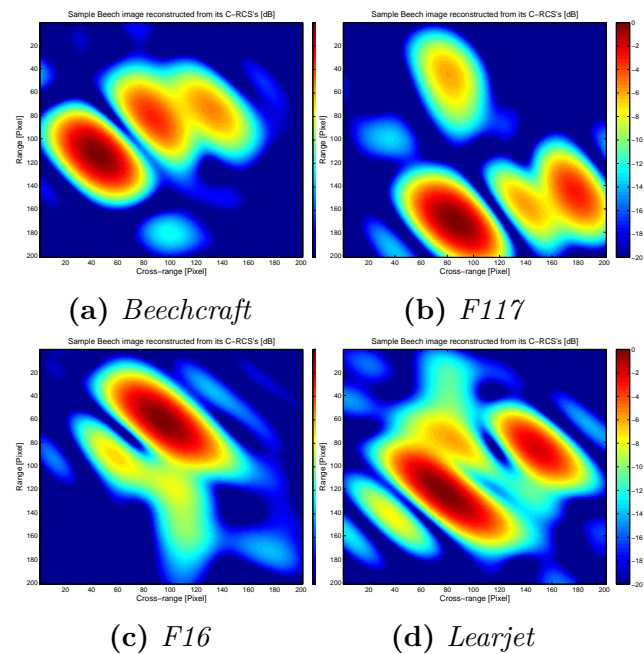
Figure 5.11: *Example radar images computed from BS-CRCSs collected over the second band FB2 ([190; 250] MHz). The images are shown using a pseudocolor scale.*

(a) *Beechcraft*   (b) *F117*

(c) *F16*   (d) *Learjet*
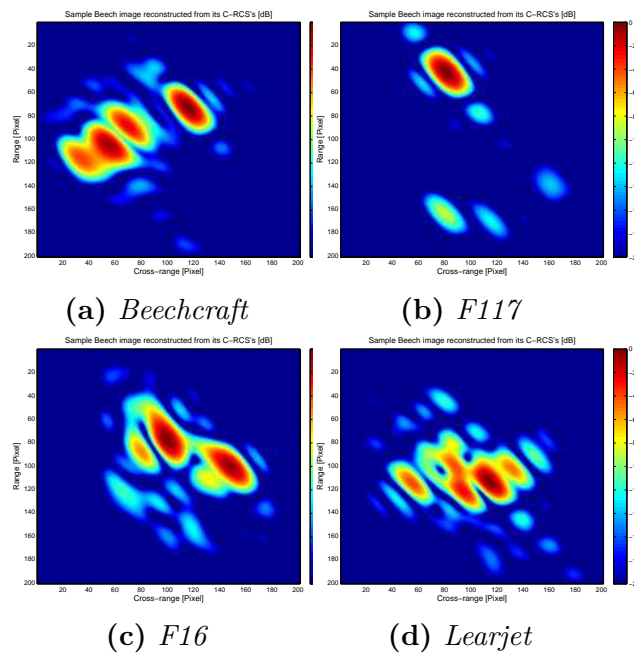
Figure 5.12: *Example radar images computed from BS-CRCSs collected over the third frequency band FB3 (*[450; 550] *MHz). The images are shown using a pseudocolor scale.*

(a) *Beechcraft*   (b) *F117*

(c) *F16*   (d) *Learjet*
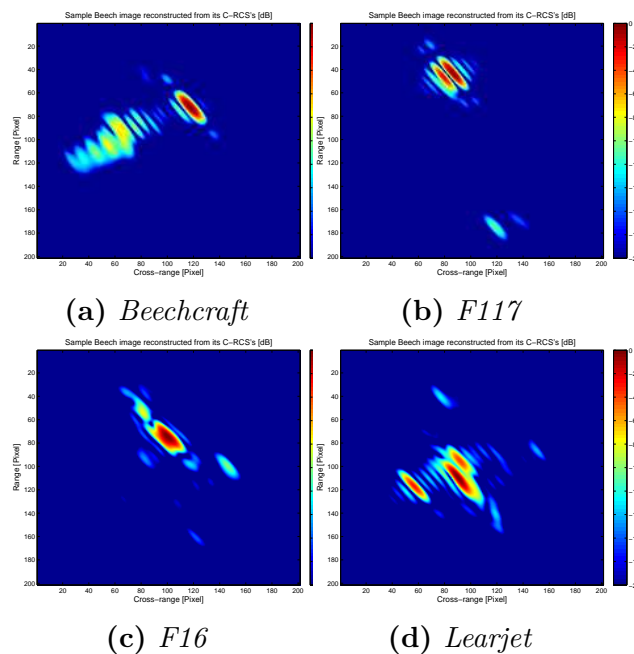
Figure 5.13: *Example radar images computed from BS-CRCSs collected over the fourth frequency band FB4 (*[1.2; 1.3] *GHz). The images are shown using a pseudo-color scale.*

5.7 Conclusion

We presented in this chapter the construction of radar images of targets, since this is the second step of the first automatic target recognition (ATR) system. We derived the expression of the two-dimensional (2D) spatial representation of an object from the complex radar cross-section (CRCS) of this object for the monostatic configuration. We then extended this expression to the bistatic configuration. In both configurations, the 2D radar image of a target is basically a 2D inverse Fourier Transform of the CRCS of this target.

We then presented the practical construction of radar images from their bistatic complex radar cross-section (BS-CRCS), for each of the frequency bands of interest. We constructed each image from a 2D array of values of BS-CRCS of targets, whose dimensions are the bistatic angle and the frequency. The size of each dimension is determined such that the ratio of the range resolution and the cross-range resolution of the obtained image is comprised between $1/\alpha$ and α. For each frequency band, the value of α was experimentally chosen in order to obtain a number of images that is large enough to perform a meaningful classification (as further discussed in Chapter 6). We showed, for each frequency band of interest, examples of radar images of each of the four airplanes of interest.

Chapter 6

Recognition of targets
by using their radar images

Contents

In this chapter, we perform the recognition of targets by using their radar images. Section 6.1 states the motivation for the recognition of targets by using their radar images. Section 6.2 describes the physical and the parameter spaces in which we express both the bistatic complex radar cross-section (BS-CRCS) and the bistatic radar cross-section (BS-RCS), and thus the images, of a target. Section 6.3 describes the recognition strategy that we use to design the recognizer. Section 6.4 describes the block diagram of the recognizer. Section 6.5 describes the production of feature vectors. Section 6.6 describes the determination of the target class model. Section 6.7 describes the determination of the class of an unknown target based on a target class model. Section 6.8 presents the criteria we use for the quantification of the performance of the recognizer. Sections 6.9 and 6.10 describe the recognition experiments we performed and the recognition rates we achieved on the MSTAR images and on the ONERA images, respectively. Section 6.11 concludes.

6.1   Motivation for the recognition of targets by using their radar images

As explained in Chapter 2, the recognition of targets by using their images is one of the most popular recognition method in automatic target recognition (ATR) for radars. Our first ATR system, whose block diagram is shown in Fig. 6.1, is designed to recognize targets by using their radar images. In this chapter, we design, implement, and test the recognition stage of this ATR system.
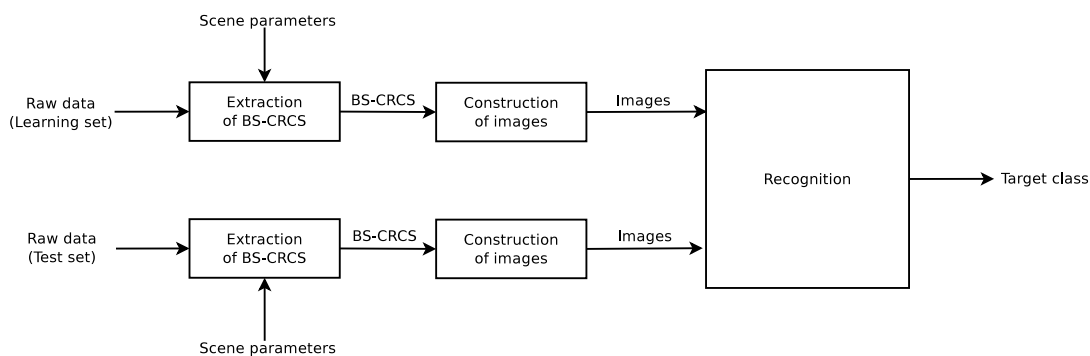
Figure 6.1: *Block diagram of our ATR system using radar images of targets.*

As explained in Chapter 5, the construction of radar images of targets from the bistatic complex radar cross-section (BS-CRCS) of these targets requires that the BS-CRCS of the targets be available over some range of frequencies and over some range of bistatic angles. However, this two-dimensional (2D) diversity is unlikely to be met in an operational system. Indeed, at a particular time instant and for a particular target, it is possible to compute the BS-CRCS of this target at a particular frequency and over a large range of bistatic angles by suitably positioning a sufficient number of receivers (Rx's). The frequency diversity requires that the signals of a sufficient number of transmitters (Tx's), operating on distinct, adjacent frequencies, and covering in an adequate way a frequency band that is large enough, be scattered

on the target at the same time instant. However, the frequency band planning does not allow transmitters of opportunity to cover such a large frequency band.

Since the construction of radar images from their BS-CRCS appears difficult to perform in an operational passive bistatic radar system, we will use the recognition of targets by using their radar images as a reference to evaluate the two subsequent ATR systems.

6.2 Physical and parameter spaces

We showed in Chapter 3 that both the complex radar cross-section (CRCS) and the radar cross-section (RCS) of a particular object depend on electromagnetic and geometric parameters. Since we construct images of targets from the CRCS of these targets, the images also depend on the same electromagnetic and geometric parameters. The two electromagnetic parameters are the frequency and the polarization (of both the transmitter (Tx) and the receiver (Rx)). For a monostatic (MS) configuration, the geometric parameter is the aspect angle α, and, for a bistatic (BS) configuration, the geometric parameters are the aspect angle α and the bistatic angle β. We refer to this set of parameters as the parameter space.

In the present context, the objects of interest are airplanes. Airplanes fly arbitrary trajectories that are expressed in the (x, y, z) coordinates, which we call the physical space. We thus need to establish the mapping between the physical space and the parameter space. We first present the physical space, and then the mapping between the physical space and the parameter space. We discuss the cases of both the RCSs and the CRCSs. The discussion is similar for the images of the targets.

6.2.1 Physical space

For ease of explanation, and as is commonly done [186], we consider that the physical space containing the Tx's, the Rx's, and the objects of interest (and, thus, their trajectories) is planar, *i.e.* 2D. Thus, we also refer to this planar physical space as the "physical plane". The positions of the above elements are given with respect to some system of orthogonal (x, y) axes located in this plane. This 2D situation is illustrated in Fig. 6.2. We consider a single frequency and a single polarization.

While the discussion to follow is cast into a 2D framework, it is conceptually easy to extend it to 3D. Furthermore, real-life situations where the objects of interest are located at sufficient distances from the Tx's and Rx's can generally be handled as though they were 2D. The physical plane can then be interpreted as an overhead view of the situation.

In this 2D framework, each object necessarily follows a continuous true trajectory in the physical plane (Fig. 6.2). Each (Tx,Rx) pair looks at this object at specific discrete time instants and, thus, at specific, corresponding discrete (true) positions along its true trajectory; these positions are shown with open circles in Fig. 6.2. The discrete "looks" thus result in a sampling of the true (unknown) trajectory. By analogy with the qualifiers "continuous time (CT)" and "discrete
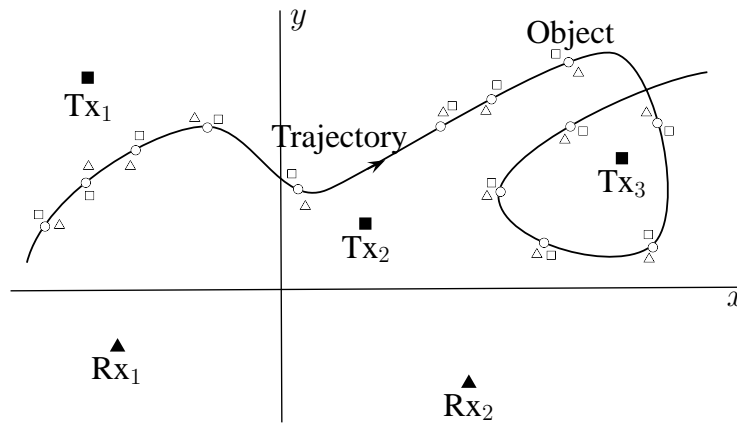
Figure 6.2: *2D physical space, also called (x, y) plane. The figure illustrates a passive radar system consisting of three transmitters Tx_i and two receivers Rx_i, and observing an object following a particular trajectory. The open circles on this true trajectory indicate the true position of S at each time instant one specific (Tx,Rx) pair looks at the object. The open triangles indicate where this pair actually estimates that the object is. The open rectangles correspond to another pair, which will generally provide other position estimates and, furthermore, will generally use different look instants.*

time (DT)" of signal processing [142], we respectively use "continuous space (CS)" and "discrete space (DS)" to qualify the continuous trajectory and the sequence of points resulting from sampling. These trajectories are the domains of definition of both the radar-cross-section (RCS) functions and the complex radar cross-section (CRCS) functions. We can thus complete the analogy by talking about CS CRCS signals and DS CRCS sequences, and, similarly, CS RCS signals and DS RCS sequences.

In practice, each (Tx,Rx) pair may "look" at different instants, so that, for each object, one must associate a specific DT trajectory (and either a corresponding DT CRCS sequence or a corresponding DT RCS sequence) to each such (Tx,Rx) pair. Furthermore, the estimates of positions for each pair will generally not fall on the true trajectory (Fig. 6.2).

We thus distinguish between true CS, true DS, and measured DS trajectories. The latter two are specific to each (Tx,Rx) pair. For illustration purpose, we often show the sampling points of a measured DS trajectory on a CS curve, but this curve is purely conceptual.

The above trajectories are those of a reference point S on the object (Fig. 6.3), typically its center of gravity. The orientation of the object is characterized by the orientation of a reference (unit) vector $\hat{\underline{s}}$ (Fig. 6.3), typically aligned with the longitudinal axis of the object and pointing to its front. A fundamental assumption of our work is that we can determine (estimates of) S and $\hat{\underline{s}}$ at each instant that each (Tx,Rx) pair looks at the object.

If there is no wind, $\hat{\underline{s}}$ essentially coincides with the oriented tangent $\hat{\underline{t}}$ to the
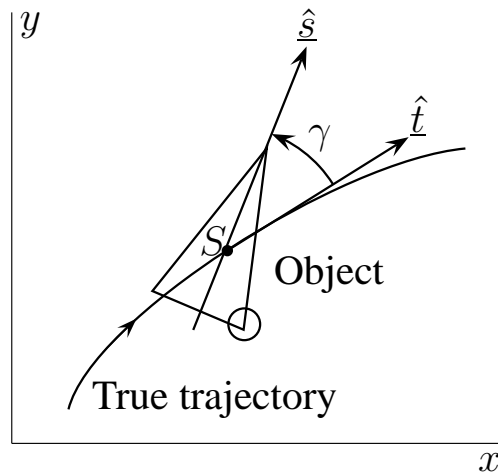
Figure 6.3: *Stylized object with reference point S on it, and reference orientation vector $\underline{\hat{s}}$ through S. When the object moves, S traces the true trajectory of the object in the (x, y) plane. Vector $\underline{\hat{t}}$ is defined by the tangent to this trajectory at S and the direction of motion of the object.*

underlying true CS trajectory at S. Otherwise, there is an angle γ from $\underline{\hat{t}}$ to $\underline{\hat{s}}$ (Fig. 6.3). (All angles are measured counterclockwise.) While it is relatively easy to get $\underline{\hat{t}}$, perhaps following an interpolation of the measured DS trajectory, it may be more difficult to get $\underline{\hat{s}}$. However, in one way or another, we need to know the position S and the orientation $\underline{\hat{s}}$. If necessary, we assume that $\underline{\hat{s}}$ is $\underline{\hat{t}}$. This is a reasonable assumption when airplanes approach or leave a runway that is well aligned with the wind direction. In an operational system, the positions of S are obtained from either secondary surveillance radars or passive bistatic radars.

For a particular frequency f and a particular polarization *Pol*, both the MS-CRCS $\sqrt{\sigma}$ and the MS-RCS σ of an object vary with the aspect angle α from the line-of-sight (LOS) vector $\underline{\hat{l}}$ to the LOS $\underline{\hat{s}}$ of the object (Fig. 6.4(a)). We conceptually represent this variation by the functions $\sqrt{\sigma}(\alpha)$ and $\sigma(\alpha)$. Below, we review some elementary "geometrical" considerations for the MS-CRCS and MS-RCS [91]. We place ourselves in a 2D configuration, *i.e.* we do not consider the elevation angle. This last elevation angle is thus not a parameter of the parameter space used here.

We distinguish between symmetric and asymmetric objects. This is why the stylized object used in Fig. 6.4 has an optional circular part that allows one to make it symmetric (by omitting this part) or not. For a symmetric object, one can intuitively deduce from Fig. 6.4(a) that $\sqrt{\sigma}(\alpha)$ and $\sigma(\alpha)$ are even in α, *i.e.* $\sqrt{\sigma}(\alpha) = \sqrt{\sigma}(-\alpha)$ and $\sigma(\alpha) = \sigma(-\alpha)$. This means that, for such an object, one only needs to examine the variations of $\sqrt{\sigma}$ and σ over the limited $[0, \pi]$ range, instead of over the full $[-\pi, \pi]$ (or $[0, 2\pi]$) range, since all values of $\sqrt{\sigma}(\alpha)$ and $\sigma(\alpha)$ for α in $[-\pi, 0]$ can be obtained from those in $[0, \pi]$. However, this does not mean that $\sqrt{\sigma}(\alpha)$ and $\sigma(\alpha)$ have period π; indeed, they have period 2π. As an aside, $\sqrt{\sigma}(\alpha)$ and $\sigma(\alpha)$ are generally not equal to $\sqrt{\sigma}(\alpha + \pi)$ and $\sigma(\alpha + \pi)$, respectively. For an asymmetric object, one obviously needs to consider $\sqrt{\sigma}(\alpha)$ and $\sigma(\alpha)$ over the full $[-\pi, \pi]$ range. In conclusion, in the MS case, we use α to parametrize the variations of both the MS-CRCS and MS-RCS.
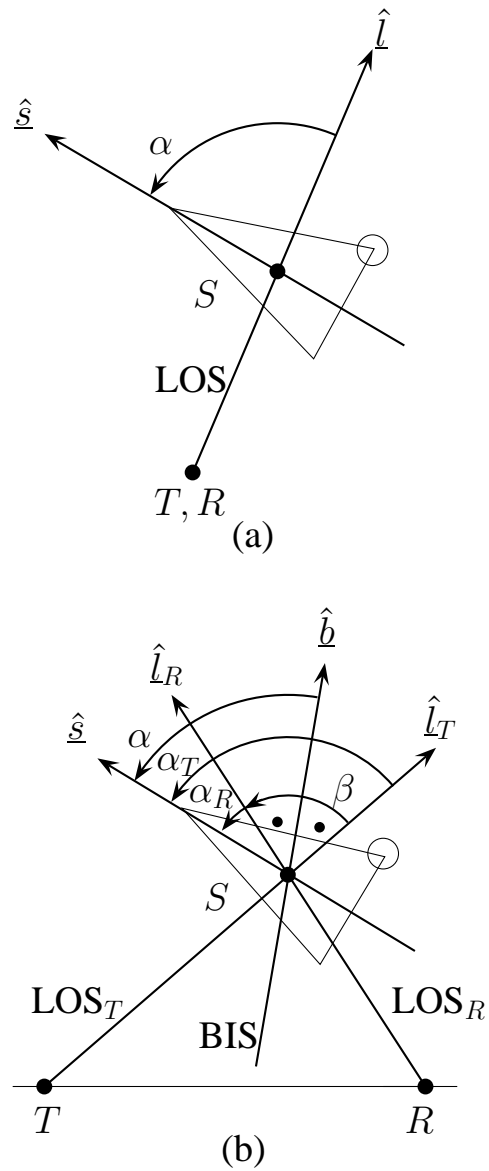
Figure 6.4: *Illustration of the aspect and bistatic angles for (a) a monostatic config-uration, and (b) a bistatic configuration.*

The BS equivalent of the MS aspect angle α is the pair of BS aspect angles α_T and α_R, defined as in the MS case, but with respect to the LOS vector $\hat{\underline{l}}_T$ (from T), and the LOS vector $\hat{\underline{l}}_R$ (from R), respectively (Fig. 6.4(b)). Although we could use α_T and α_R to parametrize the variations of both the BS-CRCS $\sqrt{\sigma}^{BS}$ and the BS-RCS σ^{BS}, we use instead the bistatic angle β defined as the angle from $\hat{\underline{l}}_T$ to $\hat{\underline{l}}_R$, and the angle α defined as the angle from $\hat{\underline{b}}$ to $\hat{\underline{s}}$, where the vector $\hat{\underline{b}}$ bisects β and points towards the outside of the triangle TSR. One can easily derive the analytical relations between the pairs (α_T, α_R) and (α, β). This shows that one can use either pair to parametrize the variations of both the BS-CRCS and the BS-RCS. Here, we use the pair (α, β).

When the BS configuration reduces to an MS configuration, (1) the BS vectors $\hat{\underline{l}}_T$, $\hat{\underline{l}}_R$, and $\hat{\underline{b}}$ coincide, and become the MS LOS vector $\hat{\underline{l}}$, (2) the BS angle α becomes the MS angle α, hence justifying the use of the same symbol α in both cases, despite the different meanings, and (3) the angle β becomes zero. We use the term "aspect angle" to refer to both the MS angle α and the BS angle α.

In [188], Skolnik states that "σ^{BS} is a function of aspect angle and bistatic angle", but he does not define this aspect angle α precisely. Even though the term "bistatic (BS) angle" generally denotes the interior angle of the triangle TSR between the sides $\overline{ST}$ and $\overline{SR}$ [186], we also use this term to refer to the β introduced above (which can take values in $[0, 2\pi]$, by contrast to the usual $[0, \pi]$).

The assumed knowledge of S and of $\hat{\underline{s}}$ at any specific time allows us to compute the values of α and β for this time. Since we assume that we know S and $\hat{s}$ at all times of interest during an observation window, we can associate a pair (α, β) to each point along any trajectory. Adding $\sqrt{\sigma}^{BS}$ and σ^{BS}, we can associate two triplets $(\alpha, \beta, \sigma^{BS})$ and $(\alpha, \beta, \sqrt{\sigma}^{BS})$ to each such point.

6.2.2 Parameter space

The parameters α and β are used to define a system of orthogonal (α, β) axes and a corresponding 2D space, referred to here as the parameter plane. We also refer to it as the (α, β) space and the (α, β) plane.

For example, consider a specific measured discrete space (DS) trajectory in the physical plane, due to one specific (Tx,Rx) pair and one specific object. For each point (x_0, y_0) along this trajectory, we can compute the corresponding values of α_0 and β_0, which define a corresponding point (α_0, β_0) in the (α, β) plane. Each point (x_0, y_0) can thus be mapped into a point (α_0, β_0). Since the mapping preserves the time ordering, the mapping of all the points (x_0, y_0) along the trajectory in the (x, y) plane results in a corresponding trajectory in the (α, β) plane. The values of both the CRCS $\sqrt{\sigma}$ and the RCS σ are also carried over in the mapping. (In the case of polarimetric radars, one complex value per polarization pair would be carried over.) It is useful to visualize one value of $\sqrt{\sigma}$, or one value of σ, associated with each point on each (x, y) and (α, β) trajectory and, thus, functions $\sqrt{\sigma}(x, y)$ and $\sqrt{\sigma}'(\alpha, \beta)$, or $\sigma(x, y)$ and $\sigma'(\alpha, \beta)$, which are continuous space (CS) functions (using "Dirac walls" [94]) or DS sequences (using "lollipops" [33]).

The customary range of β is $[0, \pi]$; the maximum range of α is $[0, \pi]$ for symmetric objects, and $[-\pi, \pi]$ for asymmetric objects; at a given β, $\sqrt{\sigma}^{BS}(\alpha)$ and $\sigma^{BS}(\alpha)$ always have a period of 2π, and $\sqrt{\sigma}^{BS}(\alpha)$ and $\sigma^{BS}(\alpha)$ are even for symmetric objects. However, when considering the (α, β) plane, we must always consider the full $[-\pi, \pi]$ range of α, even for symmetric objects. Figure 6.5 shows the "central part" of the (α, β) plane, as well as two example trajectories, corresponding either to a single trajectory observed by two (Tx,Rx) pairs, or two distinct trajectories observed by a single pair.
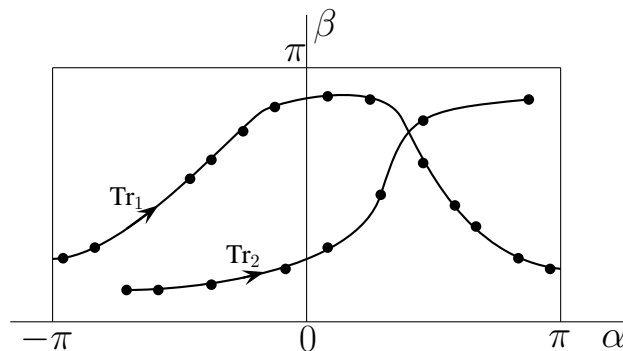
Figure 6.5: *2D parameter space, also called (α, β) plane. The rectangle shown is the boundary of the central part of the plane corresponding to $\alpha \in [-\pi, \pi]$ and $\beta \in [0, \pi]$. Two example (α, β)-plane trajectories are shown, both in continuous form and in discrete form. The dots on each trajectory correspond to the instants one (Tx,Rx) pair looks at the object.*

We will use the parameter space, in terms of which we express both the BS-CRCS and the BS-RCS of targets, in the design of each of the three recognizers.

6.3   Recognition strategy

In this section, we define the recognition strategy that we follow for the recognition stage (*i.e.* the recognizer) of each of the three automatic target recognition ATR systems. The lifecycle of any of the recognizers starts with the laboratory development, where the recognizer is constructed and tested. It continues with the operational use. The input data are either images, bistatic complex radar cross-section (BS-CRCS), or bistatic radar cross-section (BS-RCS) of the targets of interest. We partition the data into a learning set (LS) used for constructing the recognizer, and a test set (TS) used for testing it, and quantifying its performance [53, 134].

Recognition consists in assigning a "class" to data, in particular that of the TS. In supervised learning (as assumed here), this class is one among a set of N_c predefined classes, each denoted here by Class i_c, with $i_c \in [1, N_c]$.

The LS can be viewed as being organized into a set of (f, Pol, α, β) spaces, where each space corresponds to a predefined class, and is filled with data of this class. The

data corresponds to either images, BS-CRCS values, or BS-RCS values of the targets of interest.

In the present context, since the polarization pair takes discrete values (HH, HV, VH, VV), we will consider each polarization independently of the others. Similarly, since the available data is computed for different non-adjacent frequency bands (FB1 to FB4), we will also consider each frequency band independently of the others. Moreover, since the scattering mechanisms remain the same inside each frequency band, we do not partition the data within a frequency band into sub-bands. Therefore, for each frequency band, and for each polarization, the LS can very advantageously be viewed as being organized into a set of (α, β) planes, where each plane corresponds to a predefined class, and is filled with data of objects of this class.

In short, for each frequency band and for each polarization, we construct one recognizer for each of the (α, β) plane filled with data of the N_c classes. Recall that it is sufficient to consider the central part of the (α, β) plane, which corresponds to $\alpha \in [-\pi, \pi]$ and $\beta \in [0, \pi]$.

During test, one typically observes an object at a particular frequency and at a particular polarization, over a part of the (α, β) plane. The basic ingredient for using the recognizer is one (α, β) plane that contains a small amount of data. Since the goal of the recognizer is to assign one of the N_c classes to the data in this (α, β) plane, it is very advantageous to say that this plane corresponds to the unknown class, which we call "Class x", by analogy with "Class i_c". Once again, it is sufficient to consider the central part of this plane. The goal of the recognizer is to attribute one of the values i_c's to x.

We now have, for each frequency band and for each polarization, a set of N_c (α, β) planes filled with data and ready to be used for constructing the recognizer, and one (α, β) plane for holding the data to be recognized, *i.e.* a sort of scratchpad to hold data temporarily. Figure 6.6(a) illustrates, for each frequency band and for each polarization, the central part of each of these planes and the measured DS data they contain.

As will soon become clear, our approach to recognition can be applied either to the central parts of these planes, or to any common subset thereof. As illustrated in Fig. 6.7, this subset, called here "cookie-cutter region", can be of arbitrary shape. Figure 6.6(b) shows such a region overlayed on the central parts. This region automatically segments out the data in (the central part of) all (α, β) planes. One can then consider only the data that is segmented out (Fig. 6.6(c)).

A key feature of our approach is that, for each frequency band and each polarization, we use the data from the same region in the N_c planes to construct a recognizer specific to this region and the N_c classes. We call the recognizer specific to a given region a sub-recognizer. During test, the data from the same region in the plane for Class x is presented to the (sub-)recognizer.

Instead of cutting out a single region from the (α, β) plane, we can cut out several regions, whether overlapping or not, and construct one recognizer for each.
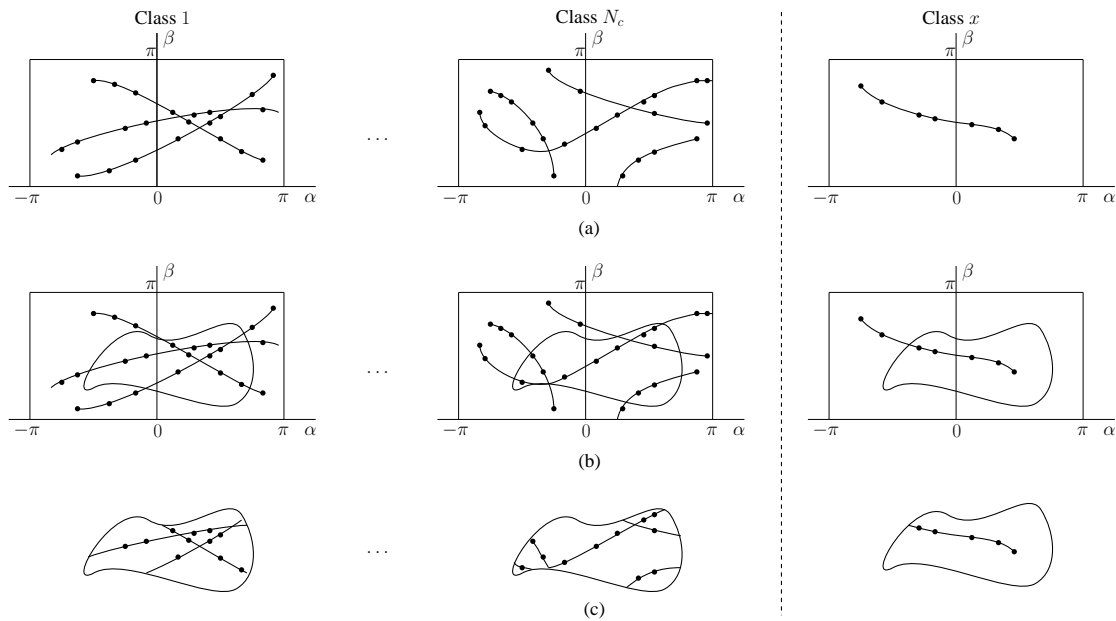
Figure 6.6: *Illustration of the use of the generic cookie-cutter region of Fig. 6.7 to extract the same corresponding region from the (α, β) plane of each class of interest, i.e. Class 1, ..., Class N_c, and Class x. The cookie-cutter region automatically segments out portions of the data present in the various (α, β) planes. The recognizer is built from the data so isolated for Classes 1 to N_c. The recognition is performed using the data so isolated for Class x.*
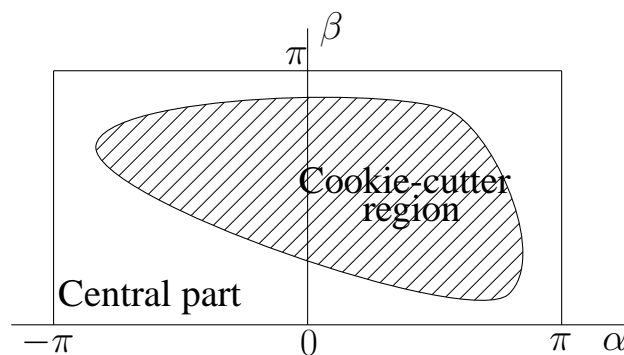
Figure 6.7: *Illustration of the (generic) cookie-cutter region. It delimits one region - consisting of one or more subregions - in the central part of the generic (α, β) plane. It is used as a cookie cutter to isolate the same region in the (α, β) planes of the classes of interest, i.e. Class 1, ..., Class N_c, and Class x.*

To handle the full central part, it is sufficient to define a collection of overlapping or non-overlapping subsets of it. One important covering is obtained by subdividing the α and β axes into contiguous intervals, and using these intervals to define rectangular tiles (Fig. 6.8). One recognizer specific to each tile must be constructed. One can choose regions/tiles that overlap or not.
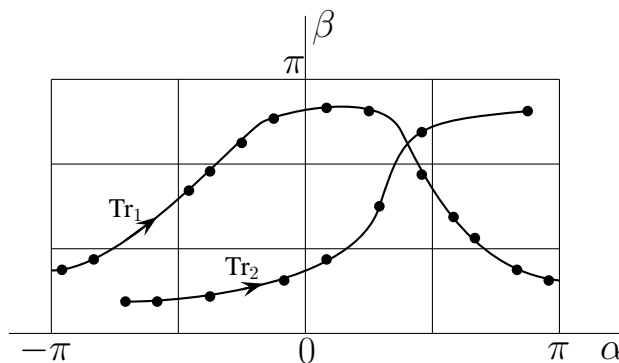
Figure 6.8: *Partitioning of the central part of the (α, β) plane using an example 4×3 array of butting, non-overlapping tiles fully covering the central part (with 4 and 3 corresponding to α and β, respectively). A recognizer would be built for each tile, and recognition would be performed tile-by-tile.*

One advantage of decomposing the central part into several regions is that the recognizer constructed for each tile will likely have better performance, since it must only deal with limited angular coverages in α and β. One disadvantage lies in the number of recognizers one must construct.

Figure 6.9 gives a bird's eye view of the recognizer we build for any given region, such as a rectangular tile for a particular frequency band and for a particular polarization. The first block diagram concerns the "construction" of the corresponding sub-recognizer, which uses the LS data for all N_c classes to produce a target class model. For each of the N_c classes, one first produces feature vectors (FVs) [134, 208], and one then computes the "best" target class model from all the FVs.

The second block diagram concerns the "test" of the recognizer and its "operational use". In both cases, one first produces one FV (at a time) from the appropriate data for the region of interest. One then determines the class that the (sub-)recognizer assigns to this FV by using the corresponding target class model. The difference between test (TS) and operational use (operational data) is the availability of the ground truth for the TS, which allows one to quantify the performance of the (sub-)recognizer for the region considered.

If enough computational power is available, one can envision adjusting the cookie-cutter region on-the-fly. This would imply recomputing the FVs and the target class model on-the-fly, prior to testing the new FV of interest on the target class model.
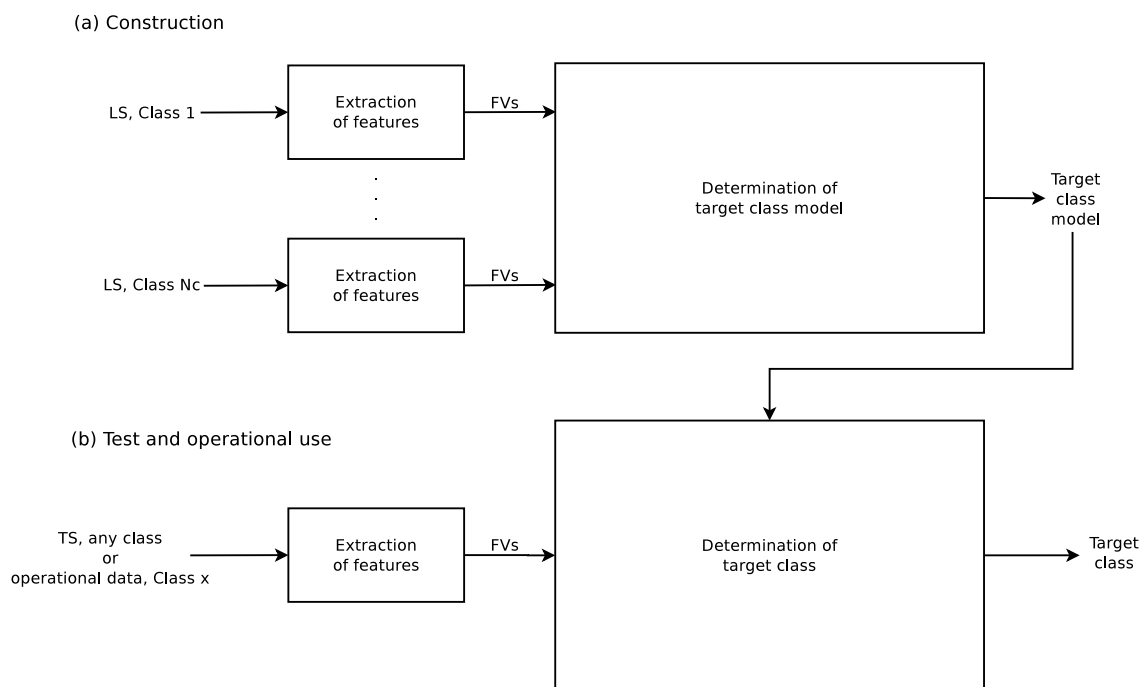
Figure 6.9: *Block diagrams summarizing the generic architecture of any of the sub-recognizers of the recognition stage (i.e. the recognizer) of each of the three ATR systems. (a) shows the successive steps in building the target class model, and (b) the successive steps in performing the recognition, either for testing (and performance evaluation) or for operational use.*

6.4 Block diagram of the recognizer

The input data of the recognizer are the images that we constructed from the bistatic complex radar cross-section (Chapter 5) of the targets of interest. The four targets of interest are a Beechcraft, an F117 fighter, an F16 fighter, and a Learjet. Each type of target corresponds to a particular target class. We thus consider $N_c = 4$ classes.

Each image is labelled a value for each of the parameters of the parameter space, which are the frequency band f, the polarization Pol, the aspect angle α, and the bistatic angle β. As described in Section 6.3, we divide the parameter space into tiles, and we build a recognizer for each tile. As explained in Chapter 5, we constructed images for the HH polarization only, for each of the four frequency bands, each of the three aspect angles, and several bistatic angles ranging from 6° to 160°. We arbitrarily divide the range of bistatic angle into 12 overlapping sectors, as described in Table 6.1. We thus build $4 \times 3 \times 12$ recognizers, one for each frequency band, and for each tile of the (α, β) plane.

Bistatic angular sector index	Bistatic angular sector (degrees)
1	(6, 43.5)
2	(18.5, 56)
3	(31, 68.5)
4	(43.5, 81)
5	(56, 93.5)
6	(68.5, 106)
7	(81, 118.5)
8	(93.5, 131)
9	(106, 143.5)
10	(118.5, 156)
11	(131, 168.5)
12	(143.5, 181)

Table 6.1: *Bistatic angular sectors considered.*

Figure 6.10 gives the block diagrams of the recognizer we build for any given tile. The first block diagram concerns the "construction" of the corresponding sub-recognizer, which uses the LS data for all N_c classes to produce a recognition "model" consisting of a list of extremely randomized trees (extra-trees). We describe the determination of the target class model in Section 6.6. For each of the N_c classes, one first produces feature vectors (FVs). Each FV consists in an ensemble of windows that we extract from each input image. We describe the extraction of windows in Section 6.5.

The second block diagram concerns the "test" of the sub-recognizer and its "operational use". In both cases, one first produces one FV (at a time) from the appropriate data for the tile of interest. One then propagates each FV through each of the extra-tree, thus assigning a class to each window of the FV for each extra-tree. A majority vote among the assigned classes determines the class that the (sub-)recognizer assigns to this FV. The difference between test (TS) and operational

(a) Construction

LS, Class 1 → Extraction of windows → Windows → Construction of extra-trees → Target class model (List of extra-trees)

⋮

LS, Class Nc → Extraction of windows → Windows

(b) Test and operational use

TS, any class or operational data, Class x → Extraction of windows → Windows → Propagation though extra-tree 1 → Assigned classes → Majority vote → Target class

⋮

Propagation though extra-tree T → Assigned classes
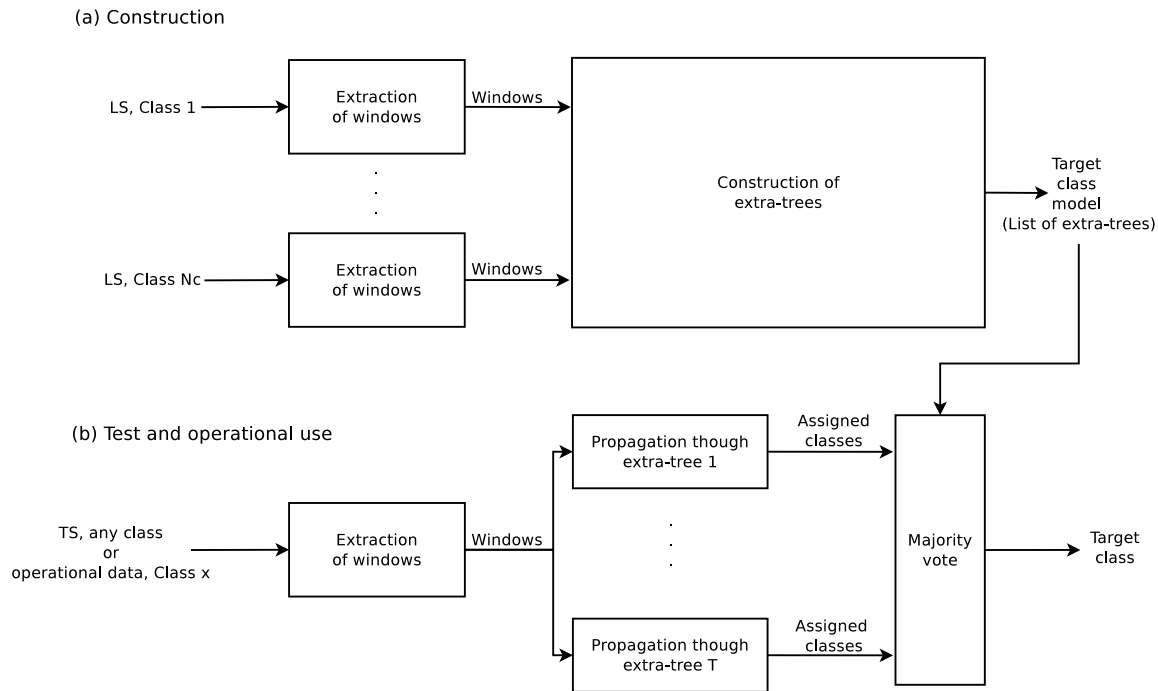
Figure 6.10: *Block diagrams summarizing the architecture of any of the sub-recognizers of the recognition stage. (a) shows the successive steps in building the target class model, and (b) the successive steps in performing the actual recognition, either for testing (and performance evaluation) or for operational use.*

use (operational data) is the availability of the ground truth for the TS, which allows one to quantify the performance of the recognizer for the tile considered.

The joint use of windows extracted from an image and of extra-trees was developed and tested by Marée for the classification/recognition of non-radar images of objects, and reported in [123, 124].

6.5 Production of feature vectors by window extraction

The first step of the recognizer, for both the construction of the target class model and the test of the target class model, consists in the production of feature vectors (FVs). Each FV consists in the pixel values inside a fixed number of windows which we extract out of each image. The method for the extraction of windows is reported in [126, 129].

For each image of the learning set (LS), we extract a large number N_{ls} of square windows of random sizes (constrained between $\alpha\%$ and $\beta\%$ of the image size), at random positions. Figure 6.11 shows an example of 4 windows that are extracted out of a particular radar image. We then resize each window to a fixed, given size $w \times h$, so that all windows are described by the same number of pixels. Each window is characterized by its pixel values i.e. $w \times h$ numerical values in the case of grayscale

images. Each window is also assigned the class of its parent image.
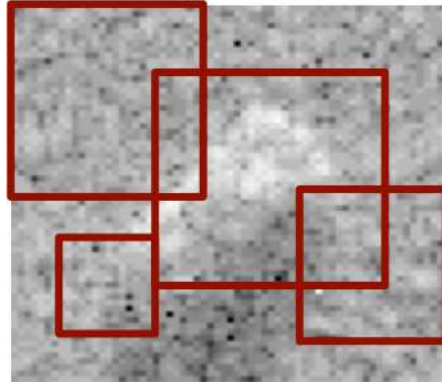
Figure 6.11: *Example of four windows that we extract out of a particular image.*

A similar process is repeated for the construction of the FV for any image of the test set (TS). The number of extracted windows can be different, and is denoted by N_{ts}. The locations of the windows extracted from images of the LS and for the TS can be different. The main difference is that each window is labelled, but only for quantifying the performance of the recognizer.

6.6 Determination of the target class model by extra-trees

In this section, we present the determination of the target class model from the feature vectors (FVs) that we extracted from the images of the learning set (LS). The target class model consists of an ensemble of extremely randomized decision trees (extra-trees). The first tree-based methods classified objects based on a single deterministic decision tree [25]. Then, tree-based methods started using ensemble of trees, called forests, to classify objects. Different methods to randomize the trees are used, such as bagging [26], random forests [27], and extra-trees [69]. A brief history of the different decision-trees methods appears in [124].

6.6.1 Deterministic decision tree

Before describing the concept of an extra-tree, we first briefly describe the classical (binary) deterministic decision tree. Below, we successively describe the construction of the tree and its use for classifying previously-unseen inputs, as illustrated in Fig. 6.12. A deterministic decision tree is a collection of "if-then" mutually exclusive decision rules that recursively separate objects of the input LS into disjoint subsets of objects, until each subset contains objects of (mainly) a single class (in case of fully-developed trees). When a subset contains objects of (mainly) a single class, it is called a terminal node, or leaf. The links between two nodes are called branches.

We first describe the construction of a (binary) decision tree. Let us consider that objects to be classified are characterized by two attributes a_1 and a_2, and belong either to class c_1 or c_2. At each node, a subset is separated into two subsets (since we deal with a binary tree) according to a decision rule performed over one of the attributes of the objects. For example, at the top node of Fig. 6.12, the objects of the learning set (LS) are separated into two subsets according to the value of their attribute a_1, either greater or smaller than a value v_1. In the example, the objects for which the value of a_1 is greater than v_1 all belong to class c_1. This terminal node, or leaf, is labelled as class c_1. The procedure is repeated for the subset of objects for which the attribute a_1 is smaller than v_1.

At each node of the decision tree, the best decision rule is applied. Different criteria, described in [54], exist for determining the best decision rule, *i.e.* for choosing the best attribute to be tested at a particular node, and the best corresponding threshold value for this attribute. The collection of rules constitutes the decision tree.
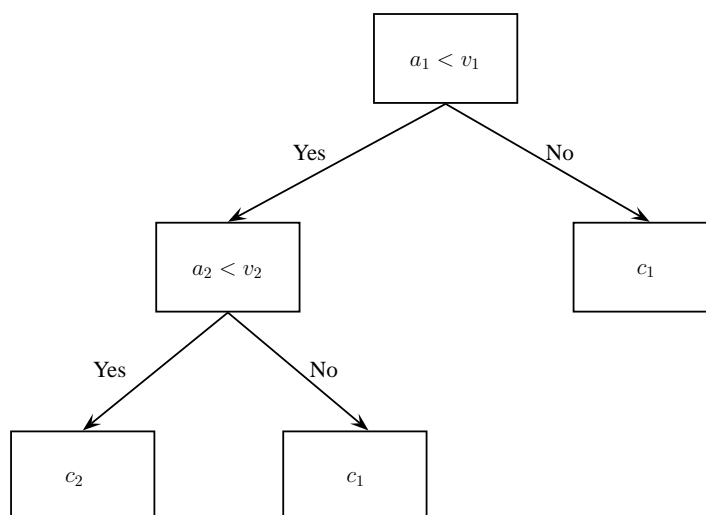
Figure 6.12: *Example of a decision tree [124].*

We continue with the use of the tree for the recognition of a previously-unseen object. During test (and operational use), an object of the test set (TS) is propagated through the trees, which means that, at each node, starting from the top node, the test that has been established at the time of construction is performed on the attributes describing the unknown object, until a leaf is reached. The class of this leaf becomes that of the unknown object.

6.6.2   Extremely randomized trees

An extremely randomized tree (extra-tree) is a randomized version of a decision tree. At each node of an extra-tree, the attribute is randomly chosen among the set of attributes describing the objects of the LS. The threshold value is also randomly chosen [124]. In the example of Fig. 6.12, the first node of the tree splits the input data according to attribute a_1 and the corresponding threshold value v_1. In the case of an extra-tree, both the attribute and its corresponding threshold value are randomly

chosen, while their choice is deterministic in the case of a decision tree.

The classification model consists in T extra-trees. Each extra-tree is built in the following way. Starting at the top node with the feature vectors (FVs), *i.e.* the windows that are extracted from the images of the LS, we build a fully-developed decision tree according to the classical top-down decision tree induction procedure [28]. The main difference between an extra-tree and other tree methods is that, while growing a tree, the extra-tree splits nodes by choosing both attributes and threshold values at random. At each node, a binary test compares the value of a pixel (graylevel intensity) at a fixed location within a window to a threshold value. In order to filter out irrelevant attributes, the filtering parameter k corresponds to the number of attributes (i.e. the number of pixels) chosen at random at each node, where k can take all possible values from 1 to the number of attributes describing each window of the FVs. For each of these k attributes, a pixel intensity value threshold is randomly chosen. The score of each binary test is then computed on the current subset of windows, according to an information criterion [220]. The best test among the k tests is chosen to split the current node. The procedure is repeated recursively on all subsets of windows until the tree is fully developed. In each terminal node, the class frequencies of windows of images of the LS that were propagated to that leaf are stored. We build the T fully-developed trees according to this scheme. (Images of the LS and their extracted windows are no longer required for test and operational use.)

6.6.3   Motivation for using extremely randomized trees

Various classification methods have been used to classify radar images of targets in radar automatic target recognition (ATR) (Section 2.3). These methods extract, from the images of the objects of interest, features that characterize these objects. The objects are then classified based on the extracted features. The more popular classifiers/recognizers used are the nearest neighbor (kNN) method, the support vector machine (SVM) method, and neural networks (NN).

Unlike these recognition methods, the extra-trees-based image classifier is generic in the sense that the algorithm only needs the (raw) images as input. No explicit feature is computed from the images, since the windows that we extract are not based on features of the objects of interest. Therefore, adding a new target class does not require to recompute any feature, thus limiting the overall processing time.

To our knowledge, few of the radar ATR methods based on images of targets published in the literature rely on the use of decision trees. However, it is empirically shown in [124] that extra-trees achieve a classification rate as high as that of other conventional classification techniques, such as SVM. Among the different tree-based classification methods, it is shown in [69] that classification results are higher for extra-trees than for classical decision trees. It is also empirically proven in [118, 124, 178, 179] that random decision trees and forests, and thus extra-trees, are as fast as other classification techniques. In [177], random trees are implemented on a GPU, thus making it available for real-time processing. Moreover, extra-trees do not need a fine tuning of the parameters, unlike other classification methods such as SVM

and NN. Extra-trees have also been successfully tested on conventional images, such as in [146, 147].

Furthermore, it has been empirically shown in [124] that the joint use of windows extraction and extra-trees is robust to the rotation of targets. Therefore, the joint use of windows extraction and of an ensemble of extremely randomized decision trees appears to be a promising classification technique.

The image classifier based on the joint use of windows extraction and extra-trees defined in [124] has been tested on numerous datasets of classical images, such as in [124, 125, 127, 128]. In order to validate the extra-trees-based method as a robust and accurate recognizer of radar images, we first test below the recognizer on the well-known MSTAR database. We compare the achieved recognition rates with the recognition rates of other ATR systems tested on the MSTAR dataset, and published in the literature.

6.7   Determination of the target class

During both test and operational use, we first produce a feature vector (FV) characterizing the input image. The FV is a set of N_{ts} windows from this image. We then propagate each window of the FV into each of the T extra-trees. The assigned classes of all windows at terminal nodes are aggregated, and the majority class is assigned to the image. This approach has also been extended for content-based image retrieval [130] and semantic segmentation [56].

6.8   Quantification of performance

We quantify the performance of the recognizer during the test phase, in the following way. The primary criterion is the error rate. The error rate is defined as the ratio of the number of images that are wrongly classified to the total number of images that are classified. The second criterion is the individual window error rate. The individual window error rate is defined as the ratio of the number of windows that are wrongly classified to the total number of windows that are classified.

The error rate and the individual window error rate are obtained from the confusion matrices. A confusion matrix is a two-dimensional matrix. The different true classes of the objects to be classified are each represented by a row, and the different classes assigned by the recognizer are each represented by a column. In the experiments performed below, the obtained confusion matrices are square, since we force the recognizer to assign a class to every image that we wish to classify. Each cell (i, j) of a confusion matrix represents the number of objects of the true class i that are labelled by the computed class j. The sum of all the elements in a row is equal to the number of objects that truly belong to the class of the row. The recognition rate for a target class i is the ratio between the number of objects of that class that are truly recognized, reported in cell (i, i), to the total number of objects of that class. The total recognition rate is the ratio of the sum of the diagonal elements of the confusion matrix to the sum of all the elements of the confusion

matrix. The total error rate is equal to one minus the total recognition rate. For the error rate, an object is an image of a target of interest, while, for the individual window error rate, an object is a window extracted from an image of a target of interest.

We choose the values of the parameters of the recognizer in order to remain computationally efficient. However, for two different sets of parameters, if both the error rates and the window error rates are equal, the set of parameters for which the error rate is achieved faster is preferred.

6.9 Recognition experiments on MSTAR images

We quantify the performance of the recognizer on images of the MSTAR data. We first describe the MSTAR data, and the six different sets of images we built for the recognition experiments. We then describe the parameters of the recognizer, and the recognition results we achieve for each of the six sets of images.

6.9.1 Description of MSTAR images

The MSTAR data is a well-known database that is collected and distributed under the DARPA Moving and Stationary Target Recognition program. The MSTAR database is shared by the synthetic aperture radar (SAR) ATR community. SAR produces images of targets with sufficient resolution (because of the high frequency used, usually in the GHz) to be classified [169, 171, 222].

The MSTAR data consist of X-band (10 GHz) SAR images of targets. We consider three targets of interest that are the BMP-2 and the BTR-70 armored personal carriers (APCs), and the T-72 tank. We also consider SLICY canonical targets that are defined in [175] as "a precisely designed and machined engineering test target containing standard radar reflector primitive shapes such as flat plates, dihedrals, trihedrals, and top hats". Images of clutter, *i.e.* containing "things" other than the targets of interest (BMP-2, BTR-70, T-72) and the SLICY targets, are also available. Figure 6.13 shows examples of images of each type.

Images of each of the three targets of interest were captured at two depression angles, which are 15° and 17°, over a full range of aspect angles, from 0° to 360°. Each image is of size 128 pixels × 128 pixels. Images of the SLICY target were captured at the depression angles of 15° and 30°. The clutter images were captured at the depression angle of 15°.

Note that the term "clutter" is used here in the sense used by the MSTAR community, *i.e.* for anything that is other than the targets of interest, whether man-made or natural.

6.9.2 Experimental sets of images

We consider the recognition of the three different targets of interest, in presence of clutter and/or SLICY targets. Each target of interest is considered here to be a class. SLICY targets are also considered to be a class. Even though it is not possible to

(a) *BMP-2 APC.*   **(b)** *BTR-70 APC.*   **(c)** *T-72 tank.*

(d) *SLICY target.*   **(e)** *CLUTTER.*   **(f)** *CLUTTER.*
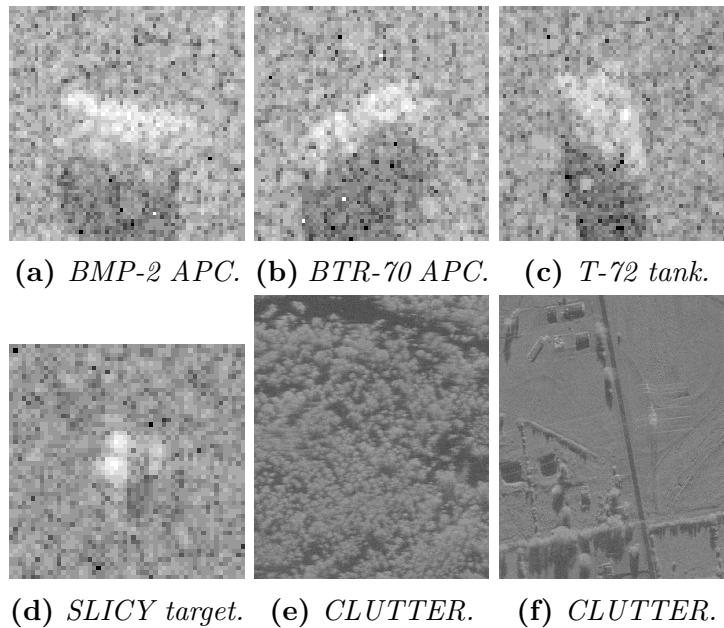
Figure 6.13: *Example SAR images of the various objects available in the MSTAR database and used for our recognition experiments.*

model the clutter, we call the class representing the clutter images the non-target class.

We make up six different sets of images. We first consider the recognition of the three targets of interest. We thus first exclusively consider images of the three targets of interest, *i.e.* images of the BMP-2 APC's, the BTR-70 APC's, and the T-72 tanks. The first set is made up of the raw images of the three targets of interest (128×128 pixels), as depicted in Table 6.2(a).

To get rid off the background speckle, we manually crop the raw images. The second set is made up of the cropped images (Table 6.2(b)). The cropped images are the central 64 pixels $\times$64 pixels of the raw images, since the target and its shadow are always located in the central part of the raw images.

We then rotate the images of the targets, in order to get rid off the aspect angle. The third set is made up of the images of the three targets of interest that we rotate to get all the targets pointing to the same direction (Table 6.2(c)). We thus assume that we know the orientation of the target. We perform the rotation by using the information provided in the header file of each image. We could use a pose estimator to get the azimuth angle for the rotation, but rotating the target using this *a priori* information is not necessary, as we will show in Section 6.9.4. It has also been empirically shown in [124] that the classifier is robust to the rotation of the targets. Furthermore, we also crop the images, for the same reason as for the second set. However, since the images are rotated, we now keep the central region of 80×80 pixels. More background speckle is present in the 80×80 images than in the 64×64 images. This additional background speckle is not a problem, as we will show when we discuss the results (Section 6.9.4).

(a)

(b)

(c)
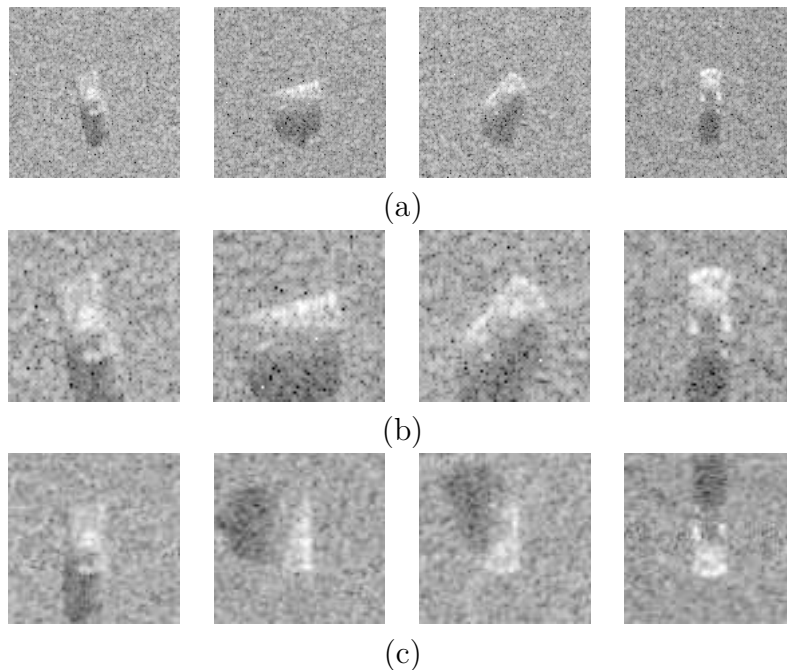
Table 6.2: *SAR images of BMP-2 targets at different aspect angles for each of the first three sets. (a)* 128×128 *raw images of the first set. (b) Cropped* 64×64 *images of the second set. (c) Cropped and rotated* 80×80 *images of the third set.*

We then consider the recognition of the three targets of interest in the presence of non-targets (*i.e.* clutter). The fourth set of images is thus made up of the images of the three targets of interest and the non-target images.

We then consider the recognition of the three targets of interest in the presence of SLICY targets, that act as false targets. The fifth set of images is thus made up of the images of the three targets of interest and the images of the SLICY targets.

Last, we consider the recognition of the three targets of interest in the presence of both SLICY targets, that act as false targets, and non-targets (*i.e.* clutter). The sixth set of images is thus made up of the images of the three targets of interest, the images of the SLICY targets, and the non-target images.

For each of the six sets, we choose to put all the images obtained for depression angles of 17° and 30° in the learning set (LS), and to put all the images obtained for a depression angle of 15° in the test set (TS). For the non-target images, since the available images were all taken at a depression angle of 15°, we choose to put half of the images in the LS, and the other half in the TS. This partitioning of the images into a LS and a TS is similar to the partitionings of the MSTAR images that are reported in the literature. We are thus able to compare our results to those reported in the literature. Table 6.3 gives, for each set, the number of images for each class, for both the LS and the TS.

	BMP-2	BTR-70	T-72	NON-TARGETS	SLICY	Total
Set 1: LS/TS	698/587	233/196	463/582	0/0	0/0	1394/1365
Set 2: LS/TS	698/587	233/196	463/582	0/0	0/0	1394/1365
Set 3: LS/TS	698/587	233/196	463/582	0/0	0/0	1394/1365
Set 4: LS/TS	698/587	233/196	463/582	50/50	0/0	1444/1415
Set 5: LS/TS	698/587	233/196	463/582	0/0	288/274	1682/1639
Set 6: LS/TS	698/587	233/196	463/582	50/50	288/274	1732/1689

Table 6.3: *Number of images of each class (BMP-2, BTR-70, T-72, NON-TARGETS, and SLICY) in each prepared set, for the LS and the TS. For each class, the number of images is indicated, both for the LS and the TS.*

6.9.3 Parameters of the recognizer

The different parameters of the recognizer that we can tune are the number $N_{ls} = N_{ts}$ of windows extracted from each image, the random sizes of the windows, the number T of trees of the target class model, and the number k of random tests performed at each node of each tree.

For the first three sets, and to stay computationally efficient, we choose to train and test the recognizer by extracting either 10 or 100 windows per image, *i.e.* $N_{ls} = N_{ts} \in \{10, 100\}$. The size of each window is randomly taken between $\alpha = 90\%$ and $\beta = 100\%$ of the size of the image. Each window is then resized to get only $w \times h = 16 \times 16$ pixel windows. The target class model consists of either 10 or 20 extra-trees, *i.e.* $T \in \{10, 20\}$, here again for computational reasons. We consider different values of the number of random tests, *i.e.* $k \in \{1, 16, 256\}$. Therefore, two recognition experiments differ by one or more of the following parameters: the number of windows extracted per image, the number of trees of the target class model, and the number of tests performed at each node.

The parameters of the recognition experiments we perform on the last three sets are those that give the best results for the first three sets.

6.9.4 Recognition results

This section describes the results achieved for the recognition experiments we perform on each of the six sets of the MSTAR data, for the different sets of parameters. We assign to each recognition experiment a label $n_1.n_2$, where n_1 corresponds to the set of images, and n_2 corresponds to the set of parameters we use for the experiment.

Recognition results for Set 1

We consider the recognition of the three targets of interest by using the raw 128×128 images of the three targets of interest only. Table 6.4 gives the error rate achieved for each set of parameters. The lowest achieved error rate is just less than 20% (Experiment 1.5). This is due to the presence of background speckle in the images. Recall that only the central 64×64 pixels contain relevant information, and that, here, we consider all the 128×128 pixels of the image. One must notice that the error rate does not diminish significantly, neither when taking more windows ($N_{ls} = 500$ instead of $N_{ts} = 100$), nor when taking more trees ($T = 20$ instead of $T = 10$). However, taking more tests ($k = 256$ instead of $k = 1$) helps to improve the results, even though we cannot, to keep our method computationally efficient, consider too many tests.

Error rates per experiment				
Experiment	$N_{ls} = N_{ts}$	T	k	Error rate
1.1	100	10	1	42.56%
1.2	100	10	16	32.97%
1.3	100	10	256	21.47%
1.4	100	20	256	21.61%
1.5	500	10	256	19.34%

Table 6.4: *Five distinct experiments carried out using the first set of MSTAR SAR images. The table shows, for each experiment, the values of the parameters $N_{ls} = N_{ts}$, T, and k, and the achieved error rate.*

We show the confusion matrix obtained for Experiment 1.5 in Table 6.5. The confusion matrix shows that the algorithm is unable to recognize BMP-2 APCs. The fact that it classifies BMP-2 APCs as T-72 tanks and not as BTR-70 APCs indicates that the background speckle plays a major role in the classification of the targets.

Confusion matrix for Experiment 1.5				
True vs. computed	BMP-2	BTR-70	T-72	Recognition rate per target
BMP-2	346	14	227	$346/587 = 58.94\%$
BTR-70	1	184	11	$184/196 = 93.88\%$
T-72	9	2	571	$571/582 = 98.11\%$
Total	356	200	809	
Mean error rate = 19.34%				

Table 6.5: *Confusion matrix obtained for the experiment of Table 6.4 giving the lowest error rate, i.e. 19.34% (Experiment 1.5).*

Recognition results for Set 2

We consider the recognition of the three targets of interest by using the cropped 64×64 images of the three targets of interest only. Table 6.6 gives the error rate achieved for each set of parameters. The lowest achieved error rate is just less than

1.5% (Experiment 2.3). The difference with the lowest achieved error rate of Set 1 is explained by the cropping of the images, which results in less speckle in each image. The same conclusions can be drawn concerning the influence of the different parameters.

Error rates per experiment				
Experiment	$N_{ls} = N_{ts}$	T	k	Error rate
2.1	100	10	1	34.72%
2.2	100	10	16	10.53%
2.3	100	10	256	1.42%
2.4	100	20	1	36.99%
2.5	100	20	256	1.48%
2.6	10	10	1	32.16%
2.7	10	10	16	13.20%
2.8	10	10	256	5.86%
2.9	10	20	16	11.16%
2.10	10	20	256	4.72%

Table 6.6: *Ten distinct experiments carried out using the second set of MSTAR SAR images. The table shows, for each experiment, the values of the parameters $N_{ls} = N_{ts}$, T, and k, and the achieved error rate.*

We show the confusion matrix obtained for Experiment 2.3 in Table 6.7. The confusion matrix shows that the algorithm is able to recognize the three targets of interest.

Confusion matrix for Experiment 2.3				
True vs. computed	BMP-2	BTR-70	T-72	Recognition rate per target
BMP-2	578	0	9	578/587 = 98.47%
BTR-70	2	584	2	584/588 = 99.32%
T-72	12	0	570	570/582 = 97.94%
Total	592	584	581	
Mean error rate = 1.42%				

Table 6.7: *Confusion matrix obtained for the experiment of Table 6.6 giving the lowest error rate, i.e. 1.42% (Experiment 2.3).*

Recognition results for Set 3

We consider the recognition of the three targets of interest by using the cropped and rotated 80×80 images of the three targets of interest only. Table 6.8 gives the error rate achieved for each set of parameters. The lowest achieved error rate is just less than 1% (Experiment 3.3). The rotation of the images improves somewhat the error rate. The same conclusions can be drawn concerning the influence of the different parameters.

We show the confusion matrix obtained for Experiment 3.3 in Table 6.9. All three targets are recognized almost perfectly.

Error rates per experiment				
Experiment	$N_{ls} = N_{ts}$	T	k	Error rate
3.1	100	10	1	22.86%
3.2	100	10	16	6.15%
3.3	100	10	256	0.88%
3.4	100	20	1	23.44%
3.5	100	20	16	5.64%
3.6	100	50	16	5.64%
3.7	10	10	1	30.40%
3.8	10	10	16	15.82%
3.9	10	10	256	6.08%
3.10	10	20	256	3.96%
3.11	10	50	256	3.37%

Table 6.8: *Eleven distinct experiments carried out using the third set of MSTAR SAR images. The table shows, for each experiment, the values of the parameters $N_{ls} = N_{ts}$, T, and k, and the achieved error rate.*

Confusion matrix for Experiment 3.3				
True vs. computed	BMP-2	BTR-70	T-72	Recognition rate per target
BMP-2	585	0	2	585/587 = 99.66%
BTR-70	0	194	2	194/196 = 98.98%
T-72	8	0	574	574/582 = 98.63%
Total	592	584	581	
Mean error rate = 0.88%				

Table 6.9: *Confusion matrix obtained for the experiment of Table 6.8 giving the lowest error rate, i.e. 0.88% (Experiment 3.3).*

Recognition results for Set 4

We consider the recognition of the three targets of interest in presence of non-targets. In this case, non-target is considered as a particular class of target. Table 6.10 gives the error rate achieved for each set of parameters. The lowest achieved error rate is just less than 4% (Experiment 4.4). A comparison with the corresponding sets of parameters of the best results achieved for the second set of MSTAR images shows that the addition of non-target images raises the error rate by about 4 to 10 percent, depending on the parameters.

We show the confusion matrix obtained for Experiment 4.4 in Table 6.11. All three targets are recognized almost perfectly, except for the BTR-70. Non-targets are perfectly classified. However, no conclusion can really be reached as the number of non-target images is quite small with respect to the number of images of the other targets. Let us emphasize that the non-target class is hard to characterize. For example, Fig. 6.13 shows two sample images of non-target images that are very different.

Error rates per experiment				
Experiment	$N_{ls} = N_{ts}$	T	k	Error rate
4.1	100	10	256	4.24%
4.2	10	10	256	10.04%
4.3	100	10	16	14.98%
4.4	100	20	256	3.6%
4.5	100	20	16	15.62%
4.6	10	10	16	23.46%

Table 6.10: *Six distinct experiments carried out using the fourth set of MSTAR SAR images. The table shows, for each experiment, the values of the parameters $N_{ls} = N_{ts}$, T, and k, and the achieved error rate.*

Confusion matrix for Experiment 4.4					
True vs. computed	BMP-2	BTR-70	NON-TARGET	T-72	Recognition rate per target
BMP-2	579	0	0	8	579/587 = 98.64%
BTR-70	28	165	0	3	165/196 = 84.18%
NON-TARGET	0	0	50	0	50/50 = 100.00%
T-72	12	0	0	570	570/582 = 97.94%
Total	619	165	50	573	
Mean error rate = 3.60%					

Table 6.11: *Confusion matrix obtained for the experiment of Table 6.10 giving the lowest error rate, i.e. 3.60% (Experiment 4.4).*

Recognition results for Set 5

We consider the recognition of the three targets of interest in presence of SLICY targets that act as false targets. In this case, SLICY targets are considered as a particular class. Table 6.12 gives the error rate achieved for each set of parameters. The lowest achieved error rate is just less than 2.5% (Experiment 5.4). A comparison with the corresponding sets of parameters of the best results achieved for the second set of MSTAR images shows that the addition of images of SLICY targets raises the error rate by about 2 to 10 percent, depending on the parameters.

We show the confusion matrix obtained for Experiment 5.4 in Table 6.13. All three targets of interest and SLICY targets are recognized almost perfectly, except for the BTR-70.

Recognition results for Set 6

We consider the recognition of the three targets of interest in presence of both SLICY targets and non-target. In this case, SLICY targets are considered as a

Error rates per experiment				
Experiment	$N_{ls} = N_{ts}$	T	k	Error rate
5.1	100	10	256	3.11%
5.2	10	10	256	9.15%
5.3	100	10	16	13.79%
5.4	100	20	256	2.26%
5.5	100	20	16	13.24%
5.6	10	10	16	22.64%

Table 6.12: *Six distinct experiments carried out using the fifth set of MSTAR SAR images. The table shows, for each experiment, the values of the parameters $N_{ls} = N_{ts}$, T, and k, and the achieved error rate..*

Confusion matrix for Experiment 5.4					
True vs. Computed	BMP-2	BTR-70	SLICY	T-72	Recognition rate per target
BMP-2	582	0	0	5	582/587 = 99.15%
BTR-70	17	174	0	5	174/196 = 88.78%
SLICY	0	1	273	0	273/274 = 99.64%
T-72	9	0	0	573	573/582 = 99.45%
Total	608	175	273	583	
Mean error rate = 2.26%					

Table 6.13: *Confusion matrix obtained for the experiment of Table 6.12 giving the lowest error rate, i.e. 2.26% (Experiment 5.4).*

particular class of target, and non-target as another class. Table 6.14 gives the error rate achieved for each set of parameters. The lowest achieved error rate is just less than 3.5% (Experiment 5.4). A comparison with the corresponding sets of parameters of the best results achieved for the second set of MSTAR images shows that the addition of images both SLICY targets and non-targets raises the error rate by about 3 to 8 percent, depending on the parameters.

We show the confusion matrix obtained for Experiment 6.4 in Table 6.15. All three targets of interest, SLICY targets, and non-targets are recognized almost perfectly, except for the BTR-70.

Discussion of the recognition results achieved for the MSTAR images

We considered the recognition of the three targets of interest, for different versions of the images of the MSTAR data. The lowest error rate achieved for Set 1 (raw images) is of about 20%, which is very high. The lowest error rate achieved for Set 3 (cropped and rotated images) is better than the lowest error rate achieved for Set 2 (cropped images). However, since we needed to rotate the images to obtain images

Error rates per experiment				
Experiment	$N_{ls} = N_{ts}$	T	k	Error rate
6.1	100	10	256	3.43%
6.2	10	10	256	9.71%
6.3	100	10	16	14.32%
6.4	100	20	256	3.43%
6.5	100	20	16	13.74%
6.6	10	10	16	22.02%

Table 6.14: *Six distinct experiments carried out using the sixth set of MSTAR SAR images. The table shows, for each experiment, the values of the parameters $N_{ls} = N_{ts}$, T, and k, and the achieved error rate.*

Confusion matrix for Experiment 6.4						
True vs. Computed	BMP-2	BTR-70	NON-TARGET	SLICY	T-72	Recognition rate per target
BMP-2	580	0	0	0	7	580/587 = 98.81%
BTR-70	24	170	0	0	2	170/196 = 86.73%
NON-TARGET	0	0	46	4	0	46/50 = 92.00%
SLICY	0	1	7	266	0	266/274 = 97.08%
T-72	13	0	0	0	569	569/582 = 97.77%
Total	617	171	53	270	578	
Mean error rate = 3.43%						

Table 6.15: *Confusion matrix obtained for the experiment of Table 6.14 giving the lowest error rate, i.e. 3.43% (Experiment 6.4).*

of Set 3, we can consider that the most significant result is the error rate of 1.42% computed for Set 2. Eliminating as much background speckle as possible from the images is nevertheless essential to get high recognition rates. The elimination of background speckle is the only image pre-processing step we used.

We then considered the recognition of the three targets of interest in presence of non-targets (Set 4), SLICY targets (Set 5), or both (Set 6). Results show that the addition of non-target images, SLICY target images, or both, increases the error rate by about 2% to 4%. Our method has thus proven to be robust for recognizing images of targets in the presence of images of both non-targets and SLICY targets. However, it must be emphasized that, since the number of images of the non-target class is small, the non-target class cannot be considered as completely characterized. Therefore, one must take the achieved results with extreme care.

Comparing the classification rates achieved by our method with the results achieved

by other methods reported in the literature (Section 2.3) is difficult in the sense that different versions of the MSTAR database are used by the various automatic target recognition (ATR) methods reported in the literature. However, when comparing our best error rate, 3%, with error rates obtained by ATR methods published in the literature, we can say that the extra-trees-based method produces one of the lowest error rates reported (between 1% and 9%). Furthermore, the extra-trees-based method does only need to crop the images in order to reduce the amount of speckle on the images. No explicit feature extraction is needed, since the algorithm classifies images based on the raw values of their pixels. Moreover, the algorithm remains generic in the sense that adding a new class does not imply to recompute new features. This is a major difference with almost all existing algorithms (listed in Section 2.3), which need to compute features.

As discussed in Section 6.6.3, a tree-based recognizer is usually faster than other recognizers based on neural networks or support vector machines. Testing the model on a few hundred SAR images only requires between a few seconds and one minute on a regular computer (a laptop with 4 Gb of RAM, equipped with a dual-core processor working at 2 GHz), depending on the parameters. The method is thus computationally efficient.

6.10   Recognition experiments on ONERA images

We now perform the recognition of the four targets of interest by using the radar images of the targets of interest. We constructed the images of these targets from the bistatic complex radar cross-section (BS-CRCS) of these targets (Chapter 5). The BS-CRCS of these targets was extracted from signals acquired in the anechoic chamber at ONERA (Chapter 4).

6.10.1   Experimental sets of images

We described in Chapter 5 the construction of the radar images of four targets of interest from the BS-CRCS of these targets at various frequencies, various bistatic angles, various azimuth angles, and various elevation angles. The four targets of interest are a Beechcraft, an F117 fighter, an F16 fighter, and a Learjet. Each target is considered as a separate class.

According to the recognizer we described in Section 6.4, we build one recognizer for each tile of the parameter space into which we express the images of the targets. We explained in Section 6.4 that the parameters of the parameter space of the images are the frequency band, the aspect angle α, and the bistatic angle β. We constructed images for four different frequency bands and three different aspect angles. Images that we constructed from values of the BS-CRCS computed at the lower half of a frequency band belong to the learning set (LS), and images that we constructed from values of the BS-CRCS computed at the upper half of the same frequency band belong to the test set (TS)

As shown in Table 6.1, we arbitrarily divided the range of bistatic angle into 12 overlapping bistatic angular sectors. We do not use the bistatic angular sectors 11 and

12 in our recognition experiments for the following reasons. For sector 11, not enough images are constructed since the bistatic angular sector is partly defined for bistatic angles greater than the maximum available bistatic angle (160°). For sector 12, no image can be constructed over that sector. Indeed, since an image is constructed from values of the BS-CRCS that are extracted for a variation of the bistatic angle of at least 20° wide, any potential constructed image belonging to sector 12 would need values of the BS-CRCS extracted for a bistatic angle ranging from 143.5° to 163.5°. However, values of the BS-CRCS are extracted for a maximum bistatic angle of 160°.

In the recognition experiments on MSTAR images, we showed that the recognition method we use is insensitive to the rotation of the targets. We thus consider that images of the same type of target computed for different azimuth angles θ and different elevation angles ϕ of the target belong to the same class.

We thus consider $4 \times 10 = 40$ tiles. We build one recognizer for each tile. Table 6.16 indicates, for both the LS and the TS, the number of images per bistatic angular sector, for each frequency band.

Frequency band	Number of images per angular sector	
	LS	TS
FB1: $[20; 80]$ MHz	648	1152
FB2: $[190; 250]$ MHz	1260	1134
FB3: $[450; 550]$ MHz	1458	729
FB4: $[1.2; 1.30]$ MHz	1404	468

Table 6.16: *Number of images per angular sector, for each frequency band, for both the LS and the TS.*

6.10.2 Parameters of the recognizer

We tune the recognizer with the same values of the parameters that we used for the recognition of the MSTAR images. The values for each of the parameters are:

- the number of windows we extract from each image of the LS and from each image of the TS is $N_{ls} = N_{ts} \in \{10, 100\}$,

- the size of each window is taken between $\alpha = 90\%$ and $\beta = 100\%$ of the size of the original image; each window is resized to get 16×16 pixels windows,

- the number of trees $T \in \{1, 10\}$,

- the number of possible tests considered at each node of each tree $k \in \{1, 16, 256\}$.

6.10.3 Recognition results

In this section, we present the results obtained for the recognition of the four targets of interest by using their constructed radar images. As explained in Section 6.4, we build a recognizer for each of the four frequency bands (FB1, FB2, FB3, and FB4),

and for each of the ten bistatic angular sectors.

We first present the recognition results achieved per frequency band, for all bistatic angular sectors. We then present, for each frequency band, the recognition results achieved for each of the ten bistatic angular sectors considered.

Recognition results per frequency band

We show below that the error rates are of the same order for each bistatic angular sector. We thus present, for each frequency band (FB), the results achieved for the first bistatic angular sector. We assign each recognition experiment a number whose first digit corresponds to the FB, and whose second digit corresponds to the set of parameters we use for the experiment.

Table 6.17 shows the error rates we achieve for the recognition of images for the first frequency band, FB1 ($[20; 80]$ MHz). As for the MSTAR data, the error rate decreases more with the number of tests k than with the number of extracted windows $N_{ls} = N_{ts}$, or with the number of trees T. The error rates are all very high, ranging from 58% to 68%. This is not surprising, since both the range resolution and the cross-range resolution are of the order of the characteristic dimension of the airplanes.

Error rates per experiment for FB1				
Experiment	$N_{ls} = N_{ts}$	T	k	Error rate
1.1	10	1	1	68.34%
1.2	10	1	16	67.30%
1.3	10	1	256	62.65%
1.4	10	10	1	65.91%
1.5	10	10	16	66.69%
1.6	10	10	256	60.11%
1.7	100	1	1	64.84%
1.8	100	1	16	65.73%
1.9	100	1	256	58.55%
1.10	100	10	1	65.74%
1.11	100	10	16	61.72%
1.12	100	10	256	63.41%

Table 6.17: *Twelve distinct experiments carried out using the ONERA images at frequency band FB1 ($[20; 80]$ MHz). The table shows, for each experiment, the values of the parameters $N_{ls} = N_{ts}$, T, and k, and the achieved error rate.*

Table 6.18 shows the confusion matrix obtained for Experiment 1.9, which is the best error rate obtained for FB1. The table shows that the four targets are not evenly recognized, with the F117 being the most accurately recognized target, while the Learjet is the least accurately recognized target. This might be explained by the fact that the F117 has a particular shape that is very distinct from the shape of the other airplanes. Indeed, we showed in Chapter 3 that the shape plays an important role at

these frequencies.

Confusion matrix for Experiment 1.9					
True vs. computed	Beech	F117	F16	Learjet	Recognition rate per target
Beech	512	374	207	59	$512/1152 = 44.44\%$
F117	82	673	366	31	$673/1152 = 58.42\%$
F16	242	426	431	53	$431/1152 = 37.41\%$
Learjet	532	287	39	294	$294/1152 = 25.52\%$
Total	1368	1760	1043	437	
Mean error rate = 58.55%					

Table 6.18: *Confusion matrix obtained for the experiment of Table 6.17 giving the lowest error rate, i.e.* 58.55% *(Experiment 1.9).*

Table 6.19 shows the error rates we achieve for the recognition of images for the second frequency band, FB2 ($[190; 250]$ MHz). The error rates are all very low, ranging from 0% to 4%. This means that, at these frequencies, the range resolution and the cross-range resolution are low enough to be able to distinguish among the different airplanes.

As we described in Section 6.8, another indicator of the good performance of the algorithm is the error rate for each individual window. One can see that, even though the individual window error rate is high, the total error rate can be very low. The individual window error rate decreases much more with the number of trees T than with the number of tests k, or with the number of windows $N_{ls} = N_{ts}$. Indeed, increasing the number of windows does not affect the correct classification of a particular window. Table 6.20 shows the (perfect) confusion matrix obtained for any of the Experiments 2.5 to 2.12, which all achieve error rates of 0%.

Tables 6.21 and 6.23 show the error rates we achieve for the recognition of images for the third frequency band, FB3 ($[450; 550]$ MHz), and the fourth frequency band, FB4 ($[1.2; 1.3]$ GHz), respectively. The error rates are all very low, ranging from 0% to 4%. As expected, both the error rate and the individual window error rates are better for the FB3 than for FB2, since the range resolution and the cross-range resolution are smaller for images constructed for FB3 than for images constructed for FB2. The reason why both the error rates and the individual window error rates are worse for FB4 than for FB2 is that, for FB4, the ratio between the range resolution and the cross-range resolution of the images is comprised between $1/2.9$ and 2.9 (Chapter 5), in order to construct a sufficient number of images.

Tables 6.22 and 6.24 show the confusion matrix obtained for any experiment from 3.5 to 3.12, and from 4.4 to 4.12, respectively, which all achieve error rates of 0%. The recognition is thus perfect.

Error rates and individual window error rates per experiment for FB2					
Experiment	$N_{ls} = N_{ts}$	T	k	Error rate	Individual window error rate
2.1	10	1	1	3.88%	29.81%
2.2	10	1	16	0.99%	20.76%
2.3	10	1	256	0.68%	17.40%
2.4	10	10	1	0.07%	9.72%
2.5	10	10	16	0%	5.69%
2.6	10	10	256	0%	4.77%
2.7	100	1	1	0%	17.07%
2.8	100	1	16	0%	9.53%
2.9	100	1	256	0%	7.35%
2.10	100	10	1	0%	2.63%
2.11	100	10	16	0%	0.99%
2.12	100	10	256	0%	0.71%

Table 6.19: *Twelve distinct experiments carried out using the ONERA images at frequency band FB2 ([190; 250] MHz). The table shows, for each experiment, the values of the parameters $N_{ls} = N_{ts}$, T, and k, and the achieved error rate.*

Confusion matrix for Experiments 2.5 to 2.12					
True \Given by model	Beech	F117	F16	Learjet	Recognition rate per target
Beech	1134	0	0	0	1134/1134 = 100%
F117	0	1134	0	0	1134/1134 = 100%
F16	0	0	1134	0	1134/1134 = 100%
Learjet	0	0	0	1134	1134/1134 = 100%
Total	1134	1134	1134	1134	
Mean error rate = 0%					

Table 6.20: *Confusion matrix obtained for the experiments of Table 6.19 giving the lowest error rate, i.e. 0% (Experiments 2.5 to 2.12).*

Error rates and individual window error rates per experiment for FB3					
Experiment	$N_{ls} = N_{ts}$	T	k	Error rate	Individual window error rate
3.1	10	1	1	1.75%	24.40%
3.2	10	1	16	0.65%	17.86%
3.3	10	1	256	0.21%	15.11%
3.4	10	10	1	0.04%	7.44%
3.5	10	10	16	0%	3.82%
3.6	10	10	256	0%	3.29%
3.7	100	1	1	0%	14.18%
3.8	100	1	16	0%	7.26%
3.9	100	1	256	0%	5.87%
3.10	100	10	1	0%	1.49%
3.11	100	10	16	0%	0.52%
3.12	100	10	256	0%	0.39%

Table 6.21: *Twelve distinct experiments carried out using the ONERA images at frequency band FB3 ([450; 550] MHz). The table shows, for each experiment, the values of the parameters $N_{ls} = N_{ts}$, T, and k, and the achieved error rate.*

Confusion matrix for Experiments 3.5 to 3.12					
True \Given by model	Beech	F117	F16	Learjet	Recognition rate per target
Beech	729	0	0	0	$729/729 = 100\%$
F117	0	729	0	0	$729/729 = 100\%$
F16	0	0	729	0	$729/729 = 100\%$
Learjet	0	0	0	729	$729/729 = 100\%$
Total	729	729	729	729	
Mean error rate = 0%					

Table 6.22: *Confusion matrix obtained for the experiments of Table 6.21 giving the lowest error rate, i.e. 0% (Experiments 3.5 to 3.12).*

Error rates and individual window error rates per experiment for FB4					
Experiment	$N_{ls} = N_{ts}$	T	k	Error rate	Individual window error rate
4.1	10	1	1	4.22%	32.72%
4.2	10	1	16	1.13%	22.50%
4.3	10	1	256	1.12%	20.51%
4.4	10	10	1	0%	10.79%
4.5	10	10	16	0%	6.57%
4.6	10	10	256	0%	5.38%
4.7	100	1	1	0%	18.43%
4.8	100	1	16	0%	10.92%
4.9	100	1	256	0%	8.95%
4.10	100	10	1	0%	2.76%
4.11	100	10	16	0%	1.16%
4.12	100	10	256	0%	0.89%

Table 6.23: *Twelve distinct experiments carried out using the ONERA images at frequency band FB4 ([1.2; 1.3] GHz). The table shows, for each experiment, the values of the parameters $N_{ls} = N_{ts}$, T, and k, and the achieved error rate.*

Confusion matrix for Experiments 4.4 to 4.12					
True \Given by model	Beech	F117	F16	Learjet	Recognition rate per target
Beech	468	0	0	0	468/468 = 100%
F117	0	468	0	0	468/468 = 100%
F16	0	0	468	0	468/468 = 100%
Learjet	0	0	0	468	468/468 = 100%
Total	468	468	468	468	
Mean error rate = 0%					

Table 6.24: *Confusion matrix obtained for the experiments of Table 6.23 giving the lowest error rate, i.e. 0% (Experiments 4.4 to 4.12).*

Recognition results per bistatic angular sector

We stated at the beginning of this section that the recognition results are similar from one bistatic angular sector to the other. In this section, we show that it is indeed the case. For each frequency band and for each bistatic angular sector, we performed 12 recognition experiments, according to the same set of parameters as above. Figures 6.14, 6.15, 6.16, and 6.17 present the error rate for each bistatic angular sector, for FB1, FB2, FB3, and FB4, respectively. In each figure, the x-axis represents the index of the experiment. One can thus see that the recognition rates are similar for all bistatic angular sectors.
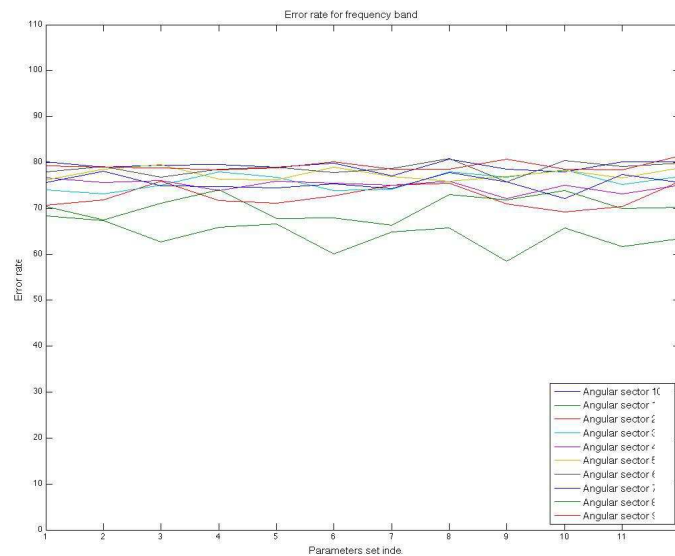
Figure 6.14: *Error rate as a function of the experiment index for frequency band FB1 (*[20; 80] *MHz), for each of the ten bistatic angular sectors considered.*

Discussion of the recognition results achieved for the ONERA images

We performed the recognition of the four targets of interest by constructing one recognizer for each frequency band (FB), and for each bistatic angular sector. We showed that the error rates we achieved for FB1 ([20; 80] MHz) are very high (at least 58%). This is due to the fact that the range resolution and the cross-range resolution of the constructed images of the targets are of the same order than the characteristic dimension of these targets. Any target is thus seen as a single bright point.

For FB2 ([190; 250] MHz), FB3 ([450; 550] MHz), and FB4 ([1.2; 1.3] GHz), we can achieve error rates of 0%, This is due to the higher range resolution and cross-range resolutions of the images of the targets. We also showed that even when the individual error rates are high (up to 18%), we can achieve error rates of 0%. This is due to the high number of windows that we extracted from each image. We also showed that the error rates are similar for all bistatic angular sectors.
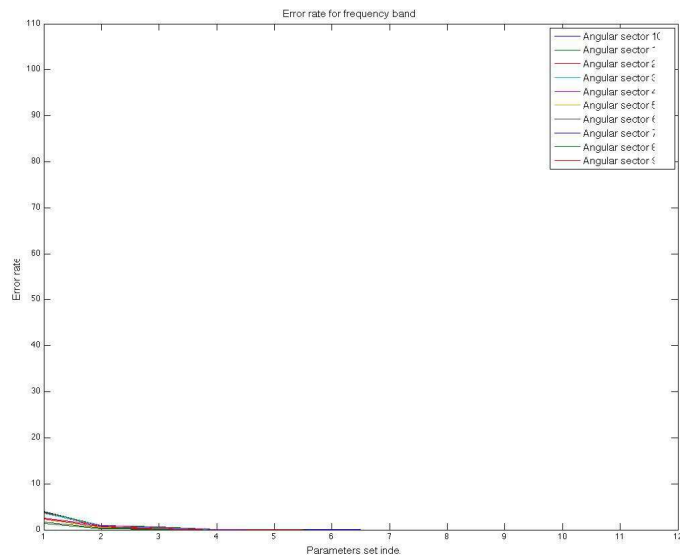
Figure 6.15: *Error rate as a function of the experiment index for frequency band FB2 ([190; 250] MHz), for each of the ten bistatic angular sectors considered.*
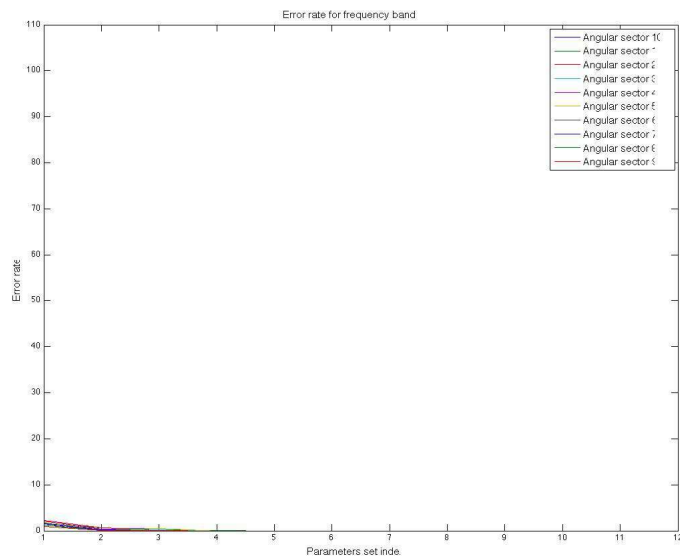
Figure 6.16: *Error rate as a function of the experiment index for frequency band FB3 ([450; 550] MHz), for each of the ten bistatic angular sectors considered.*
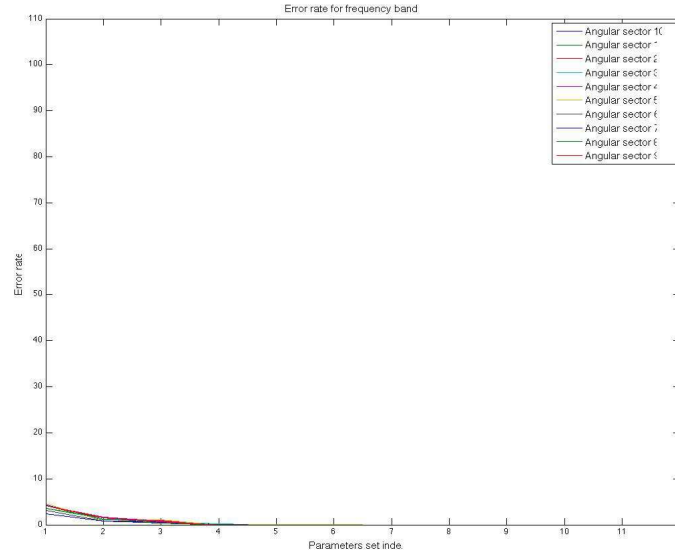
Figure 6.17: *Error rate as a function of the experiment index for frequency band FB4 ([1.2; 1.3] GHz), for each of the ten bistatic angular sectors considered.*

The difference between the error rates achieved for FB1 and for the three other FBs is also due to the difference in scattering mechanisms. Indeed, for FB1, the scattering mechanisms mainly depend on the volume of the targets while, for the three other FBs, the scattering mechanisms depend on the shape of the targets. Since the four targets of interest have different shapes but about the same volume, no clear difference could be made in the case of FB1.

6.11   Conclusion

In this chapter, we performed the recognition of targets by using their radar images. We first described the physical space into which airplanes fly, and the mapping from the physical space to the parameter space in terms of which we express the bistatic complex radar cross-section (BS-CRCS), the bistatic radar cross-section (BS-RCS), and the images of these airplanes. We defined the recognition strategy that we apply for the design of the recognition stage of each of the three automatic target recognition (ATR) systems according to this parameter space. According to the recognition strategy we defined, we build one recognizer for each tile of the parameter space.

The recognition method is based on the joint use of window extraction and extremely randomized trees (extra-trees). We used window extraction to produce feature vectors (FVs) out of each image, for both the learning set (LS) and the test set (TS). An FV consists in a set of windows extracted out of a particular image, each window being characterized by the values of the pixels inside this window. The target class model we built from the FVs of the LS consists of an ensemble of extra-trees. During test and operational use, the class of a target is determined by propagating the FV produced from the image of this target through each extra-tree of the target class model.

We motivated the use of such a recognition method by both its accuracy and efficiency that are as high as that of other classification methods. Moreover, it is, to our knowledge, one of the first use of tree-based methods in radar ATR.

We first tested our recognition method on the well-known MSTAR SAR data, which allowed us to compare the results achieved with the extra-trees-based recognition method to the results achieved by other recognition methods described in the literature. Even though the ATR methods reported in the literature use different versions of the MSTAR data, the comparison showed that the error rates we achieved using this recognition method (error rate comprised between 1% and 3% depending on the set of parameters) are among the best error rates reported in the literature. This proves that the extra-trees-based recognition method is an efficient method for the recognition of radar images.

We then tested the classification method on the ONERA images. According to the recognition strategy, we built one recognizer for each frequency band (FB) and for each bistatic angular sector. We considered neither the azimuth angle nor the elevation angle, since it was experimentally proven that the recognition method is insensitive to the rotation of targets. The error rates that we achieved are very high for FB1 ($[20; 80]$ MHz), of the order of 60%, due to the low resolution of the radar images compared to the characteristic dimension of the targets. The error rates that we achieved for FB2, FB3, and FB4 are very small (about 1% to 4%), and can even tend to 0% for some particular sets of parameters. We explain theses results by the higher resolutions of the images in these frequency bands. We also explain the difference of the recognition results for FB1 and the three other FBs by the fact that the scattering mechanisms for FB1 depend more on the volumes of the target than for the three other FBs, and by the fact that the targets of interest have about the same volumes, but different shapes.

We will compare the recognition results we achieved in this chapter for the recognition of targets from their radar images to the recognition results we achieve for the recognition of these targets from their radar cross-sections, either complex or real.

Chapter 7

Recognition of targets by using their bistatic RCS, either complex or real

Contents

In this chapter, we perform the recognition of targets by using either their bistatic complex radar cross-section (BS-CRCS) or their bistatic radar cross-section (BS-RCS). Section 7.1 states the motivation for the recognition of targets by using either their BS-CRCS or their BS-RCS. Section 7.2 describes the block diagram of the recognizer. Section 7.3 describes the production of the feature vectors. Section 7.4 describes the determination of the target class model. Section 7.5 describes the determination of the class of an unknown target based on the target class model. Section 7.6 presents

the criteria we use for the quantification of the performance of the method. Section 7.7 presents the recognition experiments we performed and the recognition rates we achieved. Section 7.8 concludes.

7.1 Motivation for the recognition of targets by using either their bistatic complex RCS or their bistatic RCS

In Chapter 6, we performed the recognition of targets by using their radar images. We constructed the radar images of targets from a two-dimensional (2D) array of values of bistatic complex radar cross-section (BS-CRCS) of these targets. The dimensions of this 2D array are the frequency and the bistatic angle.

However, in an operational outdoor passive-radar-based automatic target recognition (ATR) system, it is unlikely that both frequency diversity and angular diversity will be available. We explained the reasons for not being able to achieve this 2D diversity in Section 6.1.

To overcome the need for the necessary 2D diversity, and thus, the need for multiple transmitters (Tx's) and multiple receivers (Rx's), we perform, in this chapter, the recognition of targets directly according to either their BS-CRCS or their bistatic radar cross-section (BS-RCS). Therefore, we could *a priori* use a single (Tx,Rx) pair for the recognition of targets.

Figure 7.1 shows the block diagram of the implemented passive-radar-based automatic target recognition (ATR) system. The main difference with the ATR system discussed in Chapter 6 is that we do not construct images of the targets. We presented the extraction of both the BS-CRCS and the BS-RCS from raw data in Chapter 4. In this chapter, we design, implement, and test the recognition stage, *i.e.* the recognizer, of this ATR system.
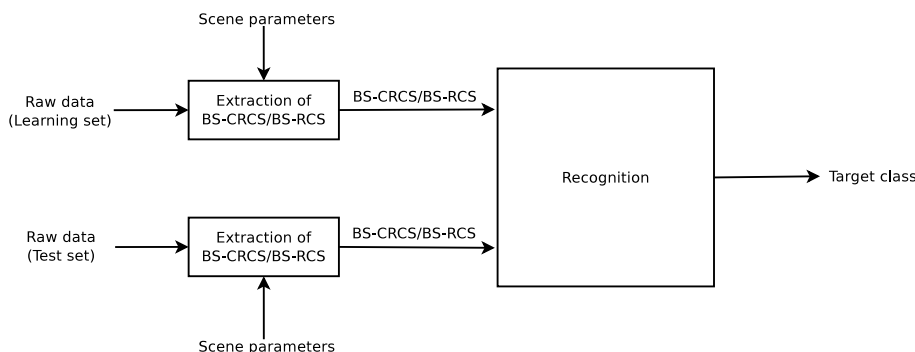
Figure 7.1: *Block diagram of our ATR system using the bistatic complex radar cross-sections or the bistatic radar cross-sections of targets.*

7.2 Block diagram of the recognizer

We explained our recognition strategy in Section 6.3. The input data of the recognizer are either the bistatic complex radar cross-section (BS-CRCS) or the bistatic radar cross-section (BS-RCS) of the targets of interest. The targets of interest are a Beechcraft, an F117 fighter, an F16 fighter, and a Learjet. Each type of target corresponds to a particular target class. We thus consider $N_c = 4$ classes.

Each value of BS-CRCS or BS-RCS is associated with a value of each of the parameters of the parameter space, which are the frequency band f, the polarization *Pol*, the aspect angle α, and the bistatic angle β (Section 6.2). As described in Section 6.3, we divide the parameter space into tiles, and we build a recognizer for each tile. As explained in Chapter 4, values of both the BS-CRCS and the BS-RCS are available for four polarizations, four frequency bands, three aspect angles, and several bistatic angles ranging from 6° to 160°. We arbitrarily divide the range of bistatic angle into 12 overlapping sectors, as described in Table 6.1, which we reproduce in Table 7.1 for convenience. We thus build $4 \times 4 \times 3 \times 12 = 576$ recognizers, one for each polarization, for each frequency band, and for each tile of the (α, β) plane.

For each frequency band, we use the values of both the BS-CRCS and the BS-RCS that we computed for the lower half of this frequency band for the learning set (LS), and the values of both the BS-CRCS and the BS-RCS that we computed for the upper half of this frequency band for the test set (TS).

Bistatic angular sector index	Bistatic angular sector (degrees)
1	(6, 43.5)
2	(18.5, 56)
3	(31, 68.5)
4	(43.5, 81)
5	(56, 93.5)
6	(68.5, 106)
7	(81, 118.5)
8	(93.5, 131)
9	(106, 143.5)
10	(118.5, 156)
11	(131, 168.5)
12	(143.5, 181)

Table 7.1: *Bistatic angular sectors considered.*

Figure 7.2 gives the block diagrams of the recognizer we build for any given tile. The first block diagram concerns the "construction" of the corresponding sub-recognizer, which uses the LS data for all N_c classes to produce a target class model consisting of a list of subspaces. We describe the determination of the target class model in Section 7.4. For each of the N_c classes, one first produces feature vectors (FVs). Each FV consists of an ensemble of values of either BS-CRCS or BS-RCS. We

describe the production of FVs in Section 7.3.
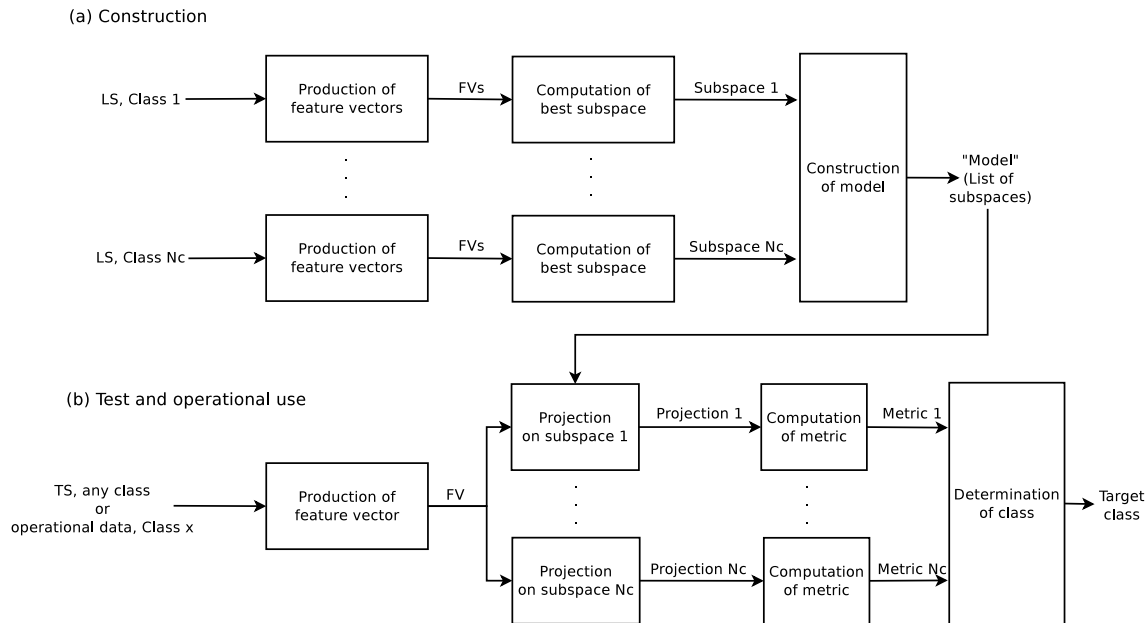
Figure 7.2: *Block diagrams summarizing the architecture of any of the sub-recognizers of the recognition stage. (a) shows the successive steps in building the target class model, and (b) the successive steps in performing the actual recognition, either for testing (and performance evaluation) or for operational use.*

The second block diagram concerns the "test" of the (sub-)recognizer and its "operational use". In both cases, one first produces one FV (at a time) from the appropriate data for the region of interest. One then projects this FV on all N_c subspaces, and computes some corresponding (projection) metric. The best metric value determines the class that the (sub-)recognizer assigns to this FV. The difference between test (TS) and operational use (operational data) is the availability of the ground truth for the TS, which allows one to quantify the performance of the (sub-)recognizer for the region considered.

7.3   Production of feature vectors

For each polarization, each frequency band, and a given region in the (α, β) plane of a specific class (*i.e.* with one of the indices 1 to N_c, or x), we must produce a set of feature vectors (FVs) from the data in this region, *i.e.* from (α, β) trajectories with either associated complex bistatic radar cross-section (BS-CRCS) values or associated bistatic radar cross-section (BS-RCS) values. The process for producing the FVs is the same for any region and for any class. The following description is thus generic for the data in one region of the (α, β) plane of one class.

The size N of each FV, and the number M of FVs for this generic region must obey the following constraints: (1) for subsequent processing, N must be the same for all classes; (2) M must be much larger than N to ensure adequate classification. The

value of N is chosen experimentally.

In the experiments described later, we build the FVs as follows. For each frequency band, each polarization, and each (α, β) region, the aspect angle α has a fixed value, since the targets were kept fixed in the anechoic chamber (Chapter 4). Thus, the variation is expressed only in terms of the bistatic angle β. Each FV represents the variation of either the BS-CRCS or the BS-RCS during a variation of the bistatic angle of $\beta = 25°$, for a fixed polarization pair and a fixed frequency. Several other ways of constructing the list and of sampling it can be envisioned, but this is not discussed here.

7.4 Determination of the target class model by vector spaces

The target class model consists in a list of vector spaces, simply called subspaces. We first describe the motivation for using subspace methods for recognition. We then describe the construction of the subspaces, and the determination of the size of each subspace.

7.4.1 Motivation for using subspace methods for recognition

In Chapter 6, the recognizer used to classify targets by using their radar images was based on extremely randomized trees. Here, we propose to use another recognition method based on subspace methods of pattern recognition [141]. Each class of target is represented by the best-approximating subspace.

Subspace methods of pattern recognition were introduced by Karhunen, Kohonen, Oja, and Watanabe, and are summarized in [141]. Subspace methods of pattern recognition are used in different applications, such as speech recognition [5, 79], and image recognition [230]. In the radar domain, subspace methods are mainly used for detection purposes [10–12, 16, 36, 70, 96]. In particular, [15, 29, 58, 176] use subspace methods for the detection of man-made objects in the context of foliage penetration (FOPEN) radar. To our knowledge, the use of subspace methods for radar automatic target recognition (ATR) is novel.

Subspace methods in the context of recognition present a particular advantage. Since each target class is characterized by a particular subspace, adding a new target class does not require to re-compute the entire target class model. Instead, the subspace representing the new target class just needs to be computed, and added to the target class model. Recognition techniques such as tree-based methods, support vector machines (SVM), and neural networks (NN) require to recompute the target class model when a new class is added.

7.4.2 Subspaces

We generically denote the feature vectors (FVs) for one region and one class by $\underline{x}_m$, with $m \in [1, M]$. A significant feature of our approach is that we represent the class

(for this region) by the best-approximating subspace, and that we project new FVs on it.

To give a true statistical spin to the problem, we consider that the $\underline{x}_m$'s are realizations of a random vector $\underline{x}$. The statistical correlation matrix of $\underline{x}$ is denoted by R_x^s and defined as $R_x^s = E\left\{\underline{x}\,\underline{x}^H\right\}$, where $E\{.\}$ is the expected-value operator. To go back to a deterministic formulation, one can approximate R_x^s as follows,

$$R_x^s \approx \frac{1}{M} \sum_{m=1}^{M} \underline{x}_m \underline{x}_m^H. \tag{7.1}$$

To go further, we introduce the data matrix X obtained by juxtaposing the $\underline{x}_m$'s, *i.e.* $X = (\underline{x}_1, \ldots \underline{x}_m, \ldots, \underline{x}_M)$. It is easy to see that

$$R_x^s \approx \frac{1}{M} \sum_{m=1}^{M} \underline{x}_m \underline{x}_m^H = \frac{1}{M} X X^H. \tag{7.2}$$

We thus refer to the right-hand side as the deterministic correlation matrix, denoted by R_x^d, with

$$R_x^d = \frac{1}{M} X X^H. \tag{7.3}$$

We thus have $R_x^s \approx R_x^d$. R_x^d is known to be the maximum-likelihood estimate of R_x^s. Observe that both R_x^s and R_x^d have size N, typically with $N \ll M$.

In the considerations to follow, it is more convenient to deal with $X X^H$ than with $(1/M) X X^H$. We thus introduce

$$C = X X^H, \tag{7.4}$$

keeping in mind that C is not the true deterministic correlation matrix R_x^d of the $\underline{x}_m$'s, but is related to it via $R_x^d = (1/M)C$. However, we will loosely refer to C as the correlation matrix.

Any symmetric matrix can be diagonalized by an orthonormal matrix, *i.e.* by a matrix the columns of which are both orthogonal and normalized to unit length. C being symmetric, we can write $C = U^H \Lambda U$, where U is the orthonormal matrix the columns of which are the eigenvectors $\underline{u}_i$ of C normalized to unit length, and Λ is the diagonal matrix the diagonal elements of which are the corresponding eigenvalues λ_i of C.

The eigenvalues of any real symmetric matrix are real. Furthermore, a matrix of the form $U U^H$ is not only symmetric but positive semi-definite, and the eigenvalues of such a matrix are non-negative. Therefore, the eigenvalues of C are real and non-negative.

Rather than using the correlation matrix, we could use the covariance matrix, which simply amounts to removing the mean from the random vector $\underline{x}$ or its realizations.

It is useful to visualize R_x^s - and thus R_x^d and C - as an ellipsoid in $\mathbb{R}^N$ if the bistatic radar cross-section (BS-RCS) is considered or in $\mathbb{C}^N$ if the bistatic complex

radar cross-section (BS-CRCS) is considered, with its principal directions given by the columns $\underline{u}_i$ of U and its "extent" along each $\underline{u}_i$ by the corresponding λ_i. This gives a conceptual, pictorial representation of the distribution of the $\underline{x}_m$'s in relation to the $\underline{u}_i$'s. The basic idea of subspace (and dimensionality-reduction) techniques is to ignore the directions $\underline{u}_i$ where the ellipsoid is relatively thin, *i.e.* for which the λ_i's are very small and, especially, zero.

Let us order the λ_i's by decreasing values, *i.e.* $\lambda_1 \geq \lambda_2 \geq \ldots \geq \lambda_N$, and keep only the $\underline{u}_i$'s corresponding to the K largest λ_i's, *i.e.* to $\lambda_1, \ldots, \lambda_K$. The selected vectors $\underline{u}_i$ can be used to define a subspace of $\mathbb{R}^N$ (for BS-RCS) or of $\mathbb{C}^N$ (for BS-CRCS). Furthermore, since the $\underline{u}_i$'s are orthonormal, they constitute a basis for this subspace, which is of size K. It is useful to introduce a matrix Q, the columns of which are the K selected $\underline{u}_i$'s, *i.e.* $Q = (\underline{u}_1, \ldots, \underline{u}_K)$. Q is of size $N \times K$ and, thus, generally rectangular. It is also orthonormal, with $Q^H Q = I$, where I is the $K \times K$ identity matrix. This matrix Q constitutes a representation of the subspace built from the $\underline{x}_m$'s.

7.4.3 Size of subspaces

Each subspace is defined by a certain number of vectors corresponding to the K largest singular values. The choice of the parameter K is crucial. On the one hand, if K is chosen too small, the corresponding subspace does not represent exactly the target class. On the other hand, if K is chosen too large, the corresponding subspace will over-describe the target of interest.

In order to choose the best value of K, we plan to use the Time Reversal Operator (TRO), defined in [107, 117, 160–163, 233]. However, the TRO method assumes that the BS-CRCS and the BS-RCS of targets can be approximated by the bright point model [35]. In short, the bright point model assumes that targets are made of a finite number of isotropic scatterers [57], which is not the case of complex targets such as airplanes. Indeed, the bright point model neglects different scattering mechanisms such as multiple reflections.

We thus choose the size of each subspace, *i.e.* the number K of singular vectors of each subspace, such that the sum of their corresponding singular values is at least equal to some percentage γ of the sum of all singular values. We tested different values of γ. According to the results achieved, we choose γ equal to 95%.

7.5 Determination of the target class

In this section, we describe the determination of the class of an unknown target from the feature vector (FV) we produced the way described in Section 7.3. We first describe the orthogonal projection of this FV onto each of the subspaces of the target class model. We then describe the determination of the target class from these projections. We also describe some reasons for not using oblique projections.

7.5.1   Orthogonal projection

Before showing how to project on the subspace defined by an orthonormal matrix such as Q, let us review how to project on the subspace defined by a general rectangular matrix A consisting of K linearly independent columns $\underline{a}_m$ [14]. The columns define a subspace, called the columnspace of A [193].

One can show that the matrix that projects any vector $\underline{b} \in \mathbb{R}^N$ (or $\mathbb{C}^N$) into this subspace is given by the projection matrix [193]

$$P = A(A^H A)^{-1} A^H. \tag{7.5}$$

The result of the projection is then $P\underline{b}$. It is well known that any such projection matrix P is symmetric and such that $P^2 = P$ (idempotency).

In the particular case where A is an orthonormal matrix, say Q, the projection matrix P is $P = Q(Q^H Q)^{-1} Q^H$. Since $Q^H Q = I$, this reduces to

$$P = QQ^H. \tag{7.6}$$

This matrix P projects any vector $\underline{b}$ into the subspace defined by the K columns $\underline{u}_i$ of Q.

The result of projecting $\underline{b}$ into the subspace defined by the columns of Q is the projection (vector)

$$\underline{p} = P\underline{b} = QQ^H \underline{b}. \tag{7.7}$$

The component x_i of this vector along $\underline{u}_i$, where $i \in [1, K]$, is given by $x_i = \underline{u}_i^H \underline{p}$. The vector $\underline{x} = (x_1 \ldots x_K)^H$ of all the components is given by

$$\underline{x} = \begin{pmatrix} \underline{u}_1^H \\ \vdots \\ \underline{u}_K^H \end{pmatrix} \underline{p} = Q^H \underline{p}. \tag{7.8}$$

Using Eq. (7.7), one gets $\underline{x} = Q^H QQ^H \underline{b} = (Q^H Q)Q^H \underline{b}$. Since $Q^H Q = I$, this reduces to

$$\underline{x} = Q^H \underline{b}, \tag{7.9}$$

which is simply a statement of the well-known fact that the components of an arbitrary vector $\underline{b} \in \mathbb{R}^N$ (or in $\mathbb{C}^N$) corresponding to the axes of an orthonormal basis are obtained via the scalar product of $\underline{b}$ with each of the corresponding unit vectors $\underline{u}_i$.

The orthonormal matrix U containing the orthonormal eigenvectors of C clearly plays a crucial role above. Of course, it can be obtained by performing the eigenvalues decomposition (EVD) of $C = XX^H$. However, this requires the calculation of the product XX^H. Since N is typically much smaller than M, the matrix $C = XX^H$, which is of size $N \times N$, is typically of reasonable size. However, the determination of the value of each element of C requires the calculation of $N \times N$ scalar products of size $1 \times M$, where M can be very large.

As it is well known, there is a way to get U quite simply by working directly with X, rather than with XX^H. The solution is to use the singular value decomposition

(SVD) [193]. The SVD allows one to decompose any rectangular $N \times M$ matrix X as $X = U\Sigma V^H$, where U is a first $N \times N$ orthonormal matrix, Σ an $N \times M$ rectangular diagonal matrix, and V a second $M \times M$ orthonormal matrix.

The columns of U are called the left singular vectors of U and are denoted by $\underline{u}_i$. One can show that the $\underline{u}_i$'s are the eigenvectors of $C = XX^H$. The matrix U obtained by SVD is thus exactly the one needed to build the matrix Q appearing in the expression for the projection matrix P.

In summary, it is generally very advantageous to compute the required projection matrix Q (and the projection components x_i) by using the SVD of X rather than the EVD of XX^T.

7.5.2 Metrics

In our experimental work, we use four different metrics. The first metric is the norm of the projection error $\underline{e} = \underline{b} - \underline{p}$ [141, 164, 219, 226], *i.e.*

$$|\underline{e}| = |\underline{b} - \underline{p}| = |\underline{b} - P\underline{b}| = |(I - P)\underline{b}|, \tag{7.10}$$

where $P = QQ^H$. The subspace for which the projection error is the lowest corresponds to the class labelled to vector $\underline{b}$.

Since we are dealing with orthogonal projections, the measure of the energy of the projection of vector $\underline{b}$ onto subspace defined by Q is equivalent to the norm of the projection vector. It is referred to in [72, 110, 141, 164, 226] as the "basic decision rule", which is expressed as

$$E_0 = \frac{\underline{b}^H P \underline{b}}{\underline{b}^H \underline{b}}. \tag{7.11}$$

The subspace for which the energy is the largest corresponds to the class labelled to vector $\underline{b}$. Taking the minimum of the projection error (Eq. (7.10)) is equivalent to taking the maximum of the projection ((7.11)). For coherency with the other metrics, we use Eq. (7.11) as the first metric.

The second and third metrics used also measure the energy E_ρ of the projection of vector $\underline{b}$ [141] onto subspace defined by Q. The difference with the first metric is that the projection of vector $\underline{b}$ onto each of the vectors $\underline{u}_i$'s of Q is weighted by the ratio of the singular value λ_i corresponding to the appropriate singular vector $\underline{u}_i$ to the first singular value, λ_1. This means that the directions of the singular vectors of each subspace are weighted by their corresponding singular values. The second and third metrics are expressed as [113]

$$E_\rho = \sum_{i=1}^{K} \left(\frac{\lambda_i}{\lambda_1} \right)^\rho \frac{\underline{b}^H \underline{u}_i \underline{u}_i^H \underline{b}}{\underline{b}^H \underline{b}}, \tag{7.12}$$

where ρ is a factor defining the importance of the weighting. When $\rho = 0$, the right-hand side of Eq. (7.12) reduces to the right-hand side of Eq. (7.11). This is why we denoted the first metric by E_0.

For the second metric, we choose $\rho = 1$, as in the Multiple Similarity Method [113]. We thus denote the second metric by E_1. For the third metric, we choose $\rho = 0.05$, as in [113]. We thus denote the third metric by $E_{0.05}$. These values have proven to give the highest classification rates, as reported in [113]. As for the first metric, the class assigned to vector $\underline{b}$ corresponds to the subspace Q for which the energy z is the highest.

The fourth metric consists in the fusion of the first three metrics. We use the majority voting rule. Each of the three metrics described above votes for a particular class. The majority voting rule consists in assigning to an object the class for which the number of votes is the largest. One could also envision fusing the data according to the Dempster-Schafer Theory of Evidence as in [34, 105]. This approach is not considered here, since the classes are mutually exclusive.

7.5.3   Oblique projection

Until now, we proposed metrics based on the orthogonal projection of a vector z onto a subspace Q. In [14], the oblique projection has been defined for detection problems. We thus explore the possibility of using such a metric in our work.

Let us consider that the target is modelled by a subspace H and the noise subspace is represented by subspace S. The oblique projection onto a subspace H according to direction defined by subspace S is defined in [14] as

$$E_{HS} = H(H^H P_S^\perp H)^{-1} H^H P_S^\perp, \tag{7.13}$$

where

$$P_S^\perp = I - P_S, \tag{7.14}$$

and P_S stands for the orthogonal projector onto subspace S.

While the orthogonal projection P_H defined in Section 7.5.1 only requires the definition of the subspace H, the oblique projection requires that the subspaces H and S be both defined.

In the case of recognition, let us consider N classes, each class being represented by a subspace denoted by H_i, with $i = 1 \ldots N$. To define the oblique projection onto subspace H_1, one could think about defining the subspace H of Eq. (7.13) as H_1, and the subspace S of Eq. (7.13) as the subspace computed from the feature vectors of all other subspaces $[H_2 \ldots H_N]$. However, this does not imply that the subspaces H and S are separated. Moreover, the addition of an extra class requires one to recompute all the oblique projectors. Eventually, the computation of the oblique projection E_{HS} is more computationally intensive than the computation of the orthogonal projection P_H. Therefore, the oblique projection will not be used in this work.

7.6   Quantification of performance

We quantify the performance of the recognizer during the test phase, according to the probability of correct recognition. The probability of correct recognition is defined as the ratio of the number of feature vectors (FVs) that are correctly recognized to

the total number of FVs. The probability of correct recognition is computed from the confusion matrix, as described in Section 6.8.

7.7 Recognition experiments

We first describe the experimental sets we use for the recognition experiments. We then present the recognition results achieved for a single transmitter (Tx) and a single receiver (Rx), and for three (Tx,Rx) pairs. For each case, the recognition results are presented for the use of both the bistatic complex radar cross-sections (BS-CRCSs) and the bistatic radar cross-sections (BS-RCSs) of targets. We then discuss the different results achieved.

7.7.1 Experimental sets

BS-CRCSs and BS-RCSs of targets are available for four frequency bands and for four polarizations. For each frequency band and for each polarization, we divide the parameter space (α, β) into 3×12 overlapping tiles, where 3 is the number of aspect angles of the targets, and 12 the number of bistatic angular sectors considered. As described in Section 7.2, we build one recognizer for each tile. Therefore, we build a total of $4 \times 4 \times 3 \times 12 = 576$ recognizers.

We first consider only a single (Tx,Rx) pair. We thus perform 576 recognition experiments, one per recognizer. We give the recognition results in Section 7.7.2 for each frequency band and for each polarization.

We then consider multiple (Tx,Rx) pairs. For computational reasons, we choose to consider three (Tx,Rx) pairs, with a single Tx operating on a particular frequency and a particular polarization, and three Rx's. All three Rx's operate on the same polarization, either H or V, which can be distinct from the polarization of the Tx. The three Rx's are assumed to operate at locations that differ in bistatic angle. There are thus $C_{12}^3 = 220$ possible combinations of the three receivers, for each polarization, and each frequency band. We thus perform $4 \times 4 \times 3 \times 220 = 10560$ experiments. As for the case of a single (Tx,Rx) pair, we give the recognition results for each frequency band and for each polarization.

Table 7.2 lists the different recognition experiments we performed. Each experiment is assigned a label $n_1.n_2$, where n_1 stands for the number of (Tx,Rx) pairs we consider, and n_2 stands for the frequency band, and whose third digit stands for the polarization used.

7.7.2 Recognition results achieved for a single (Tx,Rx) pair

We present the results achieved for a single (Tx,Rx) pair, and by using either the BS-CRCS or the BS-RCS of the targets to classify. For both the BS-CRCS and the BS-RCS cases, we show the recognition rate for each of the four metrics that we introduced in Section 7.5.2. For conciseness, we present in details the results achieved for the HH polarization pair. The results achieved for the three other polarization pairs are similar to the results achieved for the HH polarization pair. Thus, referring

Experiment index for 1 (Tx,Rx) pair	Experiment index for 3 (Tx,Rx) pairs	Frequency band	Polarization	Aspect angles	Bistatic angular sectors	Number of experiments
Exp. 1.1.1	Exp. 2.1.1	[20; 80] MHz	HH	All (3)	All (12)	36
Exp. 1.1.2	Exp. 2.1.2	[20; 80] MHz	HV	All (3)	All (12)	36
Exp. 1.1.3	Exp. 2.1.3	[20; 80] MHz	VH	All (3)	All (12)	36
Exp. 1.1.4	Exp. 2.1.4	[20; 80] MHz	VV	All (3)	All (12)	36
Exp. 1.2.1	Exp. 2.2.1	[190; 250] MHz	HH	All (3)	All (12)	36
Exp. 1.2.2	Exp. 2.2.2	[190; 250] MHz	HV	All (3)	All (12)	36
Exp. 1.2.3	Exp. 2.2.3	[190; 250] MHz	VH	All (3)	All (12)	36
Exp. 1.2.4	Exp. 2.2.4	[190; 250] MHz	VV	All (3)	All (12)	36
Exp. 1.3.1	Exp. 2.3.1	[450; 550] MHz	HH	All (3)	All (12)	36
Exp. 1.3.2	Exp. 2.3.2	[450; 550] MHz	HV	All (3)	All (12)	36
Exp. 1.3.3	Exp. 2.3.3	[450; 550] MHz	VH	All (3)	All (12)	36
Exp. 1.3.4	Exp. 2.3.4	[450; 550] MHz	VV	All (3)	All (12)	36
Exp. 1.4.1	Exp. 2.4.1	[1.2; 1.3] GHz	HH	All (3)	All (12)	36
Exp. 1.4.2	Exp. 2.4.2	[1.2; 1.3] GHz	HV	All (3)	All (12)	36
Exp. 1.4.3	Exp. 2.4.3	[1.2; 1.3] GHz	VH	All (3)	All (12)	36
Exp. 1.4.4	Exp. 2.4.4	[1.2; 1.3] GHz	VV	All (3)	All (12)	36
Total number of experiments						576

Table 7.2: *Recognition experiments performed.*

to Table 7.2, we present the results for the recognition Experiments 1.1.1, 1.2.1, 1.3.1, and 1.4.1, *i.e.* experiments for each frequency band and for the *HH* polarization.

Probabilities of correct recognition for FB1 ($[20; 80]$ **MHz)**

Tables 7.3, 7.4, 7.5, and 7.6 present the probabilities of correct recognition obtained for the recognition of targets for the first frequency band, FB1 ($[20; 80]$ MHz), for the criteria E_0, E_1, $E_{0.05}$, and for the aggregation of these three criteria, respectively. As one can see on the four tables, the probability of correct recognition is always very low for either the BS-CRCS or the BS-RCS, ranging from 0.25, which is the probability of correct recognition that would be obtained by recognizing targets randomly, and 0.63, depending on the tile of the (α, β) plane, and on the metric used. The reasons for such a low probability of correct recognition are that the BS-CRCS and the BS-RCS vary more with volume than with shape at these frequencies, and that the targets have about the same volume, as discussed in Chapter 4.

Probabilities of correct recognition for FB1						
	For BS-CRCS			For BS-RCS		
	$\alpha = 0°$	$\alpha = 45°$	$\alpha = 90°$	$\alpha = 0°$	$\alpha = 45°$	$\alpha = 90°$
$\beta \in [6°, 43.5°]$	0.41	0.33	0.45	0.36	0.32	0.38
$\beta \in [18.5°, 56°]$	0.57	0.55	0.60	0.34	0.35	0.47
$\beta \in [31°, 68.5°]$	0.57	0.48	0.53	0.33	0.34	0.30
$\beta \in [43.5°, 81°]$	0.60	0.45	0.38	0.31	0.29	0.35
$\beta \in [56°, 93.5°]$	0.50	0.27	0.47	0.34	0.35	0.30
$\beta \in [68.5°, 106°]$	0.32	0.25	0.48	0.35	0.31	0.34
$\beta \in [81°, 118.5°]$	0.35	0.32	0.31	0.32	0.29	0.33
$\beta \in [93.5°, 131°]$	0.39	0.32	0.36	0.27	0.34	0.34
$\beta \in [106°, 143.5°]$	0.63	0.32	0.33	0.37	0.38	0.35
$\beta \in [118.5°, 156°]$	0.42	0.33	0.47	0.33	0.34	0.34

Table 7.3: *Probabilities of correct recognition, shown tile-by-tile, **for metric** E_0 applied to BS-CRCS and BS-RCS, computed for the frequency band FB1 ($[20; 80]$ MHz) and polarization HH. The table is divided in tiles in the same way as the (α, β) plane is.*

Probabilities of correct recognition for FB1					
	For BS-CRCS			For BS-RCS		
	$\alpha = 0°$	$\alpha = 45°$	$\alpha = 90°$	$\alpha = 0°$	$\alpha = 45°$	$\alpha = 90°$
$\beta \in [6°, 43.5°]$	0.46	0.46	0.41	0.36	0.33	0.38
$\beta \in [18.5°, 56°]$	0.60	0.50	0.44	0.42	0.47	0.44
$\beta \in [31°, 68.5°]$	0.63	0.44	0.47	0.31	0.41	0.51
$\beta \in [43.5°, 81°]$	0.55	0.37	0.41	0.35	0.33	0.39
$\beta \in [56°, 93.5°]$	0.49	0.39	0.39	0.34	0.35	0.36
$\beta \in [68.5°, 106°]$	0.50	0.52	0.43	0.33	0.38	0.34
$\beta \in [81°, 118.5°]$	0.63	0.47	0.37	0.39	0.37	0.34
$\beta \in [93.5°, 131°]$	0.54	0.48	0.40	0.39	0.35	0.36
$\beta \in [106°, 143.5°]$	0.38	0.49	0.34	0.39	0.42	0.31
$\beta \in [118.5°, 156°]$	0.42	0.5	0.29	0.40	0.40	0.31

Table 7.4: *Probabilities of correct recognition, shown tile-by-tile, **for metric E_1** applied to BS-CRCS and BS-RCS, computed for the frequency band FB1 ([20; 80] MHz) and polarization HH. The table is divided in tiles in the same way as the (α, β) plane is.*

Probabilities of correct recognition for FB1					
	For BS-CRCS			For BS-RCS		
	$\alpha = 0°$	$\alpha = 45°$	$\alpha = 90°$	$\alpha = 0°$	$\alpha = 45°$	$\alpha = 90°$
$\beta \in [6°, 43.5°]$	0.42	0.38	0.36	0.36	0.32	0.40
$\beta \in [18.5°, 56°]$	0.52	0.42	0.39	0.36	0.43	0.49
$\beta \in [31°, 68.5°]$	0.49	0.42	0.34	0.33	0.39	0.48
$\beta \in [43.5°, 81°]$	0.48	0.35	0.31	0.35	0.35	0.39
$\beta \in [56°, 93.5°]$	0.45	0.37	0.36	0.37	0.38	0.32
$\beta \in [68.5°, 106°]$	0.41	0.41	0.38	0.37	0.40	0.38
$\beta \in [81°, 118.5°]$	0.51	0.35	0.32	0.36	0.39	0.36
$\beta \in [93.5°, 131°]$	0.42	0.41	0.29	0.32	0.38	0.36
$\beta \in [106°, 143.5°]$	0.29	0.40	0.26	0.36	0.43	0.35
$\beta \in [118.5°, 156°]$	0.32	0.43	0.24	0.37	0.38	0.33

Table 7.5: *Probabilities of correct recognition, shown tile-by-tile, **for metric $E_{0.05}$** applied to BS-CRCS and BS-RCS, computed for the frequency band FB1 ([20; 80] MHz) and polarization HH. The table is divided in tiles in the same way as the (α, β) plane is.*

Probabilities of correct recognition for FB1						
	For BS-CRCS			For BS-RCS		
	$\alpha = 0°$	$\alpha = 45°$	$\alpha = 90°$	$\alpha = 0°$	$\alpha = 45°$	$\alpha = 90°$
$\beta \in [6°, 43.5°]$	0.47	0.47	0.41	0.37	0.33	0.41
$\beta \in [18.5°, 56°]$	0.63	0.51	0.45	0.42	0.46	0.47
$\beta \in [31°, 68.5°]$	0.63	0.47	0.46	0.33	0.40	0.51
$\beta \in [43.5°, 81°]$	0.55	0.39	0.41	0.36	0.34	0.41
$\beta \in [56°, 93.5°]$	0.52	0.41	0.38	0.34	0.39	0.33
$\beta \in [68.5°, 106°]$	0.49	0.50	0.42	0.36	0.41	0.37
$\beta \in [81°, 118.5°]$	0.63	0.48	0.38	0.41	0.38	0.36
$\beta \in [93.5°, 131°]$	0.49	0.49	0.37	0.43	0.39	0.38
$\beta \in [106°, 143.5°]$	0.35	0.48	0.32	0.37	0.43	0.32
$\beta \in [118.5°, 156°]$	0.42	0.51	0.30	0.36	0.40	0.35

Table 7.6: *Probabilities of correct recognition, shown tile-by-tile,* **for the aggregation of the three metrics** *applied to BS-RCS and BS-RCS, computed for the frequency band FB1 ([20; 80] MHz) and polarization HH. The table is divided in tiles in the same way as the (α, β) plane is.*

Probabilities of correct recognition for FB2 ($[190; 250]$ **MHz**)

Tables 7.7, 7.8, 7.9, and 7.10 present the probabilities of correct recognition obtained for the recognition of targets for the second frequency band, FB2 ($[190; 250]$ MHz), for the criteria E_0, E_1, $E_{0.05}$, and for the aggregation of these three criteria, respectively. The probability of correct recognition ranges from 0.32 to 0.90, depending on the tile of the (α, β) plane, and on the metric used. The probabilities of correct recognition are higher than for the lowest frequency band when using either the BS-CRCSs or the BS-RCSs. This can be explained by the fact that the BS-CRCS is influenced by both the volume of the targets, as at the lowest frequency band, and the shape of the targets. One can also see that, for a constant β, the highest probabilities of correct recognition are obtained for $\alpha = 0°$. This is due to the shape of the targets. No bistatic angular sector seems to be preferable. When using BS-CRCSs, metric E_0, that does not weight the vectors of the subspaces, appears to give better results than the weighting metrics E_1 and $E_{0.05}$, while, when using BS-RCSs, metric $E_{0.05}$ appears to give the best results.

Probabilities of correct recognition for FB2						
	For BS-CRCS			For BS-RCS		
	$\alpha = 0°$	$\alpha = 45°$	$\alpha = 90°$	$\alpha = 0°$	$\alpha = 45°$	$\alpha = 90°$
$\beta \in [6°, 43.5°]$	0.80	0.78	0.68	0.43	0.49	0.40
$\beta \in [18.5°, 56°]$	0.84	0.65	0.81	0.53	0.41	0.64
$\beta \in [31°, 68.5°]$	0.68	0.69	0.72	0.48	0.40	0.67
$\beta \in [43.5°, 81°]$	0.73	0.47	0.78	0.43	0.38	0.43
$\beta \in [56°, 93.5°]$	0.64	0.62	0.50	0.57	0.55	0.40
$\beta \in [68.5°, 106°]$	0.74	0.56	0.58	0.59	0.48	0.41
$\beta \in [81°, 118.5°]$	0.72	0.66	0.66	0.57	0.38	0.39
$\beta \in [93.5°, 131°]$	0.90	0.57	0.55	0.67	0.43	0.44
$\beta \in [106°, 143.5°]$	0.86	0.68	0.59	0.52	0.49	0.45
$\beta \in [118.5°, 156°]$	0.87	0.67	0.64	0.50	0.58	0.48

Table 7.7: *Probabilities of correct recognition, shown tile-by-tile, **for metric** $\mathbf{E_0}$ applied to BS-CRCS and BS-RCS, computed for the frequency band FB2 ($[190; 250]$ MHz) and polarization HH. The table is divided in tiles in the same way as the (α, β) plane is.*

Probabilities of correct recognition for FB2						
	For BS-CRCS			For BS-RCS		
	$\alpha = 0°$	$\alpha = 45°$	$\alpha = 90°$	$\alpha = 0°$	$\alpha = 45°$	$\alpha = 90°$
$\beta \in [6°, 43.5°]$	0.73	0.56	0.50	0.45	0.42	0.36
$\beta \in [18.5°, 56°]$	0.80	0.58	0.76	0.53	0.37	0.57
$\beta \in [31°, 68.5°]$	0.74	0.52	0.78	0.49	0.32	0.63
$\beta \in [43.5°, 81°]$	0.71	0.50	0.63	0.45	0.42	0.47
$\beta \in [56°, 93.5°]$	0.77	0.66	0.60	0.48	0.47	0.53
$\beta \in [68.5°, 106°]$	0.76	0.62	0.48	0.52	0.41	0.39
$\beta \in [81°, 118.5°]$	0.67	0.56	0.52	0.44	0.35	0.42
$\beta \in [93.5°, 131°]$	0.81	0.65	0.64	0.50	0.34	0.42
$\beta \in [106°, 143.5°]$	0.81	0.70	0.59	0.53	0.39	0.50
$\beta \in [118.5°, 156°]$	0.82	0.71	0.58	0.60	0.51	0.45

Table 7.8: *Probabilities of correct recognition, shown tile-by-tile, **for metric E_1** applied to BS-CRCS and BS-RCS, computed for the frequency band FB2 ([190; 250] MHz) and polarization HH. The table is divided in tiles in the same way as the (α, β) plane is.*

Probabilities of correct recognition for FB2						
	For BS-CRCS			For BS-RCS		
	$\alpha = 0°$	$\alpha = 45°$	$\alpha = 90°$	$\alpha = 0°$	$\alpha = 45°$	$\alpha = 90°$
$\beta \in [6°, 43.5°]$	0.60	0.43	0.35	0.52	0.53	0.41
$\beta \in [18.5°, 56°]$	0.61	0.45	0.62	0.60	0.47	0.69
$\beta \in [31°, 68.5°]$	0.62	0.39	0.60	0.54	0.41	0.69
$\beta \in [43.5°, 81°]$	0.52	0.40	0.48	0.48	0.45	0.51
$\beta \in [56°, 93.5°]$	0.52	0.57	0.47	0.59	0.63	0.55
$\beta \in [68.5°, 106°]$	0.59	0.49	0.41	0.65	0.54	0.44
$\beta \in [81°, 118.5°]$	0.60	0.47	0.41	0.59	0.41	0.43
$\beta \in [93.5°, 131°]$	0.67	0.47	0.54	0.69	0.47	0.46
$\beta \in [106°, 143.5°]$	0.57	0.54	0.49	0.56	0.51	0.49
$\beta \in [118.5°, 156°]$	0.67	0.53	0.41	0.68	0.66	0.51

Table 7.9: *Probabilities of correct recognition, shown tile-by-tile, **for metric $E_{0.05}$** applied to BS-CRCS and BS-RCS, computed for the frequency band FB2 ([190; 250] MHz) and polarization HH. The table is divided in tiles in the same way as the (α, β) plane is.*

Probabilities of correct recognition for FB2					
	For BS-CRCS			For BS-RCS		
	$\alpha = 0°$	$\alpha = 45°$	$\alpha = 90°$	$\alpha = 0°$	$\alpha = 45°$	$\alpha = 90°$
$\beta \in [6°, 43.5°]$	0.74	0.59	0.47	0.56	0.54	0.41
$\beta \in [18.5°, 56°]$	0.8	0.55	0.75	0.64	0.46	0.66
$\beta \in [31°, 68.5°]$	0.74	0.49	0.78	0.56	0.40	0.70
$\beta \in [43.5°, 81°]$	0.67	0.49	0.62	0.50	0.47	0.57
$\beta \in [56°, 93.5°]$	0.73	0.68	0.58	0.58	0.59	0.62
$\beta \in [68.5°, 106°]$	0.75	0.60	0.48	0.69	0.53	0.45
$\beta \in [81°, 118.5°]$	0.71	0.55	0.53	0.58	0.44	0.47
$\beta \in [93.5°, 131°]$	0.82	0.62	0.65	0.72	0.49	0.48
$\beta \in [106°, 143.5°]$	0.79	0.70	0.60	0.61	0.53	0.55
$\beta \in [118.5°, 156°]$	0.82	0.68	0.57	0.71	0.64	0.52

Table 7.10: *Probabilities of correct recognition, shown tile-by-tile, **for the aggregation of the three metrics** applied to BS-CRCS and BS-RCS, computed for the frequency band FB2 ([190; 250] MHz) and polarization HH. The table is divided in tiles in the same way as the (α, β) plane is.*

Probabilities of correct recognition for FB3 ($[450; 550]$ **MHz)**

Tables 7.11, 7.12, 7.13, and 7.14 present the probabilities of correct recognition obtained for the recognition of targets for the third frequency band, FB3 ($[450; 550]$ MHz), for the criteria E_0, E_1, $E_{0.05}$, and for the aggregation of these three criteria, respectively. The probability of correct recognition ranges between 0.36 and 0.98, depending on the tile of the (α, β) plane, and on the metric used. The probability of correct recognition is better than for FB1 and FB2. This is explained by the fact that, for FB3, the shape of the targets influence the BS-CRCS more than their volume, as depicted in Chapter 6. The same other conclusions can be drawn as for FB2.

Probabilities of correct recognition for FB3						
	For BS-CRCS			For BS-RCS		
	$\alpha = 0°$	$\alpha = 45°$	$\alpha = 90°$	$\alpha = 0°$	$\alpha = 45°$	$\alpha = 90°$
$\beta \in [6°, 43.5°]$	0.85	0.88	0.77	0.65	0.72	0.54
$\beta \in [18.5°, 56°]$	0.89	0.58	0.89	0.66	0.54	0.68
$\beta \in [31°, 68.5°]$	0.79	0.56	0.95	0.58	0.52	0.68
$\beta \in [43.5°, 81°]$	0.93	0.72	0.93	0.61	0.36	0.67
$\beta \in [56°, 93.5°]$	0.96	0.88	0.65	0.81	0.46	0.58
$\beta \in [68.5°, 106°]$	0.98	0.78	0.84	0.87	0.64	0.52
$\beta \in [81°, 118.5°]$	0.96	0.75	0.92	0.79	0.63	0.56
$\beta \in [93.5°, 131°]$	0.97	0.64	0.81	0.72	0.63	0.56
$\beta \in [106°, 143.5°]$	0.96	0.90	0.79	0.72	0.74	0.59
$\beta \in [118.5°, 156°]$	0.93	0.88	0.82	0.72	0.78	0.57

Table 7.11: *Probabilities of correct recognition, shown tile-by-tile, **for metric** E_0 applied to BS-CRCS and BS-RCS, computed for the frequency band FB3 ($[450; 550]$ MHz) and polarization HH. The table is divided in tiles in the same way as the (α, β) plane is.*

Probabilities of correct recognition for FB3					
	For BS-CRCS			For BS-RCS		
	$\alpha = 0°$	$\alpha = 45°$	$\alpha = 90°$	$\alpha = 0°$	$\alpha = 45°$	$\alpha = 90°$
$\beta \in [6°, 43.5°]$	0.77	0.63	0.59	0.56	0.46	0.42
$\beta \in [18.5°, 56°]$	0.86	0.73	0.85	0.63	0.45	0.53
$\beta \in [31°, 68.5°]$	0.73	0.71	0.81	0.52	0.41	0.57
$\beta \in [43.5°, 81°]$	0.85	0.60	0.78	0.55	0.46	0.53
$\beta \in [56°, 93.5°]$	0.73	0.78	0.76	0.48	0.47	0.58
$\beta \in [68.5°, 106°]$	0.92	0.80	0.58	0.70	0.57	0.38
$\beta \in [81°, 118.5°]$	0.82	0.77	0.60	0.61	0.52	0.51
$\beta \in [93.5°, 131°]$	0.78	0.82	0.76	0.52	0.60	0.56
$\beta \in [106°, 143.5°]$	0.83	0.83	0.70	0.48	0.56	0.58
$\beta \in [118.5°, 156°]$	0.92	0.73	0.59	0.65	0.54	0.37

Table 7.12: *Probabilities of correct recognition, shown tile-by-tile, **for metric** $\mathbf{E_1}$ applied to BS-CRCS and BS-RCS, computed for the frequency band FB3 ([450; 550] MHz) and polarization HH. The table is divided in tiles in the same way as the (α, β) plane is.*

Probabilities of correct recognition for FB3					
	For BS-CRCS			For BS-RCS		
	$\alpha = 0°$	$\alpha = 45°$	$\alpha = 90°$	$\alpha = 0°$	$\alpha = 45°$	$\alpha = 90°$
$\beta \in [6°, 43.5°]$	0.62	0.53	0.40	0.76	0.73	0.56
$\beta \in [18.5°, 56°]$	0.66	0.54	0.69	0.77	0.62	0.77
$\beta \in [31°, 68.5°]$	0.62	0.55	0.64	0.68	0.56	0.72
$\beta \in [43.5°, 81°]$	0.68	0.48	0.61	0.72	0.44	0.71
$\beta \in [56°, 93.5°]$	0.54	0.65	0.58	0.83	0.60	0.70
$\beta \in [68.5°, 106°]$	0.72	0.66	0.46	0.92	0.74	0.56
$\beta \in [81°, 118.5°]$	0.65	0.62	0.52	0.87	0.67	0.65
$\beta \in [93.5°, 131°]$	0.62	0.58	0.67	0.81	0.70	0.68
$\beta \in [106°, 143.5°]$	0.70	0.65	0.51	0.75	0.79	0.71
$\beta \in [118.5°, 156°]$	0.64	0.66	0.45	0.74	0.82	0.60

Table 7.13: *Probabilities of correct recognition, shown tile-by-tile, **for metric** $\mathbf{E_{0.05}}$ applied to BS-CRCS and BS-RCS, computed for the frequency band FB3 ([450; 550] MHz) and polarization HH. The table is divided in tiles in the same way as the (α, β) plane is.*

Probabilities of correct recognition for FB3						
	For BS-CRCS			For BS-RCS		
	$\alpha = 0°$	$\alpha = 45°$	$\alpha = 90°$	$\alpha = 0°$	$\alpha = 45°$	$\alpha = 90°$
$\beta \in [6°, 43.5°]$	0.77	0.66	0.54	0.75	0.70	0.60
$\beta \in [18.5°, 56°]$	0.84	0.71	0.85	0.77	0.63	0.76
$\beta \in [31°, 68.5°]$	0.76	0.70	0.80	0.67	0.57	0.72
$\beta \in [43.5°, 81°]$	0.85	0.60	0.76	0.73	0.47	0.69
$\beta \in [56°, 93.5°]$	0.73	0.81	0.75	0.82	0.61	0.71
$\beta \in [68.5°, 106°]$	0.91	0.81	0.57	0.92	0.72	0.55
$\beta \in [81°, 118.5°]$	0.83	0.78	0.62	0.86	0.64	0.65
$\beta \in [93.5°, 131°]$	0.77	0.79	0.80	0.83	0.74	0.70
$\beta \in [106°, 143.5°]$	0.83	0.83	0.70	0.77	0.80	0.77
$\beta \in [118.5°, 156°]$	0.90	0.76	0.58	0.77	0.77	0.57

Table 7.14: *Probabilities of correct recognition, shown tile-by-tile, **for the aggregation of the three metrics** applied to BS-CRCS and BS-RCS, computed for the frequency band FB3 ([450; 550] MHz) and polarization HH. The table is divided in tiles in the same way as the (α, β) plane is.*

Probabilities of correct recognition for FB4 ([1.2; 1.3] **GHz**)

Tables 7.15, 7.16, 7.17, and 7.18 present the probabilities of correct recognition obtained for the recognition of targets for the fourth frequency band, FB4 ([1.2; 1.3] GHz), for the criteria E_0, E_1, $E_{0.05}$, and for the aggregation of these three criteria, respectively. The probability of correct recognition ranges from 0.27 to 1, depending on the tile of the (α, β) plane, and on the metric used. The same conclusions can be drawn as for FB3.

Probabilities of correct recognition for FB4						
	For BS-CRCS			For BS-RCS		
	$\alpha = 0°$	$\alpha = 45°$	$\alpha = 90°$	$\alpha = 0°$	$\alpha = 45°$	$\alpha = 90°$
$\beta \in [6°, 43.5°]$	1.0	0.77	0.67	0.73	0.27	0.48
$\beta \in [18.5°, 56°]$	0.99	0.95	0.98	0.56	0.60	0.84
$\beta \in [31°, 68.5°]$	0.99	0.84	0.96	0.68	0.53	0.83
$\beta \in [43.5°, 81°]$	0.99	0.79	0.93	0.68	0.36	0.78
$\beta \in [56°, 93.5°]$	1.0	0.91	0.92	0.83	0.33	0.81
$\beta \in [68.5°, 106°]$	1.0	0.93	0.94	0.83	0.63	0.59
$\beta \in [81°, 118.5°]$	1.0	0.86	0.98	0.84	0.66	0.59
$\beta \in [93.5°, 131°]$	0.99	0.94	0.86	0.73	0.73	0.61
$\beta \in [106°, 143.5°]$	1.0	0.91	0.95	0.75	0.84	0.65
$\beta \in [118.5°, 156°]$	0.96	0.97	0.92	0.62	0.81	0.63

Table 7.15: *Probabilities of correct recognition, shown tile-by-tile, **for metric** E_0 applied to BS-CRCS and BS-RCS, computed for the frequency band FB4 ([1.2; 1.3] GHz) and polarization HH. The table is divided in tiles in the same way as the (α, β) plane is.*

Probabilities of correct recognition for FB4						
	For BS-CRCS			For BS-RCS		
	$\alpha = 0°$	$\alpha = 45°$	$\alpha = 90°$	$\alpha = 0°$	$\alpha = 45°$	$\alpha = 90°$
$\beta \in [6°, 43.5°]$	0.76	0.69	0.75	0.64	0.37	0.44
$\beta \in [18.5°, 56°]$	0.89	0.88	0.89	0.52	0.49	0.50
$\beta \in [31°, 68.5°]$	0.90	0.78	0.90	0.52	0.48	0.67
$\beta \in [43.5°, 81°]$	0.89	0.81	0.80	0.53	0.46	0.65
$\beta \in [56°, 93.5°]$	0.84	0.81	0.82	0.58	0.58	0.64
$\beta \in [68.5°, 106°]$	0.87	0.84	0.67	0.70	0.51	0.39
$\beta \in [81°, 118.5°]$	0.83	0.83	0.67	0.66	0.41	0.61
$\beta \in [93.5°, 131°]$	0.88	0.77	0.71	0.61	0.55	0.60
$\beta \in [106°, 143.5°]$	0.91	0.85	0.78	0.58	0.61	0.53
$\beta \in [118.5°, 156°]$	0.80	0.82	0.70	0.59	0.46	0.41

Table 7.16: *Probabilities of correct recognition, shown tile-by-tile, **for metric E_1** applied to BS-CRCS and BS-RCS, computed for the frequency band FB4 ([1.2; 1.3] GHz) and polarization HH. The table is divided in tiles in the same way as the (α, β) plane is.*

Probabilities of correct recognition for FB4						
	For BS-CRCS			For BS-RCS		
	$\alpha = 0°$	$\alpha = 45°$	$\alpha = 90°$	$\alpha = 0°$	$\alpha = 45°$	$\alpha = 90°$
$\beta \in [6°, 43.5°]$	0.68	0.58	0.59	0.85	0.33	0.51
$\beta \in [18.5°, 56°]$	0.82	0.68	0.78	0.68	0.67	0.86
$\beta \in [31°, 68.5°]$	0.75	0.65	0.81	0.78	0.61	0.85
$\beta \in [43.5°, 81°]$	0.75	0.65	0.75	0.72	0.48	0.83
$\beta \in [56°, 93.5°]$	0.64	0.69	0.69	0.87	0.50	0.84
$\beta \in [68.5°, 106°]$	0.74	0.71	0.49	0.94	0.74	0.63
$\beta \in [81°, 118.5°]$	0.70	0.67	0.53	0.92	0.71	0.74
$\beta \in [93.5°, 131°]$	0.71	0.62	0.50	0.80	0.84	0.81
$\beta \in [106°, 143.5°]$	0.74	0.73	0.56	0.78	0.90	0.77
$\beta \in [118.5°, 156°]$	0.70	0.75	0.53	0.75	0.85	0.75

Table 7.17: *Probabilities of correct recognition, shown tile-by-tile, **for metric $E_{0.05}$** applied to BS-CRCS and BS-RCS, computed for the frequency band FB4 ([1.2; 1.3] GHz) and polarization HH. The table is divided in tiles in the same way as the (α, β) plane is.*

Probabilities of correct recognition for FB4					
	For BS-CRCS			For BS-RCS		
	$\alpha = 0°$	$\alpha = 45°$	$\alpha = 90°$	$\alpha = 0°$	$\alpha = 45°$	$\alpha = 90°$
$\beta \in [6°, 43.5°]$	0.78	0.70	0.75	0.85	0.34	0.50
$\beta \in [18.5°, 56°]$	0.91	0.87	0.90	0.67	0.65	0.81
$\beta \in [31°, 68.5°]$	0.90	0.78	0.91	0.75	0.58	0.85
$\beta \in [43.5°, 81°]$	0.90	0.81	0.82	0.74	0.57	0.83
$\beta \in [56°, 93.5°]$	0.86	0.83	0.83	0.85	0.58	0.84
$\beta \in [68.5°, 106°]$	0.91	0.86	0.66	0.92	0.73	0.63
$\beta \in [81°, 118.5°]$	0.89	0.84	0.68	0.88	0.70	0.75
$\beta \in [93.5°, 131°]$	0.89	0.78	0.68	0.79	0.83	0.79
$\beta \in [106°, 143.5°]$	0.92	0.87	0.76	0.78	0.85	0.76
$\beta \in [118.5°, 156°]$	0.83	0.86	0.69	0.78	0.75	0.76

Table 7.18: *Probabilities of correct recognition, shown tile-by-tile, **for the aggregation of the three metrics** applied to BS-CRCS and BS-RCS, computed for the frequency band FB4 ([1.2; 1.3] GHz) and polarization HH. The table is divided in tiles in the same way as the (α, β) plane is.*

Discussion of the recognition results achieved for a single (Tx,Rx) pair

We showed above that, for a particular frequency band and for a particular polarization, the probability of correct recognition varies according to the tile of the (α, β) plane, and according to the metric used. While it appears that there is no particular bistatic angular sector that favors a high probability of correct recognition, the value $\alpha = 0°$ gives a higher probability of correct recognition, for any value of β, when considering the BS-CRCS. This can be explained by the fact that the shapes of the front of the targets are very different, while the shapes of the sides of the targets are rather similar. When considering the BS-RCS of targets, no particular value of α seems to be preferable.

The best metric appears to be the non-weighting metric E_0 when using BS-CRCS. This means that the vectors of the subspaces must be considered of equal importance. When using BS-RCS, the best metric appears to be metric $E_{0.05}$, thus giving more importance to the vectors corresponding to the largest eigenvalues.

To illustrate the variation of the probability of correct recognition with frequency and polarization, the overall probability of correct recognition achieved for each frequency band, each polarization, and each metric, when considering the BS-CRCS of targets, is shown in Table 7.19, and in Table 7.20 when considering the BS-RCS of targets. One can clearly see that the probability of correct recognition increases with frequency. This is explained by the fact that, for the higher frequencies considered, the BS-CRCS is more influenced by the shape of the targets than by their volume, while it is exactly the opposite at the lower frequencies considered. One can also see that we achieve the highest probabilities of correct recognition for the HH polarization, even though the probabilities of correct recognition we achieve for the three other polarizations are not much smaller. This can be intuitively understood by the fact that the shapes of the different targets differ more according to their horizontal planes than their vertical planes. One can also see that the E_0 metric gives the best probabilities of correct recognition when considering BS-CRCS, and that the metric $E_{0.05}$ gives the best probabilities of correct recognition when considering BS-RCS.

We achieve higher probabilities of correct recognition for the BS-CRCS of targets than for their BS-RCS. For FB2, FB3, and FB4, the difference is on the order of 10% to 20%, when comparing the results of the best metric for each case. The phase of the BS-CRCS differs from one airplane to the other, and is thus significant for the recognition of these four targets.

7.7.3   Recognition results achieved for three (Tx,Rx) pairs

We showed in Section 7.7.2 the probabilities of correct recognition we achieved when considering either the BS-CRCS or the BS-RCS of the targets of interest, and a single (Tx,Rx) pair. This means that we considered a one-dimensional (1D) diversity (the bistatic angle). In Chapter 6, we achieved probabilities of correct recognition of about 1 for the frequency bands FB2, FB3, and FB4. As we explained in Chapter 5, we built the radar images from the BS-CRCS extracted with a 2D diversity. In order to increase the diversity of the data used to recognize targets, and thus in order to hopefully increase the probability of correct recognition, we can use multiple (Tx,Rx)

Overall probabilities of correct recognition for BS-CRCS					
Frequency band	Polarization	Metric E_0	Metric E_1	Metric $E_{0.05}$	Aggregation
FB1: [20; 80] MHz	HH	0.43	0.46	0.38	0.46
FB1: [20; 80] MHz	HV	0.37	0.42	0.39	0.43
FB1: [20; 80] MHz	VH	0.34	0.38	0.34	0.38
FB1: [20; 80] MHz	VV	0.38	0.47	0.44	0.48
FB2: [190; 250] MHz	HH	0.69	0.66	0.52	0.65
FB2: [190; 250] MHz	HV	0.60	0.60	0.49	0.60
FB2: [190; 250] MHz	VH	0.62	0.61	0.48	0.60
FB2: [190; 250] MHz	VV	0.63	0.59	0.50	0.60
FB3: [450; 550] MHz	HH	0.84	0.76	0.60	0.75
FB3: [450; 550] MHz	HV	0.76	0.69	0.54	0.69
FB3: [450; 550] MHz	VH	0.82	0.69	0.54	0.69
FB3: [450; 550] MHz	VV	0.79	0.70	0.56	0.70
FB4: [1.2; 1.3] GHz	HH	0.93	0.81	0.67	0.82
FB4: [1.2; 1.3] GHz	HV	0.87	0.75	0.61	0.76
FB4: [1.2; 1.3] GHz	VH	0.93	0.78	0.62	0.79
FB4: [1.2; 1.3] GHz	VV	0.89	0.80	0.65	0.81

Table 7.19: *Overall probabilities of correct recognition achieved per frequency band and per polarization, for the four different metrics, when using the BS-CRCS of targets.*

Overall probabilities of correct recognition for BS-RCS					
Frequency band	Polarization	Metric E_0	Metric E_1	Metric $E_{0.05}$	Aggregation
FB1: [20; 80] MHz	HH	0.34	0.37	0.38	0.39
FB1: [20; 80] MHz	HV	0.30	0.33	0.32	0.32
FB1: [20; 80] MHz	VH	0.32	0.35	0.36	0.35
FB1: [20; 80] MHz	VV	0.30	0.34	0.33	0.34
FB2: [190; 250] MHz	HH	0.49	0.46	0.54	0.56
FB2: [190; 250] MHz	HV	0.38	0.38	0.42	0.43
FB2: [190; 250] MHz	VH	0.41	0.39	0.46	0.47
FB2: [190; 250] MHz	VV	0.43	0.36	0.46	0.47
FB3: [450; 550] MHz	HH	0.64	0.53	0.71	0.71
FB3: [450; 550] MHz	HV	0.46	0.40	0.52	0.53
FB3: [450; 550] MHz	VH	0.51	0.43	0.57	0.57
FB3: [450; 550] MHz	VV	0.53	0.41	0.57	0.57
FB4: [1.2; 1.3] GHz	HH	0.66	0.54	0.74	0.74
FB4: [1.2; 1.3] GHz	HV	0.60	0.45	0.66	0.67
FB4: [1.2; 1.3] GHz	VH	0.67	0.47	0.72	0.71
FB4: [1.2; 1.3] GHz	VV	0.63	0.45	0.69	0.68

Table 7.20: *Overall probabilities of correct recognition achieved per frequency band and per polarization, for the four different metrics, when using the BS-RCS of targets.*

pairs. For computational reasons, we choose to use three (Tx,Rx) pairs, and more specifically, we consider a single Tx and three Rx's.

We determine the class of a target by performing a majority vote on the class assigned by each single (Tx,Rx) pair considered. The class assigned by each (Tx,Rx) pair is the class obtained by aggregating the results for each of the four metrics. We present, in Tables 7.21 and 7.22, the overall probabilities of correct recognition we achieve for each experiment, from 2.1.1 to 2.4.4, and for each of the three aspect angles of the targets ($\alpha = \{0°, 45°, 90°\}$) and the mean value among all aspect angles. Indeed, we showed in the previous section that the probability of correct recognition varies more with the aspect angle than with the bistatic angular sector.

Overall probabilities of correct recognition for BS-CRCS					
Frequency band	Polarization	$\alpha = 0°$	$\alpha = 45°$	$\alpha = 90°$	Overall
FB1: $[20; 80]$ MHz	HH	0.49	0.36	0.33	0.39
FB1: $[20; 80]$ MHz	HV	0.38	0.36	0.43	0.39
FB1: $[20; 80]$ MHz	VH	0.25	0.27	0.3	0.28
FB1: $[20; 80]$ MHz	VV	0.35	0.5	0.43	0.42
FB2: $[190; 250]$ MHz	HH	0.76	0.59	0.53	0.63
FB2: $[190; 250]$ MHz	HV	0.72	0.53	0.33	0.53
FB2: $[190; 250]$ MHz	VH	0.67	0.56	0.49	0.58
FB2: $[190; 250]$ MHz	VV	0.63	0.5	0.5	0.54
FB3: $[450; 550]$ MHz	HH	0.93	0.8	0.82	0.85
FB3: $[450; 550]$ MHz	HV	0.91	0.81	0.67	0.8
FB3: $[450; 550]$ MHz	VH	0.84	0.83	0.71	0.79
FB3: $[450; 550]$ MHz	VV	0.92	0.72	0.73	0.79
FB4: $[1.2; 1.3]$ GHz	HH	0.98	0.92	0.87	0.92
FB4: $[1.2; 1.3]$ GHz	HV	0.94	0.85	0.81	0.87
FB4: $[1.2; 1.3]$ GHz	VH	0.95	0.95	0.86	0.92
FB4: $[1.2; 1.3]$ GHz	VV	0.96	0.88	0.89	0.91

Table 7.21: *Probabilities of correct recognition achieved when considering the BS-CRCS of targets, and three (Tx,Rx) pairs.*

The probabilities of correct recognition we achieve for three (Tx,Rx) pairs are of about 10% higher than for a single (Tx,Rx) pair. It is thus experimentally proven that considering multiple (Tx,Rx) pairs improves the probability of correct recognition. As we can also expect from the previous experiments, the probabilities of correct recognition are lower when considering the BS-RCS of targets rather than their BS-CRCS.

Overall probabilities of correct recognition for BS-RCS					
Frequency band	Polarization	$\alpha = 0°$	$\alpha = 45°$	$\alpha = 90°$	Overall
FB1: $[20; 80]$ MHz	HH	0.28	0.3	0.35	0.31
FB1: $[20; 80]$ MHz	HV	0.28	0.23	0.21	0.24
FB1: $[20; 80]$ MHz	VH	0.19	0.25	0.26	0.24
FB1: $[20; 80]$ MHz	VV	0.27	0.32	0.19	0.26
FB2: $[190; 250]$ MHz	HH	0.5	0.41	0.42	0.44
FB2: $[190; 250]$ MHz	HV	0.24	0.27	0.24	0.25
FB2: $[190; 250]$ MHz	VH	0.34	0.34	0.28	0.32
FB2: $[190; 250]$ MHz	VV	0.45	0.35	0.28	0.36
FB3: $[450; 550]$ MHz	HH	0.84	0.73	0.69	0.75
FB3: $[450; 550]$ MHz	HV	0.64	0.49	0.46	0.53
FB3: $[450; 550]$ MHz	VH	0.68	0.6	0.45	0.58
FB3: $[450; 550]$ MHz	VV	0.7	0.57	0.52	0.6
FB4: $[1.2; 1.3]$ GHz	HH	0.91	0.69	0.83	0.81
FB4: $[1.2; 1.3]$ GHz	HV	0.82	0.56	0.65	0.68
FB4: $[1.2; 1.3]$ GHz	VH	0.89	0.81	0.76	0.82
FB4: $[1.2; 1.3]$ GHz	VV	0.76	0.72	0.73	0.73

Table 7.22: *Probabilities of correct recognition achieved when considering the BS-RCS of targets, and three (Tx,Rx) pairs.*

7.8 Conclusion

In this chapter, we performed the recognition of targets by using either their bistatic complex radar cross-section (BS-CRCS) or their bistatic radar cross-section (BS-RCS). According to the recognition strategy, we built one recognizer for each region of the parameter space, *i.e.* one recognizer for each of the four frequency bands (FB), for each of the four polarizations, for each of the three aspect angles, and for each of the twelve bistatic angular sectors.

The recognition method is based on subspace methods. From a discrete-space trajectory, we produced feature vectors (FVs) that consist of an ensemble of values of either the BS-CRCS or the BS-RCS of targets. Each value of either the BS-CRCS or the BS-RCS is associated with a value of each paramater of the parameter space. The target class model we built from FVs of the learning set (LS) consists in a list of subspaces. We determined the class of an unknown target by four different metrics that are based on a measure of the energy of the projection of the FV of this target onto each subspace of the target class model.

We motivated the use of such a recognition method by the fact that subspace methods are mainly used in the radar area for detection purposes. The use of subspaces for recognition purposes is, to our knowledge, novel. Moreover, when each target class is characterized by a subspace, the addition of a target class does not require to re-compute the entire target class model.

We first performed recognition experiments by using FVs computed for a single

(Tx,Rx) pair. We successively used FVs consisting of the BS-CRCS and of the BS-RCS. The recognition results show that an overall probability of correct recognition of 0.93 can be achieved for a single (Tx,Rx) pair operating at a frequency between 1.2 GHz and 1.3 GHz. The achieved probability of correct recognition increases with frequency. The probability of correct recognition is sensitive to the aspect angle α, but not to the bistatic angle β. The probability of correct recognition also varies according to the polarization used, HH being the best polarization for the targets considered. This can be intuitively understood by the fact that the shapes of the different targets differ more according to their horizontal planes than their vertical planes. We also showed that recognizing targets by using their BS-CRCS gives better results than by using their BS-RCS.

We then performed recognition experiments by using FVs computed for three (Tx,Rx) pairs. We successively used FVs consisting of the BS-CRCS and of the BS-RCS. An overall probability of correct recognition of 0.98 can be achieved at the highest frequency band considered, and at polarization HH, when considering the BS-CRCS of targets. As for a single (Tx,Rx) pair, the probability of correct recognition increases with frequency, and varies according to polarization, HH being the best polarization. The recognizer is less sensitive to the aspect angle α when considering three (Tx,Rx) pairs.

Compared to the recognition of targets by using their radar images (Chapter 6), we need fewer transmitters and receivers to recognize targets. Indeed, while we need 2D diversity to compute radar images of targets, we simply need a 1D diversity to compute FVs of either BS-CRCS or BS-RCS.

In comparison to the probabilities of correct recognition achieved for the recognition of targets by using their radar images, the probabilities of correct recognition achieved for a single (Tx,Rx) pair are of the same order for the first frequency band ($[20; 80]$ MHz), and are lower for the three other frequency bands. This can be explained by the fact that the images contain much more information than the FVs of BS-CRCS or BS-RCS. When using multiple (Tx,Rx) pairs, *i.e.* three in the experiments performed here, the probability of correct recognition rises by about 10%, thus approaching the probabilities of correct recognition achieved when dealing with radar images of targets. Increasing the number of (Tx,Rx) pairs thus increases the probability of correct recognition.

The recognition results we obtained in this chapter showed experimentally that the recognition of targets by using either their BS-CRCS or their BS-RCS, without reconstructing their radar images, is efficient, especially when considering multiple (Tx,Rx) pairs. In Chapter 8, we apply this recognition method on experimentally-acquired, real-life BS-RCS of airplanes.

Chapter 8

Recognition of targets by using their experimentally-acquired, real-life bistatic RCS

Contents

In this chapter, we perform the recognition of air targets by using their bistatic radar cross-section (BS-RCS) that we compute from real-life signals acquired using a passive radar testbed. Section 8.1 describes the motivation for this problem. Section 8.2 presents the block diagram of the implemented automatic target recognition (ATR) system. Section 8.3 presents the detection and discrimination stages of this ATR system. Section 8.4 discusses the grouping of the types of detected airplanes into classes. Section 8.5 describes the computation of the scene geometry. Section 8.6 presents the extraction of the BS-RCS of detected airplanes, and the generation of the BS-RCS for small airplanes, which we cannot detect. Section 8.7 presents the recognition stage of the ATR system. Section 8.8 presents the experimental setup that we use to collect real-life signals. Section 8.9 presents the collected data, and shows example of received signals. Section 8.10 describes the error on the position of the airplanes, its influence on the value of the BS-RCS, and the reasons for using the BS-RCS of the airplanes instead of their bistatic complex radar cross-section (BS-CRCS). Section 8.11 presents the recognition experiments we perform and the achieved probabilities of correct recognition. Section 8.12 concludes.

8.1   Motivation for the recognition of targets by using their real-life bistatic RCSs

In Chapter 7, we performed the recognition of (air) targets by using either their bistatic complex radar cross-section (BS-CRCS) or their bistatic radar cross-section (BS-RCS). The BS-CRCS and the BS-RCS of the targets of interest were extracted from signals transmitted and received in an anechoic chamber. We now plan to test the recognizer developed in Chapter 7 on BS-RCS of (air) targets computed from real-life signals, acquired in the real, outdoor world. In this chapter, we deal with the recognition of targets by using their BS-RCS, which are extracted from real-life passive bistatic radar signals.

To demonstrate the validity of our approach, we built a passive-radar-system testbed consisting of one transmitter (Tx) of opportunity and one receiver (Rx). We deployed the testbed - produced by the SONDRA lab of SUPELEC - in the vicinity of Orly Airport, near Paris, France. We collected the data almost continuously for

ten days, which allows us to perform recognition experiments involving three classes of airplanes. (The data for the last class were generated by simulation.)

8.2 Block diagram of the automatic target recognition system

Figure 8.1 shows the block diagram of the automatic target recognition (ATR) system. Since we are in a real, outdoor configuration, we first detect targets in the detection stage. We then determine whether the detected targets are of interest or not in the discrimination and pre-classification stage. These detection and discrimination/pre-classification stages are the only differences with the ATR system that is discussed in Chapter 7. For each target of interest, we extract its bistatic radar cross-section (BS-RCS) from (1) the signal transmitted by an illuminator of opportunity and scattered on the target, and (2) the scene parameters, which consist in the scene geometry, the polarizations of the Tx and the Rx, and the frequency of the Tx. We assume that the scene parameters are known.
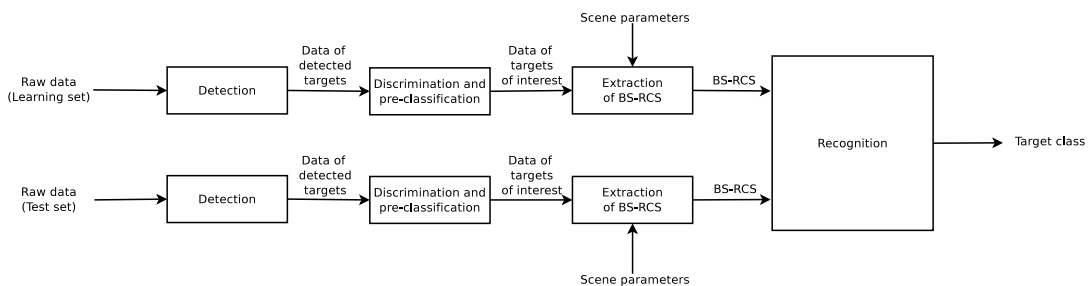
Figure 8.1: *Block diagram of our ATR system using real-life bistatic radar cross-sections of air targets.*

For a particular detected target, the scattered signals belong to either the learning set (LS) or the test set (TS). The LS is used to generate the target class model, while the TS is used to evaluate the performance of the target class model by assigning a class to each object of the TS.

8.3 Detection, discrimination, and pre-classification

We must first detect targets, one at a time. Among the signals scattered by targets, we must discriminate whether a scattered signal corresponds to a target of interest to us. We define a target of interest as being the air target that we detected. For both the detection and the discrimination (and pre-classification), we use the automatic dependent surveillance - broadcast (ADS-B) signals that are sent by airplanes following an interrogation.

As described in Chapter 1, secondary surveillance radars (SSRs), in S-mode, send interrogation signals to the airplanes, on request from the control tower. The airplane

transponder transmits omnidirectional (DPSK) signals at 1090 MHz. ADS-B receivers collect such signals. In our testbed, we detect airplanes from the analysis of ADS-B signals. In an operational system, the detection of an air target would be performed by a conventional moving target detector (MTD) radar, such as an airport primary radar.

ADS-B signals provide the International Civil Aviation Organization (ICAO) code (such as AFR for Air France) and the callsign (such as AFR123) of the detected airplane. By interrogating an Internet database such as [67], we can determine the type of airplane we detect. We use this information to define the different classes of airplanes (8.4).

We discriminate between targets of interest and other targets in two ways. First, a detected target is thus necessarily an airplane, since only airplanes send ADS-B signals. Second, in order to discriminate between the signals scattered by different airplanes that might be in the vicinity of the ground ADS-B receiver at the same time, we use the position information contained in ADS-B signals to compute the Doppler shift of the detected airplane. Therefore, by using a Doppler filter, we select the part of the received signal that corresponds to the signal scattered by the appropriate airplane, as shown in Fig. 8.2.
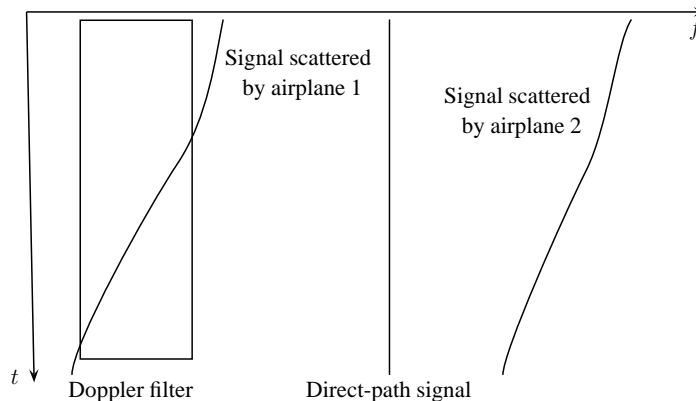
Figure 8.2: *Illustration of the Doppler filter applied to select the signal scattered by airplane 1 when two airplanes are in the vicinity of the passive radar system at the same time.*

8.4   Classes of targets

In this section, we present the types of airplanes that we detected during the measurement campaign. We then discuss the grouping of airplanes into classes.

8.4.1   Types of detected airplanes

We detected a total of 1329 airplanes during the measurement campaign. We list the 32 different types of airplanes per type of airplane family in Table 8.1.

Family	Number of observations	Type	Number of observations
A300	4	A30B	4
A320	661	A318	6
		A319	235
		A320	308
		A321	112
A330	156	A332	79
		A333	77
A340	47	A342	1
		A343	45
		A346	1
B737	206	B733	9
		B734	2
		B735	3
		B736	4
		B737	13
		B738	175
B747	53	B744	53
B757	18	B752	11
		B753	7
B767	70	B762	8
		B763	54
		B764	8
B777	99	B772	35
		B773	55
		B77F	2
		B77L	1
		B77W	6
Embraer 190	3	E190	3
Avro RJ85	5	RJ85	5
Avro RJ100	1	RJ1H	1
Falcon FA10	1	FA10	1
Fokker F100	1	F100	1
Unidentified	6		

Table 8.1: *List of the types and families of airplanes we detected during the measurement campaign.*

We define the classes of airplanes according to the physical characteristics of these airplanes. We thus describe the characteristics of the different airplanes we detected in Tables 8.2, 8.3, 8.4, 8.5, and 8.6. For each type of airplane, we show its length, height, wingspan, wing area, wing position, fuselage width, and number of engines.

Type of Plane	A300	A310	A318	A319
Length [m]	54.10	46.66	34.10	33.84
Height [m]	16.5	15.8	12.51	11.76
Wing span [m]	44.84	43.89	34.10	34.10
Wing area [m^2]	260.0	219.0	122.0	122.4
Wing position	low	low	low	low
Fuselage width [m]	5.64	5.64	3.95	3.95
Number of engines	2	2	2	2

Table 8.2: *Characteristics of the Airbus airplanes, from A300 to A319 [2].*

Type of Plane	A320	A321	A330	A340
Length [m]	37.57	44.51	63.69	67.93
Height [m]	11.0	11.76	16.83	17.28
Wing span [m]	34.10	34.10	60.30	63.45
Wing area [m^2]	122.6	123.0	363.1	363.1
Wing position	low	low	low	low
Fuselage width [m]	3.95	3.95	5.64	5.64
Number of engines	2	2	2	4

Table 8.3: *Characteristics of the Airbus airplanes, from A320 to A340 [2].*

Type of Plane	BAe Avro RJ85	BAe Avro RJ100
Length [m]	28.60	26.34
Height [m]	8.59	8.59
Wing span [m]	26.34	26.34
Wing area [m^2]	77.3	77.3
Wing position	high	high
Fuselage width [m]	3.56	3.56
Number of engines	4	4

Table 8.4: *Characteristics of the British Aerospace airplanes RJ85 and RJ100 [90].*

8.4.2   Grouping of targets into classes

Tables 8.2, 8.3, 8.4, 8.5, and 8.6 show that the size, and thus, the characteristic dimension of the (detected) airplanes vary from 26 m to 74 m. At the frequency of the transmitter of opportunity (further discussed below) of 114.7 MHz, with

Type of Plane	B737	B747	B757	B767-400	B777-300
Length [m]	42.1	70.66	46.7	61.3	73.9
Height [m]	12.6	19.41	6.45	16.8	18.5
Wing span [m]	35.8	64.44	38.05	51.9	60.9
Wing area [m^2]	91.1	511.0	181.25	-	427.8
Wing position	low	low	low	low	low
Fuselage width [m]	5.7	6.50	3.76	9.3	6.50
Number of engines	2	4	2	2	2

Table 8.5: *Characteristics of the Boeing airplanes [19].*

Type of Plane	Embraer E190	Falcon 10	Fokker 100
Length [m]	36.24	13.86	35.53
Height [m]	10.28	4.61	8.50
Wing span [m]	28.72	13.08	28.08
Wing area [m^2]	92.5	24.1	93.5
Wing position	low	low	low
Fuselage width [m]	3.01	-	3.08
Number of engines	2	2	2

Table 8.6: *Characteristics of various other airplanes [90].*

corresponding wavelength λ of 2.62 m, the key ratio λ/D varies from 0.035 to 0.1. We saw in Chapter 3 that, for such ratios, the scattering mechanisms are mainly a function of the shape of the airplanes.

The tables show that all detected commercial airplanes have essentially the same shapes, except for the overall size and the number of engines. It thus makes sense to define two classes for commercial airplanes: large-size airplane with four engines and mid-size airplanes with two engines.

Table 8.1 does not include smaller airplanes, such as private planes, because most of the smaller airplanes do not have ADS-B, the result being that we were unable to detect them. However, it makes sense to define a third class to include these smaller airplanes. We thus decide to define the following three classes based upon the overall size S [m] (the largest of wing span and fuselage length) and the number of engines

- $S < 20$: class of small-size airplanes

- $20 \leq S < 30$: no class defined

- $30 \leq S < 40$ and 2 engines: class of mid-size airplanes

- $40 \leq S < 50$: no class defined

- $50 \leq S$ and 2 engines: no class defined

- $50 \leq S$ and 4 four engines: class of large-size airplanes.

8.5   Scene parameters

The scene parameters, *i.e.* the positions of the transmitter (Tx) and the receiver (Rx), the position of a detected airplane throughout its trajectory, the polarizations of the Tx and the Rx, and the frequency of the Tx, are an input of the automatic target recognition (ATR) system. The positions of both the Tx and the Rx are known since they are fixed. The polarizations of the Tx and the Rx, and the frequency of the Tx are known by construction of the passive radar testbed.

In order to compute the position of a detected airplane, we use the information sent via the ADS-B signals. In an operational system, the position of a detected airplane would be given by a radar such as an airport primary surveillance radar.

The information sent by the ADS-B system aboard an airplane (upon interrogation) contains the position of the airplane. Each position is provided as latitude, longitude, and barometric altitude, and is encoded according to the Compact Position Reporting (CPR) format. We use the position of the airplane over time to compute the Doppler shift of the signal scattered by this airplane, as explained in Section 8.3. We also use the position of the airplane to compute its bistatic radar cross-section (BS-RCS), aspect angle α, and bistatic angle β, which are the parameters of the parameter space (Section 6.2).

We also know the polarization and the frequency of the Tx, and the polarization of the Rx.

8.6   Extraction of the bistatic RCS for the three airplane classes of interest

We describe our method for the extraction of the bistatic radar cross-section (BS-RCS) from real-life data for the mid-size and large-size airplanes. Since we could not detect small-size airplanes, we generate the BS-RCS of small-size airplanes from a simple, adjustable model.

8.6.1   Extraction of the bistatic RCS from real-life data for mid-size and large-size airplane classes.

Consider the bistatic (BS) configuration shown in Fig. 8.3 for a single (Tx,Rx) pair. The transmitter (Tx) is located at T and the receiver (Rx) at R. The object of interest is located at S. We assume that the geometry is known. The Tx sends out a transmit signal - which can be viewed as being a continuous-wave (CW) signal - and the Rx receives the sum of the direct signal (from R) and the scattered signal (from S) [186]. However, as explained later, our technique requires that we are able to separate these two signals.

These signals differ by their different arrival times, but the difference between these signals is too short to allow one to separate the signals in the time domain, the reason for this being the sampling frequency of 48 kHz. The different arrival times
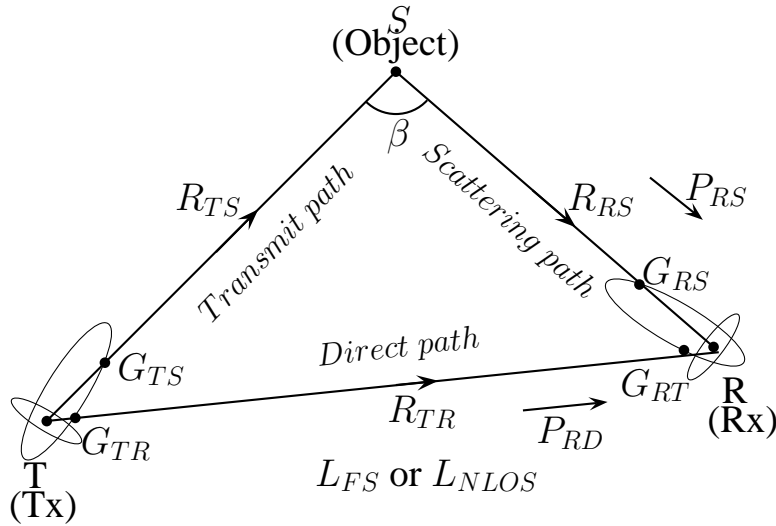
Figure 8.3: *Bistatic (BS) radar configuration corresponding to one (Tx,Rx) pair look-ing at one object. T, R, and S are the positions of the Tx, Rx, and object, respec-tively. The figure shows the antenna beampatterns for the Tx and Rx. It also shows the transmit path $\overline{TS}$, the scattering path $\overline{SR}$, and the direct path $\overline{TR}$, along each of which the corresponding signal travels. The various parameters shown are discussed in the text. The figure is used as a support to explain how the BS-RCS of the object is obtained from the signal received at R, which is the sum of the direct signal and the scattered signal (if any).*

could be computed if the sampling frequency was much higher. However, the motion of the object induces a Doppler shift in the scattered signal received from S, and this leads to both signals being generally (but not always) well separated in frequency. The only hope is thus to separate the two signals of interest in the frequency domain. In the analysis below, we assume that the direct and scattered signals can be separated. This allows us to get their respective power.

We denote by P_T the power transmitted (by the Tx). We denote by P_{RX} the power received (by the Rx), with X replaced by D for the direct path, and by S for the scattering path.

The scattered power P_{RS} received from S is given by the BS radar equation [224], expressed in natural units (*i.e. Watts*),

$$P_{RS} = \frac{P_T G_{TS} G_{RS} \lambda^2 \sigma}{(4\pi)^3 R_{TS}^2 R_{RS}^2}, \tag{8.1}$$

where the G_{XS}'s and R_{XS}'s are the antenna gains and the ranges shown in Fig. 8.3, λ the wavelength of the transmitted signal, and σ the BS-RCS of the object for the given configuration and object orientation. More specifically, G_{TS} is the gain of the Tx antenna in the direction of S, and G_{RS} is the combined gain of the Rx antenna in the direction of S and of the gain of the Rx chain.

The power P_{RD} received directly from T is given by the link budget equation [99],

expressed in natural units,

$$P_{RD} = \frac{P_T G_{TR} G_{RT}}{L},$$
(8.2)

where G_{TR} and G_{RT} are the antenna gains shown in Fig. 8.3, and L the propagation loss, which is further discussed later.

The desired BS-RCS σ is directly obtained from the ratio

$$\frac{P_{RS}}{P_{RD}} = \frac{G_{TS} G_{RS} \lambda^2 \sigma L}{(4\pi)^3 R_{TS}^2 R_{RS}^2 G_{TR} G_{RT}}.$$
(8.3)

One finds

$$\sigma = \frac{P_{RS}}{P_{RD}} \frac{G_{TR} G_{RT}}{G_{TS} G_{RS}} \frac{(4\pi)^3 R_{TS}^2 R_{RS}^2}{\lambda^2 L}.$$
(8.4)

Observe that P_T, which is unknown (since the Tx is an illuminator of opportunity), does not appear in the above equation for σ.

By introducing the gain-ratio parameter $G = G_{TR}/G_{TS}$, we can rewrite the last equation as

$$\sigma = \frac{P_{RS}}{P_{RD}} \frac{G_{RT}}{G_{RS}} G \frac{(4\pi)^3 R_{TS}^2 R_{RS}^2}{\lambda^2 L}.$$
(8.5)

On the right-hand side of this equation, the two powers P_{RS} and P_{RD} can be measured from the received signals; the ranges R_{TS} and R_{RS} can easily be found since the configuration geometry is known; the gains G_{RT} and G_{RS} of the Rx antenna can be obtained from the configuration geometry and the Rx antenna beampattern (and thus, for each position S of the object); and, of course, λ is known. Since the beampattern of the Tx antenna is unknown, the gains of the transmitted signals G_{TR} and G_{TS} are unknown. The last quantity to be discussed is the loss L.

If the direct path $\overline{TR}$ between T and R is unobstructed, *i.e.* "line of sight (LOS)", also called "free space (FS)", then the corresponding loss L is denoted by L_{LOS}, or L_{FS}, and is given by [99]

$$L_{LOS} = \left(\frac{4\pi R_{TR}}{\lambda}\right)^2,$$
(8.6)

where $\lambda = c/f$ is the wavelength, and R_{TR} the distance from T to R (in km).

If the path $\overline{TR}$ is obstructed, *i.e.* "non-LOS (NLOS)", then the corresponding loss is denoted by L_{NLOS}, and is given by

$$L_{NLOS} = L_{LOS} L_{TER},$$
(8.7)

and, in dBs, by

$$L_{NLOS} = L_{LOS} + L_{TER} \quad [\text{dB}],$$
(8.8)

where L_{TER} is the additional loss due to the terrain and other obstructions, referred to here as the terrain loss.

The terrain loss L_{TER} is unknown. However, it is important to observe that, for our configuration geometry, L_{TER} is approximately constant. While we could try to

estimate L_{TER}, here we simply use L_{LOS} in Eq. (8.5), which yields a "biased" BS-RCS, denoted by σ', and given by

$$\sigma' = K\frac{G}{L_{LOS}}, \tag{8.9}$$

where

$$K = \frac{P_{RS}}{P_{RD}}\frac{G_{RT}}{G_{RS}}\frac{(4\pi)^3 R_{TS}^2 R_{RS}^2}{\lambda^2}. \tag{8.10}$$

This biased BS-RCS σ' is related to the true BS-RCS $\sigma = KG/L_{NLOS}$ via

$$\sigma' = G\frac{L_{NLOS}}{L_{LOS}}\sigma = GL_{TER}\sigma, \tag{8.11}$$

and, in dBs, via

$$\sigma' = \sigma + G + L_{TER} \quad \text{[dB]}. \tag{8.12}$$

More generally, the value σ' obtained for the BS-RCS is related to the true BS-RCS σ via $\sigma' = \sigma + \Delta\sigma$ [dB], where $\Delta\sigma$ includes the terrain loss, the non-omnidirectional beampattern of the Tx antenna, and other systematic errors that are assumed to remain quasi constant during the measurement campaign, as shown in Fig. 8.4. Our recognizer is trained and tested on the biased σ', rather than on the true σ. However, the biased BS-RCS will, in the sequel, still be denoted by σ, rather than by σ'.
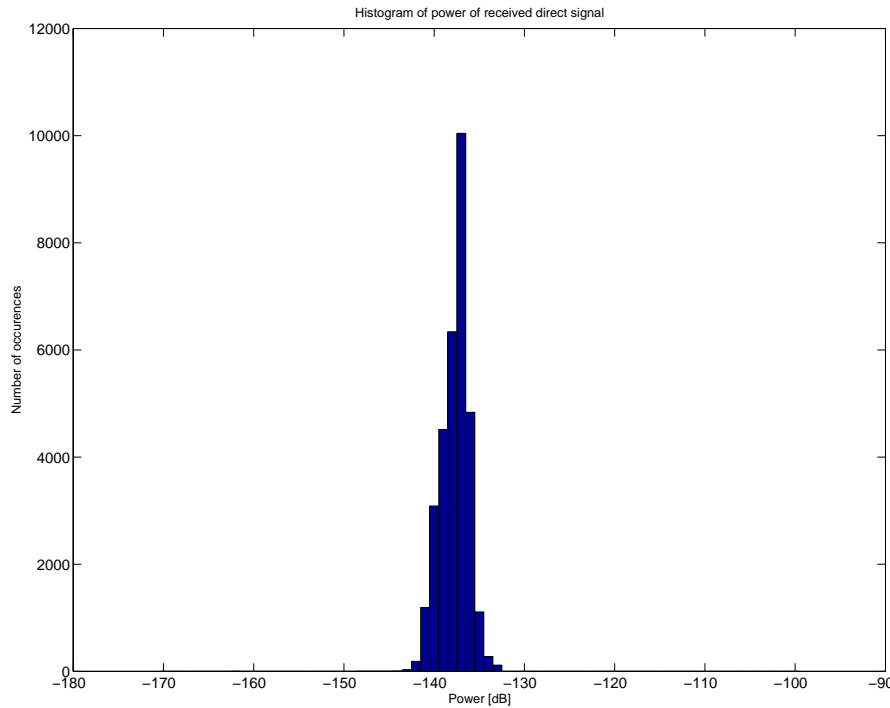
Figure 8.4: *Histogram of the power of the received direct signal. One clearly sees that the terrain loss and other systematic errors are quasi constant through the measurement campaign, thus validating the approach for the computation of the BS-RCS.*

8.6.2   Generation of the bistatic RCS from a simple, adjustable model for small-size airplane class

Since we could not detect small-size airplanes, we produced BS-RCS data for the small-size airplane class by using a simple model consisting of one wire for the body and one wire for each wing (Fig. 8.5).
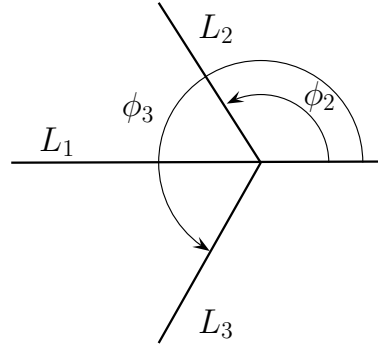
Figure 8.5: *Model for the airplanes in the small-size airplane class. This simple model consists of three wires, one for the body and one for each wing.*

The BS-RCS σ corresponding to a model consisting of N wires of length L_i and angle ϕ_i is computed according to the following formula,

$$\sigma = \sum_{i=1}^{N} L_i \operatorname{sinc}(X_i), \tag{8.13}$$

where

$$X_i = \frac{2\pi L_i}{\lambda} \sin \frac{\alpha_T + \alpha_R + \phi_i}{2} \cos \frac{\beta}{2}, \tag{8.14}$$

and where α_T and α_R are the angles between the pointing direction of the airplane and $\overline{TS}$ and $\overline{SR}$, respectively (Fig. 6.4).

To position and orient the small-size airplanes, we use the information recorded for all real mid-size airplanes observed. Therefore, we have as many samples for the small-size airplanes as we have for the mid-size airplanes. To provide size diversity, the length of each model wire was varied randomly in an interval centered on 4 m for the body, and 2 m for each wing, the width of the intervals being 20% of the center value.

8.7   Recognition stage

We use the same recognizer that we used in Chapter 7. For each tile of the parameter space (α, β), we build one recognizer. Each of the three target classes is characterized by a subspace. The subspaces are formed from feature vectors (FVs) exactly as described in Section 7.4.2. We produce FVs exactly as in Section 7.3. Each FV is a one-dimensional array of N bistatic radar cross-section (BS-RCS) values expressed in decibel units. Each BS-RCS value is associated to a point in the parameter space. We emphasize that, for a given airplane, and thus a given trajectory, we can produce several FVs that correspond to several tiles of the parameter space.

The class assigned to an unknown target, characterized by its FV, is decided based on the projection and metrics defined in Sections 7.5.1 and 7.5.2, respectively.

We separate the detected airplanes of each of the three classes into a learning set (LS) and a test set (TS). For each class of airplanes, the first third of the total number of detected airplanes (and thus their corresponding trajectories and their corresponding BS-RCS values) is used for the LS, and the last two thirds for the TS.

8.8 Experimental setup

Our goal is to perform the recognition of airplanes of three categories, *i.e.* large-size airplanes (*e.g.* A343), mid-size airplanes (*e.g.* A319), and small-size airplanes (*e.g.* private planes and UAVs), by using the bistatic radar cross-section (BS-RCS) of these airplanes. We describe the experimental setup we deployed to get real-life data for the large-size and mid-size airplanes.

8.8.1 Testbed

The passive-radar testbed was designed and put together by Sylvain Azarian from SUPELEC/SONDRA, and then deployed in the vicinity of Orly Airport, south of Paris, France (Fig. 8.6). This allowed us to observe airplanes in approach for landing, climbing after take-off, or following airways.

The testbed ends up consisting of a single (Tx,Rx) pair. The transmitter (Tx) of opportunity is the VOR (VHF Omni Range) Tx located at Rambouillet, with identifier RMB, and operating on frequency of 114.7 MHz and vertical polarization (Fig. 8.6). A VOR is a navigation aid widely used in aviation. The choice of such an illuminator of opportunity is discussed below. The receiver (Rx) is based on a software-defined radio (SDR) [135] designed at SONDRA lab. The Rx is located at the point marked "Rx" in Fig. 8.6, and operates on vertical polarization. The distance between the Tx and the Rx is of 15.5 km. To obtain the necessary information about each observed airplane, *i.e.* identity (such as callsign) and position, we use an ADS-B receiver co-located with the SDR-based Rx.

We planned to use, as a second Tx of opportunity, the VOR located at Epernon (EPR, 115.65 MHz), but the corresponding signal-to-noise ratio (SNR) at our Rx proved to be too small to be usable.

Using this experimental setup, we recorded the trajectories of 1329 airplanes of 32 different types (as defined according to [67]) of airplanes listed in Section 8.4, over a period of ten days.

8.8.2 The VOR as a simple illuminator of opportunity

We define the following requirements for the choice of the transmitter of opportunity of our passive-radar-based system:
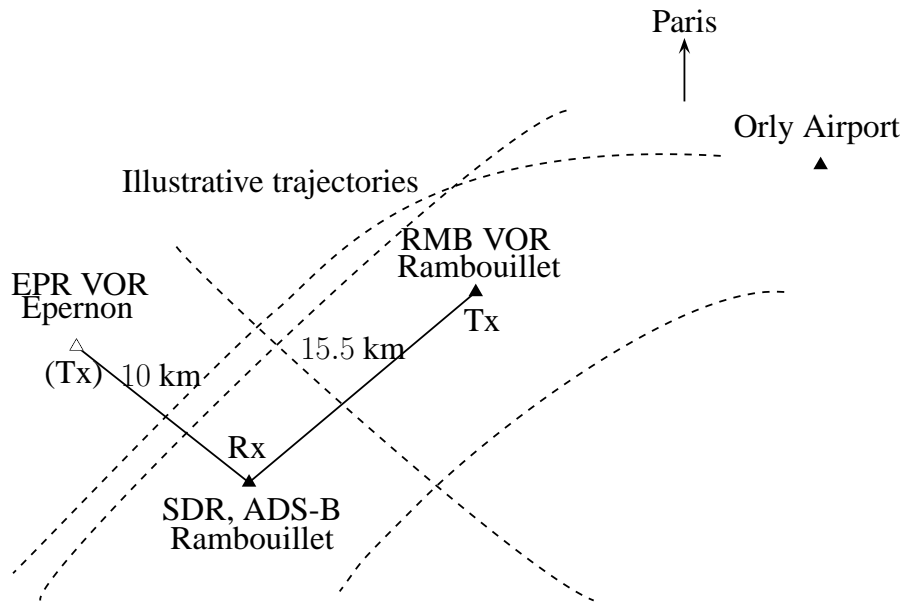
Figure 8.6: *Schematic of the Orly Airport area showing the location of the Tx and Rx used in our passive radar testbed. The Tx is the RMB VOR located at Rambouillet. The Rx - consisting of a software-defined radio (SDR) - is located at a private home. The figure also shows the EPR VOR of Epernon, which we tried to use, but the SNR of which was too small to be usable. The figure also shows samples of four different airplanes trajectories (dashed lines).*

- The transmitting power shall be constant through time since it is used in the computation of the BS-RCS. The knowledge of the transmitting power is not required (Section 8.6)

- The transmitted signal shall not be modulated, in order to keep the system simple. The ideal case is that of a carrier frequency.

- The transmitter shall operate on low frequencies, *i.e.* on frequencies smaller than 1 GHz. The operating frequency shall remain constant through time.

- The beampattern of the transmitting antenna shall not be only directed towards the ground, since we want the transmitted signal to be scattered by airplanes.

The VHF Omni-Range (VOR) is a quasi-ideal transmitter of opportunity, since it satisfies all of these constraints. Figure 8.7 shows the spectrum of the signal transmitted by a VOR. The spectrum of the signal of the VOR consists of one hump centered at the carrier frequency f_c corresponding to audio information (such as the VOR callsign), one "sinusoid" (or at least one very narrow-band signal) at the frequency of $f_c + 9,960$ Hz, called the subcarrier, and two weaker sinusoids located 30 Hz away on each side of the subcarrier, and due to the physical rotation of the VOR antenna. The subcarrier is important because it is well separated from the other frequency components and is thus an almost ideal monochromatic illuminator of opportunity.
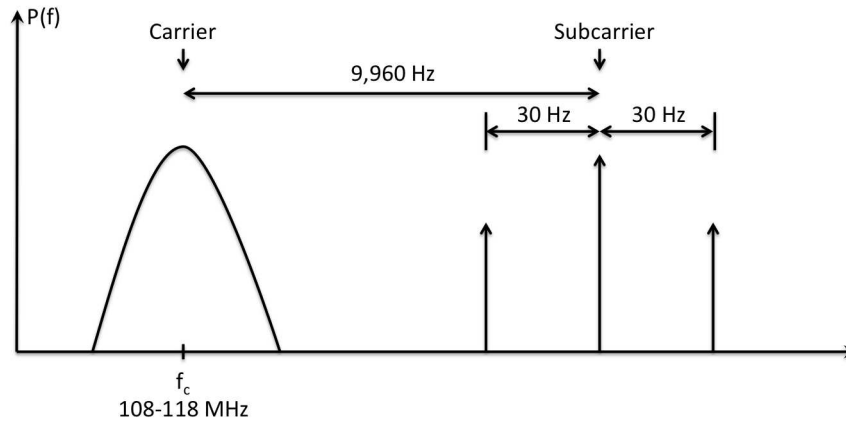
Figure 8.7: *Idealized spectrum of a VOR. The "sinusoid" corresponding to the subcarrier is the effective signal used as an illuminator of opportunity.*

The chosen illuminator of opportunity is the VOR transmitter located at Rambouillet, with callsign RMB, and operating on 114.7 MHz. The spectrogram of a direct signal received from the VOR is shown in Section 8.9.

8.8.3 Collecting the direct and scattered signals by an SDR receiver

As shown in Section 8.6, we have to collect (1) the direct signal, which is the signal transmitted by the VOR and directly (*i.e.* without any scattering) collected by the Rx, and (2) the scattered signal, which is the signal transmitted by the VOR, scattered by the target, and collected by the Rx.

We collect these two signals by using a software-defined radio (SDR) receiver [3, 99, 135]. The role of the SDR is to convert the radiofrequency (RF) signals to their baseband in-phase and quadrature components. Figure 8.8 shows a schematic of the SDR used in our experiments. The SDR converts the RF signals to baseband by using a cascade of three filters and three mixers.

The input RF signal is first passed through an 8th-order low-pass filter with cutoff frequency of 200 MHz, and then through a band-pass filter centered on 115 MHz (about the frequency of the VOR). The resulting signal is mixed to an intermediate frequency (IF) $f_{IF} = 22.94$ MHz. The resulting signal is passed through a band-pass filter centered on f_{IF}. The resulting IF signal is mixed to produce the baseband in-phase and quadrature components, $I(t)$ and $Q(t)$, respectively.

8.8.4 Digital processing of received signals

The $I(t)$ and $Q(t)$ components are digitized by using a computer sound card, to get the digital in-phase and quadrature components, $I[n]$ and $Q[n]$, respectively. A setup procedure is performed before acquisition to compensate the I/Q mismatch caused by different gains and delays in the left and right audio channel.
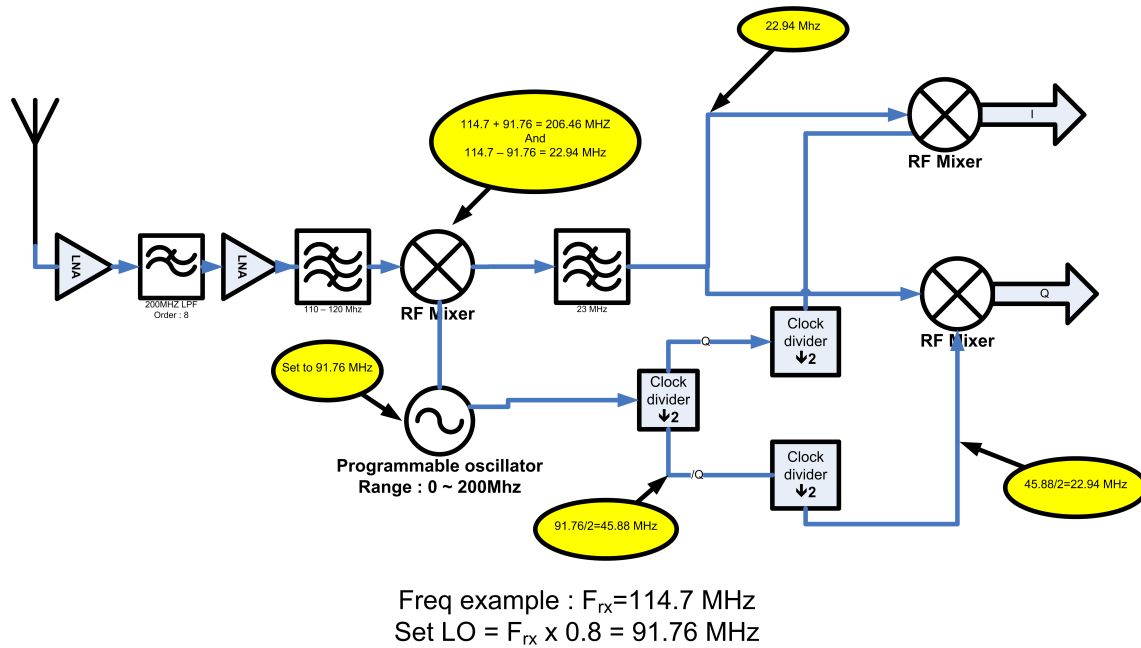
Figure 8.8: *Conversion of the RF input signals to baseband performed by the SDR receiver. The input signal is first filtered twice and then successively converted from RF to IF and from IF to baseband.*

The Fast Fourier Transform (FFTs) is applied to successive segments of the complex sequence $I[n] + jQ[n]$ to obtain the spectrum of the received signal. A spectrogram, which shows the variation of the spectrum as a function of time, of the received signal is obtained by repeating the same operations at successive time instants. Examples of spectrograms are shown in Section 8.9.

8.9   Data collected and examples of received signals

In this section, we present the data available for our recognition experiments. We also show examples of data computed from the received ADS-B signals. We then show examples of spectrograms of signals received by the SDR receiver. We then show the signal-to-noise ratios of both the direct and the scattered signals, and an example of the variations of the bistatic radar cross-section (BS-RCS) as a function of time. Finally, we last show, for each class of airplanes, the distributions of the BS-RCS in the (α, β) parameter space.

8.9.1   Data available for our recognition experiments

The first two sections of Table 8.7 summarize the part of the real data we collected with our passive radar testbed during the measurement campaign that lasted ten days, and that we use for our recognition experiments. The table only shows the types of airplanes for which a significant amount of data is available. Airplanes are divided into the three classes defined earlier. The first two consist of real data. For each type of airplane (in each class), the table gives the number of trajectories observed and the total number of samples obtained, for both the learning set (LS) and the test set (TS).

The number of trajectories is also the number of times an airplane of a given type was tracked. The number of samples is also the number of BS-RCS values available for all trajectories. The last section of Table 8.7 summarizes the synthetic data produced.

Type of airplane	Learning set		Test set	
	Number of trajectories	Number of samples	Number of trajectories	Number of samples
Large-size airplanes - Real data				
A342	1	11	0	0
A343	15	973	30	1680
A346	1	8	0	0
Total	17	992	30	1680
Mid-size airplanes - Real data				
A318	2	56	4	159
A319	78	3316	157	6208
A320	102	5472	206	10530
Total	182	8844	367	16897
Small-size airplanes - Synthetic data				
Misc.	182	8546	367	17195
Total (all)	381	18382	764	35772

Table 8.7: *Data available for our recognition experiments. The types of airplanes are organized in the three categories of large-size, mid-size, and small-size airplanes. The first two categories contain real data collected with our passive radar testbed. The last one contains synthetic data we produced. The table gives the number of trajectories and samples available for each type of airplane.*

8.9.2 Received ADS-B data

We compute the trajectory of airplanes from the positions received by ADS-B signals. Figure 8.9 shows the reconstructed trajectory of an airplane. We also compute the bistatic angle and the (smoothed) Doppler shift as a function of time, *i.e.* essentially along the airplane trajectory, shown in Figs. 8.10 and 8.11, respectively. The Doppler shift is smoothed by using a low-pass filter. Indeed, since commercial airplanes fly according to simple trajectories such as straight lines, the Doppler shift varies smoothly along the airplane trajectory, *i.e.* from one time instant to the next.

8.9.3 Spectrograms

Figure 8.12 shows a spectrogram of the signal received by our (SDR) Rx tuned to the frequency of the RMB VOR, this in the absence of any airplane in the field of view. The spectrogram thus corresponds to the direct signal only. By definition, the spectrogram shows the variation of the power received as a function of frequency and time. The figure also shows a cut at a given time, *i.e.* the spectrum of the signal at that time.
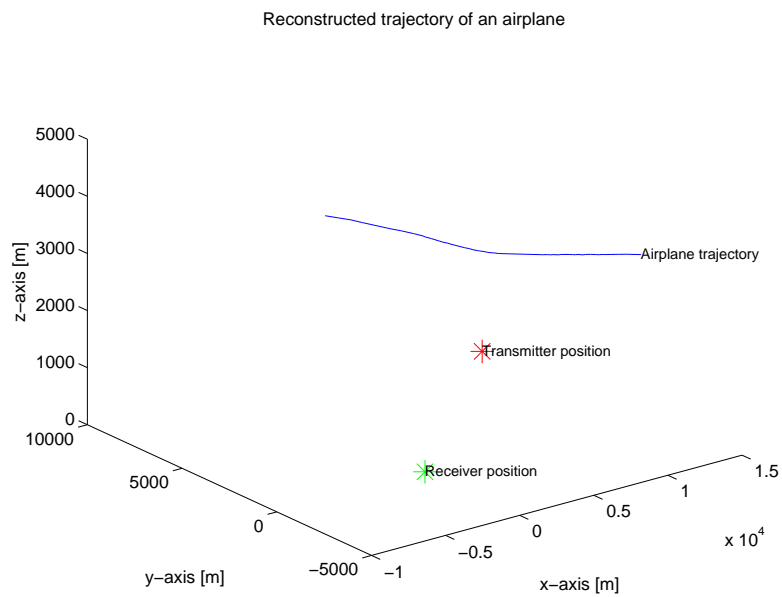
Figure 8.9: *Reconstructed trajectory of an airplane. The locations of the Tx and the Rx are also shown.*
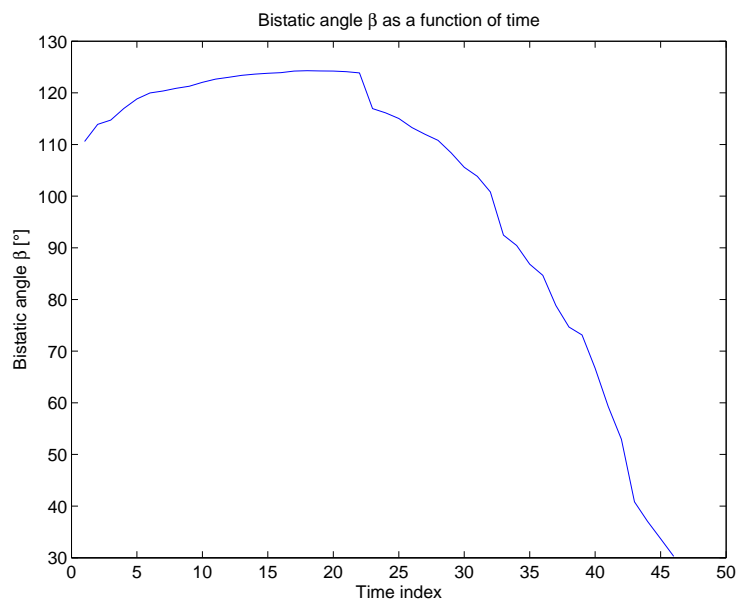
Figure 8.10: *Variation of the bistatic angle β as a function of time, i.e. essentially along the trajectory of an airplane. (Same as Fig. 4.6.)*
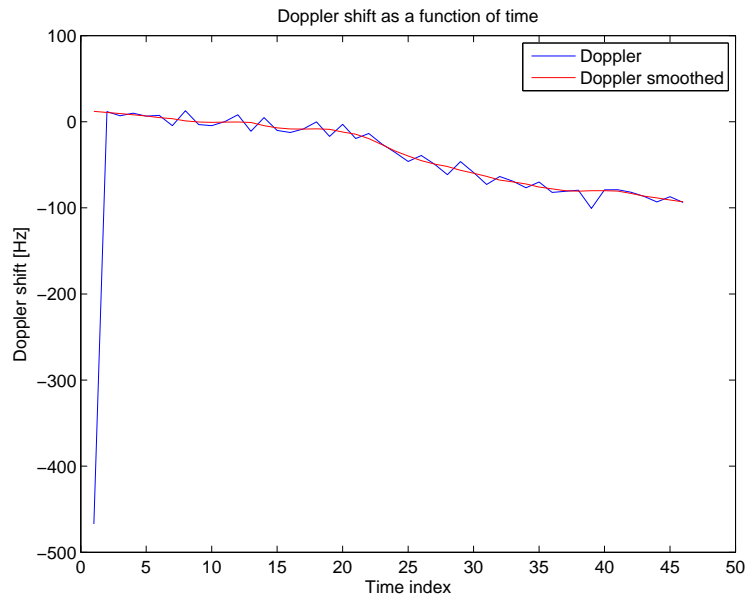
Figure 8.11: *Variation of the Doppler shift as a function of time, i.e. essentially along the trajectory of an airplane.*

Not surprisingly, the spectrum remains virtually the same at all times. This spectrum can be understood in terms of the idealized spectrum of a VOR shown in Fig. 8.7.

Figure 8.13 shows a spectrogram of the signal consisting in the sum of the direct signal and the scattered signal, the latter being due to an (A319) airplane. It is clear that the three vertical traces correspond to the direct signal received from the VOR, and that the three curved traces correspond to the scattered signal from the airplane. The "curving" is due to the time-dependent Doppler shift due to the motion of the airplane.

Spectrograms such as that of Fig. 8.13 automatically separate (at least to the eye) the direct signal and the scattered signal. At any time t, and as long as the separation in frequency is sufficient, we can easily read off the powers P_{RS} and P_{RD} (Fig. 8.3) that are required to compute the airplane radar cross-section (RCS) σ at this time.

8.9.4 Signal-to-noise-ratios

To read off the above powers of the direct and scattered signals, the signal-to-noise ratios (SNRs) must be sufficient. The SNR at some instant is defined as the ratio of the signal power to the noise power at this instant, for a given frequency bandwidth. The power of the noise is measured at any time instant by taking the mean of the power of the received signal in zones outside that of the signal of interest, such as in frequency indices 120 to 140 in Fig. 8.13.

Figure 8.14 shows the SNR of the received direct signal from the RMB VOR as a function of time. As expected, this SNR is relatively constant. Its value is from 40 to 50 dB. Figure 8.15 shows the SNR of the scattered signal as a function of time. As
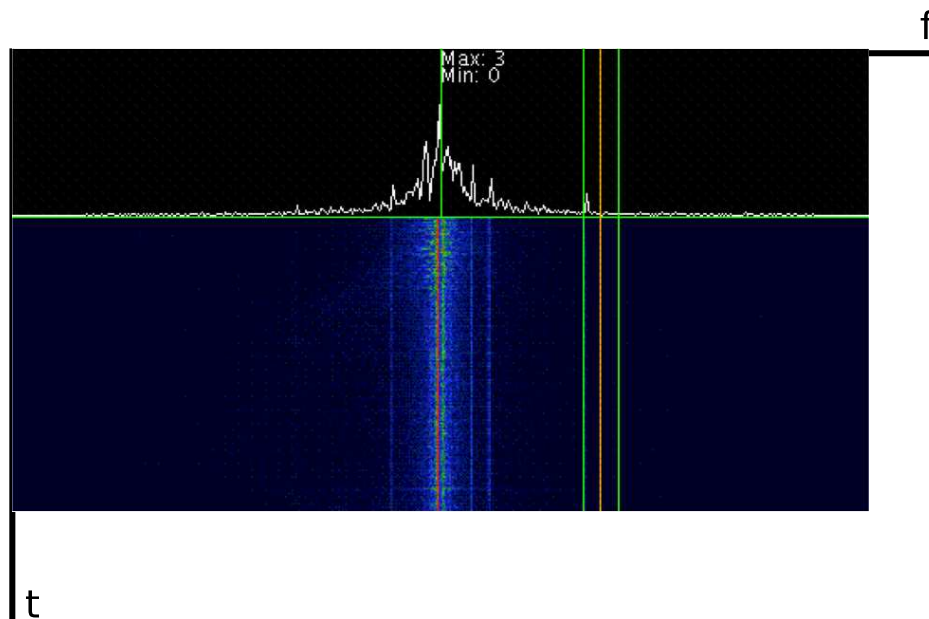
Figure 8.12: *Spectrogram (in "waterfall view") of the signal received in the absence of airplanes. It thus corresponds to the spectrogram of the signal received from the RMB VOR over the direct path. The spectrogram can be interpreted with the help of Fig. 8.7.*
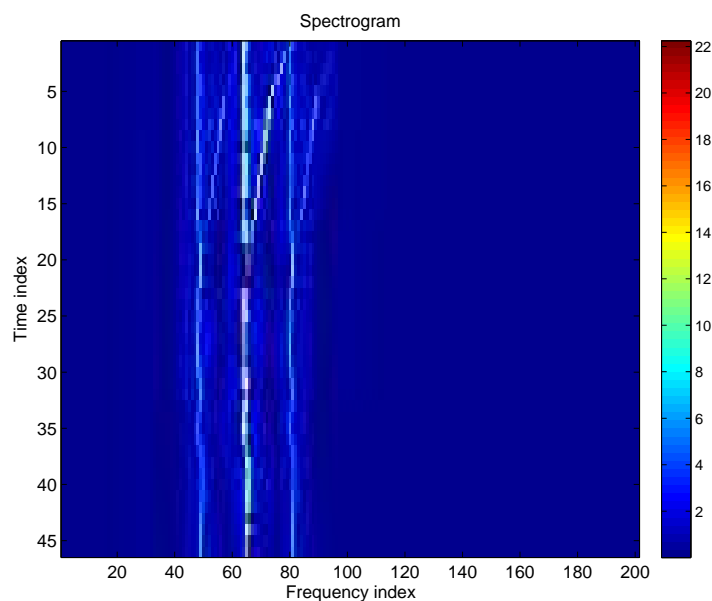
Figure 8.13: *Spectrogram (in "waterfall view") of the signal received in the presence of one airplane. The figure only shows the frequency region near the subcarrier frequency. At most instants, one can easily distinguish between the straight traces due to the direct signal and the curved traces due to the scattered signal. We exploit the separation in frequency between these two components at most instants to get the powers required to compute the RCS values.*

time increases, the position and "view" of the airplane varies, resulting in variations of its bistatic radar cross-section (BS-RCS). The observed variations in SNR with time are directly linked to the variations in BS-RCS with time. However, the value of the SNR is almost always above 25 dB, which guarantees an accurate calculation of the BS-RCS from the measurement of the powers P_{RS} and P_{RD}. We were not able to use the VOR of Epernon, France, precisely because the SNR of the received signal was too small. The sharp transition at the beginning of each of Figs. 8.14 and 8.15 can be ignored.
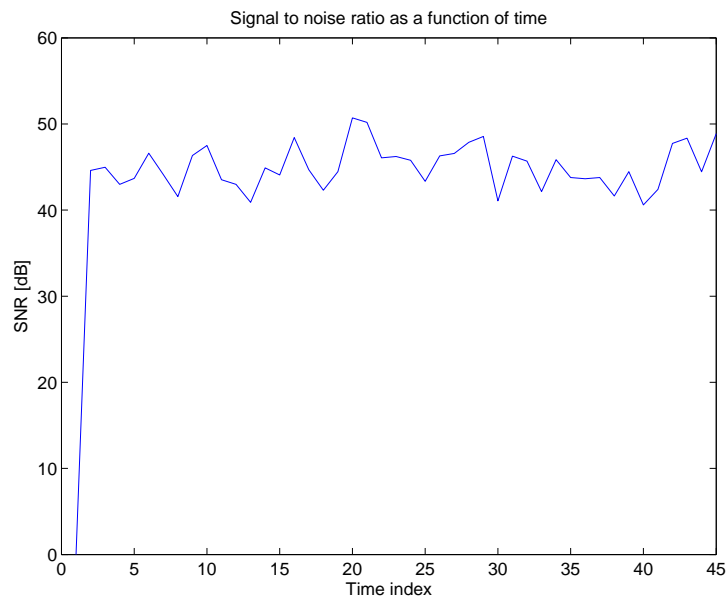
Figure 8.14: *Variation, as a function of time, of the signal-to-noise ratio (SNR) of the signal received in the absence of airplanes and, thus, corresponding to the direct-signal component only.*

8.9.5 Variations of the bistatic RCS as a function of time

Using the values of P_{RS} and P_{RD} obtained as a function of time from a spectrogram such as that of Fig. 8.13, one can determine, from Eq (8.5), the value of the BS-RCS as a function of time. Figure 8.16 shows an example of the variation of BS-RCS as a function of time. Once again, as time increases, the airplane moves and presents different aspect angles.

8.9.6 Distributions of the bistatic RCS in (α, β) plane

Since we know the configuration geometry at any time, we can map the measured (discrete space (DS)) trajectories and corresponding BS-RCS values from the (x, y) plane to the (α, β) plane. The resulting distributions of BS-RCS in the (α, β) plane are illustrated in Figs. 8.17, 8.18, and 8.19 for the three classes of airplanes. Figure 8.17 shows the 2672 real BS-RCS values corresponding to the 47
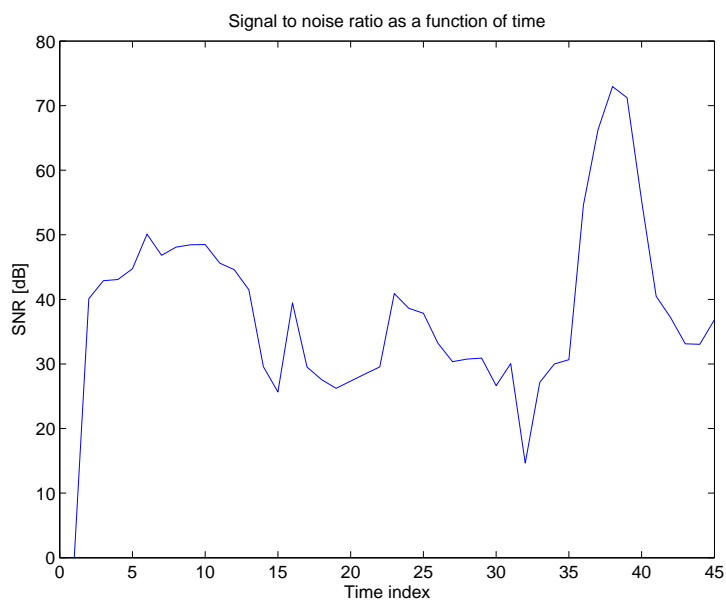
Figure 8.15: *Variation, as a function of time, of the signal-to-noise ratio (SNR) of the signal received from one airplane and, thus, corresponding to the scattered-signal component only. The variations are due to the changes in aspect angle and in bistatic angle as the airplane goes by.*
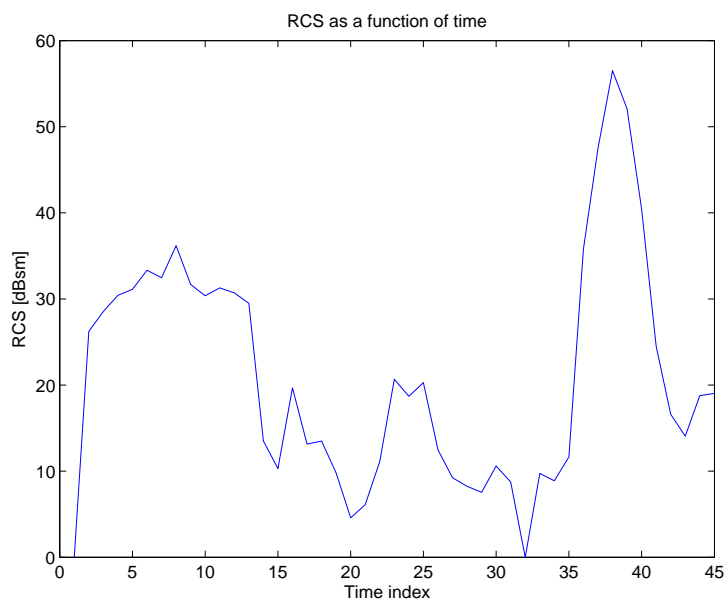
Figure 8.16: *Variation, as a function of time, of the BS-RCS extracted from the received data, via a spectrogram, such as the one shown in Fig. 8.13.*

large-size airplanes observed during our measurement campaign; Fig. 8.18 shows the 25741 real BS-RCS values corresponding to the 549 mid-size airplanes observed over this campaign; Fig. 8.19 shows the 25741 BS-RCS values produced synthetically for the small-size airplanes. The various numbers just cited are those of Table 8.7.
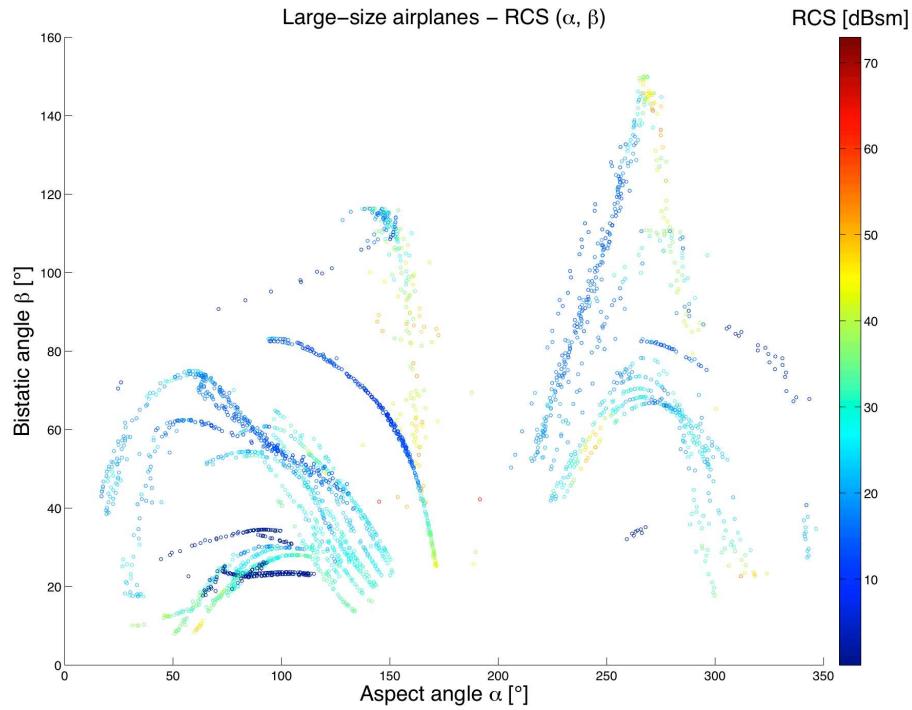
Figure 8.17: *Values of the bistatic RCS for all our (real) large-size airplanes, shown in the (α, β) plane.*

The comparison of the plots of Figs. 8.17, 8.18, and 8.19 shows that the three BS-RCS values at, or near, a given (α, β) point are generally quite different. Of course, our recognition system is designed to exploit these differences.
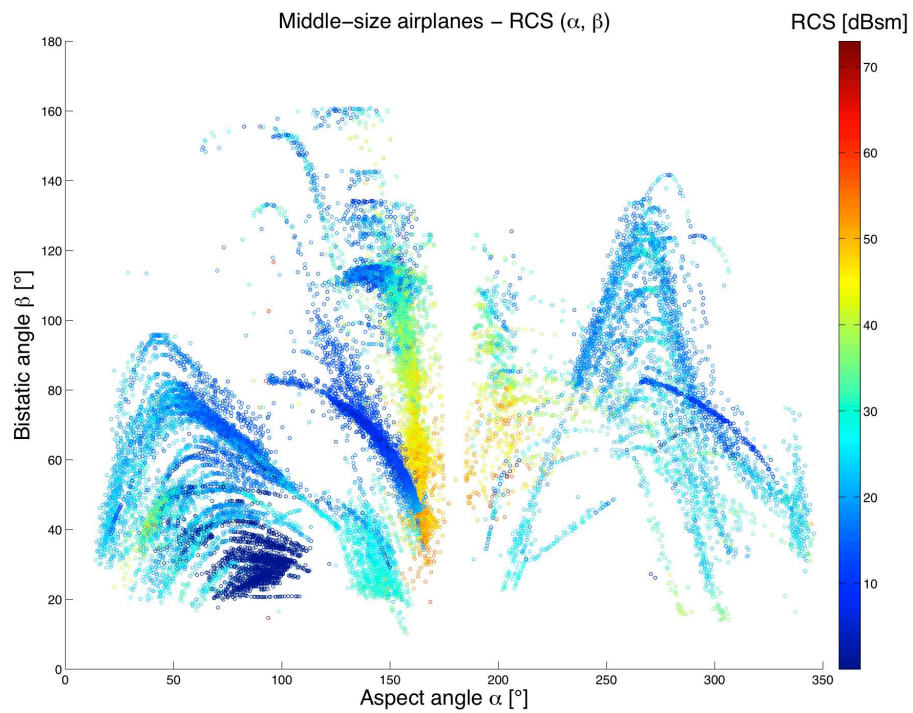
Figure 8.18: *Values of the bistatic RCS for all our (real) mid-size airplanes, shown in the (α, β) plane.*
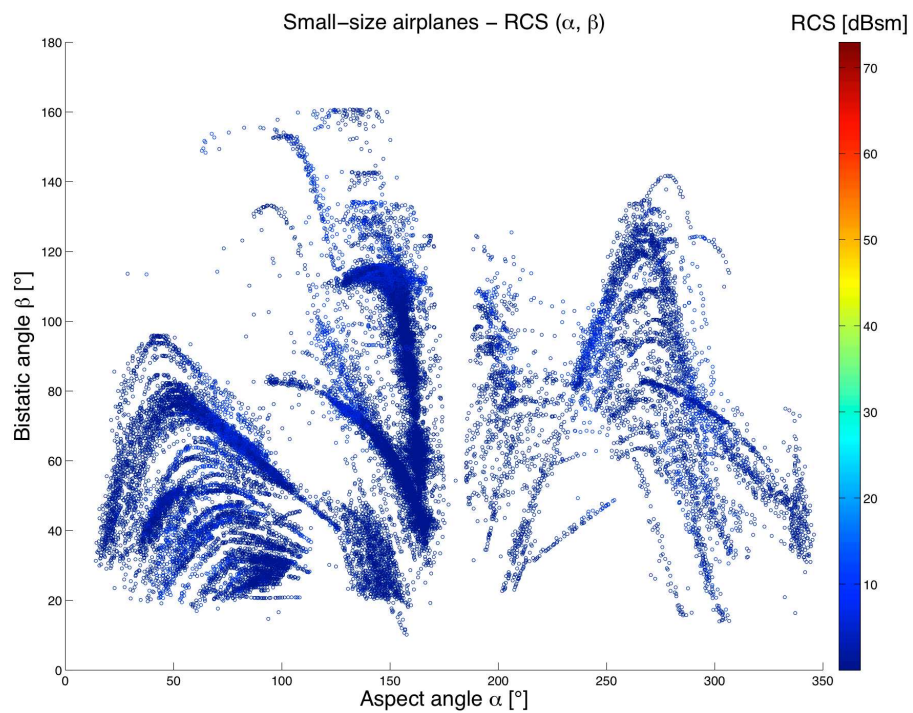
Figure 8.19: *Values of the bistatic RCS for all our (synthetic) small-size airplanes, shown in the (α, β) plane.*

8.10 Errors on the position, the bistatic angle, and the bistatic RCS

The data we receive from ADS-B signals in not free of errors. In this section, we first quantify the error on the position of the airplane. We then express the influence of the error on the position on the values of the bistatic angle and the bistatic radar cross-section (BS-RCS). We also express the reasons for using the BS-RCS instead of the bistatic complex radar cross-section (BS-CRCS).

8.10.1 Error on the position of a target

As shown in Section 8.6, we compute the BS-RCS of an airplane by using the distances transmitter-target (R_{TS}) and receiver-target (R_{RS}) and the powers of both the received scattered signal (P_{RS}) and the received direct signal (P_{RD}). Equation (8.10) is valid for any particular time instant, provided that R_{TS}, R_{RS}, P_{RD}, and P_{RS} are known at the same particular time instant. However, there is some delay between the time instant at which any ADS-B signal is sent from the plane transponder, and the time instant at which the ADS-B signal is received (and decoded) at the ADS-B receiver. There is also some delay for the data processing. These delays induce an error between the computed position of the airplane and to its true position.

To compute the maximum error on the position of an airplane, we assume that the maximum speed of an aircraft is 1000 km/h, *i.e.* roughly 280 m/s. The position is given by a GPS on-board the aircraft, once every second. The accuracy of the GPS is assumed to be of 10 m. The encoding error due to the Compact Position Reporting format (CPR) is of 5.1 m.

In the worst case, there is a delay of 1 s between the times the airplane acquires its position and sends it. Assuming a decoding and post-processing delay of 100 ms at the receiver, the total delay is of 1.1 s between the times the airplane acquires its position and the actual position of the airplane for which we collect the scattered signal. We assume the delay due to the propagation to be negligible. By converting the delay into distances, the maxium distance difference between the position the airplane transmits and its actual position is of 10+5.1+280+28 = 323.1 m.

As can be seen in Figs. 8.20 and 8.21, R_{TS} and R_{RS} are of the order of several kilometers. Therefore, the error ϵ_{Pos} on the position is limited to about 5% of the distances R_{TS} and R_{RS}.

8.10.2 Influence of the error in position on the value of the bistatic RCS

Let us assume that errors in measurement lead us to estimate that the object is positioned at S' rather than at S. The parameters of interest below are the distances between the Tx and S, and between the Rx and S, *i.e.* R_{TS} and R_{RS}. We naturally denote the corresponding distances for S' by $R_{TS'}$ and $R_{RS'}$.
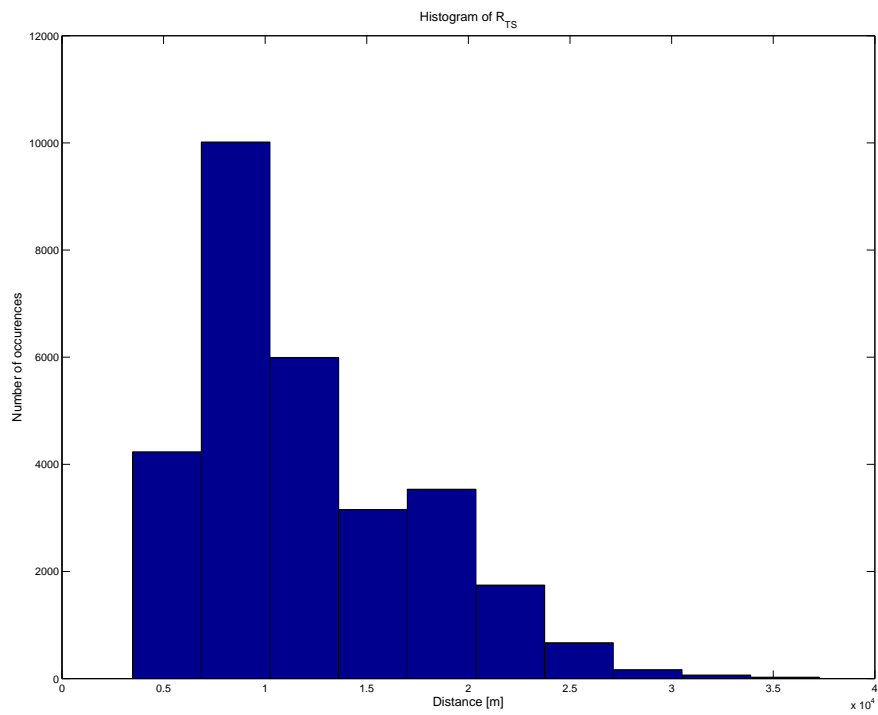
Figure 8.20: *Histogram of the distance R_{TS} between the transmitter and the airplane.*
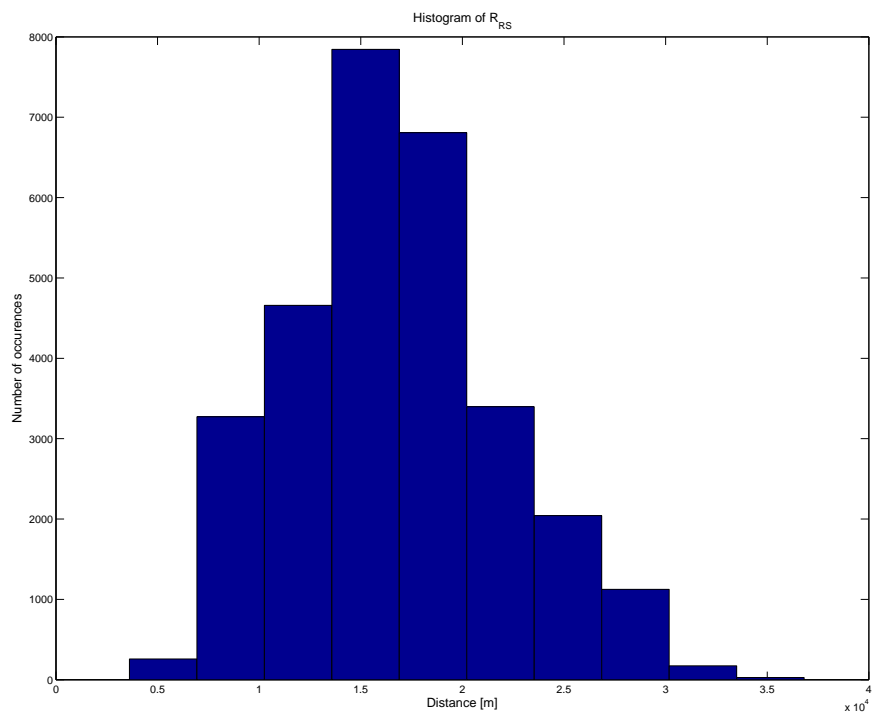
Figure 8.21: *Histogram of the distance R_{RS} between the receiver and the airplane.*

When we compute the BS-RCS based on the true position S of the object (and thus on the corresponding R_{TS} and R_{RS}), we denote this BS-RCS by σ. When we compute this BS-RCS based on the erroneous position S' of the object (and thus based on the corresponding $R_{TS'}$ and $R_{RS'}$), we denote the erroneous BS-RCS by σ'. (This σ' should not be confused with the σ' used in Section 8.6.1.)

The relative error on the value of the BS-RCS, denoted by ϵ_σ, is defined as

$$\epsilon_\sigma = \frac{|\sigma - \sigma'|}{\sigma}. \tag{8.15}$$

Below, we assume that the antenna gains G_{TS} and G_{RS} are not significantly affected by the error in the position of the object. In other words, we assume that $G_{TS} \approx G_{TS'}$ and $G_{RS} \approx G_{RS'}$.

The expression for σ is given by Eq. (8.5), and the corresponding expression for σ' is obtained by using the same equation, with the appropriate adjustments,

$$\sigma' = \frac{P_{RS'}}{P_{RD}} \frac{G_{RT}}{G_{RS'}} \frac{G_{TR}}{G_{TS'}} \frac{(4\pi)^3}{\lambda^2 L} \frac{R_{TS'}^2 R_{RS'}^2}{R_{TR}^2}. \tag{8.16}$$

By substituting Eqs (8.5) and (8.16) into Eq. (8.15), one gets

$$\epsilon_\sigma = \left| 1 - \frac{R_{TS'}^2 R_{RS'}^2}{R_{TS}^2 R_{RS}^2} \right|. \tag{8.17}$$

In the worst case, $R_{TS'}$ and $R_{RS'}$ can be expressed in terms of R_{TS} and R_{RS} respectively as

$$R_{TS'} = R_{TS} + \epsilon_{Pos}, \tag{8.18}$$

$$R_{RS'} = R_{RS} + \epsilon_{Pos}. \tag{8.19}$$

By neglecting factors of order two and higher, Eq. (8.17) reduces to

$$\epsilon_\sigma = \left| 2\epsilon_{Pos} \left(\frac{1}{R_{TS}} + \frac{1}{R_{RS}} \right) \right|. \tag{8.20}$$

This shows that the highest relative error ϵ_σ is achieved for the minimum values of R_{TS} and R_{RS}. Histograms of R_{TS} and R_{RS} are shown in Figs. 8.20 and 8.21, respectively. According to the histograms, the minimum distances are 3478 m and 3653 m. Due to the geometry of the configuration, these two values cannot hold simultaneously. We however use them for the computation of the value of the maximum error on the BS-RCS. We also use the maximum error on the position of the object, which is 323 m. We thus get a maximum relative error on the value of the BS-RCS of 36.44%. In dB units, this gives an error of maximum $10 \log 1.3644 < 1.35$ dB on the value of the BS-RCS. This error is negligible compared to the values of the BS-RCS, as seen in Section 8.9.6.

8.10.3 Reasons for using the bistatic RCS instead of the bistatic complex RCS

Whereas the recognizer of Chapter 7 used bistatic complex radar cross-section (BS-CRCS) of targets the present recognizer uses their bistatic radar cross-section (BS-RCS). We explain the reasons for this below.

We use here the bright point model, which is widely used in the radar domain [35]. According to this model, a target can be considered as being made of a number N of isotropic bright points. According to this model, the scattered signal received at any instant t, $s_{RS}(t)$, is expressed as

$$s_{RS}(t) = \sum_{n=1}^{N} \sqrt{\sigma}_n e^{j[2\pi f(t-\tau_n)+\phi_{Tx}]}, \tag{8.21}$$

where $\sqrt{\sigma}_n$ is the complex radar cross-section associated to bright point n, f the frequency of the signal, τ_n the time delay due to the position of the bright point n, and ϕ_{Tx} the phase of the transmitted signal. Equation (8.21) shows that the scattered signal $s_{RS}(t)$ depends on τ_n and ϕ_{Tx}.

The time delay τ_n depends on the distances from any bright point n of the target to both the transmitter and the receiver. As seen above, the error on the position of the target can be up to 323 m. Since the wavelength of the VOR signal is of about 3 m, the error on the phase due to the error on the position of the bright points can range from 0 to 2π. Therefore, we cannot use the phase of the scattered signal, and, as a consequence, not the (complex-valued) BS-CRCS.

8.11 Recognition experiments performed

We can perform two main types of recognition experiments, corresponding to narrow and broad classes, respectively. In the first type, we take one type of airplane in each of the three categories, *e.g.* an A343, an A319, and a small airplane (of a specific size). We then build the corresponding recognizer and quantify its performance. In the second type, we lump together several types of airplanes from the same category. This amounts to effectively considering the three categories/classes of large-size airplanes, mid-size airplanes, and small-size airplanes. We then build the corresponding recognizer and quantify its performance. Here, we only describe a recognition experiment of the second type.

We compactly denote the three broad classes of airplanes by CL, CM, and CS, respectively, where C stands for "class" and the second letter for the size of the airplanes. We perform four recognition experiments. Each experiment performed aims at discriminating between the following classes of targets:

- Experiment 1: large-size airplanes and small-size airplanes

- Experiment 2: mid-size airplanes and small-size airplanes

- Experiment 3: large-size airplanes and mid-size airplanes

- Experiment 4: large-size airplanes, mid-size airplanes, and small-size airplanes.

8.11.1   Amount of data

For each experiment, the central part of the (α, β) plane is arbitrarily divided into a covering of 12×6 rectangular tiles, corresponding to tiles that are 30° wide on each side. All tables below reflect this structure, providing tile-by-tile information. The 30° width is chosen based upon the typical variations of these angles for the observed trajectories.

Tables 8.8 and 8.9 provide, for the learning set (LS), the numbers of available trajectories (TR), available BS-RCS values (RCS), and computed feature vectors (FV) for each of the three classes (CL, CM, and CS) for each tile. Table 8.8 is for $\alpha \in [-\pi, 0[$, and Table 8.9 for $\alpha \in [0, \pi[$. For memory, the FVs are the basic ingredients for building the class subspaces that make up the target class model. Tables 8.10 and 8.11 provide the corresponding information for the test set (TS).

		$\alpha \in [-180°, -150°]$			$\alpha \in [-150°, -120°]$			$\alpha \in [-120°, -90°]$			$\alpha \in [-90°, -60°]$			$\alpha \in [-60°, -30°]$			$\alpha \in [-30°, 0°]$		
		CL	CM	CS	CL	CM	CS	CL	CM	CS	CL	CM	CS	CL	CM	CS	CL	CM	CS
$\beta \in [0°, 30°]$	TR	2	3	3	1	3	3	4	4	4	4	4	6	1	1	1	0	0	0
	RCS	50	175	175	308	344	344	577	1185	1185	1273	2468	2514	532	299	299	0	0	0
	FV	0	0	0	0	0	0	0	0	0	8	190	190	37	28	28	0	0	0
$\beta \in [30°, 60°]$	TR	3	25	25	4	19	19	7	15	15	6	15	16	2	13	13	0	0	0
	RCS	176	4261	4261	1469	8895	8895	2442	5757	5757	4365	11073	11089	1653	2523	2523	0	0	0
	FV	0	152	152	27	2127	2127	0	180	180	184	1123	1123	54	66	66	0	183	183
$\beta \in [60°, 90°]$	TR	3	24	24	4	19	19	7	20	20	6	24	25	2	21	22	0	0	0
	RCS	298	6894	6894	2570	6871	6871	4078	10435	10435	7269	17008	17382	3255	4148	4258	0	0	0
	FV	0	881	881	46	682	682	213	892	892	143	1732	1732	27	3	3	0	1	1
$\beta \in [90°, 120°]$	TR	2	9	9	2	7	7	2	7	7	1	7	7	1	7	7	0	0	0
	RCS	260	3700	3700	2776	2988	2988	3518	7939	7939	5428	8387	8387	4484	1652	1652	0	0	0
	FV	0	516	516	12	1	1	124	2659	2659	385	704	704	0	0	0	0	0	0
$\beta \in [120°, 150°]$	TR	1	2	2	1	3	3	1	2	2	0	2	2	0	2	2	0	0	0
	RCS	8	226	226	60	422	422	32	945	945	0	924	924	0	192	192	0	0	0
	FV	0	0	0	0	0	0	0	15	15	0	0	0	0	0	0	0	0	0
$\beta \in [150°, 180°]$	TR	0	0	0	0	0	0	0	0	0	0	0	0	0	0	0	0	0	0
	RCS	0	0	0	0	0	0	0	0	0	0	0	0	0	0	0	0	0	0
	FV	0	0	0	0	0	0	0	0	0	0	0	0	0	0	0	0	0	0

Table 8.8: *High-level description of the **first part** (i.e. for $\alpha \in [-180°, -0°]$) of the **learning set** used in our experiments. The table is divided in tiles in the same way as the (α, β) plane is. Each tile shows the number of trajectories (TR), the number of BS-RCS values (RCS), and the number of feature vectors (FVs), for each of the three classes of large-size airplanes (CL), mid-size airplanes (CM), and small-size airplanes (CS).*

		$\alpha \in [0°, 30°]$			$\alpha \in [30°, 60°]$			$\alpha \in [60°, 90°]$			$\alpha \in [90°, 120°]$			$\alpha \in [120°, 150°]$			$\alpha \in [150°, 180°]$		
		CL	CM	CS	CL	CM	CS	CL	CM	CS	CL	CM	CS	CL	CM	CS	CL	CM	CS
$\beta \in [0°, 30°]$	TR	1	1	1	1	4	4	2	6	17	8	5	18	7	13	13	3	7	7
	RCS	28	98	98	60	2015	2015	3028	3167	6313	1876	119	2560	2431	1818	1818	1864	858	858
	FV	0	0	0	0	189	189	1228	332	332	12	0	0	207	1	1	15	45	45
$\beta \in [30°, 60°]$	TR	2	16	16	1	27	32	3	29	46	8	36	49	8	89	89	3	87	87
	RCS	987	4246	4246	636	23114	24267	1806	18368	23049	4069	4231	9893	5721	31042	31042	6483	42097	42097
	FV	70	320	320	0	3706	3706	0	2017	2017	559	431	431	32	371	371	2098	8359	8359
$\beta \in [60°, 90°]$	TR	2	15	15	1	17	17	3	21	22	6	38	39	6	86	86	3	83	83
	RCS	867	7441	7441	492	22731	22731	1512	17899	17995	3859	4056	4136	7369	39773	39773	10757	55172	55172
	FV	0	28	28	33	4868	4868	559	4272	4272	254	1	1	564	6896	6896	526	3539	3539
$\beta \in [90°, 120°]$	TR	1	4	4	0	4	4	1	6	6	1	12	12	1	29	29	1	28	28
	RCS	236	625	625	0	2931	2931	236	1664	1664	590	748	748	6018	49419	49419	6490	81878	81878
	FV	0	0	0	0	1184	1184	0	0	0	0	0	0	1065	12088	12088	198	10679	10679
$\beta \in [120°, 150°]$	TR	0	0	0	0	0	0	0	1	1	0	3	3	0	4	4	0	4	4
	RCS	0	0	0	0	0	0	0	24	24	0	375	375	0	6474	6474	0	5383	5383
	FV	00	0	0	0	0	0	0	0	0	0	0	0	0	2141	2141	0	155	155
$\beta \in [150°, 180°]$	TR	0	0	0	0	0	0	0	0	0	0	0	0	0	0	0	0	0	0
	RCS	0	0	0	0	0	0	0	0	0	0	0	0	0	0	0	0	0	0
	FV	0	0	0	0	0	0	0	0	0	0	0	0	0	2158	2158	0	0	0

Table 8.9: *High-level description of the **second part** (i.e. for $\alpha \in [0°, 180°]$) of the **learning set** used in our experiments. See Table 8.8 for additional comments.*

		α ∈ [−180°, −150°]			α ∈ [−150°, −120°]			α ∈ [−120°, −90°]			α ∈ [−90°, −60°]			α ∈ [−60°, −30°]			α ∈ [−30°, 0°]		
		CL	CM	CS	CL	CM	CS	CL	CM	CS	CL	CM	CS	CL	CM	CS	CL	CM	CS
$\beta \in [0°, 30°]$	TR	0	5	5	0	4	5	0	4	4	0	3	3	0	2	2	0	0	0
	RCS	0	146	146	0	127	130	0	471	471	0	1460	1460	0	186	186	0	0	0
	FV	0	0	0	0	0	0	0	0	0	8	190	190	37	28	28	0	0	0
$\beta \in [30°, 60°]$	TR	0	38	39	4	36	37	4	35	35	5	31	31	2	27	27	0	0	0
	RCS	0	3721	3769	1452	4233	4247	2017	13181	13181	1487	13713	13713	92	5123	5123	0	0	0
	FV	0	152	152	46	2127	2127	0	180	180	184	1123	1123	54	66	66	0	183	183
$\beta \in [60°, 90°]$	TR	0	37	37	5	33	33	6	42	42	6	42	42	2	38	38	0	0	0
	RCS	0	8633	8633	3631	4754	4754	5219	21119	21119	2796	23332	23332	150	7254	7254	0	0	0
	FV	0	881	881	46	682	682	242	892	892	171	1732	1732	27	3	3	0	1	1
$\beta \in [90°, 120°]$	TR	0	14	14	3	17	17	3	19	19	2	18	18	1	16	16	0	0	0
	RCS	0	7474	7474	3000	4693	4693	4184	31422	31422	1637	28020	28020	41	9757	9757	0	0	0
	FV	0	516	516	12	1	1	124	2659	2659	385	704	704	0	0	0	0	0	0
$\beta \in [120°, 150°]$	TR	0	2	2	3	12	12	3	13	13	2	12	12	1	12	12	0	0	0
	RCS	0	151	151	3855	1995	1995	5082	12456	12456	2030	10500	10500	48	3699	3699	0	0	0
	FV	0	0	0	0	0	0	0	15	15	0	0	0	0	0	0	0	0	0
$\beta \in [150°, 180°]$	TR	0	0	0	0	0	0	0	0	0	0	0	0	0	0	0	0	0	0
	RCS	0	0	0	0	0	0	0	0	0	0	0	0	0	0	0	0	0	0
	FV	0	0	0	0	0	0	0	0	0	0	0	0	0	0	0	0	0	0

Table 8.10: *High-level description of the **first part** (i.e. for $\alpha \in [−180°, 0°]$) of the **test set** used in our experiments. See Table 8.8 for additional comments.*

		$\alpha \in [0°,30°]$			$\alpha \in [30°,60°]$			$\alpha \in [60°,90°]$			$\alpha \in [90°,120°]$			$\alpha \in [120°,150°]$			$\alpha \in [150°,180°]$		
		CL	CM	CS	CL	CM	CS	CL	CM	CS	CL	CM	CS	CL	CM	CS	CL	CM	CS
$\beta \in [0°,30°]$	TR	3	2	2	5	12	12	5	13	39	13	6	32	10	38	39	3	17	17
	RCS	318	100	100	4122	1928	1928	8772	3819	11393	8186	62	4926	2645	4326	4371	45	1019	1019
	FV	0	0	0	0	189	189	1228	564	564	12	0	0	207	1	1	15	45	45
$\beta \in [30°,60°]$	TR	3	30	30	5	55	60	7	62	89	16	69	89	15	191	195	6	178	179
	RCS	2243	6005	6005	4888	49296	50589	7651	40712	47973	6691	10189	20595	6578	58002	58305	1787	71019	71103
	FV	70	320	320	0	3588	3588	0	2017	2017	559	431	431	32	371	371	2199	8636	8636
$\beta \in [60°,90°]$	TR	3	28	28	4	34	34	4	45	48	6	67	70	7	162	162	4	169	169
	RCS	2107	16020	16020	2877	44889	44889	5364	39856	39898	3046	9826	9956	1881	77973	77973	2179	105930	105930
	FV	0	28	28	33	4868	4868	559	4272	4272	254	1	1	565	7100	7100	526	3539	3539
$\beta \in [90°,120°]$	TR	0	2	2	0	4	4	0	8	8	0	17	17	1	63	63	1	68	68
	RCS	0	408	408	0	1245	1245	0	1245	1245	0	5319	5319	1794	107743	107743	5175	185494	185494
	FV	0	0	0	0	1184	1184	0	0	0	0	0	0	1065	12088	12088	198	10679	10679
$\beta \in [120°,150°]$	TR	0	0	0	0	2	2	0	2	2	0	4	4	0	9	9	0	9	9
	RCS	0	0	0	0	50	50	0	440	440	0	6606	6606	0	17224	17224	0	13959	13959
	FV	0	0	0	0	0	0	0	0	0	0	0	0	0	2141	2141	0	155	155
$\beta \in [150°,180°]$	TR	0	0	0	0	0	0	0	0	0	0	0	0	0	0	0	0	0	0
	RCS	0	0	0	0	0	0	0	0	0	0	0	0	0	0	0	0	0	0
	FV	0	0	0	0	0	0	0	0	0	0	0	0	0	2158	2158	0	0	0

Table 8.11: *High-level description of the **second part** (i.e. for $\alpha \in [0°, 180°]$) of the **test set** used in our experiments. See Table 8.8 for additional comments.*

8.11.2 Statistics of the feature vectors and brief analysis thereof

For each tile, we can compute the mean and standard deviation of each of the N components of all FVs built for this tile, for one class, and for one set (either the LS or the TS). Figure 8.22 shows, for one tile, for each of the three classes, and for the TS, the N values of the mean of the components of the corresponding FVs. Similarly, the figure shows the standard deviation of these components.

One can view the graph as showing representations of the mean vector and standard deviation vector. Note that this last vector corresponds to the values along the diagonal of the covariance matrix of the FVs of interest.
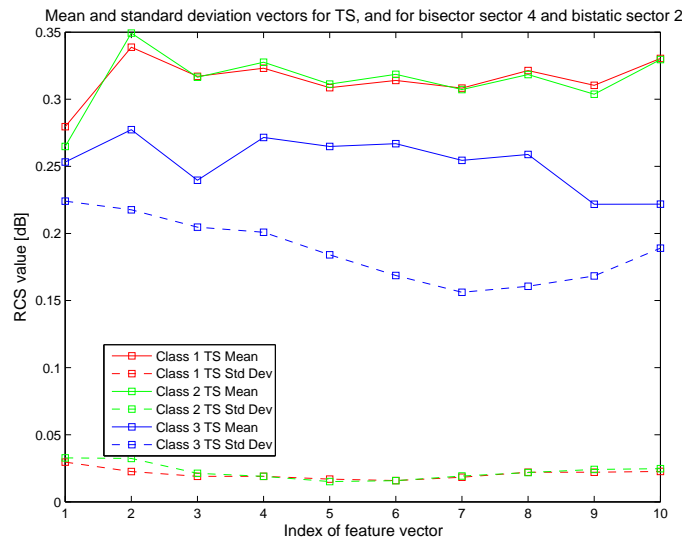
Figure 8.22: *The figure shows the representation of the mean vector and the standard deviation vector (diagonal of covariance matrix) of all FVs corresponding to the tile defined by $\alpha \in [90°; 120°]$ and $\beta \in [30°; 60°]$ and to the TS.*

In Fig. 8.22, the mean vectors and the standard deviation vectors are about the same for classes 1 and 2. Therefore, the probability of correct recognition is expected to be low for the tile considered in the figure, as seen in Table 8.12.

In Fig. 8.23, the mean vectors and the standard deviation vectors are different for all three classes. Therefore, the probability of correct recognition is expected to be high for the tile considered in the figure, as seen in Table 8.12.

8.11.3 Recognition results for the three-class experiment

We present in details the probabilities of correct recognition for the recognition experiments involving the three classes of targets. Tables 8.12, 8.13, 8.14, and 8.15 give the probabilities of correct recognition for each of the four metrics defined in Section 7.5. We give in Appendix A the confusion matrices obtained for each metric and for each tile.
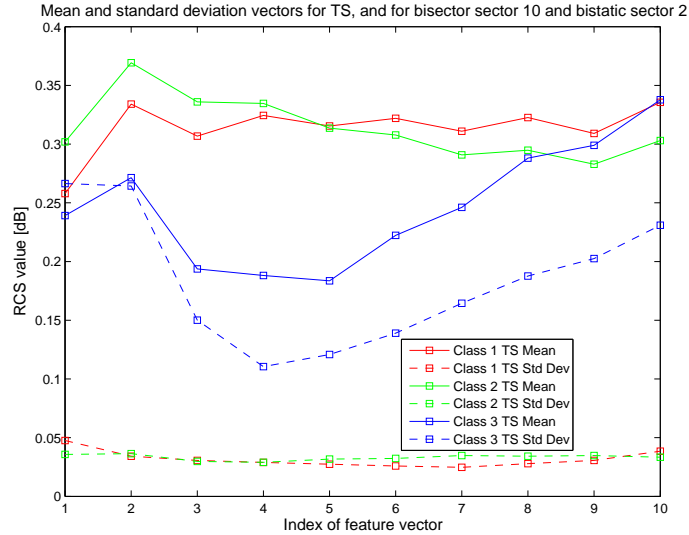
Figure 8.23: *The figure shows the representation of the mean vector and the standard deviation vector (diagonal of covariance matrix) of all FVs corresponding to the tile defined by $\alpha \in [-120°; -90°]$ and $\beta \in [30°; 60°]$ and to the TS.*

For all metrics, the probability of correct recognition varies from tile to tile. For metric E_0, it ranges from 0.39 to 1. The overall probability of correct recognition, *i.e.* the probability of correct recognition achieved over all tiles, is of about 0.66, which is quite low. For metric E_1, the probability of correct recognition varies from 0.35 to 0.99. The overall classification rate is of about 0.79, which is better than the overall classification rate achieved for the metric E_0. For metric $E_{0.05}$, the probability of correct recognition varies from 0.49 to 1. The overall probability of correct recognition is of about 0.83, which is better than the overall probability of correct recognition achieved for metrics E_0 and E_1. For the aggregation of the three metrics, the probability of correct recognition varies from 0.49 to 0.99. The overall probability of correct recognition is of about 0.82. Therefore, it seems that metric $E_{0.05}$ is to be preferred over the other metrics.

For all metrics, there are tiles for which the recognition is almost perfect. A high probability of correct recognition is reached for $\alpha \leq 0°$, for a constant β. No conclusion can be drawn concerning suitable values of β, since the values of the BS-RCS are available for values of β ranging from 30° to 120°. According to the high variation of probability of correct recognition from one tile to the other, a high probability of correct recognition can be achieved by suitably locating the receiver(s) of the passive bistatic radar.

	$\alpha \in [-180°, -150°]$	$\alpha \in [-150°, -120°]$	$\alpha \in [-120°, -90°]$	$\alpha \in [-90°, -60°]$	$\alpha \in [-60°, -30°]$	$\alpha \in [-30°, 0°]$	$\alpha \in [0°, 30°]$	$\alpha \in [30°, 60°]$	$\alpha \in [60°, 90°]$	$\alpha \in [90°, 120°]$	$\alpha \in [120°, 150°]$	$\alpha \in [150°, 180°]$
$\beta \in [0°, 30°]$	-	-	-	0.55	-	-	-	0.65	0.47	-	-	-
$\beta \in [30°, 60°]$	1.0	0.76	0.99	0.52	0.92	0.88	0.66	0.58	0.61	0.66	0.63	0.51
$\beta \in [60°, 90°]$	0.5	0.77	0.61	0.54	-	-	-	0.62	0.52	-	0.56	0.39
$\beta \in [90°, 120°]$	0.82	-	0.77	0.54	-	-	-	0.9	-	-	0.4	0.5
$\beta \in [120°, 150°]$	-	-	-	-	-	-	-	-	-	-	0.62	0.9
$\beta \in [150°, 180°]$	-	-	-	-	-	-	-	-	-	-	0.75	-

Table 8.12: *Weighted probabilities of correct recognition **for metric** $\mathbf{E_0}$, shown tile-by-tile, in a way similar to that of Table 8.8.*

	$\alpha \in [-180°, -150°]$	$\alpha \in [-150°, -120°]$	$\alpha \in [-120°, -90°]$	$\alpha \in [-90°, -60°]$	$\alpha \in [-60°, -30°]$	$\alpha \in [-30°, 0°]$	$\alpha \in [0°, 30°]$	$\alpha \in [30°, 60°]$	$\alpha \in [60°, 90°]$	$\alpha \in [90°, 120°]$	$\alpha \in [120°, 150°]$	$\alpha \in [150°, 180°]$
$\beta \in [0°, 30°]$	-	-	-	0.92	-	-	-	0.7	0.72	-	-	-
$\beta \in [30°, 60°]$	0.93	0.85	0.88	0.86	0.88	0.93	0.74	0.77	0.89	0.84	0.82	0.77
$\beta \in [60°, 90°]$	0.93	0.78	0.77	0.72	-	-	-	0.71	0.69	-	0.77	0.5
$\beta \in [90°, 120°]$	0.89	-	0.87	0.71	-	-	-	0.89	-	-	0.72	0.35
$\beta \in [120°, 150°]$	-	-	-	-	-	-	-	-	-	-	0.77	0.99
$\beta \in [150°, 180°]$	-	-	-	-	-	-	-	-	-	-	0.8	-

Table 8.13: *Weighted probabilities of correct recognition **for metric** $\mathbf{E_1}$, shown tile-by-tile, in a way similar to that of Table 8.8.*

	$\alpha \in [-180°, -150°]$	$\alpha \in [-150°, -120°]$	$\alpha \in [-120°, -90°]$	$\alpha \in [-90°, -60°]$	$\alpha \in [-60°, -30°]$	$\alpha \in [-30°, 0°]$	$\alpha \in [0°, 30°]$	$\alpha \in [30°, 60°]$	$\alpha \in [60°, 90°]$	$\alpha \in [90°, 120°]$	$\alpha \in [120°, 150°]$	$\alpha \in [150°, 180°]$
$\beta \in [0°, 30°]$	-	-	-	1.0	-	-	-	0.6	0.76	-	-	-
$\beta \in [30°, 60°]$	0.98	0.98	1.0	0.84	0.99	0.99	0.92	0.68	0.82	0.76	0.99	0.78
$\beta \in [60°, 90°]$	0.87	0.94	0.69	0.79	-	-	-	0.86	0.78	-	0.85	0.49
$\beta \in [90°, 120°]$	0.94	-	0.91	0.72	-	-	-	0.98	-	-	0.73	0.5
$\beta \in [120°, 150°]$	-	-	-	-	-	-	-	-	-	-	0.77	1.0
$\beta \in [150°, 180°]$	-	-	-	-	-	-	-	-	-	-	0.86	-

Table 8.14: *Weighted probabilities of correct recognition **for metric** $\mathbf{E_{0.05}}$, shown tile-by-tile, in a way similar to that of Table 8.8.*

	$\alpha \in$ $[-180°, -150°]$	$\alpha \in$ $[-150°, -120°]$	$\alpha \in$ $[-120°, -90°]$	$\alpha \in$ $[-90°, -60°]$	$\alpha \in$ $[-60°, -30°]$	$\alpha \in$ $[-30°, 0°]$	$\alpha \in [0°, 30°]$	$\alpha \in [30°, 60°]$	$\alpha \in [60°, 90°]$	$\alpha \in$ $[90°, 120°]$	$\alpha \in$ $[120°, 150°]$	$\alpha \in$ $[150°, 180°]$
$\beta \in [0°, 30°]$	-	-	-	0.99	-	-	-	0.7	0.76	-	-	-
$\beta \in [30°, 60°]$	0.98	0.91	0.96	0.88	0.99	0.96	0.88	0.78	0.91	0.85	0.93	0.79
$\beta \in [60°, 90°]$	0.93	0.87	0.79	0.74	-	-	-	0.81	0.74	-	0.8	0.5
$\beta \in [90°, 120°]$	0.91	-	0.88	0.72	-	-	-	0.93	-	-	0.73	0.49
$\beta \in [120°, 150°]$	-	-	-	-	-	-	-	-	-	-	0.77	0.99
$\beta \in [150°, 180°]$	-	-	-	-	-	-	-	-	-	-	0.83	-

Table 8.15: *Weighted probabilities of correct recognition **for the aggregation of the three metrics**, shown tile-by-tile, in a way similar to that of Table 8.8.*

8.11.4   Recognition results for all four recognition experiments

In order to give a general overview of the performance of the recognition system, we show in Table 8.16 the overall probability of correct recognition for each metric and for each of the four experiments. As can be expected from the recognition experiment involving the three classes of targets described above, the best probability of correct recognition is always obtained by the $E_{0.05}$ metric, for each experiment. For the three-class experiment, the overall correct recognition rate is of 0.82. The recognition rate is a few percent higher for the three other experiments.

Metric used	Recognition experiment			
	CL vs. CS	CM vs. CS	CL vs. CM	CL vs. CM vs. CS
E_0	0.78	0.74	0.76	0.66
E_1	0.77	0.87	0.76	0.79
$E_{0.05}$	0.87	0.88	0.83	0.84
Aggregation	0.86	0.88	0.83	0.82

Table 8.16: *Overall probability of correct recognition for each of the four metrics and for each of the four recognition experiments performed.*

The probabilities of correct recognition are of the same order as the probabilities of correct recognition achieved for the recognition of the airplanes from their bistatic complex radar cross-sections, when considering a single (Tx,Rx) pair in an anechoic chamber. But, the comparison with the results achieved on data acquired in the anechoic chamber is not pursued further as the airplanes, the frequencies, and the covering of the (α, β) plane are different. We simply draw the conclusion that the recognizer proposed in Chapter 7 has been successfully tested on data acquired both in an anechoic chamber and in real outdoor conditions.

8.12   Conclusion

In this chapter, we performed the recognition of air targets by using their bistatic radar cross-sections (BS-RCSs) that we extracted from real-life signals. We presented the operational passive radar testdbed that we used for the acquisition of these real-life signals. We deployed the testbed in the vicinity of Orly Airport, using a VOR as transmitter of opportunity and a software-defined radio (SDR) as receiver. We collected signals from a total of 1329 trajectories for 32 types of airplanes.

We performed the detection of airplanes by using the ADS-B signals they transmit following interrogation. We computed the Doppler shift, the aspect angle α, the bistatic angle β, and the scene geometry from the position information present in the transmitted ADS-B signals. We discriminated between an airplane of interest and other targets by using a Doppler filter.

We then discussed the grouping of the different detected airplanes into classes. We defined three classes that are the large-size airplanes, the mid-size airplanes, and the

small-size airplanes. For both the large-size and the mid-size airplanes, we presented the computation of their BS-RCS. Since small-size airplanes could not be detected by our testbed, we presented the generation of their BS-RCS from a simple model.

We also presented the data we collected, and we showed examples of received signals, including spectrograms, signal-to-noise ratios, and distributions of the BS-RCS of each class of airplanes in the (α, β) plane.

We discussed the error on the position of an airplane, and showed that it has a limited influence on the value of the BS-RCS. We also expressed the reasons for using the BS-RCS of the airplanes instead of their bistatic complex radar cross-section (BS-CRCS).

We used the recognizer described in Chapter 7. A significant feature of this recognizer is that it breaks the overall recognition problem down into a set of recognition sub-problems by decomposing the central part of the (α, β) parameter plane into regions. We partitioned the central part of the parameter plane into a covering of 12×6 rectangular regions. For each region, we built one recognizer, and thus one target class model that consists in a list of subspaces that are computed from the feature vectors (FVs) of the airplanes. Each FV is a vector of values of BS-RCS.

We performed four recognition experiments involving the three classes of airplanes. Recognition experiment consisting in classifying air vehicles of two broad classes (large-size airplanes such as A343's, and/or mid-size airplanes such as A319's, and/or small-size airplanes such as private airplanes and UAVs), led to an overall probability of correct recognition varying between 0.82 and 0.88. The recognition experiment consisting in classifying air vehicles of the three broad classes, led to an overall probability of correct recognition of about 0.82. However, the probability of correct recognition varies strongly according to the tile, *i.e.* according to the region of the parameter space, in which the recognition experiment is performed, ranging from 0.49 to 0.99. Therefore, in an operational system, one should choose the location of the receiver(s) appropriately to achieve a high probability of correct recognition.

This overall probability of correct recognition of 0.82 achieved when recognizing the three broad classes of targets is lower than the probability of correct recognition achieved when recognizing targets based on their radar images (Chapter 6), since feature vectors contain less information than images. The overall probability of correct recognition is however of the same order as the overall probability of correct recognition achieved when recognizing targets based on their BS-CRCS, for a single (Tx,Rx) pair (Chapter 7). This demonstrates the potential of the recognition strategy defined in Chapters 7 and 8.

Chapter 9

Conclusions and perspectives

Contents

9.1 Conclusions

9.1.1 Summary of the thesis

In this thesis, we discuss the recognition of non-cooperative air targets based on passive bistatic radar signals, *i.e.* on signals transmitted by one or more illuminators of opportunity (operating at low frequency) and scattered by an air target. The use of passive bistatic radar signals for recognition purposes is a key feature of this thesis. We indeed explained that passive bistatic radars are usually used for detection and location purposes. Since illuminators of opportunity are already present, the cost of the passive radar system is put on the receiver(s).

We focus on the recognition process. We thus assume that the targets of interest are detected and tracked, and that we know their position. We also know the locations, the operating frequency, and the polarization of the transmitter(s) (Tx) and the receiver(s) (Rx). We thus know the parameters of the scene.

We implement three automatic target recognition (ATR) systems. For the first ATR system, we perform the recognition of air targets by using their radar images, since many ATR systems reported in the literature use radar images for the recognition of targets. (We explained some reasons for not recognizing targets by using their high-resolution range profiles in the case of passive bistatic radar.) A radar image

of a target is defined as the spatial representation of the bistatic complex radar cross-section (BS-CRCS) of this target. We construct the radar images of the targets by applying a two-dimensional (2D) inverse Fourier Transform to a 2D array of values of BS-CRCS of these targets.

However, we explain that the 2D diversity needed to compute 2D arrays of values of BS-CRCS would hardly be met in an operational system. For the second ATR system, we thus perform the recognition of the air targets by directly using either the BS-CRCS or the bistatic radar cross-section (BS-RCS) of these targets.

Since the second ATR system is successfully tested on BS-CRCS values and BS-RCS values computed from signals that are acquired in an anechoic chamber, we test this ATR system on BS-RCS values that we compute from real-life signals acquired using a passive radar testbed that we deploy around Orly airport, France. We use the ADS-B signals transmitted by commercial airplanes to detect and locate these airplanes. We use a VOR Tx as illuminator of opportunity, and a software-defined radio (SDR) as Rx.

Each of the three ATR systems relies on either the BS-CRCS or the BS-RCS of the targets of interest. We thus present the parameters the BS-CRCS and the BS-RCS are functions of, which are the nature of the target, the polarization of both the Tx and the Rx, the frequency of the transmitted signal, the aspect angle of the target, and the bistatic angle between the Tx and the Rx. In particular, the variations of both the BS-CRCS and the BS-RCS as a function of frequency allows one to define three scattering regions. For each scattering region, the scattering mechanisms are function of either the shape of the target, its volume, or a combination of both.

The frequency f, the polarization couple Pol, the aspect angle α, and the bistatic angle β make up the parameter space in terms of which we express both the BS-CRCS and the BS-RCS. We use this parameter space for the design of the recognition stage of each of the three ATR systems. For each recognizer, we cover the parameter space with tiles (overlapping or not). For each tile, we build one recognizer. The covering of the parameter space into tiles is a key feature of the recognizer of each of the three ATR systems, and thus of this thesis.

We build each recognizer in the following way. From the input data, we produce feature vectors (FVs). From the FVs, we construct a target class model. The class of an unknown target is determined by passing its FV through the recognizer.

For the first ATR system, an FV consists in pixel values of an ensemble of windows extracted out of each image. The target class model consists in an ensemble of extremely randomized trees (extra-trees). The class of an unknown target is determined by propagating each window extracted from the image of this target through each of the extra-trees. The use of tree-based methods and, thus, of extra-trees, for recognition purposes in the radar domain is, to our knowledge, novel. Prior to our application to radar images, this classification/recognition method has been used by others on non-radar images.

For the second and third ATR systems, an FV consists in a vector of values of

either BS-CRCS or BS-RCS. The target class model consists in an ensemble of subspaces, each subspace characterizing a target class. The class of an unknown target is determined by projecting the FV of this target onto each of the subspaces of the target class model. We use four projection metrics to assign a class to the FV. The use of subspace methods for recognition purposes in the radar domain is, to our knowledge, novel.

9.1.2 Comparison of the performances of the three ATR systems

We express the performances of the different ATR systems in terms of their probability of correct recognition, and in terms of the number of Tx's and Rx's used. In this section, we compare the performances of each of the three ATR systems.

We first test the first ATR system on different configurations of the well-known MSTAR data, consisting of SAR images of ground-vehicle targets, non-targets, and SLICY targets. The highest achieved probabilities of correct recognition vary between 0.96 and 0.99, depending on the configuration of the MSTAR data (targets of interest only, targets of interest and non-targets, targets of interest and SLICY targets, or targets of interest and SLICY and non-targets). The recognizer also proves to be quasi insensitive to the rotation of targets.

We then test the first ATR system is on the images constructed from the ONERA data. The images are constructed for four frequency bands, for a single polarization, for three aspect angles, and for a range of bistatic angles. We separated the range of bistatic angles into overlapping bistatic angular sectors. The probabilities of correct recognition are very low for the lowest frequency band, and are almost perfect for the three highest frequency bands, this for any bistatic angular sector. The low probabilities of correct recognition achieved at the lowest frequency band is explained by the fact that, at theses frequencies, the BS-RCS of targets, and thus the images, are more influenced by the volume of the targets than by their shape, the four targets having the same characteristic dimension, but different shapes. The high probabilities of correct recognition achieved at the higher frequencies are explained by the fact that, at these frequencies, the BS-RCS of targets, and thus the images, are more influenced by the shapes of the targets than by their volume. Even though the probabilities of correct recognition are very high, we need a high number of Tx's and Rx's in order to be able to construct the radar images of the targets.

We test the second ATR system on the ONERA data. We first recognize targets by using their BS-CRCSs extracted for a single (Tx,Rx) pair. For the same reason as for the images, the probabilities of correct recognition achieved for the lowest frequency band are low, this for any polarization, any aspect angle, and any bistatic angular sector. Exactly for the same reason as for the images, the probabilities of correct recognition increase with frequency. The probabilities of correct recognition also vary according to the tile of the parameter space, *i.e.* according to the polarization, the aspect angle, and the bistatic angular sector. The best probabilities of correct recognition vary from 0.33 for the lowest frequency band, up to 0.93 for the highest frequency band.

We then recognize targets by using their BS-RCSs, for a single (Tx,Rx) pair. The best probabilities of correct recognition vary from 0.29 for the lowest frequency band, up to 0.74 for the highest frequency band. The conclusions are exactly the same as for the BS-RCSs. However, one must notice that the probabilities of correct recognition achieved for the BS-CRCSs are higher than for the BS-RCSs. Therefore, the phase of the BS-CRCS is important, since the targets of interest have the same volume, but different shapes.

The probabilities of correct recognition achieved for the recognition of targets by using either their BS-CRCSs or their BS-RCSs extracted for a single (Tx,Rx) pair, are much lower than the probabilities of correct recognition achieved for the recognition of targets by using their radar images. We thus perform the recognition of targets by using either their BS-CRCSs or their BS-RCSs extracted for three (Tx,Rx) pairs. The probabilities of correct recognition increase by about 10%. Therefore, increasing the number of (Tx,Rx) pairs allows one to increase the probability of correct recognition.

We then test the third ATR system on real-life BS-RCSs of commercial airplanes, extracted for a single (Tx,Rx) pair. We achieve an overall probability of correct recognition of about 0.82, with significant differences among the tiles of the (α, β) plane. We thus experimentally proved that the recognition of targets by using either their BS-CRCSs or their BS-RCSs extracted from signals acquired at low frequency, in a bistatic configuration, using a limited number of (Tx,Rx) pairs gives high probabilities of correct recognition.

According to the work presented in this thesis, an ATR system recognizing airplanes by using either their BS-CRCS or their BS-RCS, is viable, and the achieved probabilities of correct recognition are promising. The achieved probabilities of correct recognition for RCS tend to be similar to the probabilities of correct recognition achieved for radar images, depending on the nature of the targets of interest, their aspect angle, the bistatic angle of the configuration, the polarization of both the transmitter and the receiver, the frequency of the transmitted signals, and the number of (Tx,Rx) pairs used.

9.2   Perspectives

In order to completely develop and assess the performances of an ATR system using either the BS-RCS or the BS-RCS of targets, we need to perform further work. We suggest perspectives for this. These perspectives fall into four categories, discussed below:

- Addition of different types of targets

- Study of bistatic radar phenomenology

- Use of different illuminators of opportunity

- Refinement of the recognizer.

9.2.1 Addition of different types of targets

In this work, we considered a small number of different types of airplanes. Indeed, we tested the ATR systems on two different sets of data. The airplanes of the first dataset were of the same size and different shapes, and the airplanes of the second dataset were of about the same shape and different sizes. In order to validate the principle of recognizing air targets by using either their BS-CRCS or their BS-RCS, we should consider on a wider variety of airplanes, *e.g.* airplanes having both different sizes and different shapes.

In Chapter 8, a detection stage was added to the ATR system in order to be able to detect and locate airplanes. The detection and location of airplanes, based on ADS-B signals, limited us to consider cooperative targets. In future work, other detection and location means should be envisioned, so that we can consider other targets, such as small-size airplanes (whose BS-RCS was simulated since our testbed could not detect them).

We could also potentially apply our ATR system to other types of targets, such as ground vehicles, sea vehicles, or a mix of air, ground, and sea vehicles.

9.2.2 Study of bistatic radar phenomenology

In Chapter 3, we showed that both the BS-CRCS and the BS-RCS of targets vary according to the shape and size of the target, the frequency of the incident wave, the polarization of both the incident and scattered signals, the aspect angle of the target, and the bistatic angle between the transmitter and the receiver. In particular, we saw that the scattering mechanisms differ, for a given target, according to the frequency band. We also experimentally showed in Chapter 6 that both the BS-CRCS and the BS-RCS of targets vary according to frequency, aspect angle, and bistatic angle.

However, a complete theoretical study of the variations of both the BS-CRCS and the BS-RCS of different targets according to polarization, aspect angle, and bistatic angle would allow one to understand the achieved probabilities of correct recognition in terms of these physical parameters. Indeed, we can simply conclude that transmitting and receiving signals at some polarization (here HH) gives higher probabilities of correct recognition than at other polarizations, but we did not investigate the physical meaning of this observation.

Moreover, a complete phenomenological study of both the BS-CRCS and the BS-RCS would allow one to define the target classes *a priori* and objectively. In this work, targets were separated into different classes according to either their shape (Chapters 6 and 7) or their size (Chapter 8). Other ways of defining target classes can be envisioned according, for example, to the effect of the polarization on the BS-CRCS and the BS-RCS of targets.

9.2.3 Use of different illuminators of opportunity

As we experimentally showed in Chapter 7, the probability of correct recognition increases when using multiple (Tx,Rx) pairs. For computational reasons, we simulated

the use of three (Tx,Rx) pairs, with a single Tx and three Rx's. In future work, one should envision the use of more than three (Tx,Rx) pairs. Intuitively, the use of as many (Tx,Rx) pairs as for the construction of the radar images should give similar probabilities of correct recognition for both the images and the BS-CRCS (or the BS-RCS).

However, according to the work performed in Chapter 7, high probabilities of correct recognition could be achieved even by using fewer (Tx,Rx) pairs than for the construction of radar images. Moreover, the use of more than a single Tx would allow one to perform recognition experiments over different frequency bands and different polarizations. The recognizer would assign a class to a given unknown target for each frequency band or each polarization. The final class would be given by performing a majority vote on all classes, thus resulting in a higher confidence in the recognition results.

The consideration of multiple (Tx,Rx) pairs would also allow one to obtain values of either the BS-CRCS or the BS-RCS, or both, of different targets at different frequencies, different polarizations, different aspect angles, and different bistatic angles, which could be used for other purposes than recognition, such as validating the theoretical study of bistatic phenomenology suggested above.

The VOR transmitter is the only illuminator of opportunity that we used in this thesis, for simplicity reasons (Chapter 8). In future work, one should envision the use of other illuminators of opportunity. The different illuminators of opportunity could be used, simultaneously for detection, location, and recognition purposes, at low frequency, in a passive multistatic configuration.

In Chapter 8, we tested the ATR system on outdoor, real-life BS-RCSs. In future work, one could process the phase of the scattered signal in order to use the BS-CRCS instead of the BS-RCS, since we achieved higher probabilities of correct recognition for the BS-CRCS than for the BS-RCS.

9.2.4   Refinement of the recognizer

In this thesis, we considered the recognition problem as a classification problem (in the sense of machine learning), and thus as a supervised learning problem. We performed the recognition of targets by using either extremely randomized trees or subspace methods. Even though we justified the use of these two recognition techniques in Chapters 6 and 7, one should envision investigating other classification/recognition techniques.

In this thesis, we forced the recognizer to assign a class to each unknown target, among the N_c pre-defined classes. In future work, one could envision adding the class "none" (which would stand for "none of the above"), thereby allowing the recognizer to assign to a target this additional class. This would require assigning a target class with some degree of confidence, and to define margins between the degrees of confidence.

The partitioning of the parameter space in any number of regions offers the

possibility of running several recognizers in parallel, *e.g.* on a graphics processing unit (GPU), thereby enabling real-time operation.

In the different recognition experiments we performed, we defined the target classes according to the sizes and shapes of the different targets. The use of unsupervised learning techniques, such as a clustering, would allow one to experimentally define the separation of targets into classes. Moreover, the clustering of different types of targets should allow one to experimentally assess the phenomenological study suggested above.

If more types of targets had been available, we could have considered classes and meta-classes of targets, where meta-classes would be defined as groups of classes. We could have applied the Dempster-Schafer Theory of Evidence to compute the probabilities of correct recognition of these meta-classes.

Appendices

Appendix A

Confusion matrices for the recognition of targets by using their experimentally-acquired, real-life bistatic RCS

In Chapter 8, we perform the recognition of targets by using the bistatic radar cross-section (BS-RCS) of airplanes. The recognition experiments involve three classes of targets, which are the large-size airplanes (CL), the mid-size airplanes (CM), and the small-size airplanes (CS). We use the recognizer we defined in Chapter 7. For each recognition experiment, *i.e.* for each tile of the parameter space, the class of an unknown target is determined by four different metrics, which are E_0, E_1, $E_{0.05}$, and the aggregation of the three metrics. In this appendix, we give the confusion matrix that we obtained for each metric and for each tile of the parameter space. In each confusion matrix, the rows correspond to the true classes, and the columns to the computed classes.

Tables A.1 and A.2 show the confusion matrices achieved for each tile by using metric E_0. Tables A.3 and A.4 show the confusion matrices achieved for each tile by using metric E_1. Tables A.5 and A.6 show the confusion matrices achieved for each tile by using metric $E_{0.05}$. Tables A.7 and A.8 show the confusion matrices achieved for each tile for the aggregation of the three metrics.

		$\alpha \in [-180°, -150°]$			$\alpha \in [-150°, -120°]$			$\alpha \in [-120°, -90°]$			$\alpha \in [-90°, -60°]$			$\alpha \in [-60°, -30°]$			$\alpha \in [-30°, 0°]$		
		CM_c	CL_c	CS_c	CM_c	CL_c	CS_c	CM_c	CL_c	CS_c	CM_c	CL_c	CS_c	CM_c	CL_c	CS_c	CM_c	CL_c	CS_c
$\beta \in [0°, 30°]$	CM_t	-	-	-	-	-	-	-	-	-	0.11	-	-	-	-	-	-	-	-
	CL_t	-	-	-	-	-	-	-	-	-	-	-	-	-	-	-	-	-	-
	CS_t	-	-	-	-	-	-	-	-	-	0.89	-	1.0	-	-	-	-	-	-
$\beta \in [30°, 60°]$	CM_t	1.0	-	-	0.54	-	0.014	1.0	-	0.011	0.25	0.13	0.12	0.97	0.24	-	0.77	-	0
	CL_t	-	-	-	0.008	-	0.0028	-	-	-	0.17	0.42	0.064	-	0.76	-	-	-	-
	CS_t	-	-	1.0	0.45	-	0.98	-	-	0.99	0.58	0.45	0.81	0.03	-	1.0	0.23	-	1.0
$\beta \in [60°, 90°]$	CM_t	-	-	-	0.55	-	0.021	0.48	0.26	0.1	0.29	0.16	0.11	-	-	-	-	-	-
	CL_t	-	-	-	-	-	-	0.053	0.07	0.019	0.14	0.33	0.098	-	-	-	-	-	-
	CS_t	1.0	-	1.0	0.45	-	0.98	0.47	0.67	0.88	0.57	0.5	0.8	-	-	-	-	-	-
$\beta \in [90°, 120°]$	CM_t	0.7	-	0.066	-	-	-	0.68	0.19	0.11	0.33	0.19	0.11	-	-	-	-	-	-
	CL_t	-	-	-	-	-	-	0.12	0.71	0.024	0.29	0.5	0.12	-	-	-	-	-	-
	CS_t	0.3	-	0.93	-	-	-	0.2	0.1	0.87	0.38	0.31	0.77	-	-	-	-	-	-
$\beta \in [120°, 150°]$	CM_t	-	-	-	-	-	-	-	-	-	-	-	-	-	-	-	-	-	-
	CL_t	-	-	-	-	-	-	-	-	-	-	-	-	-	-	-	-	-	-
	CS_t	-	-	-	-	-	-	-	-	-	-	-	-	-	-	-	-	-	-
$\beta \in [150°, 180°]$	CM_t	-	-	-	-	-	-	-	-	-	-	-	-	-	-	-	-	-	-
	CL_t	-	-	-	-	-	-	-	-	-	-	-	-	-	-	-	-	-	-
	CS_t	-	-	-	-	-	-	-	-	-	-	-	-	-	-	-	-	-	-

Table A.1: ***First set*** *of confusion matrices (for* $\alpha \in [-180°, 0°]$*) obtained **for metric** $\mathbf{E_0}$, shown tile-by-tile. The table is divided in tiles in the same way as the* (α, β) *plane is. The subscripts "t" and "c" attached to CL, CM, and CS stand for "true" and "computed", respectively.*

		$\alpha \in [0°, 30°]$			$\alpha \in [30°, 60°]$			$\alpha \in [60°, 90°]$			$\alpha \in [90°, 120°]$			$\alpha \in [120°, 150°]$			$\alpha \in [150°, 180°]$		
		CM_c	CL_c	CS_c	CM_c	CL_c	CS_c	CM_c	CL_c	CS_c	CM_c	CL_c	CS_c	CM_c	CL_c	CS_c	CM_c	CL_c	CS_c
$\beta \in [0°, 30°]$	CM_t	-	-	-	0.5	-	0.21	0.1	0.027	0.013	-	-	-	-	-	-	-	-	-
	CL_t	-	-	-	-	-	-	0.19	0.22	0.081	-	-	-	-	-	-	-	-	-
	CS_t	-	-	-	0.5	-	0.79	0.71	0.76	0.91	-	-	-	-	-	-	-	-	-
$\beta \in [30°, 60°]$	CM_t	0.62	0.34	0.19	0.39	-	0.23	0.18	-	0.068	0.2	0.068	0.029	0.28	-	0.032	0.17	0.32	0.051
	CL_t	-	0.19	-	-	-	-	-	-	-	0.088	0.13	0.02	-	-	-	0.049	0.17	0.0087
	CS_t	0.38	0.47	0.81	0.61	-	0.77	0.82	-	0.93	0.71	0.81	0.95	0.72	-	0.97	0.78	0.51	0.94
$\beta \in [60°, 90°]$	CM_t	-	-	-	0.48	-	0.23	0.31	0.32	0.18	-	-	-	0.81	0.72	0.66	0.72	0.14	0.7
	CL_t	-	-	-	0.005	-	0.0002	0.092	0.22	0.043	-	-	-	0.03	0.11	0.01	0.28	0.86	0.27
	CS_t	-	-	-	0.52	-	0.77	0.6	0.47	0.78	-	-	-	0.16	0.17	0.33	-	-	-
$\beta \in [90°, 120°]$	CM_t	-	-	-	0.92	-	0.12	-	-	-	-	-	-	0.43	0.31	0.36	1.0	0.81	1.0
	CL_t	-	-	-	-	-	-	-	-	-	-	-	-	0.3	0.44	0.27	0.0008	0.19	0.0002
	CS_t	-	-	-	0.084	-	0.88	-	-	-	-	-	-	0.27	0.26	0.37	-	-	-
$\beta \in [120°, 150°]$	CM_t	-	-	-	-	-	-	-	-	-	-	-	-	0.6	-	0.35	0.81	-	0.013
	CL_t	-	-	-	-	-	-	-	-	-	-	-	-	-	-	-	-	-	-
	CS_t	-	-	-	-	-	-	-	-	-	-	-	-	0.4	-	0.65	0.19	-	0.99
$\beta \in [150°, 180°]$	CM_t	-	-	-	-	-	-	-	-	-	-	-	-	0.66	-	0.15	-	-	-
	CL_t	-	-	-	-	-	-	-	-	-	-	-	-	-	-	-	-	-	-
	CS_t	-	-	-	-	-	-	-	-	-	-	-	-	0.34	-	0.85	-	-	-

Table A.2: ***Second set*** *of confusion matrices (for* $\alpha \in [0°, 180°]$*) obtained **for metric** $\mathbf{E_0}$, shown tile-by-tile. The table is divided in tiles in the same way as the* (α, β) *plane is. The subscripts "t" and "c" attached to CL, CM, and CS stand for "true" and "computed", respectively.*

		$\alpha \in [-180°, -150°]$			$\alpha \in [-150°, -120°]$			$\alpha \in [-120°, -90°]$			$\alpha \in [-90°, -60°]$			$\alpha \in [-60°, -30°]$			$\alpha \in [-30°, 0°]$		
		CM_c	CL_c	CS_c	CM_c	CL_c	CS_c	CM_c	CL_c	CS_c	CM_c	CL_c	CS_c	CM_c	CL_c	CS_c	CM_c	CL_c	CS_c
$\beta \in [0°, 30°]$	CM_t	-	-	-	-	-	-	-	-	-	1.0	-	0.16	-	-	-	-	-	-
	CL_t	-	-	-	-	-	-	-	-	-	-	-	-	-	-	-	-	-	-
	CS_t	-	-	-	-	-	-	-	-	-	-	-	0.84	-	-	-	-	-	-
$\beta \in [30°, 60°]$	CM_t	1.0	-	0.13	0.92	-	0.19	0.86	-	-	0.8	0.16	0.041	0.83	-	0.061	1.0	-	0.016
	CL_t	-	-	-	0.077	-	0.041	0.14	-	0.11	0.2	0.84	0.023	0.17	1.0	0.12	-	-	0.12
	CS_t	-	-	0.87	-	-	0.77	-	-	0.89	-	-	0.94	-	-	0.82	-	-	0.86
$\beta \in [60°, 90°]$	CM_t	0.95	-	0.095	0.87	-	0.3	0.78	0.49	0.068	0.69	0.34	0.077	-	-	-	-	-	-
	CL_t	-	-	-	0.13	-	0.004	0.13	0.15	-	0.29	0.58	0.15	-	-	-	-	-	-
	CS_t	0.054	-	0.9	-	-	0.69	0.095	0.36	0.93	0.024	0.082	0.77	-	-	-	-	-	-
$\beta \in [90°, 120°]$	CM_t	1.0	-	0.21	-	-	-	0.92	0.1	0.049	0.63	0.3	0.077	-	-	-	-	-	-
	CL_t	-	-	-	-	-	-	0.075	0.9	0.13	0.37	0.65	0.11	-	-	-	-	-	-
	CS_t	-	-	0.79	-	-	-	0.001	-	0.82	0.001	0.044	0.82	-	-	-	-	-	-
$\beta \in [120°, 150°]$	CM_t	-	-	-	-	-	-	-	-	-	-	-	-	-	-	-	-	-	-
	CL_t	-	-	-	-	-	-	-	-	-	-	-	-	-	-	-	-	-	-
	CS_t	-	-	-	-	-	-	-	-	-	-	-	-	-	-	-	-	-	-
$\beta \in [150°, 180°]$	CM_t	-	-	-	-	-	-	-	-	-	-	-	-	-	-	-	-	-	-
	CL_t	-	-	-	-	-	-	-	-	-	-	-	-	-	-	-	-	-	0
	CS_t	-	-	-	-	-	-	-	-	-	-	-	-	-	-	-	-	-	-

Table A.3: ***First set*** *of confusion matrices (for* $\alpha \in [-180°, 0°]$*) obtained* ***for metric*** $\mathbf{E_1}$*, shown tile-by-tile. The table is divided in tiles in the same way as the* (α, β) *plane is. The subscripts "t" and "c" attached to CL, CM, and CS stand for "true" and "computed", respectively.*

		$\alpha \in [0°, 30°]$			$\alpha \in [30°, 60°]$			$\alpha \in [60°, 90°]$			$\alpha \in [90°, 120°]$			$\alpha \in [120°, 150°]$			$\alpha \in [150°, 180°]$		
		CM_c	CL_c	CS_c	CM_c	CL_c	CS_c	CM_c	CL_c	CS_c	CM_c	CL_c	CS_c	CM_c	CL_c	CS_c	CM_c	CL_c	CS_c
$\beta \in [0°, 30°]$	CM_t	-	-	-	0.66	-	0.25	0.66	0.31	0.15	-	-	-	-	-	-	-	-	-
	CL_t	-	-	-	-	-	-	0.32	0.69	0.067	-	-	-	-	-	-	-	-	-
	CS_t	-	-	-	0.34	-	0.75	0.016	0.004	0.78	-	-	-	-	-	-	-	-	-
$\beta \in [30°, 60°]$	CM_t	0.69	0.39	0.17	0.74	-	0.19	0.92	-	0.13	0.52	0.31	0.0006	0.8	-	0.13	0.77	0.34	0.007
	CL_t	0.31	0.61	0.025	-	-	-	-	-	-	0.38	0.59	0.001	0.2	-	0.024	0.14	0.66	0.19
	CS_t	-	-	0.81	0.26	-	0.81	0.083	-	0.87	0.097	0.095	1.0	-	-	0.85	0.09	-	0.81
$\beta \in [60°, 90°]$	CM_t	-	-	-	0.74	-	0.24	0.7	0.33	0.27	-	-	-	0.78	0.33	0.2	0.94	0.13	0.39
	CL_t	-	-	-	0.19	-	0.084	0.28	0.63	0.045	-	-	-	0.15	0.67	0.04	0.06	0.87	0.59
	CS_t	-	-	-	0.065	-	0.67	0.026	0.038	0.69	-	-	-	0.066	-	0.76	-	-	-
$\beta \in [90°, 120°]$	CM_t	-	-	-	0.98	-	0.2	-	-	-	-	-	-	0.83	0.24	0.24	0.7	0.4	0.93
	CL_t	-	-	-	-	-	-	-	-	-	-	-	-	0.093	0.33	0.1	0.3	0.6	0.065
	CS_t	-	-	-	0.016	-	0.8	-	-	-	-	-	-	0.08	0.44	0.65	-	-	-
$\beta \in [120°, 150°]$	CM_t	-	-	-	-	-	-	-	-	-	-	-	-	0.87	-	0.33	1.0	-	0.026
	CL_t	-	-	-	-	-	-	-	-	-	-	-	-	-	-	-	-	-	-
	CS_t	-	-	-	-	-	-	-	-	-	-	-	-	0.13	-	0.67	-	-	0.97
$\beta \in [150°, 180°]$	CM_t	-	-	-	-	-	-	-	-	-	-	-	-	0.86	-	0.27	-	-	-
	CL_t	-	-	-	-	-	-	-	-	-	-	-	-	-	-	-	-	-	-
	CS_t	-	-	-	-	-	-	-	-	-	-	-	-	0.14	-	0.73	-	-	-

Table A.4: ***Second set*** *of confusion matrices (for $\alpha \in [0°; 180°]$) obtained **for metric** $\mathbf{E_1}$, shown tile-by-tile. The table is divided in tiles in the same way as the (α, β) plane is. The subscripts "t" and "c" attached to CL, CM, and CS stand for "true" and "computed", respectively.*

		α ∈ [−180°, −150°]			α ∈ [−150°, −120°]			α ∈ [−120°, −90°]			α ∈ [−90°, −60°]			α ∈ [−60°, −30°]			α ∈ [−30°, 0°]		
		CM_c	CL_c	CS_c	CM_c	CL_c	CS_c	CM_c	CL_c	CS_c	CM_c	CL_c	CS_c	CM_c	CL_c	CS_c	CM_c	CL_c	CS_c
$\beta \in [0°, 30°]$	CM_t	-	-	-	-	-	-	-	-	-	1.0	-	-	-	-	-	-	-	-
	CL_t	-	-	-	-	-	-	-	-	-	-	-	-	-	-	-	-	-	-
	CS_t	-	-	-	-	-	-	-	-	-	-	-	1.0	-	-	-	-	-	-
$\beta \in [30°, 60°]$	CM_t	1.0	-	0.039	0.98	-	0.01	1.0	-	0.006	0.7	0.14	0.021	0.98	-	-	1.0	-	-
	CL_t	-	-	-	0.024	-	0.004	-	-	-	0.18	0.85	0.001	0.015	1.0	-	-	-	0.016
	CS_t	-	-	0.96	0.0005	-	0.99	-	-	0.99	0.12	0.011	0.98	-	-	1.0	-	-	0.98
$\beta \in [60°, 90°]$	CM_t	0.74	-	0.008	0.92	-	0.034	0.59	0.29	0.02	0.67	0.22	0.059	-	-	-	-	-	-
	CL_t	-	-	-	0.004	-	-	0.034	0.05	-	0.26	0.64	0.031	-	-	-	-	-	-
	CS_t	0.26	-	0.99	0.075	-	0.97	0.38	0.66	0.98	0.065	0.13	0.91	-	-	-	-	-	-
$\beta \in [90°, 120°]$	CM_t	0.98	-	0.11	-	-	-	0.9	0.056	0.03	0.51	0.2	0.06	-	-	-	-	-	-
	CL_t	-	-	-	-	-	-	0.083	0.94	0.055	0.45	0.74	0.018	-	-	-	-	-	-
	CS_t	0.016	-	0.89	-	-	-	0.015	-	0.91	0.036	0.062	0.92	-	-	-	-	-	-
$\beta \in [120°, 150°]$	CM_t	-	-	-	-	-	-	-	-	-	-	-	-	-	-	-	-	-	-
	CL_t	-	-	-	-	-	-	-	-	-	-	-	-	-	-	-	-	-	-
	CS_t	-	-	-	-	-	-	-	-	-	-	-	-	-	-	-	-	-	-
$\beta \in [150°, 180°]$	CM_t	-	-	-	-	-	-	-	-	-	-	-	-	-	-	-	-	-	-
	CL_t	-	-	-	-	-	-	-	-	-	-	-	-	-	-	-	-	-	-
	CS_t	-	-	-	-	-	-	-	-	-	-	-	-	-	-	-	-	-	-

Table A.5: *__First set__ of confusion matrices (for $\alpha \in [-180°, 0°]$) obtained __for metric__ $\mathbf{E_{0.05}}$, shown tile-by-tile. The table is divided in tiles in the same way as the (α, β) plane is. The subscripts "t" and "c" attached to CL, CM, and CS stand for "true" and "computed", respectively..*

		$\alpha \in [0°,30°]$			$\alpha \in [30°,60°]$			$\alpha \in [60°,90°]$			$\alpha \in [90°,120°]$			$\alpha \in [120°,150°]$			$\alpha \in [150°,180°]$		
		CM_c	CL_c	CS_c	CM_c	CL_c	CS_c	CM_c	CL_c	CS_c	CM_c	CL_c	CS_c	CM_c	CL_c	CS_c	CM_c	CL_c	CS_c
$\beta \in [0°,30°]$	CM_t	-	-	-	0.43	-	0.22	0.37	0.2	0.011	-	-	-	-	-	-	-	-	-
	CL_t	-	-	-	-	-	-	0.32	0.73	0.018	-	-	-	-	-	-	-	-	-
	CS_t	-	-	-	0.57	-	0.78	0.31	0.068	0.97	-	-	-	-	-	-	-	-	-
$\beta \in [30°,60°]$	CM_t	0.97	0.56	0.037	0.43	-	0.081	0.6	-	0.02	0.43	0.21	0.001	0.99	-	0.016	0.62	0.33	0.002
	CL_t	0.025	0.44	-	-	-	-	-	-	-	0.13	0.31	-	0.011	-	-	0.089	0.65	0.007
	CS_t	-	-	0.96	0.57	-	0.92	0.4	-	0.98	0.43	0.48	1.0	-	-	0.98	0.29	0.018	0.99
$\beta \in [60°,90°]$	CM_t	-	-	-	0.85	-	0.12	0.77	0.42	0.15	-	-	-	0.9	0.46	0.17	0.93	0.14	0.64
	CL_t	-	-	-	0.016	-	0.003	0.097	0.31	0.011	-	-	-	0.035	0.49	0.004	0.072	0.86	0.33
	CS_t	-	-	-	0.14	-	0.87	0.13	0.27	0.84	-	-	-	0.07	0.051	0.83	-	-	-
$\beta \in [90°,120°]$	CM_t	-	-	-	0.98	-	0.024	-	-	-	-	-	-	0.8	0.17	0.24	1.0	0.69	1.0
	CL_t	-	-	-	-	-	-	-	-	-	-	-	-	0.1	0.46	0.077	0.003	0.31	0.0005
	CS_t	-	-	-	0.017	-	0.98	-	-	-	-	-	-	0.099	0.37	0.69	-	-	-
$\beta \in [120°,150°]$	CM_t	-	-	-	-	-	-	-	-	-	-	-	-	0.85	-	0.3	1.0	-	-
	CL_t	-	-	-	-	-	-	-	-	-	-	-	-	-	-	-	-	-	-
	CS_t	-	-	-	-	-	-	-	-	-	-	-	-	0.15	-	0.7	-	-	1.0
$\beta \in [150°,180°]$	CM_t	-	-	-	-	-	-	-	-	-	-	-	-	0.82	-	0.091	-	-	-
	CL_t	-	-	-	-	-	-	-	-	-	-	-	-	-	-	-	-	-	-
	CS_t	-	-	-	-	-	-	-	-	-	-	-	-	0.18	-	0.91	-	-	-

Table A.6: *Second set of confusion matrices (for $\alpha \in [0°; 180°]$) obtained **for metric** $\mathbf{E_{0.05}}$, shown tile-by-tile. The table is divided in tiles in the same way as the (α, β) plane is. The subscripts "t" and "c" attached to CL, CM, and CS stand for "true" and "computed", respectively.*

		α ∈ [−180°,−150°]			α ∈ [−150°,−120°]			α ∈ [−120°,−90°]			α ∈ [−90°,−60°]			α ∈ [−60°,−30°]			α ∈ [−30°,0°]		
		CM_c	CL_c	CS_c	CM_c	CL_c	CS_c	CM_c	CL_c	CS_c	CM_c	CL_c	CS_c	CM_c	CL_c	CS_c	CM_c	CL_c	CS_c
$\beta \in [0°,30°]$	CM_t	-	-	-	-	-	-	-	-	-	1.0	-	0.016	-	-	-	-	-	-
	CL_t	-	-	-	-	-	-	-	-	-	-	-	-	-	-	-	-	-	-
	CS_t	-	-	-	-	-	-	-	-	-	-	-	0.98	-	-	-	-	-	-
$\beta \in [30°,60°]$	CM_t	1.0	-	0.046	0.95	-	0.12	0.92	-	-	0.82	0.11	0.038	0.97	-	-	1.0	-	0.006
	CL_t	-	-	-	0.047	-	0.016	0.083	-	-	0.18	0.89	0.013	0.03	1.0	-	-	-	0.077
	CS_t	-	-	0.95	-	-	0.87	-	-	1.0	0.005	-	0.95	-	-	1.0	-	-	0.92
$\beta \in [60°,90°]$	CM_t	0.94	-	0.07	0.97	-	0.23	0.79	0.46	0.027	0.71	0.25	0.13	-	-	-	-	-	-
	CL_t	-	-	-	0.028	-	0.002	0.059	0.095	-	0.27	0.66	0.097	-	-	-	-	-	-
	CS_t	0.064	-	0.93	0.003	-	0.77	0.15	0.44	0.97	0.027	0.094	0.78	-	-	-	-	-	-
$\beta \in [90°,120°]$	CM_t	1.0	-	0.18	-	-	-	0.92	0.081	0.052	0.63	0.25	0.089	-	-	-	-	-	-
	CL_t	-	-	-	-	-	-	0.079	0.92	0.11	0.37	0.7	0.082	-	-	-	-	-	-
	CS_t	-	-	0.82	-	-	-	0.001	-	0.83	0.001	0.042	0.83	-	-	-	-	-	-
$\beta \in [120°,150°]$	CM_t	-	-	-	-	-	-	-	-	-	-	-	-	-	-	-	-	-	-
	CL_t	-	-	-	-	-	-	-	-	-	-	-	-	-	-	-	-	-	-
	CS_t	-	-	-	-	-	-	-	-	-	-	-	-	-	-	-	-	-	-
$\beta \in [150°,180°]$	CM_t	-	-	-	-	-	-	-	-	-	-	-	-	-	-	-	-	-	-
	CL_t	-	-	-	-	-	-	-	-	-	-	-	-	-	-	-	-	-	-
	CS_t	-	-	-	-	-	-	-	-	-	-	-	-	-	-	-	-	-	-

Table A.7: ***First set*** *of confusion matrices (for $\alpha \in [−180°; 0°]$) obtained **for the aggregation of the three metrics**, shown tile-by-tile. The table is divided in tiles in the same way as the (α, β) plane is. The subscripts "t" and "c" attached to CL, CM, and CS stand for "true" and "computed", respectively.*

		$\alpha \in [0°, 30°]$			$\alpha \in [30°, 60°]$			$\alpha \in [60°, 90°]$			$\alpha \in [90°, 120°]$			$\alpha \in [120°, 150°]$			$\alpha \in [150°, 180°]$		
		CM_c	CL_c	CS_c	CM_c	CL_c	CS_c	CM_c	CL_c	CS_c	CM_c	CL_c	CS_c	CM_c	CL_c	CS_c	CM_c	CL_c	CS_c
$\beta \in [0°, 30°]$	CM_t	-	-	-	0.64	-	0.25	0.57	0.25	0.063	-	-	-	-	-	-	-	-	-
	CL_t	-	-	-	-	-	-	0.41	0.74	0.07	-	-	-	-	-	-	-	-	-
	CS_t	-	-	-	0.36	-	0.75	0.023	0.015	0.87	-	-	-	-	-	-	-	-	-
$\beta \in [30°, 60°]$	CM_t	0.97	0.49	0.14	0.69	-	0.14	0.87	-	0.056	0.61	0.31	0.001	0.95	-	0.092	0.76	0.34	0.004
	CL_t	0.028	0.51	-	-	-	-	-	-	-	0.26	0.57	-	0.051	-	0.003	0.13	0.66	0.13
	CS_t	-	-	0.86	0.31	-	0.86	0.13	-	0.94	0.13	0.12	1.0	-	-	0.91	0.11	-	0.86
$\beta \in [60°, 90°]$	CM_t	-	-	-	0.88	-	0.25	0.76	0.36	0.25	-	-	-	0.84	0.35	0.22	0.94	0.12	0.55
	CL_t	-	-	-	0.049	-	0.015	0.2	0.61	0.024	-	-	-	0.079	0.65	0.017	0.059	0.88	0.45
	CS_t	-	-	-	0.068	-	0.74	0.037	0.036	0.73	-	-	-	0.077	-	0.77	-	-	-
$\beta \in [90°, 120°]$	CM_t	-	-	-	0.98	-	0.12	-	-	-	-	-	-	0.83	0.22	0.25	0.99	0.56	1.0
	CL_t	-	-	-	-	-	-	-	-	-	-	-	-	0.089	0.35	0.093	0.01	0.44	0.002
	CS_t	-	-	-	0.017	-	0.88	-	-	-	-	-	-	0.084	0.44	0.66	-	-	-
$\beta \in [120°, 150°]$	CM_t	-	-	-	-	-	-	-	-	-	-	-	-	0.87	-	0.32	1.0	-	0.013
	CL_t	-	-	-	-	-	-	-	-	-	-	-	-	-	-	-	-	-	-
	CS_t	-	-	-	-	-	-	-	-	-	-	-	-	0.13	-	0.68	-	-	0.99
$\beta \in [150°, 180°]$	CM_t	-	-	-	-	-	-	-	-	-	-	-	-	0.86	-	0.2	-	-	-
	CL_t	-	-	-	-	-	-	-	-	-	-	-	-	-	-	-	-	-	-
	CS_t	-	-	-	-	-	-	-	-	-	-	-	-	0.14	-	0.8	-	-	-

Table A.8: ***Second set*** *of confusion matrices (for* $\alpha \in [0°; 180°]$*) obtained **for the aggregation of the three metrics**, shown tile-by-tile. The table is divided in tiles in the same way as the* (α, β) *plane is. The subscripts "t" and "c" attached to CL, CM, and CS stand for "true" and "computed", respectively.*

Appendix B

Publications

Different parts of this work have been published as journal articles or as conference papers. We list them below.

2.1 Journal articles

- J. Pisane, S. Azarian, M. Lesturgie, J. G. Verly, *Automatic target recognition (ATR) for passive radar*, To appear in IEEE Transactions on Aerospace and Electronic Systems.

2.2 Conference papers

- J. Pisane, S. Azarian, M. Lesturgie, J. G. Verly, *Passive radar testbed and preliminary experiments in recognition of non-cooperative aircraft intruding into controlled airspace*, URSI Benelux Forum, Sept. 2012 [150].

- J. Pisane, S. Azarian, M. Lesturgie, J. G. Verly, *Automatic real-time collection of RCS of airplanes in a real bistatic low-frequency configuration using a software defined passive radar based on illuminators of opportunity*, International Radar Conference, May 2012 [149].

- J. Pisane, M. Lesturgie, J. G. Verly, *Target classification system based on the characterization of targets by subspaces*, IEEE CIE International Conference on Radar, Oct. 2011 [154].

- J. Pisane, M. Lesturgie, J. G. Verly, *Passive target classification based on low-frequency bistatic backscattering coefficients*, Ocean & Coastal Observation: Sensors and Systems, Passive Session, June 2010 [152].

- J. Pisane, R. Marée, L. Wehenkel, and J. G. Verly, *Robust Automatic Target Recognition Using Extra-trees*, International Radar Conference, IEEE, May 2010 [157].

- J. Pisane, M. Lesturgie, and J. G. Verly. *Target classification of experimentally-acquired low-frequency backscattering coefficients by construction of subspaces*, URSI Benelux Forum, April 2010 [153].

- J. Pisane, R. Marée, P. Ries, L. Wehenkel, and J. G. Verly, *An Extra-trees-based Automatic Target Recognition Algorithm*, International Radar Conference, IEEE, Oct. 2009 [155].

2.3   Other publications

- J. Pisane, S. Azarian, M. Lesturgie, J. G. Verly, *Target classification in bistatic low frequency radar*, 2nd Thales Radar PhD Day, Sept. 2012 [151].

- J. Pisane, R. Marée, L. Wehenkel, and J. G. Verly, *Radar Classification based on Extra-Trees*, SONDRA Workshop, May 2010 [156].

Bibliography

[1] ABRAMOWITZ, M., AND STEGUN, I. *Handbook of mathematical functions: with formulas, graphs, and mathematical tables.* Dover publications, 1965. (page 40).

[2] AIRBUS. Airbus, an EADS company. Website, 2012. `http://www.airbus.com/aircraftfamilies/`. (page 174).

[3] ALCATEL LUCENT CHAIR ON FLEXIBLE RADIO. Sdr4all. Website, 2012. http://www.flexible-radio.com/sdr4all. (page 183).

[4] ANDERSON, S. Target classification, recognition and identification with HF radar. In *Proceedings of the NATO Research and Technology Agency. Sensors and Electronics Technology Panel Symposium SET–080/RSY17/RFT: "Target identification and recognition using RF systems", RTO–MP–SET* (2004). (page 18).

[5] ASANO, F., HAYAMIZU, S., YAMADA, T., AND NAKAMURA, S. Speech enhancement based on the subspace method. *IEEE Transactions on Speech and Audio Processing* (2000). (page 143).

[6] BAKER, C., AND GRIFFITHS, H. Bistatic and multistatic radar sensors for homeland security. *Advances in sensing with security applications* (2006). (page 16).

[7] BAKER, C., GRIFFITHS, H., AND PAPOUTSIS, I. Passive coherent location radar systems. Part 2: Waveform properties. In *IEE Proceedings Radar, Sonar, and Navigation* (2005). (page 16).

[8] BALANIS, C. *Antenna theory: analysis and design.* J. Wiley, 1982. (pages 26, 32).

[9] BALDWIN, J., SMITH, A., AND CASSELL, R. General aviation collision avoidance-challenges of full implementation. In *Proceedings of the 13th AIAA/IEEE Digital Avionics Systems Conference (DASC)* (1994). (page 11).

[10] BANDIERA, F., BESSON, O., ORLANDO, D., RICCI, G., AND SCHARF, L. GLRT-based direction detectors in noise and subspace interference. In *Proceedings of the IEEE International Conference on Acoustics, Speech, and Signal Processing (ICASSP)* (2006). (page 143).

[11] BANDIERA, F., DE MAIO, A., GRECO, A., AND RICCI, G. Adaptive radar detection of distributed targets in homogeneous and partially homogeneous noise plus subspace interference. *IEEE Transactions on Signal Processing* (2007). (page 143).

[12] BANDIERA, F., ORLANDO, D., RICCI, G., AND SCHARF, L. Adaptive radar detection: A subspace identification approach. In *Proceedings of the 2nd International Workshop on Cognitive Information Processing (CIP)* (2010). (page 143).

[13] BARÈS, C. *Développement et application de méthodes d'identification de cibles aériennes dans les bandes HF et VHF*. PhD thesis, Université de Rennes I, 2007. (page 20).

[14] BEHRENS, R., SCHARF, L., INC, C., AND BROOMFIELD, C. Signal processing applications of oblique projection operators. *IEEE Transactions on Signal Processing* (1994). (pages 146, 148).

[15] BELKACEMI, H. *Approches de sous-espaces pour le traitement adaptatif spatio-temporel en radar aéroporté monostatique/bistatique*. PhD thesis, Université de Paris XI Orsay, 2006. (page 143).

[16] BENCHEIKH, M. L., WANG, Y., AND HE, H. A subspace-based technique for joint DOA-DOD estimation in bistatic MIMO radar. In *Proceedings of the 11th International Radar Symposium (IRS)* (2010). (page 143).

[17] BHANU, B. Automatic target recognition: State of the art survey. *IEEE Transactions on Aerospace and Electronic Systems* (1986). (pages 2, 17, 18).

[18] BLYAKHMAN, A., AND RUNOVA, I. Forward scattering radiolocation bistatic RCS and target detection. In *The Record of the 1999 IEEE Radar Conference* (1999). (page 16).

[19] BOEING. Boeing, commercial airplanes. Website, 2012. http://www.boeing.com/commercial/products.html. (page 175).

[20] BOERNER, W., YAN, W., XI, A., AND YAMAGUCHI, Y. Basic concepts of radar polarimetry. *Proceedings of the NATO Advanced Research Workshop on Direct and Inverse Methods in Radar Polarimetry* (1988). (page 50).

[21] BOERNER, W., YAN, W., XI, A., AND YAMAGUCHI, Y. On the basic principles of radar polarimetry: The target characteristic polarization state theory of Kennaugh, Huynen's polarization fork concept, and its extension to the partially polarized case. *Proceedings of the IEEE* (1991). (page 50).

[22] BOISVERT, R., AND ORLANDO, V. ADS-Mode S system overview. In *Proceedings of the 12th AIAA/IEEE Digital Avionics Systems Conference (DASC)* (1993). (page 11).

[23] BORN, M., AND WOLF, E. *Principles of optics: electromagnetic theory of propagation, interference and diffraction of light*. Pergamon Press, 1965. (pages 32, 35).

[24] BRACEWELL, R. *Two-dimensional imaging*. Prentice-Hall, 1995. (pages 19, 80, 81, 82, 84, 87).

[25] BREIMAN, L. *Classification and regression trees*. Chapman & Hall/CRC, 1984. (page 113).

[26] BREIMAN, L. Bagging predictors. *Machine learning* (1996). (page 113).

[27] BREIMAN, L. Random forests. *Machine learning* (2001). (page 113).

[28] BREIMAN, L., FRIEDMAN, J., OLSEN, R., AND STONE, C. *Classification and regression trees.* Wadsworth International, 1984. (page 115).

[29] BRIGUI, F. *Algorithmes d'imagerie SAR polarimétrique basés sur des modèles à sous-espace.* PhD thesis, SUPELEC, 2010. (page 143).

[30] BROUSSEAU, C. *Caractérisation Large Bande de Fréquence: Application au radar et au sondage de canal.* PhD thesis, Université Rennes 1, 2005. (page 20).

[31] CETIN, M., KARL, W., AND CASTANON, D. Analysis of the impact of feature-enhanced SAR imaging on ATR performance. In *Proceedings of SPIE* (2002), vol. 4727. (page 20).

[32] CETIN, M., AND LANTERMAN, A. Region-enhanced passive radar imaging. In *IEE Proceedings Radar, Sonar, and Navigation* (2005). (page 19).

[33] CHA, P., AND MOLINDER, J. *Fundamentals of signals and systems: a building block approach.* Cambridge Univ Press, 2006. (page 105).

[34] CHALLA, S., AND KOKS, D. Bayesian and Dempster-Shafer fusion. *Sadhana* (2004). (page 148).

[35] CHASSAY, G. Justification du modèle des points brillants. intégration dans le modèle des interactions entre différentes parties d'une cible. In *9eme Colloque sur le traitement du signal et des images* (1983), Groupe d'Etudes du Traitement du Signal et des Images (GRETSI). (pages 145, 196).

[36] CHEN, C.-Y., AND VAIDYANATHAN, P. A Subspace Method for MIMO Radar Space-Time Adaptive Processing. In *Proceedings of the IEEE International Conference on Acoustics, Speech, and Signal Processing (ICASSP)* (2007). (page 143).

[37] CHEN, J., AND WALTON, E. Comparison of two target classification techniques. *IEEE Transactions on Aerospace and Electronic Systems* (1986). (page 19).

[38] CHEN, V., AND LING, H. Joint time-frequency analysis for radar signal and image processing. *IEEE Signal Processing Magazine* (1999). (page 20).

[39] CHERNIAKOV, M., ABDULLAH, R., JANCOVIC, P., AND SALOUS, M. Forward scattering micro sensor for vehicle classification. In *Proceedings of the IEEE International Radar Conference* (2005). (page 39).

[40] CHERNIAKOV, M., ABDULLAH, R., JANCOVIC, P., SALOUS, M., AND CHAPURSKY, V. Automatic ground target classification using forward scattering radar. In *IEE Proceedings Radar, Sonar, and Navigation* (2006). (page 39).

[41] CHERNIAKOV, M., AND NEZLIN, D. *Bistatic radar: principles and practice.* John Wiley, 2007. (pages 27, 30, 41, 42, 92).

[42] CHERNIAKOV, M., NEZLIN, D., AND KUBIK, K. Air target detection via bistatic radar based on LEOS communication signals. In *IEE Proceedings Radar, Sonar, and Navigation* (2002). (page 17).

[43] CHERNIAKOV, M., SALOUS, M., KOSTYLEV, V., AND ABDULLAH, R. Analysis of forward scattering radar for ground target detection. In *Proceedings of the IEEE European Radar Conference (EURAD)* (2005). (page 39).

[44] COHEN, M. An overview of radar-based, automatic, noncooperative target recognition techniques. In *Proceedings of the IEEE International Conference on Systems Engineering* (1991). (pages 17, 18).

[45] COLEMAN, C., WATSON, R., AND YARDLEY, H. A practical bistatic passive radar system for use with DAB and DRM illuminators. In *Proceedings of the IEEE Radar Conference* (2008). (page 17).

[46] COLIN-KOENIGUER, E., AND THIRION-LEFEVRE, L. Bistatic scattering from forest components. Part II: first validation of a bistatic polarimetric forest model in the VHF-UHF band [225–475 MHz] using indoor measurements. *Waves in Random and Complex Media* (2010). (pages 26, 55).

[47] COLONE, F., O'HAGAN, D., LOMBARDO, P., AND BAKER, C. A multi-stage processing algorithm for disturbance removal and target detection in passive bistatic radar. *IEEE Transactions on Aerospace and Electronic Systems* (2009). (page 16).

[48] CRISPIN, J., SIEGEL, K., AND BOWMAN, J. *Methods of radar cross-section analysis*. Academic Press, 1968. (pages 15, 42).

[49] CRISPIN JR, J., GOODRICH, R., AND SIEGEL, K. A theoretical method for the calculation of radar cross section of aircraft and missiles. Tech. rep., University of Michigan, 1959. (pages 15, 31, 32, 35, 36, 37, 40, 41).

[50] CRISPIN JR, J., AND MAFFETT, A. Radar cross-section estimation for simple shapes. *Proceedings of the IEEE* (1965). (pages 31, 32).

[51] CUMMING, I., AND WONG, F. *Digital signal processing of synthetic aperture radar data: algorithms & implementation*. Artech House, 2005. (page 19).

[52] DU, L., LIU, H., AND BAO, Z. Radar HRRP statistical recognition: Parametric model and model selection. *IEEE Transactions on Signal Processing* (2008). (page 19).

[53] DUDA, R., AND HART, P. *Pattern classification and scene analysis*. Wiley, 1996. (page 106).

[54] DUDA, R., HART, P., AND STORK, D. *Pattern classification and scene analysis 2nd ed.* Wiley Interscience, 1995. (pages 2, 114).

[55] DUDGEON, D., AND LACOSS, R. An overview of automatic target recognition. *The Lincoln Laboratory Journal* (1993). (page 18).

[56] DUMONT, M., MARÉE, R., WEHENKEL, L., AND GEURTS, P. Fast multi-class image annotation with random subwindows and multiple output randomized trees. In *Proceedings of the International Conference on Computer Vision Theory and Applications (VISAPP)* (2009). (page 116).

[57] DUQUENOY, M. *Analyse temps-fréquence appliquée à l'imagerie SAR polarimétrique.* PhD thesis, Université Rennes 1, 2009. (page 145).

[58] DURAND, R. *Processeurs SAR basés sur des détecteurs de sous-espaces.* PhD thesis, SUPELEC, 2007. (page 143).

[59] EHRMAN, L. Automatic target recognition using passive radar and a coordinated flight model. Master's thesis, Georgia Institute of Technology, 2004. (page 21).

[60] EHRMAN, L. *An algorithm for automatic target recognition using passive radar and an EKF for estimating aircraft orientation.* PhD thesis, Georgia Institute of Technology, 2005. (page 21).

[61] EHRMAN, L., AND LANTERMAN, A. Automatic target recognition via passive radar, using precomputed radar cross sections and a coordinated flight model. *IEEE Transactions on Aerospace and Electronic Systems* (2003). (page 21).

[62] EHRMAN, L., AND LANTERMAN, A. Target identification using modeled radar cross sections and a coordinated flight model. In *Proceedings from the Third Multi-National Conference on Passive and Covert Radar* (2003). (page 21).

[63] EHRMAN, L., AND LANTERMAN, A. A robust algorithm for automated target recognition using precomputed radar cross sections. In *Proceedings of SPIE* (2004), vol. 5426, Citeseer. (page 21).

[64] EHRMAN, L., AND LANTERMAN, A. A robust algorithm for automatic target recognition using passive radar. In *System Theory, Proceedings of the Thirty-Sixth Southeastern Symposium on* (2004), IEEE. (page 21).

[65] EIGEL JR, R., COLLINS, P., TERZUOLI JR, A., NESTI, G., AND FORTUNY, J. Bistatic scattering characterization of complex objects. *IEEE Transactions on Geoscience and Remote Sensing* (2000). (pages 28, 30, 31, 42).

[66] EISENBIES, C. Classification of ultra high range resolution radar using decision boundary analysis. Tech. rep., DTIC Document, 1994. (page 19).

[67] FLIGHTRADAR24 AB. Flightradar24, live air traffic. Website, 2012. http://www.flightradar24.com. (pages 172, 181).

[68] FLORIN, C. *Automated traffic control for smart landing facilities.* PhD thesis, Virginia Polytechnic Institute and State University, 2002. (page 10).

[69] GEURTS, P., ERNST, D., AND WEHENKEL, L. Extremely randomized trees. *Machine learning* (2006). (pages 113, 115).

[70] GINI, F., GIANNAKIS, G., GRECO, M., AND ZHOU, G. T. Time-averaged subspace methods for radar clutter texture retrieval. *IEEE Transactions on Signal Processing* (2001). (page 143).

[71] GLENDE, M., HECKENBACH, J., KUSCHEL, H., MÜLLER, S., SCHELL, J., AND SCHUMACHER, C. Experimental passive radar systems using digital illuminators (DAB/DVB-T). In *Proceedings of the International Radar Symposium (IRS)* (2007). (page 17).

[72] GRECO, M., GINI, F., AND FARINA, A. A multiple hypotheses testing approach to radar detection and pre-classification. In *Proceedings of the IEEE Radar Conference* (2004). (page 147).

[73] GRIFFITHS, H. Bistatic radar - principles and practice. In *Proceedings of the SBMO International Microwave Conference* (1993). (page 16).

[74] GRIFFITHS, H. From a different perspective: principles, practice and potential of bistatic radar. In *Proceedings of the International Radar Conference* (2003). (page 16).

[75] GRIFFITHS, H. New directions in bistatic radar. In *Proceedings of the IEEE Radar Conference* (2008), IEEE. (page 16).

[76] GRIFFITHS, H., AND BAKER, C. Passive coherent location radar systems. Part 1: Performance prediction. In *IEE Proceedings Radar, Sonar, and Navigation* (2005). (page 16).

[77] GRIFFITHS, H., AND LONG, N. Television-based bistatic radar. *IEE Proceedings Communications, Radar, and Signal Processing* (1986). (page 17).

[78] GRIFFITHS, H., AND WILLIS, N. Klein Heidelberg - The first modern bistatic radar system. *IEEE Transactions on Aerospace and Electronic Systems* (2010). (page 16).

[79] GUNAL, S., AND EDIZKAN, R. Use of novel feature extraction technique with subspace classifiers for speech recognition. In *Proceedings of the IEEE International Conference on Pervasive Services* (2007). (page 143).

[80] GUO, H., COETZEE, S., MASON, D., WOODBRIDGE, K., AND BAKER, C. Passive radar detection using wireless networks. In *Proceedings of the IET International Conference on Radar Systems* (2007). (page 17).

[81] GUO, H., WOODBRIDGE, K., AND BAKER, C. Evaluation of WiFi beacon transmissions for wireless based passive radar. In *Proceedings of the IEEE Radar Conference* (2008). (page 17).

[82] HERMAN, S., AND MOULIN, P. A particle filtering approach to FM-band passive radar tracking and automatic target recognition. In *IEEE Aerospace Conference Proceedings* (2002). (page 21).

[83] HERNANDEZ, N., RODRIGUEZ, J., MARTIN, J., MATA, F., GONZALEZ, R., AND ALVAREZ, R. An approach to automatic target recognition in radar images using SVM. *Lecture Notes in Computer Science* (2006). (page 20).

[84] HOLPP, W. The century of radar. *Deutsche Gesellschaft für Ortung und Navigation (DGON)* (2003). (page 15).

[85] Howland, P. Target tracking using television-based bistatic radar. In *IEE Proceedings Radar, Sonar, and Navigation* (1999). (page 17).

[86] Howland, P., Maksimiuk, D., and Reitsma, G. FM radio based bistatic radar. In *IEE Proceedings Radar, Sonar and Navigation* (2005), IET. (page 17).

[87] Huynen, J. *Phenomenological theory of radar targets.* PhD thesis, Drukkerij Bronder-Offset NV, 1970. (pages 52, 53).

[88] Hwang, J., Lin, K., Chiu, Y., and Deng, J. Automatic target recognition based on high-resolution range profiles with unknown circular range shift. In *Proceedings of the IEEE International Symposium on Signal Processing and Information Technology* (2006). (page 19).

[89] IEEE Std. IEEE Standard Radar Definitions. *IEEE Std 686-2008 (Revision of IEEE Std 686-1997)* (2008). (page 3).

[90] Inc., D. M. Aircraft technical data and specifications. Website, August 2012. http://www.airliners.net/aircraft-data/. (pages 174, 175).

[91] Jackson, M. The geometry of bistatic radar systems. *IEE Proceedings Communications, Radar, and Signal Processing* (1986). (pages 16, 38, 103).

[92] Jacobs, S., and O'Sullivan, J. High resolution radar models for joint tracking and recognition. In *Proceedings of the IEEE National Radar Conference* (1997). (page 19).

[93] Jacobs, S., and O'Sullivan, J. Automatic target recognition using sequences of high resolution radar range-profiles. *IEEE Transactions on Aerospace and Electronic Systems* (2000). (page 19).

[94] James, J. *A student's guide to Fourier transforms: with applications in physics and engineering.* Cambridge Univ Press, 2011. (page 105).

[95] Javidi, B. *Image recognition and classification: algorithms, systems, and applications.* CRC Press, 2002. (page 2).

[96] Jian, W., Kirlin, R., Xiaoli, L., and Dizaji, R. Small ship detection with high frequency radar using an adaptive ocean clutter pre-whitened subspace method. In *Proceedings of the Sensor Array and Multichannel Signal Processing Workshop* (2002). (page 143).

[97] Kak, A., and Slaney, M. *Principles of computerized tomographic imaging.* Society for Industrial Mathematics, 2001. (page 80).

[98] Kell, R. On the derivation of bistatic RCS from monostatic measurements. *Proceedings of the IEEE* (1965). (pages 15, 31, 38, 42).

[99] Kenington, P. *RF and baseband techniques for software defined radio.* Artech House, 2005. (pages 177, 178, 183).

[100] Kennaugh, E., and Sloan, R. Effects of type of polarization on echo characteristics. Tech. rep., DTIC Document, 1952. (pages 52, 53).

[101] KIM, K., SEO, D., AND KIM, H. Efficient radar target recognition using the MUSIC algorithm and invariant features. *IEEE Transactions on Antennas and Propagation* (2002). (page 19).

[102] KIM, K., SEO, D., AND KIM, H. Efficient classification of ISAR images. *IEEE Transactions on Antennas and Propagation* (2005). (page 19).

[103] KNOTT, E. RCS reduction of dihedral corners. *IEEE Transactions on Antennas and Propagation* (1977). (page 24).

[104] KNOTT, E., SHAEFFER, J., AND TULEY, M. *Radar cross section.* SciTech Publishing, 2004. (pages 27, 28, 30, 60).

[105] KOKS, D., AND CHALLA, S. An Introduction to Bayesian and Dempster-Shafer data fusion. Tech. rep., Systems Sciences Lab, Defence Science and Technology Organisation, 2003. (page 148).

[106] KOKSAL, A., SHAPIRO, J., AND WELLS, W. Model-based object recognition using laser radar range imagery. In *Proceedings of SPIE* (1999), vol. 3718. (page 17).

[107] KOMILIKIS, S., PRADA, C., AND FINK, M. Characterization of extended objects with the DORT method. In *Proceedings of the IEEE Ultrasonics Symposium* (1996). (page 145).

[108] KONG, J. *Electromagnetic wave theory.* Higher Education Press, 2002. (pages 33, 48, 49).

[109] KRAUS, J. *Antennas.* McGraw-Hill, 1988. (pages 32, 35).

[110] KRAUT, S., SCHARF, L., AND McWHORTER, L. Adaptive subspace detectors. *IEEE Transactions on Signal Processing* (2001). (page 147).

[111] KSIENSKI, A., LIN, Y., AND WHITE, L. Low-frequency approach to target identification. *Proceedings of the IEEE* (1975). (page 19).

[112] KUBICA, M., KUBICA, V., NEYT, X., RAOUT, J., ROQUES, S., AND ACHEROY, M. Optimum target detection using illuminators of opportunity. In *Proceedings of the IEEE Radar Conference* (2006). (page 16).

[113] LAAKSONEN, J., AND OJA, E. Subspace dimension selection and averaged learning subspace method in handwritten digit classification. In *Proceedings of the International Conference on Artificial Neural Networks (ICANN)* (1996), Springer. (pages 147, 148).

[114] LANTERMAN, A., MUNSON JR, D., AND WU, Y. Wide-angle radar imaging using time-frequency distributions. In *IEE Proceedings Radar, Sonar, and Navigation* (2003). (page 19).

[115] LAURI, A., CARDINALI, R., COLONE, F., LOMBARDO, P., AND BUCCIARELLI, T. A geometrically based multipath channel model for passive radar. In *Proceedings of the IET International Conference on Radar Systems* (2007). (page 16).

[116] LAURI, A., COLONE, F., CARDINALI, R., BONGIOANNI, C., AND LOMBARDO, P. Analysis and emulation of FM radio signals for passive radar. In *Proceedings of the IEEE Aerospace Conference* (2007). (page 17).

[117] LEHMANN, N., FISHLER, E., HAIMOVICH, A., BLUM, R., CHIZHIK, D., CIMINI, L., AND VALENZUELA, R. Evaluation of transmit diversity in MIMO radar direction finding. *IEEE Transactions on Signal Processing* (2007). (page 145).

[118] LEPETIT, V., LAGGER, P., AND FUA, P. Randomized trees for real-time keypoint recognition. In *Proceedings of the IEEE International Conference on Computer Vision and Pattern Recognition (CVPR)* (2005). (page 115).

[119] LESTURGIE, M. Methodology of outdoor RCS measurement on scale models. Tech. rep., ONERA, 2001. (page 59).

[120] LU, Y., TAN, D., AND SUN, H. Air target detection and tracking using a multichannel GSM based passive radar. In *Proceedings of the IEEE International Waveform Diversity and Design Conference* (2007). (page 17).

[121] MALANOWSKI, M., AND KULPA, K. Two methods for target localization in multistatic passive radar. *IEEE Transactions on Aerospace and Electronic Systems* (2012). (page 16).

[122] MARCELLIN, J. Methodology of indoor RCS measurement on scale models. Tech. rep., ONERA, 2001. (page 59).

[123] MARÉE, R. PiXiT, an automatic image classification software in Java. Website. `http://www.montefiore.ulg.ac.be/~maree/pixit.html`. (page 112).

[124] MARÉE, R. *Classification automatique d'images par arbres de décision.* PhD thesis, University of Liège, 2005. (pages 112, 113, 114, 115, 116, 118).

[125] MARÉE, R., GEURTS, P., PIATER, J., AND WEHENKEL, L. A generic approach for image classification based on decision tree ensembles and local sub-windows. In *Proceedings of the 6th Asian Conference on Computer Vision* (2004). (page 116).

[126] MARÉE, R., GEURTS, P., PIATER, J., AND WEHENKEL, L. Random subwindows for robust image classification. In *Proceedings of the IEEE Conference on Computer Vision and Pattern Recognition* (2005). (page 112).

[127] MARÉE, R., GEURTS, P., AND WEHENKEL, L. Une méthode générique pour la classification automatique d'images à partir des pixels. *Revue des Nouvelles Technologies de l'Information* (2003). (page 116).

[128] MARÉE, R., GEURTS, P., AND WEHENKEL, L. Biological image classification with random subwindows and extra-trees. Workshop on Multiscale Biological Imaging, Data Mining & Informatics, 2006. (page 116).

[129] MARÉE, R., GEURTS, P., AND WEHENKEL, L. Random subwindows and extremely randomized trees for image classification in cell biology. *BMC Cell Biology supplement on Workshop of Multiscale Biological Imaging, Data Mining and Informatics* (2007). (page 112).

[130] MARÉE, R., GEURTS, P., AND WEHENKEL, L. Content-based image retrieval by indexing random subwindows with randomized trees. *IPSJ Transactions on Computer Vision and Applications.* (2009). (page 116).

[131] MENSA, D., HALEVY, S., AND WADE, G. Coherent Doppler tomography for microwave imaging. *Proceedings of the IEEE* (1983). (page 19).

[132] MISHRA, A., AND MULGREW, B. Bistatic SAR ATR. *IET Proceedings Radar, Sonar, and Navigation* (2007). (page 20).

[133] MITCHELL, R., AND DEWALL, R. Overview of high range resolution radar target identification. In *Proceedings of the Automatic Target Recognition Working Group Conference* (1994). (page 19).

[134] MITCHELL, T. *Machine learning.* McGraw-Hill, 1997. (pages 2, 106, 109).

[135] MITOLA III, J., AND MAGUIRE JR, G. Cognitive radio: making software radios more personal. *IEEE Personal Communications* (1999). (pages 181, 183).

[136] MORUZZIS, M., AND GUILLEROT, J. Analysis of experimental data for NCTR target modelling. *Thomson-CSF, Radar Signature Analysis and Imaging of Military Targets* (1997). (page 19).

[137] MUEHE, C. The moving target detector. *IEEE Transactions on Aerospace and Electronic Systems* (2006). (page 9).

[138] NATTERER, F. *The mathematics of computerized tomography.* Society for Industrial Mathematics, 2001. (pages 19, 80).

[139] NATTERER, F., AND WUBBELING, F. *Mathematical methods in image reconstruction.* Society for Industrial Mathematics, 2001. (page 80).

[140] NOVAK, L. State-of-the-art of SAR automatic target recognition. In *The Record of the IEEE International Radar Conference* (2000). (page 19).

[141] OJA, E. *Subspace methods of pattern recognition.* Research Studies Press Letchworth, 1983. (pages 143, 147).

[142] OPPENHEIM, A., WILLSKY, A., AND NAWAB, S. *Signals and systems.* Prentice-Hall, 1983. (pages 80, 81, 102).

[143] PARK, S., PARK, K., JUNG, J., KIM, H., AND KIM, K. Construction of training database based on high frequency RCS prediction methods for ATR. *Journal of Electromagnetic Waves and Applications* (2008). (page 19).

[144] PARK, S., SMITH, M., AND MERSEREAU, R. Target recognition based on directional filter banks and higher-order neural networks. *Digital Signal Processing* (2000). (page 20).

[145] PATNAIK, R., AND CASASENT, D. MINACE filter classification algorithms for ATR using MSTAR data. In *Proceedings of SPIE* (2005), vol. 5807. (page 20).

[146] PIÉRARD, S., LEROY, D., HANSEN, J., AND VAN DROOGENBROECK, M. Estimation of human orientation in images captured with a range camera. *Advances Concepts for Intelligent Vision Systems* (2011). (page 116).

[147] PIÉRARD, S., AND VAN DROOGENBROECK, M. Estimation of human orientation based on silhouettes and machine learning principles. In *Proceedings of the International conference on pattern recognition applications and methods (ICPRAM)* (2012). (page 116).

[148] PIETTE, M. Réponse impulsionnelle de cibles militaires tridimensionnelles: Conception, développement et validation d'un banc de mesure. In *AGARD Conference Proceedings* (1997). (page 18).

[149] PISANE, J., AZARIAN, S., LESTURGIE, M., AND VERLY, J. Automatic real-time collection of RCS of airplanes in a real bistatic low-frequency configuration using a software defined passive radar based on illuminators of opportunity. In *Proceedings of the IEEE Radar Conference* (2012). (page 231).

[150] PISANE, J., AZARIAN, S., LESTURGIE, M., AND VERLY, J. Passive radar testbed and preliminary experiments in recognition of non-cooperative aircraft intruding into controlled airspace. In *URSI Benelux Forum* (2012). (page 231).

[151] PISANE, J., AZARIAN, S., LESTURGIE, M., AND VERLY, J. Target classification in bistatic low frequency radar. In *2nd Thales Radar PhD Day* (2012). (page 232).

[152] PISANE, J., LESTURGIE, M., AND VERLY, J. Passive target classification based on low-frequency bistatic backscattering coefficients. In *Proceedings of the Conference on Ocean & Coastal Observation: Sensors and Systems* (2010). (page 231).

[153] PISANE, J., LESTURGIE, M., AND VERLY, J. Target classification of experimentally-acquired low-frequency backscattering coefficients by construction of subspaces. In *URSI Benelux Forum* (2010). (page 231).

[154] PISANE, J., LESTURGIE, M., AND VERLY, J. Target classification system based on the characterization of targets by subspaces. In *Proceedings of the IEEE CIE International Conference on Radar* (2011). (page 231).

[155] PISANE, J., MARÉE, R., RIES, P., WEHENKEL, L., AND VERLY, J. An extra-trees-based automatic target recognition algorithm. In *Proceedings of the IEEE International Radar Conference* (2009). (page 232).

[156] PISANE, J., MARÉE, R., WEHENKEL, L., AND VERLY, J. Radar classification based on extra-trees. In *2nd SONDRA Workshop Cargese* (2010). (page 232).

[157] PISANE, J., MARÉE, R., WEHENKEL, L., AND VERLY, J. Robust automatic target recognition using extra-trees. In *Proceedings of the IEEE International Radar Conference* (2010). (page 231).

[158] POMMET, D., MORRIS, J., MCGAHAN, R., AND FIDDY, M. Imaging of unknown targets from measured scattering data. *IEEE Antennas and Propagation Magazine* (1999). (page 19).

[159] POULLIN, D. Passive detection using digital broadcasters (DAB, DVB) with COFDM modulation. In *IEE Proceedings on Radar, Sonar, and Navigation* (2005). (page 17).

[160] PRADA, C., AND FINK, M. Eigenmodes of the time reversal operator: A solution to selective focusing in multiple-target media. *Wave motion* (1994). (page 145).

[161] PRADA, C., MANNEVILLE, S., SPOLIANSKY, D., AND FINK, M. Decomposition of the time reversal operator: Detection and selective focusing on two scatterers. *Journal of the Acoustical Society of America* (1996). (page 145).

[162] PRADA, C., THOMAS, J., ET AL. Experimental subwavelength localization of scatterers by decomposition of the time reversal operator interpreted as a covariance matrix. *Journal of the Acoustical Society of America* (2003). (page 145).

[163] PRADA, C., THOMAS, J., AND FINK, M. The iterative time reversal process: Analysis of the convergence. *The Journal of the Acoustical Society of America* (1995). (page 145).

[164] PRAKASH, M., AND MURTY, M. Extended subspace methods of pattern recognition. *Pattern recognition letters* (1996). (page 147).

[165] QUINQUIS, A., RADOI, E., AND TOTIR, F. Some radar imagery results using superresolution techniques. *IEEE Transactions on Antennas and Propagation* (2004). (pages 19, 92).

[166] RADOI, E., QUINQUIS, A., AND TOTIR, F. Supervised self-organizing classification of superresolution ISAR images: an anechoic chamber experiment. *EURASIP Journal on Applied Signal Processing* (2006). (page 20).

[167] RAMM, A., AND KATSEVICH, A. *The Radon transform and local tomography.* CRC Press, 1996. (pages 19, 80).

[168] REGISTER, A., BLAIR, W., EHRMAN, L., AND WILLETT, P. Using measured RCS in a serial, decentralized fusion approach to radar-target classification. In *IEEE Aerospace Conference* (2008). (page 21).

[169] RICHARDS, M. *Fundamentals of radar signal processing.* McGraw-Hill, 2005. (page 117).

[170] RIEGGER, S., AND WIESBECK, W. Wide-band polarimetry and complex radar cross section signatures. *Proceedings of the IEEE* (1989). (pages 26, 55).

[171] RIHACZEK, A. *Principles of high-resolution radar.* Artech House, 1996. (page 117).

[172] RINGER, M., AND FRAZER, G. Waveform analysis of transmissions of opportunity for passive radar. In *Proceedings of the Fifth IEEE International Symposium on Signal Processing and Its Applications (ISSPA'99)* (1999). (pages 16, 17).

[173] SADJADI, F. *Physics of automatic target recognition.* Springer, Feb 2007. (page 2).

[174] Sensor Data Management System, US Air Force. MSTAR overview. Website, 2012. `https://www.sdms.afrl.af.mil/content/mstar/MSTAR_Public_Data_References_040421.doc`. (page 20).

[175] Sensor Data Management System, US Air Force. MSTAR public targets. Website, 2012. `https://www.sdms.afrl.af.mil/index.php?collection=mstar&page=targets`. (page 117).

[176] Sharma, A., and Moses, R. Matched subspace detectors for discrimination of targets from trees in SAR imagery. In *Conference Record of the Thirty-Fourth IEEE Asilomar Conference on Signals, Systems and Computers* (2000). (page 143).

[177] Sharp, T. Implementing decision trees and forests on a GPU. In *Proceedings of the European Conference on Computer Vision (ECCV)* (2008), Springer. (page 115).

[178] Shotton, J., Fitzgibbon, A., Cook, M., Sharp, T., Finocchio, M., Moore, R., Kipman, A., and Blake, A. Real-time human pose recognition in parts from single depth images. In *Proceedings of the IEEE International Conference on Computer Vision and Pattern Recognition (CVPR)* (2011). (page 115).

[179] Shotton, J., Johnson, M., and Cipolla, R. Semantic texton forests for image categorization and segmentation. In *Proceedings of the IEEE International Conference on Computer Vision and Pattern Recognition (CVPR)* (2008). (page 115).

[180] Siegel, K. Far field scattering from bodies of revolution. *Applied scientific research: Electrophysics, acoustics, optics, mathematical methods* (1957). (pages 31, 32).

[181] Siegel, K., Alperin, H., Bonkowski, R., Crispin, J., Maffett, A., Schensted, C., and Schensted, I. Bistatic radar cross sections of surfaces of revolution. *Journal of Applied Physics* (1955). (pages 31, 39, 40, 41).

[182] Siegel, K., Bonkowski, R., Crispin, J., Maffett, A., Schensted, C., Schensted, I., and Alperin, H. Theoretical cross-sections as a function of separation angle between transmitter and receiver at small wavelengths. Tech. rep., University of Michigan, 1953. (pages 31, 32, 35, 37, 38, 40, 41).

[183] Sinclair, G. The transmission and reception of elliptically polarized waves. *Proceedings of the IRE* (1950). (pages 52, 53).

[184] Sizov, V., Cherniakov, M., and Antoniou, M. Forward scatter RCS estimation for ground targets. In *Proceedings of the IEEE European Microwave Conference* (2007). (page 39).

[185] Sizov, V., Cherniakov, M., and Antoniou, M. Forward scattering radar power budget analysis for ground targets. *IET Proceedings Radar, Sonar, and Navigation* (2007). (page 39).

[186] SKOLNIK, M. An analysis of bistatic radar. *IRE Transactions on Aerospace and Navigational Electronics* (1961). (pages 15, 101, 105, 176).

[187] SKOLNIK, M. Introduction to radar. *Radar Handbook* (1962). (pages 2, 3, 9, 15, 16, 30).

[188] SKOLNIK, M. Radar handbook (3rd edition), 2008. (pages 24, 26, 30, 31, 32, 38, 105).

[189] SLANEY, M., AND KAK, A. *Principles of computerized tomographic imaging.* SIAM, 1988. (page 19).

[190] SLOMKA, S., GIBBINS, D., GRAY, D., AND HAYWOOD, B. Features for high resolution radar range profile based ship classification. In *Proceedings of the Fifth IEEE International Symposium on Signal Processing and Its Applications (ISSPA)* (1999). (page 19).

[191] SOUMEKH, M. *Synthetic aperture radar signal processing.* Wiley, 1999. (page 19).

[192] STEVENS, M. *Secondary surveillance radar.* Artech House, 1988. (page 10).

[193] STRANG, G. *Introduction to linear algebra.* Wellesley Cambridge Pr, 2003. (pages 146, 147).

[194] STRATTON, J. *Electromagnetic theory.* McGraw-Hill, 1941. (pages 31, 32, 35).

[195] STRATTON, J., AND CHU, L. Diffraction theory of electromagnetic waves. *Physical Review* (1939). (pages 31, 32, 35).

[196] SULLIVAN, R. *Radar foundations for imaging and advanced concepts.* SciTech Publishing, 2004. (page 19).

[197] SUN, H., TAN, D., AND LU, Y. Design and implementation of an experimental GSM based passive radar. In *Proceedings of the International IEEE Radar Conference* (2003). (page 17).

[198] SUN, H., TAN, D., AND LU, Y. Aircraft target measurements using a GSM-based passive radar. In *Proceedings of the IEEE Radar Conference* (2008). (page 17).

[199] SUN, Y., LIU, Z., TODOROVIC, S., AND LI, J. Synthetic aperture radar automatic target recognition using adaptive boosting. In *Proceedings of SPIE* (2005), vol. 5808. (page 20).

[200] TAN, D., LESTURGIE, M., SUN, H., AND LU, Y. Target detection performance analysis for airborne passive bistatic radar. In *Proceedings of the IEEE Internaional Geoscience and Remote Sensing Symposium (IGARSS)* (2010). (page 16).

[201] TAN, D., SUN, H., AND LU, Y. Sea and air moving target measurements using a GSM based passive radar. In *Proceedings of the IEEE International Radar Conference* (2005). (page 17).

[202] TAN, D., SUN, H., LU, Y., LESTURGIE, M., AND CHAN, H. Passive radar using global system for mobile communication signal: theory, implementation and measurements. In *IEE Proceedings Radar, Sonar, and Navigation* (2005). (page 17).

[203] TAN, D., SUN, H., LU, Y., AND LIU, W. Feasibility analysis of GSM signal for passive radar. In *Proceedings of the IEEE Radar Conference* (2003). (page 17).

[204] TAYLOR JR, J., AND BRUNINS, G. Design of a new airport surveillance radar (ASR-9). *Proceedings of the IEEE* (1985). (page 9).

[205] THIRION-LEFEVRE, L., COLIN-KOENIGUER, E., AND DAHON, C. Bistatic scattering from forest components. Part I: coherent polarimetric modelling and analysis of simulated results. *Waves in Random and Complex Media* (2010). (page 26).

[206] THOMAS, J., BAKER, C., AND GRIFFITHS, H. DRM signals for HF passive bistatic radar. In *Proceedings of the IET International Conference on Radar Systems* (2007), IET. (page 17).

[207] THOMAS, J., BAKER, C., AND GRIFFITHS, H. HF passive bistatic radar potential and applications for remote sensing. In *New Trends for Environmental Monitoring Using Passive Systems* (2008), IEEE. (page 16).

[208] TOU, J., AND GONZÁLEZ, R. *Pattern recognition principles.* Addison Wesley, 1974. (page 109).

[209] TRIM, R. Mode S: An introduction and overview. *Electronics & Communication Engineering Journal* (1990). (page 11).

[210] UK, D. 3D CAD Browser. Website, 2012. `http://www.3dcadbrowser.com/`. (pages 63, 64).

[211] VAN DE HULST, H. *Light scattering by small particles.* Wiley, 1957. (pages 52, 53).

[212] VERLY, J. Physical optics polarization scattering matrix for a right-angle dihedral. Tech. rep., M.I.T., 1995. (pages 26, 32, 47, 50, 52, 53, 55, 56).

[213] VERLY, J., AND DELANOY, R. Model-based automatic target recognition (ATR) system for forwardlooking groundbased and airborne imaging laser radars (LADAR). *Proceedings of the IEEE* (1996). (page 20).

[214] VERLY, J., DELANOY, R., AND DUDGEON, D. Machine intelligence technology for automatic target recognition. *The Lincoln Laboratory Journal* (1989). (page 17).

[215] VERLY, J., DUDGEON, D., AND LACOSS, R. Progress report on the development of the automatic target recognition system for the UGV/RSTA LADAR. Tech. rep., M.I.T., 1995. (pages 17, 20).

[216] VERLY, J., DUDGEON, D., AND LACOSS, R. Model-Based Automatic Target Recognition System for the UGV/RSTA Ladar: Status at Demo C. Tech. rep., M.I.T., 1996. (page 20).

[217] VIGNAUD, L. Wavelet-relax feature extraction in radar images. In *IEE Proceedings Radar, Sonar, and Navigation* (2003). (page 20).

[218] WALTON, E., AND JOUNY, I. Bispectrum of radar signatures and application to target classification. *Radio Science* (1990). (page 19).

[219] WATANABE, S. *Knowing and guessing: a quantitative study of inference and information.* John Wiley & Sons, 1969. (page 147).

[220] WEHENKEL, L. *Automatic learning techniques in power systems.* Kluwer Academic Publishers, 1997. (page 115).

[221] WEHENKEL, L. *Applied inductive learning, note de cours.* Université de Liège, 2000. (pages 3, 91).

[222] WEHNER, D. *High resolution radar.* Artech House, 1987. (pages 19, 117).

[223] WILLIAMS, R., WESTERKAMP, J., GROSS, D., AND PALOMINO, A. Automatic target recognition of time critical moving targets using 1D high range resolution (HRR) radar. *IEEE Aerospace and Electronic Systems Magazine* (2000). (page 19).

[224] WILLIS, N. *Bistatic radar.* SciTech Publishing, 2005. (pages 3, 15, 16, 41, 88, 177).

[225] WILLIS, N., AND GRIFFITHS, H. *Advances in bistatic radar.* SciTech Publishing, 2007. (pages 4, 15, 41).

[226] XU, L., KRZYZAK, A., AND OJA, E. Neural-net method for dual subspace pattern recognition. In *Proceedings of the IEEE International Joint Conference on Neural Networks (IJCNN)* (1991). (page 147).

[227] YANG, C., AND BLASCH, E. Pose-angular tracking of maneuvering targets with high range resolution (HRR) radar. In *Proceedings of the International Conference on Information Fusion* (2008). (page 19).

[228] YANG, Y., QIU, Y., AND LU, C. Automatic target classification: Experiments on the MSTAR SAR images. In *Proceedings of the Sixth International Conference on Software Engineering, Artificial Intelligence, Networking, and Parallel/Distributed Computing (SNPD), and First ACIS International Workshop on Self-Assembling Wireless Networks (SAWN)* (2005). (page 20).

[229] YI, J., BHANU, B., AND LI, M. Target indexing in SAR images using scattering centers and the Hausdorff distance. *Pattern Recognition Letters* (1996). (page 17).

[230] ZHANG, P., PENG, J., AND DOMENICONI, C. Kernel pooled local subspaces for classification. *IEEE Transactions on Systems, Man, and Cybernetics. Part B: Cybernetics* (2005). (page 143).

[231] Zhao, Q., and Principe, J. Support vector machines for SAR automatic target recognition. *IEEE Transactions on Aerospace and Electronic Systems* (2001). (page 20).

[232] Zhao, Q., Xu, D., and Principe, J. Pose estimation of SAR automatic target recognition. In *Proceedings of Image Understanding Workshop* (1998). (page 20).

[233] Ziade, Y., Roussel, H., Lesturgie, M., and Tabbara, W. A coherent model of forest propagation: Application to detection and localization of targets using the DORT method. *IEEE Transactions on Antennas and Propagation* (2008). (page 145).

[234] Zyweck, A., and Bogner, R. Radar target classification of commercial aircraft. *IEEE Transactions on Aerospace and Electronic Systems* (1996). (page 19).